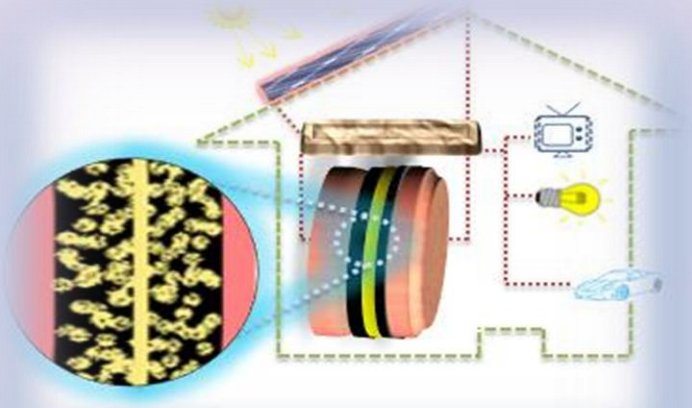

DOCTORAL THESIS

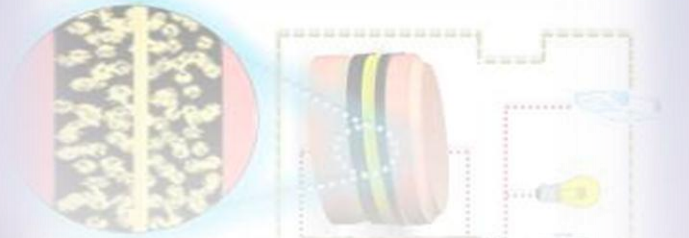

APPLICATION OF IONIC LIQUIDS, INNOVATIVE POLYMER ELECTROLYTES AND NOVEL CARBONACEOUS MATERIALS IN SUPERCAPACITORS

GIRUM AYALNEH TIRUYE

APPLICATION OF IONIC LIQUIDS, INNOVATIVE POLYMER ELECTROLYTES AND NOVEL CARBONACEOUS MATERIALS IN SUPERCAPACITORS

BY

GIRUM AYALNEH TIRUYE

A Thesis

Submitted to the Autonomous University of Madrid in Fulfilment of the Requirements for the Degree of Doctor of Philosophy in Energies and Fuels for the Future, from Department of Applied Physical Chemistry

Electrochemical Process Unit, IMDEA Energy Institute

Madrid, Spain

April 2016

Supervisor:

Dr. Rebeca Marcilla

IMDEA Energy Institute, Madrid, Spain

Tutor:

Dr. Pilar Ocón Esteban

Autonomous University of Madrid, Madrid Spain

Declaration

I, Girum Ayalneh Tiruye, declare that the thesis submitted is my own orginal work, except where work that has formed part of jointly project and authored publications has been included and that appropriate credit has been given where reference has been made to the work of others.

Dedicated To

My Family

ABSTRACT

The burgeoning world energy crisis and concerns about climate change have recently promoted the use of renewable energy resources (for *e.g.*, sun and wind). Nevertheless, energy from such renewable energy resources is weighed down by fluctuations (*e.g.*, due to intermittent availability of sun and wind). This results in a mismatch between energy supply and energy demand if the energy supplied from such resources is used. An important solution to this problem is coupling renewable energy resources with electrochemical energy storage devices (*i.e.*, batteries and supercapacitors). Currently, the dominant electrochemical energy storage technologies are batteries despite they suffer from slow power delivery and uptake. Similarly, the shortcoming of the current supercapacitors is unable to store high energy. Yet, a device that could concurrently store high energy and power densities is required for different applications such as portable electronic device, electric vehicles, and different energy storage industries. Supercapacitors are complementary to batteries, since they present higher power density, higher charge-discharge rates, better cycle stability, and safer operation than batteries. Nevertheless, the energy density of supercapacitors is lower than the one in batteries. Consequently, it has raised the question of how to increase the energy density of supercapacitors without deteriorating its power density and safety. To tackle this problem, two main strategies are considered in the scientific community. The first one is the development of novel electrode materials with high intrinsic capacitance and second, the use of electrochemically stable electrolytes such as ionic liquids that allow supercapacitors to operate at higher voltages. However, using liquid electrolytes in conventional supercapacitors is usually accompanied by additional heavy encapsulation materials to prevent liquid leakage, and separator to avoid short circuit. These construction restrictions prevent the development of lightweight and flexible supercapacitors for application in emerging market niche such as flexible electronics or textile integration. To overcome this issue, the development of solid or quasi-solid polymer electrolytes is being investigated to replace both liquid electrolytes and separator that are present in conventional supercapacitors.

In an attempt to circumvent all the above mentioned drawbacks of supercapacitors technology, this PhD Thesis is aimed at the development of high performance supercapacitors based on novel carbon based materials and electrochemically stable electrolytes including innovative polymer electrolytes.

This PhD Thesis is structured into six chapters. ***Chapter I*** includes a general introduction to fundamental principles of supercapacitors technology, electrode

materials and electrolytes for supercapacitors. Additionally, the current limitations, and challenges of supercapacitors and the main motivation and objectives of this PhD Thesis are briefly presented at the end of ***Chapter I***. Then, the principal part of the Thesis, devoted to the description of the results, is divided into four chapters. ***Chapter II*** and ***Chapter III*** are devoted to the synthesis of novel carbon based composite materials and their application as electrode for supercapacitors using ionic liquid (IL) electrolytes. ***Chapter IV*** and ***Chapter V*** are focused on the development of innovative polymer electrolytes based on ionic liquids (IL-b-PE) and their application in solid state supercapacitors. A final chapter, ***Chapter VI*****,** summarizes the main conclusions of this Thesis and future perspectives of supercapacitors technology. A short summary of those chapters is described below.

Chapter II presents the synthesis of nitrogen-doped carbons (N-dC) and their application in supercapacitors. By using a simple "salt templating method", highly microporous N-doped carbons (N-dC) were synthesized by simple heat-treatment of mixtures of precursors and eutectic salts. A sustainable and cheap tannic acid (TA) as carbon precursor, urea as nitrogen precursor and different eutectic salts ($NaCl/ZnCl_2$, $LiCl/ZnCl_2$, or $KCl/ZnCl_2$) as porogens were used for the synthesis of N-doped carbons. Physicochemical properties of N-dC were determined by adsorption-desorption isotherms, X-Ray diffraction, X-ray photoelectron spectroscopy, scanning electron microscope, etc. It was shown that properties of these materials (textural properties, nitrogen content, or electrical conductivity) can be easily controlled by the variation of composition of precursor mixtures, the salt amount, as well as the type of salts that were used as porogens. For instance, nitrogen content in N-doped carbons increases with the amount of urea. It reaches up to 8.8 % N with mixtures of 17:1 molar ratio of urea to TA (urea:TA) and 1:3 ratio of precursors (urea+TA) to $NaCl/ZnCl_2$ (urea+TA:$NaCl/ZnCl_2$) (GT_17_NaZ). Unexpectedly, the maximum electrical conductivity was not obtained for the carbon synthesized with 17:1 ratio of urea to TA (GT_17_NaZ). The highest electrical conductivity (76 Scm^{-1}) was obtained from the carbon synthesized with 9:1 molar ratio of urea to TA (GT_9_NaZ) that exhibited 8.3 % N due to its higher content of structural nitrogen functionalities compared with others. Moreover, textural analysis reveals that addition of urea to the precursor mixture decreases the specific surface area and total pore volume of N-doped carbons compared with the non-doped carbon. This is due to the incorporation of nitrogen functionalities into the carbon matrix which resulted in collapse of the carbon walls and blocks some micro pores within the walls. Similar studies were also carried out by varying the amount and type of eutectic salts. It shows that the amount and the type of eutectic salts significantly influence the textural properties of N-doped carbons.

Chapter II also includes the electrochemical performance of N-doped carbons in aqueous electrolyte (1 M H_2SO_4) and in 1-butyl-1-methylpyrrolidinium bis(fluorosulfonyl) imide ($PYR_{14}FSI$). The synergetic effect of physico-electrochemical properties of N-doped carbons and intrinsic properties of electrolytes significantly influence the performance of supercapacitors. Specifically, the carbon synthesized with a mixtures of 9:1 molar ratio of urea to tannic acid (urea:TA) and 1:3 mass ratio of precursors (urea+TA) to eutectic salt $NaCl/ZnCl_2$ (GT_9_NaZ carbon) presents the highest capacitance of 295 Fg^{-1} and 119 Fg^{-1} in 1 M H_2SO_4 and $PYR_{14}FSI$, respectively. It was also revealed that the maximum real energy stored in supercapacitors based on N-doped carbons is as high as 6-7 $Whkg^{-1}$ and 33 $Whkg^{-1}$ in H_2SO_4 and $PYR_{14}FSI$, respectively. This due to the combination of high electrical conductivity (76 $mScm^{-1}$), high specific area (1329 m^2g^{-1}), and high nitrogen content presented by GT_9_NaZ N-doped carbon compared with others. The huge difference in the performance of N-doped carbons in 1 M H_2SO_4 and $PYR_{14}FSI$ electrolytes is probably due to the difference in ionic conductivity of the two electrolytes. Moreover, the variation of effective surface area (S_{eff}) that can be accessed by ions of the respective electrolyte is also significantly influences the performance of supercapacitors.

Chapter III presents the synthesis of composites of Vanadium nitride (VN) nanoparticles in N-doped carbons (VN@N-dC) by heating mixtures of Vanadium precursors ($VOCl_3$ or NH_4VO_3), ionic liquid 1-ethyl-3-methyl-imidazolium dicyanamide (Emim-dca) and salts, *i.e.*, cesium or zinc acetate, as porogens. ***Chapter III*** describes the effect of porogen salts and vanadium precursors on physico-chemical and electrochemical properties of composites. For instance, using low concentration of cesium acetate (CsAc) resulted in microporous carbon with small VN nanoparticles (VN@N-dC) and a specific surface area of 1000 m^2g^{-1}, while increasing salt amount promotes generation of small meso-pores with bigger nanoparticles and higher specific surface area up to 2400 m^2g^{-1}. In addition, utilizing zinc acetate (ZnAc) salt enabled the synthesis of entirely mesoporous composites with very small vanadium nitride nanoparticles (VN@N-dC) and specific surfaces areas of 800 m^2g^{-1}. Mixtures of these two salt porogens (CsAc & ZnAc) gave access to independently tuneable pore size, pore volume, particle size, and intermediate surfaces areas. ***Chapter III*** also includes the electrochemical performance of VN@N-dC and their applications as electrodes for supercapacitors in two different ionic liquids; $PYR_{14}FSI$ and 1-butyl-1-methylpyrrolidinium bis(trifluoromethanesulfonyl)imide ($PYR_{14}TFSI$). Better results were obtained in $PYR_{14}FSI$ electrolyte probably due to the higher ionic conductivity of this IL and the smaller size of FSI anion that could easily access the VN nanoparticles. Moreover, considering the synergetic properties of the composite materials, the

maximum specific capacitance and real energy was stored by VN@N-dC synthesized with high content of CsAc salt and $VOCl_3$ (VN@N-dc-1000-CsAc-$VOCl_3$), exhibiting 125 Fg^{-1} and 37 $Whkg^{-1}$, respectively. This confirms an improvement of specific energy density by 15 % from that of the best performing N-doped carbon (GT_9_NaZ) in $PYR_{14}FSI$ electrolyte. This is due to the high specific surface area of VN@N-dC and the presence of big VN nanoparticles that contribute to additional pseudocapacitance.

Chapter IV & V present the synthesis of novel polymer electrolytes and their applications in solid state supercapacitors. In ***Chapter IV*** a polymer electrolyte based on a binary mixture of a Polymeric Ionic Liquid, Poly(diallyldimethylammonium) bis(trifluoromethanesulfonyl)imide (PILTFSI) and a ionic liquid ($PYR_{14}TFSI$) was synthesized and characterized. All-solid state supercapacitors based on this polymer electrolyte (IL-b-PE), having 60 % wt. of IL, and activated carbon as electrodes were assembled and characterized. Due to the variation of double layer formation at the interfaces of electrolyte and electrodes, impregnation of activated carbon electrodes with a solution of IL-b-PE enhances capacitance of all-solid state supercapacitors compared with supercapacitors assembled by sandwiching an IL-b-PE membrane between two carbon electrodes. Moreover, supercapacitors with different impregnation ratios (electrolyte mass/active material mass) ranging from 5 to 18 were assembled simply by facing two impregnated electrodes without additional separator. All-solid state supercapacitors with impregnation ratio of 7 showed the best performance with specific capacitance and real energy of 100 Fg^{-1} and 32 Wh kg^{-1}, respectively at 1 $mAcm^{-2}$ and 3.5 V.

Chapter V describes how the nature of ionic liquid in the polymer matrix affects the properties of polymer electrolytes and the final supercapacitor device. In particular, four different polymer electrolytes were prepared by blending the same Polymeric Ionic Liquid, PILTFSI, with four different ionic liquids; ($PYR_{14}TFSI$) (IL-b-PE1), ($PYR_{14}FSI$) (IL-b-PE2),1-(2-hydroxyethyl)-3-methylimidazolium bis(trifluoromethylsulfonyl)imide (HEMimTFSI) (IL-b-PE3), and 1-butyl-1-methylpyrrolidinium dicyanamide, ($PYR_{14}DCA$) (IL-b-PE4). Physicochemical properties of IL-b-PE such as ionic conductivity, thermal and electrochemical stability were found to be dependent on the intrinsic properties of IL embedded in the polymer matrix. Specifically, ionic conductivity was significantly higher for IL-b-PE2 (2.1 $mScm^{-1}$) and IL-b-PE4 (2.09 $mScm^{-1}$) containing IL with small size anions (FSI, 0.3 nm and DCA, 0.24 nm) than IL-b-PE1 (0.41 $mScm^{-1}$) and IL-b-PE3 (0.86 $mScm^{-1}$) bearing IL with bigger anion (TFSI, 0.8 nm). On the other hand, wider electrochemical stability window (ESW) was found for IL-b-PE1 and IL-b-PE2 (up to 3.5 V) having ILs with electrochemically stable pyrrolidinium cation and FSI and TFSI anions. The best electrochemical performance

was obtained by IL-b-PE2, exhibiting maximum specific capacitance and maximum real energy density as high as 150 Fg^{-1}, and 36 $Whkg^{-1}$, respectively at 1 $mAcm^{-2}$ and 3.5 V. Those values are higher than the one reported in literature for solid supercapacitors based on conventional polymer electrolytes probably due to the higher operating voltage (up to 3.5 V) of IL-b-PE. It was demonstrated that a conscious selection of stable polymer matrixes such as PILTFSI and compatible ILs as well as integrating and optimizing IL-b-PE with activated carbon electrodes result in high performance all-solid state supercapacitors. For future perspective, this strategy will pave the way for the development of novel solid state, lightweight, and flexible energy storage devices.

RESUMEN

La creciente crisis energética mundial y la preocupación sobre el cambio climático han promovido recientemente el uso de energías renovables tales como la energía solar o la eólica. Sin embargo, la generación de energía a partir de estas fuentes renovables está sometida a muchas fluctuaciones debido a la intermitente disponibilidad de sol o viento. Esto hace que exista un desequilibrio entre la producción y la demanda de energía. El acoplamiento de dispositivos de almacenamiento electroquímico de energía, como baterías y supercondensadores, a la producción de energía renovable se plantea como solución a este problema. Actualmente son las baterías los dispositivos predominantes para el almacenamiento electroquímico debido a su alta densidad de energía aunque sólo pueden entregar y absorber energía a baja potencia. No obstante, existen diferentes aplicaciones como dispositivos electrónicos portátiles, vehículos eléctricos y diferentes industrias que requieren dispositivos que puedan almacenar grandes cantidades de potencia y energía al mismo tiempo. Los supercondensadores pueden complementar a las baterías debido a que, pese a que su densidad de energía es menor, pueden suministrar energía a altas densidades de potencia, tienen alta velocidad de carga-descarga, soportan muchos más ciclos de operación y son más seguros que las baterías. Como consecuencia, uno de los retos a los que se enfrenta la tecnología de los supercondensadores es cómo aumentar su densidad energética sin deteriorar su densidad de potencia, robustez y seguridad. Para hacer frente a este problema, se han considerado dos estrategias principales entre la comunidad científica. El desarrollo de nuevos materiales de electrodo con alta capacidad intrínseca y la utilización de electrolitos electroquímicamente estables tales como líquidos iónicos que permitan operar a altos voltajes. Por otro lado, la utilización de electrolitos líquidos lleva consigo el uso de un separador para evitar cortocircuitos así como la necesidad de un sellado hermético, generalmente con materiales pesados, para evitar fugas del electrolito. Todo esto limita al supercondensador para su uso en nuevos nichos de mercado como en aplicaciones flexibles o integración en textiles. Para poder solucionar este problema se están desarrollado electrolitos poliméricos sólidos o cuasi-sólidos para reemplazar tanto al electrolito y al separador, presentes en supercondensadores convencionales.

En un intento de eludir los inconvenientes actuales de la tecnología de supercondensadores, esta tesis doctoral tiene como objetivo el desarrollo de supercondensadores de alto rendimiento mediante el uso de nuevos materiales carbonosos y electrolitos electroquímicamente estables entre los que se incluyen electrolitos poliméricos innovadores.

Seis capítulos componen esta tesis doctoral. El **Capítulo I** incluye una introducción general de los principios fundamentales de la tecnología de los supercondensadores; materiales que componen los electrodos y electrolitos; actuales limitaciones y desafíos de los supercondensadores y finalmente, la motivación y objetivos principales de la tesis. Tras este primer capítulo se encuentra la parte principal de la tesis, dedicada a la descripción de los resultados y que está formada por cuatro capítulos. El **Capítulo II** y el **Capítulo III** están dedicados a la síntesis de materiales carbonosos y composites innovadores y su aplicación como electrodos para supercondensadores usando líquido iónico como electrolito. El **Capítulo IV** y el **Capítulo V** se centran en el desarrollo de electrolitos poliméricos basados en líquidos iónicos (IL-b-PE) y su aplicación en supercondensadores sólidos. El capítulo final, **Capítulo VI**, resume las principales conclusiones de esta tesis y futuras perspectivas de la tecnología de supercondensadores. Un pequeño resumen de estos capítulos se encuentra a continuación.

El **Capítulo II**, presenta un método de síntesis de carbones dopados con nitrógeno (N-dC) y la aplicación de dichos materiales en supercondensadores. Mediante la aplicación del método "salt-templating" se sintetizaron, de manera sencilla y en una sola etapa, carbones dopados con nitrógeno (N-dC) altamente porosos. Se trata de someter a un tratamiento térmico una mezcla compuesta de un precursor de carbón sostenible y barato (ácido tánico, TA) un precursor de nitrógeno (urea) y diferentes sales eutécticas ($NaCl/ZnCl_2$, $LiCl/ZnCl_2$ o $KCl/ZnCl_2$) que actúan de agentes porógenos. Las propiedades físico-químicas de estos N-dC se caracterizaron mediante isotermas de adsorción de gases, difracción de rayos X, espectroscopia de fotoelectrones de rayos-X (XPS) y microscopía electrónica de barrido (SEM). Se demostró que modificando las condiciones de síntesis se pueden modificar las propiedades texturales (tamaño de poro, volumen de poro, morfología y área superficial específica), el contenido en nitrógeno o la conductividad eléctrica de los carbones. Por ejemplo, la cantidad de nitrógeno de los N-dC aumenta con la cantidad de urea alcanzando el 8.8% con una proporción molar 17:1 de urea frente a acido tánico y una relación 1:3 para los precursores frente a la sal $NaCl/ZnCl_2$ (urea+TA: $NaCl/ZnCl_2$) (GT_17_NaZ). La conductividad eléctrica máxima (76 Scm^{-1}) no se obtuvo para este carbón sino para el (GT_9_NaZ) sintetizado con una relación molar de urea frente a TA de 9:1 y que tiene un contenido de nitrógeno del 8.3%. El análisis XPS muestra que GT_9_NaZ presenta un mayor contenido relativo de nitrógeno estructural responsable de la mayor densidad electrónica en el nivel de Fermi y por tanto, de una mayor conductividad eléctrica. Además, el análisis textural revela que la adición de urea disminuye el área superficial específica del carbón dopado con nitrógeno en

comparación con el carbono no dopado. Esto se debe a que la incorporación de grupos funcionales de nitrógeno en la matriz de carbón produce el colapso de las paredes de carbono y bloquea algunas microporosidades. Se llevaron a cabo estudios similares mediante la variación tanto de la cantidad como del tipo de sal eutéctica utilizada demostrándose que estos factores afectan de manera significativa a las propiedades texturales de los carbones dopados con nitrógeno.

En el **Capítulo II** también se estudia el comportamiento electroquímico de los N-dC en electrolito acuoso (1 M H_2SO_4) y en 1-butil-3-metilpirrolodinio bistrifluorometanosulfonimida ($PYR_{14}TFSI$). En ese capítulo de investiga cómo afectan al comportamiento de los supercondensadores las propiedades físico-químicas de los carbones sintetizados y las propiedades intrínsecas de los electrolitos estudiados. Específicamente, el carbón sintetizado con una proporción molar 1:9 de urea:TA y una proporción de 1:3 de precursores frente a NaCl/ZnCl2 (GT_9_NaZ) obtuvo los valores más altos de capacitancia específica de 295Fg^{-1} en medio acuoso y de 119Fg^{-1} en $PYR_{14}TFSI$. Los valores de densidad de energía del supercondensador fueron tan altos como 6-7 $Whkg^{-1}$ y 33 $Whkg^{-1}$ en 1M H_2SO_4 y $PYR_{14}FSI$, respectivamente. El excelente comportamiento de este carbón se debe a la alta conductividad eléctrica (76$mScm^{-1}$), al alta área superficial (1329m^2g^{-1}) y al alto contenido de nitrógeno, comparado con los otros. La gran diferencia en el comportamiento de estos carbones dopados en electrolitos acuosos o líquidos iónicos se debe probablemente a la diferencia en la conductividad iónica de los electrolitos y a la variación del área superficial efectiva (S_{eff}) a la que los iones de sendos electrolitos pueden acceder.

El **Capítulo III** describe la síntesis de materiales compuestos basados en N-dC que incorporan nanopartículas de nitruro de vanadio (VN). Este material, que denominaremos VN@N-dC, se sintetizó mediante tratamiento térmico de mezclas compuestas por precursor de vanadio ($VOCl_3$ o NH_4VO_3), el líquido iónico 1-etil-3-metil-imidazolio de dicianamida (Emim-dca) usado como disolvente así como fuente de nitrógeno y carbón y sales como el acetato de zinc o de cesio como agentes porógenos. En este capítulo se investiga el efecto de las sales que actúan como agentes porógenos y los precursores de vanadio en las propiedades físico-químicas y electroquímicas de los materiales compuestos sintetizados. Por ejemplo, el uso de una baja concentración de acetato de cesio (CsAc) como porógeno, dio lugar a una estructura microporosa con pequeñas nanopartículas de VN con una superficie específica en torno a 1000 m^2g^{-1}. El aumento de la cantidad de sal dio lugar a la generación de pequeños mesoporos con nanopartículas más grandes y mayor área superficial específica, 2400 m^2g^{-1}. Además, la utilización de acetato de Zinc (ZnAc) como sal promueve la síntesis de compuestos enteramente mesoporosos con

nanopartículas de nitruro de vanadio de pequeño tamaño y áreas superficies específicas de 800 m^2g^{-1}. La utilización de mezclas de las dos sales porógenas (CsAc y ZnAc) permiten modificar el tamaño poro, el volumen de poro, el tamaño de partícula y el área superficial de los VN@N-dC. En el **Capítulo III** se incluye el estudio del comportamiento electroquímico de VN@N-dC y sus aplicaciones como electrodos en supercondensadores utilizando dos líquidos iónicos diferentes; $PYR_{14}FSI$ y bistrifluorometanosulfonimida de 1-butil-1metilpirrolidinio ($PYR_{14}TFSI$). Se obtuvieron mejores resultados en $PYR_{14}FSI$ probablemente debido a la mayor conductividad iónica de este líquido iónico y el menor tamaño del anión FSI, por lo que podría acceder fácilmente a las nanopartículas de VN. Además, teniendo en consideración las propiedades sinérgicas de los materiales compuestos, los valores de capacitancia específica y energía real más elevados (125 Fg^{-1} y 37 $Whkg^{-1}$ respectivamente) se obtuvieron para el VN@N-dC sintetizado con alto contenido en sal de CsAc y con $VOCl_3$ (VN@NdC-1000-CsAc-$VOCl_3$). Estos valores confirman una mejora en la densidad de energía específica de un 15% en comparación con el N-dC que muestra el mejor rendimiento (GT_9_NaZ) con $PYR_{14}FSI$ como electrolito. Esto se debe a la alta superficie específica de este VN@N-dC y la presencia de grandes nanopartículas VN que contribuyen a la pseudocapacitancia adicional.

Los **Capítulos IV** y **V** presentan la síntesis de electrolitos poliméricos novedosos y su aplicación en supercondensadores sólidos. En el **Capítulo IV** se estudia la síntesis y caracterización de un electrolito polimérico basado en una mezcla binaria de un líquido iónico polimérico, poli(bistrifluorometanosulfonimida) de dimetilamonio (PILTFSI) y un líquido iónico ($PYR_{14}TFSI$). Se montaron y caracterizaron supercondensadores sólidos formados por dos electrodos de carbón activado y un electrolito polimérico (IL-b-PE) que contiene un 60% de IL en peso. Cuando se montan los supercondensadores introduciendo una membrana de electrolito polimérico entre dos electrodos la falta de penetración de la membrana en los microporos del carbón hace que la capacitancia sea muy pequeña porque la formación de la doble capa se limita a la interfase electrodo/electrolito. Para resolver este problema, previamente al montaje del supercondensador, los electrodos se impregnaron con una disolución del electrolito polimérico de modo que, al evaporarse el electrolito el electrolito polimérico llenara los poros del carbón. El montaje final del supercondensador se realizó enfrentando dos electrodos impregnados sin separador adicional. Se montaron supercondensadores con ratios masa electrolito/masa de material activo que iban del 5 a 18. Los supercondensadores sólidos que mostraron mejor comportamiento mostraron fueron aquellos que tenían un ratio 7 con una capacitancia específica y una energía real

de 100 Fg^{-1} y 32 $Whkg^{-1}$ respectivamente, bajo condiciones de operación de 1 $mAcm^{-2}$ y 3.5 V.

En el **Capítulo V** se describe como la naturaleza del líquido iónico en la matriz polimérica afecta a las propiedades del electrolito polimérico y al supercondensador final. En particular, se prepararon cuatro electrolitos poliméricos diferentes mediante combinación del mismo líquido iónico polimérico, PILTFSI y cuatro líquidos iónicos diferentes: PYR_{14}TFSI (IL-b-PE1), PYR_{14}FSI (IL-b-PE2), bistrifluorometanosulfonimida de 1-2-hidroxiletil-3-metilimidazolio, HEmim-TFSI (IL-b-PE3) y dicianamida de 1-butil-1metilpirrolidinio, PYR_{14}DCA (IL-b-PE4). Se descubrió que las propiedades físico-químicas de los diferentes electrolitos poliméricos como la conductividad iónica, la estabilidad térmica y la ventana electroquímica dependen de las propiedades intrínsecas de los líquidos iónicos incorporados en el electrolito polimérico. Específicamente, las conductividades iónicas más altas se obtuvieron para IL-b-PE2 (2.1 $mScm^{-1}$) y IL-b-PE4 (2.09 $mScm^{-1}$) que contienen IL con aniones de pequeño tamaño (FSI, 0.3 nm y DCA, 0.24 nm) en comparación con IL -b-PE1 (0.41 $mScm^{-1}$) y IL-b-PE3 (0.86 $mScm^{-1}$) que contienen IL con un anión más grande (TFSI, 0.8 nm). Por otra parte, las ventanas de estabilidad electroquímica (ESW) más amplias fueron obtenidas para el IL-b-PE1 y el IL-b-PE2 (hasta 3.5 V) que tienen ILs con cationes pirrolidinio y aniones FSI y TFSI que son muy estables electroquímicamente. El mejor comportamiento electroquímico se obtuvo con el IL-b-PE2, exhibiendo valores de capacitancia y de energía específicas tan altas como 150 Fg^{-1}, y 36 $Whkg^{-1}$, respectivamente, en 1 $mAcm^{-2}$ y 3.5 V. Se ha demostrado que una cuidadosa y racional selección de matrices poliméricas estables como PILTFSI con ILs compatibles, así como la integración y optimización del electrolito polimérico con los electrodos de carbón activado dan como resultado supercondensadores sólidos con altas prestaciones. Para una perspectiva del futuro, esta estrategia va a allanar el camino para el desarrollo de dispositivos de almacenamiento de energía novedosos, sólidos, ligeros y flexibles.

Passion Gives You Energy and Power. Fill Yourself Up With Passion Daily!

ACKNOWLEDGMENT

First and above all, I praise God, the almighty for providing me strength, courage and granting me *the capacity* to proceed successfully this work.

Now it is time to acknowledge those amaizing individuals who helped me through one way or the other way for the successful completion of this Thesis.

This PhD Thesis represents not only my work at the keyboard but also it is a milestone in solid three years of work experience at IMDEA Energy Institute, specifically within Electrochemical Process unit as well as three months experience at Max Planck Institute for Colloids and Interfaces (MPI), Potsdam, Germany. My experience at these two institutes has been nothing short of amazing. Since my first day of arrival in March 2013 during the mild winter weather of Madrid, I have felt like home at IMDEA. I have been given opportunities and taken advantage of them. This includes working with diverse and multicultural teams, learning Spanish language and culture, and attending several national and international conferences which gave me opportunities to present my work and to be networked nationally and internationally. Throughout three years, I have gained experiences in interdisciplinary researches that encompass developing, designing, and charactering of electrochemical energy storage devices, material synthesis and characterizations as well as polymers and ILs on which this PhD thesis is dealing about. But it is also the result of many experiences I have encountered at IMDEA and MPI from dozens of remarkable individuals who I also wish to acknowledge.

First, and foremost, I wish to thank my supervisor, Dr**.** Rebeca Marcilla**.** She has been super in encouraging, advising and supporting me since the days I began working on Supercaps as predoctoral researcher. Thanks to Rebeca, I had the opportunity to develop “All-solid state Supercap” on which the work is already published in peer reviewed Journals! Ever since, Rebeca has supported me not only academically, but also helped me others: I remember, she gave me a lift from airport to my Hotel on my first day in Madrid, giving a phone call to landlords and ask a house for rent when Spanish language was a barrier to communicate for me, *pero ahora que no es un problema más: puedo llamar y hablar en Español, aún todaviá estoy aprendiendo todos los diás!* She also takes care of me when time was rough due to health problem during my research and she did everything for me what my sisters could do if they were here in Madrid, and what I can only say is *muchas gracias por todo*, Rebeca!

Besides, I would like to thank Prof. Marc Anderson for his insight full advice in research, and constrictive comments on the work during every teleconference of once per week for the last three years. Of course, I should take this advantage to thank Marc for taking out all of us from lab and inviting in Trufa Restaurant every time when he came from Wisconsin for short period visit. Thank you very much for everything Marc! I would also like to extend my sincere thanks to Dr. Jesus Palma for his insightful advices, comments on the work, invested his full effort in guiding the team in achieving the goal, listening always with patience, and solve issues related to administrations, especially great help with visa problem at the end of my PhD thesis. Thank you very much for everything, Jesus!

I would like to express my deepest appreciation to all of my great colleagues in Electrochemical process Unit : my great fellow lab mates: Cleis (thanks for page formatting), Paula, Nacho, David, Evgeny (*spasiba el crack Brat-"from half way line"*), Jaime, Dr. Afshin (thank you for proof reading a chapter), Dr. Enrique, Nabil , Vesselin and Dr. Puiki, all of you for helping in one way or the other way, for all the fun we have had in the lab and outside in every social event, teaching me Spanish language and culture, giving me a lift after a long & busy day in the lab to either train station or Madrid city, and for every stimulating discussion.....etc *Muchisimas gracias mis amigos!* Without you guys, it could have been difficult. My especial thank goes to David Muñoz: I would like to extend and express my apreciation for his extraordinary help during each experiment, translation and editing the abstract of this Thesis into Spanish. It could have been difficult to finisah all experiments within the given time unless he has helped me. Thank you very much David! Again, I would like to also extend my especial thanks to Paula N. She was the one who showed me how to prepare carbon paste at the very beginning of my PhD and great help as well in translating and editing the conclusion of this thesis into Spanish. *Muchas gracias Paula!*

I would also thank Prof. David Serrano (director of Imdea Energy) for his constractive advice and motivations on my work during our annual meetings and evaluation period. Furthermore I would also like to acknowledge with much appreciation for the crucial role of the Administration staff of IMDEA for every facility in the lab and office, and all Lab Technicians (especially, Laura Garcia, Dr. Fernanodo, and Maria Eugenia), who helped me to use all required equipment and the necessary materials to complete the task. Thank you very much all of you!

In addition, I would like to thank everybody from each unit of IMDEA for helping me in one way or the other way. Dozens of people have helped & taught me immensely at IMDEA. Especially, I am grateful to *"IMDEA Hipsters"* for the fun we have had together, football, trip together, of course doing party as well...etc*, Gracias Chavales!*

My sincere thanks also goes to Prof. Markus Antonietti and Dr. Nina Fechler, who provided me an opportunity to join their team as guest researcher for three months at MPI Germany, and gave me access to their laboratory and research facilities. Specially, I thank to Nina and Thomas (Berti) for great discussions during my work at MPI. I also forward my appreciations to all friends at MPI for the fun we have had in “schibril” after work.

I would also like to acknowledge with much appreciation to Dr. Jiayin Yuan (MPI, Golm-Potsdam, Germany) and Dr. Andrea Balducci (Helmholtz Institute, Ulm, Germany) for their kind acceptance as international reviewer for this PhD Thesis before submission. I would also like to thank Dr. Pilar Ocón Esteban (UAM, Madrid Spain) for the advice related to Thesis and important adiminstration issues in the University.

My especial thank goes to my dearest friend Dr. Tadhg O’mahony for his motivation, immense knowledge in every aspect, the fun we have had together for two years, and also I remember he was cooking a food for me when I was sick ... thank you very much for everything TO. My especial thanks also go to Dr. Barry Heyes and his wife, Jane Hayes for their hospitality to host me during the time of searching a house to rent, thank you so much Baz y Jane!

Moreover, I would like to thank all of Marie-Curie fellows and Principal Investigators in the Renaissance-ITN project for stimulating discussions in every ITN meeting and conference and the fun we have had together. In particular, I am grateful to Prof. David Mecerreyes and Dr. Monica Moreno Rodríguez for managing, directing the renaissance project, and organizing every meeting successfully!

My daily life after work would have been more than boring if I had not spent time and enjoyed with my flatmates: Juancarlos, Juan, Manuel, Diego, and Luis! Thank you very much for the amazing time we have spent, and teaching me Spanish language, and culture.

At Last but not least, my deepest gratitude goes to Bure, Ethiopia: to my amazing family. They stand firm each and every challenge and brought me to the place where I am today, they have shown me unconditional love, and supported me in every journey of my life. So, I would like to dedicate this Thesis to my family. And now I should thank them in their own language, Amharic!

ከሁሉም አስቀድሜ ለዚች ጊዜ እና ሰዓት ስላደረሰን ልዑል እግዝአብሄር ይመስገን!!!

"የመጨረሻዉን ቃል ለጅግናው ተዉለት ይላሉ አበዉ ሲተርቱ":: እናም የመጨረሻዉን ምስጋና ለጅግኖች ቤተሰቦቼ ቀን እና ሌሊት ደክመው እኔ እንደምፈልገው ስላደርጉልኝ እጅግ ምስጋና ይገባቸዋል:: ዉድ የተከበራችሁ ቤተሰቦቼ "ልጅ እና ወረቀት የያዘዉን አይለቅም" አንደሚባለዉ ሁሉ ያው እስከዛሬ እድሜዬን ሙሉ ስማር የኖረዉን እዚህ ደረሰ:: በተለይ እመ እና የኔዋበ ገና በልጅነቴ ከምትወዱት ሥራ እና ከፍየል ጥበቃ አስቁማችሁ እኔን ወደ ትምህርት ቤት እንድሄድ ስላደርጋችሁ እና በየጊዜው ትምህርት እንድከታተል ስላደርጋችሁ ከልቤ እጅግ በጣም አመሰኛችሁአለሁ:: በተልይ

የኔውዱአበ በወጣትነት ዘመንህ ያሳለፍሄዉን ዉጣ ዉረድ ካንተ የበለጠ ማንም አያዉቀዉም፡፡ የሕይወትን ዉጣ ዉረድ ገና በወጣትነትህ ብቻህን ተጋፍጠህ፡ እኔንም ችግርን እንዴት መጋፈጥ እና እንዴት ወደ ስኬት ጎዳና መግባት እንደሚቻ በተግባር አስተማርከኝ፡፡ አንድ ቀን ያንተን ታሪክ ለወድፊት ወንድሞቻችን እና እህቶቻችን ትምህርት ይሆን ዘንድ መዝግቤ አበርክታለሁ፡፡ያን ሁሉ ዉጣ ዉረድ ዛሬ ላይ ሁነህ ስታስበው ምን እንደሚሰማህ ያንተን ታሪክ ለምያዉቁ መገምት አያዳግትም፡፡ በጣም አመሰግንሃለሁ የኔውዱአበ!!!

ትዝ ይለኛል በ ፤፤፤፤ አ/ም የደርግ ዘመነ መንግስት ሲያበቃ እና የአሁንኑ (የኢህአዲግ) መንግስት ወንበሩን ሲይዝ በነበረው ግርግር ምክንያት ሁሉም የአካባቢው ተማሪዎች በሙሉ ትምህርቱን ሲያቆም በማየት እኔም በልጅነት አስተሳሰብ ትምህርት አልሄድም ስል በግድ ስለሰደዳችሁኝ እጅግ በጣም አመሰኛችሁአለሁ፡፡ ትዝ ይለኛል እመ እና የኔውዱአበ የወደፊት እድሌን ስተነቢዩ፡ የኔውዱአበ "ትንሽ የዳቦ ብታገኝ ተማር አድልህን ምክረው ይለኝ እና ፡ ለነገሩ አዲስ እና ሌሎች ነበዝ ተማሪዎችም አላለፉ መችም እንዴው በሁአላ ከምትወቅሰኝ ተማር ብዬ ነው እንጅ ይለኝ" ነበር፣ አዲስ የናቴ ትንሽ ወንድም በጣም ታታሪ ተማሪ ሁልጊዜ የሚያነብ ነበር እና ከዛ ከ ፤፤ ኛ ክፍል የብሔራዊ ፈተና ነጥብ ስላለገኘ ስላልተሳካለት እኔንም የምወድቅ መስሎት ይጠራጠረኝ ነበር፡፡ በአንፃሩ እመ ደግሞ ለምን አንደዚህ ትለዋለህ የኔሁን (የቤት ስሜ ነው) የራሱ ዕድል አለው ለምን ገና ሳይደርስ እድሉን በከፉ ታየዋለህ ትል እና ትመልስለት ነበር፡፡ከዛ ሁለቱም ያም ሆነ ይህ እኔ በመቀጠሉ እና አስፈላጊውን ሁሉ ለማሟላት ተስማምተው ነገሩ ይደመደም ነበር፡፡ አንድ የተረዳሁት ነገር ቢኖር ሁለቱም ስለኔ ጥሩ ነገር ይታያቸው ነበር፡፡ እርግጠኛ ነኝ አሁንም ስለኔ ጥሩ ነገር ይታያቸዋል፣ እኔም አንደዛው፡፡ ስላደርጋችሁልኝ እግዚአብሔር ዉለታችሁን ይከፈለው እላለሁ፡፡ እኔ የዚህ መድረስ የአንበሳውን ድርሻ የያዙ ወድሞቼ እና እህቶቼንም ስላደንቅ እና ሳላመሰግን አላልፍም!! ግዜ (አሁን ሻለቃ ግዛቸው ብለው ስምህን ቀይረዉታል መሰለኝ፣ ይሁን መችም ወላጅ ያወጣዉን ስም ያለ ፍቃድ መቀየር የሚያስጠይቅ ሕግ ባይኖርም ቅሉ ፡ የዚህ አይነት አሰራር ባለስሙ እራሱ አስቀፈቀደ ድረስ እኛም ተቀብለናል፡፡ ለነገሩ የኔም ስም በቅርቡ ይቀየራል) አንተ ያደርግልኝ ሁሉ በህዮት እስካለሁ ድረስ አልረሳዉም ፡ ምንም አንተ እስከምትፈልገው ባትማርም እኔ እንድማር የሚያስፍገዉን ነገር ሁሉ ስላደርግህልኝ በጣም አመሰግናለሁ ግዜ!!! ማተቤ፡ ከታዘዝንበት ስራ ሁሉ የኔን ድርሻ እየሰራህ እኔን ወደ ትምህርት ቤት እንድሄድ ስላደርግህ፡ እና የሚያስፈልጉ ነገሮችን በመግዛት እንድማር ስላደርግህልኝ በጣም አመሰግናለሁ!!! እመነሽ ሁሌ ምግብ አዘጋጅተሽ ስለምተብቂኝ እና የኔን ስራ ደርበሽ በመስራት እኔ አንድማር ስላደርግሽ፡ ዝማም ፡ ትሁኔ እና ታምሬ እና አስሬ ሁላችሁም ስለምታሳዩኝ ፍቅር እና ፈገግታ እንዲሁም ባንድም ወይም በሌላ ከደረስኩበት ደረጃ እንድደርስ ስላደርጋችሁ ምስጋናዬ ላቅ ያለ ነው፡፡
ልዩ ምስጋና፡ ሁሉም ዘመዶቼ (አያት አጎት አክስት ከነ ቤተሰባቸው) ባንድም ወይም በሌላ መልኩ የረዳቺሁኝ በሙሉእጅግ በጣም አመሰኛቺሁአለሁ፡፡ በተለይ የኔሁን ሰዉነት ከነቤ ተሰቦቼ (እናት፣ ብርሽ፣ አሴ እና ቤብ) አዲስ አበባ ሲሄድ ሁልጊዜ ሳይሰለቹ ስላስተናገዱኝ እጅግ በጣም እድርጌ አመሰግናለሁ፡፡ ካሴ ደነቀው ለመጀመርያ ጊዜ አምቦ ዩኒቨርሲቲ ስላደረስከኝ በጣም አመሰግናለሁ፡፡

አንዴ ያበደረ ሁሌ ተከበረ እንደሚባለው ሁሉ ሁላችሁንም ሁሌ አቀብራችሁአለሁ!!!

እጅግ በጣም አመሰግናለሁ!! ግሩም አይልህ ጥሩዩ ማድሪድ፣ ስፔን፡መጋቢት ፭ ፤፤፤፤ (2008) አ/ም

My PhD was funded by EU-FP7 through Marie Sklodowska Curie Renaisance Innovative Training Network Project (RENASIANCE –ITN) (Grant Agreement no. 289347).

TABLE OF CONTENTS

LIST OF FIGURES

Chapter I

Chapter II

Chapter III

Chapter IV

Chapter V

LIST OF TABLES

LIST OF SCHEMES

ACRONYMS

SCs	Supercapacitors
EDLC	Electricalchemical double layer capacitors
IL-b-E	Ionic liquid based polymer electrolytes
PIL	Polymeric ionic liquid
CsAc	Cesium acetate
VN@N -dC	Vanadium nitride nanoparticles in nitrogen doped carbon
$VOCl_3$	Vanadium Oxytrichloride
CsOH	Cesium hydroxide
NH_4VO_3	Ammonium metavanadate
$ZnAc_2$	Zinc acetate
NaCl	Sodium chloride
LiCl	Lithium chloride
KCl	Potassium chloride
$ZnCl_2$	Zinc chloride
TA-	Tannic acid
N-dC	Nitrogen doped carbon
VN	Vanadium nitride
SEM	Scanning electron microscope
XRD	X-ray diffraction
XPS	X-ray photoelectron spectroscopy
GTA	Gravimetric thermal analysis
S_{eff}	Effective surface area
σ	Conductivity

V_{eff}	Effective pore volume
BET	Brunauer Emmett and Teller
DFT	Density functional theory
S_{BET}	BET specific surface area
S_{DFT}	DFT specific surface area
ICP-OES	Inductively coupled plasma optical emission spectrometry
TEM	Transmission electron microscopy
WAXS	Wide angle X-ray Scattering
FTIR	Fourier transform infrared spectroscopy
CV	Cyclic voltammetry
DC	Charge.discharge
EIS	Electrochemical impedance spectroscopy
$PYR_{14}TFSI$	N-methyl-N-butylpyrrolidinium bis(trifluoromethanesulfonyl)imide
$PYR_{14}FSI$	N-butyl-N-methylpyrrolidinium bis(fluorosulfonyl)imide
HEMimTFSI	1-(2-hydroxy ethyl)-3-methylimidazolium bis(trifluoromethylsulfonyl)imide
$PYR_{14}DCA$	1-butyl-1-methylpyrrolidinium dicyanamide
Pdadmac	Poly(diallyldimethylammonium)chloride solution
LiTFSI	Lithium bis(trifluoromethanesulfonyl)imide
Emim-DCA	Ethyl methylimidazolium dicyanamide
pDADMTFSI	poly(diallyldimethylammonium)bis(trifluoromethanesulfonyl)imide
E_{real}	Real specific energy density
E_{max}	Maximum energy density
Pr_{eal}	Real specific power density
P_{max}	Maximum power density
C_{am}	Specific capacitance
ESR	Equivalent series resistance
ESW	Electrochemical stability window
η	Efficiency

CHAPTER I: INTRODUCTION[1]

[1] A part of this chapter is published as a book chapter: "GA .Tiruye, R.Marcilla. Ionic Liquids and Polymers in Energy. In: Mecerreyes D, editor. Application of Ionic Liquids in Polymer Science and Technology. Berlin Heidelberg: Mecerreyes, David; 2015, p. 199–221".

CHAPTER I: INTRODUCTION

1.1. The Need for Energy Storage

Nowadays, energy is one of the leading topics for debate and discussion at all levels of society. Water, food, and energy are among the most fundamental to the well-being of society, and without safe, sustainable and economic energy, much of the contemporary civilization would nose-dive. Historically, energy supply has changed gradually; fuels have changed from wood to coal, oil, gas and now include biomass. The humankind has used the power of the sun for drying, baking and now electricity generation; the power of wind to turn sails of windmills; and the power of water to rotate waterwheels and tidal turbines. Despite huge energy resource availability, accessing sustainable and clean energy is of high importance and remains as challenge yet.

In the contemporary society, the majority of energy consumers are mainly reliant on non-renewable energy sources. However, it is worth noting that dependence on primary energy sources such as coal, oil, and gas is an extravagant use of the Earth's limited natural resources. More importantly, fossil fuels turned out to be the main source of greenhouse gases (CH_4, CO_2) and other environmental pollutants from the result of fossil fuel combustion. By doing so, we have already started living in the epoch of "Anthropocene"- where the change of global environmental ecosystem is induced by human activities [1–3]. For instance, in a 2010 Gallup poll on the cause of climate change, 50% of the sample of American respondents said that global warming was the result of human causes or human and natural causes combined, 88 % of Japanese, 75 % of Chinese, and 70 % of Russians [4]. It seems that the success of using fossil fuels as a primary energy source became a failure in environmental sustainability and other social complexities.

Until recently, the concept of a total energy revolution remained on the margins of world politics. Despite the idea of "carbon emissions should be cut" is now became an accepted policy across most of the developed world, still most of the current sustainable energy policies are aimed at more conservative targets than diverse and renewable energy policies [5].

So far, the trend is that the energy dependence on fossil fuels will continue to rise in a context of concerns about climate change and unpredictable energy prices caused by increased demand for energy. This will create political, economic, and societal instabilities unless alternative energy resources come to the rescue and integrate with

the current energy system. Therefore, because of global concerns about present energy policy which relies on fossil fuels, a paradigm shift from non-renewable to renewable energy resources policy is vital to address energy insecurity in the future [6].

Renewable energy resources such as solar power, wind power, hydropower, geothermal, and biomass, provide an alternative cleaner energy, and have vast potential to reduce dependence on fossil fuels. Moreover, they are also environmental friendly and help to mitigate the effect of some environmental pollutants. Nevertheless, some of renewable energy resources (*i.e.,* sun power and wind power) have intermittent output and even peaks in generation that do not necessarily match with the demand for energy. This has led to a growing concern about the reliability and unpredictability in both supply and demand for energy.

As a result, there has been an increased call for the use of energy storage as an essential component of future energy systems coupled with renewable energy resources. This will increase the use of renewable energy resources in households, industry, and the massive replacement of internal combustion engine vehicles by those with low or zero emission. Therefore, a variety of different energy storage technologies in many configurations will be required. So far, different energy storage technologies have been developed for various applications [6] as shown Figure 1.1

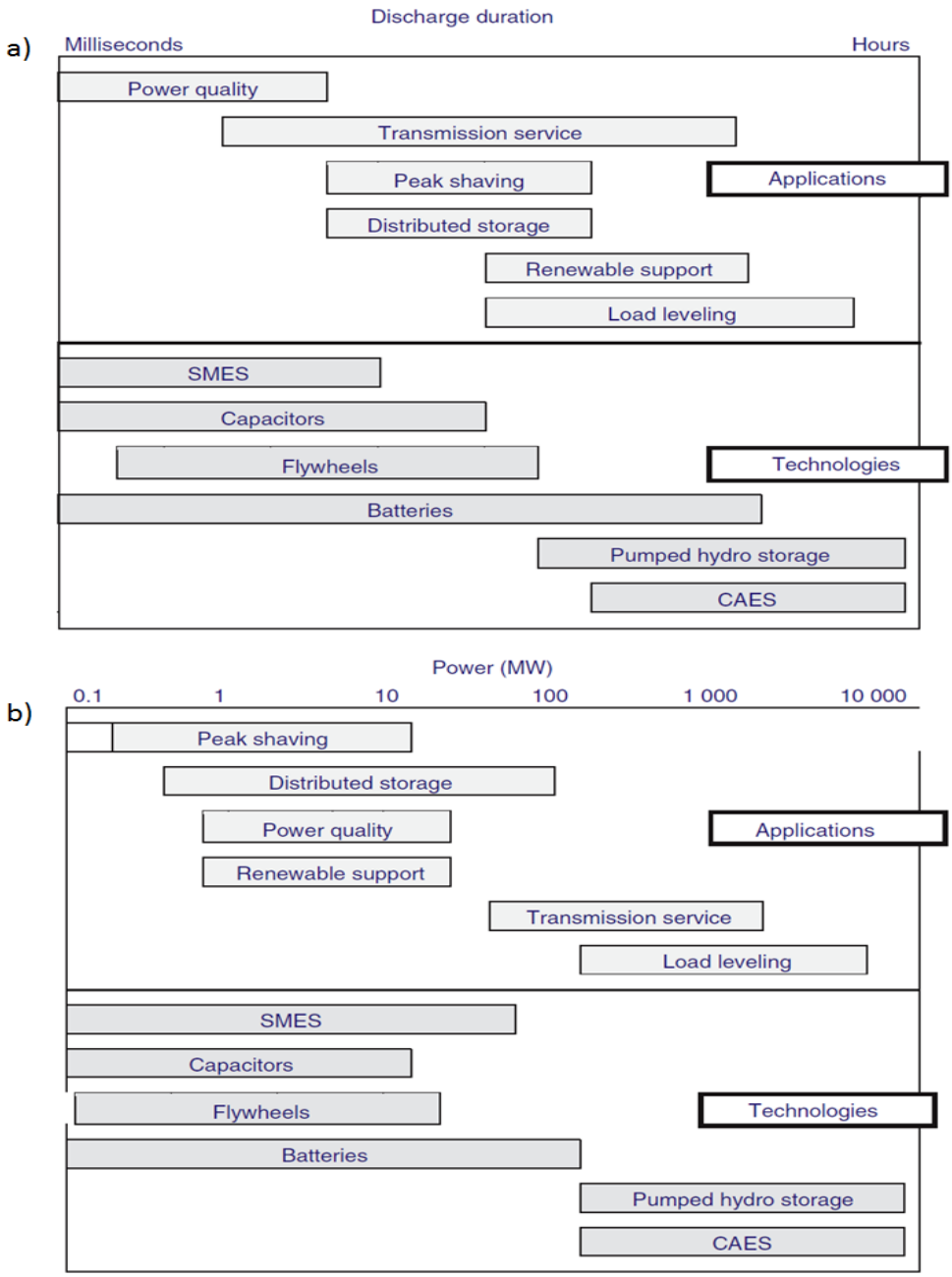

Figure 1.1. Different energy storage technologies and applications in a common scale a) discharge durations of different applications and technologies b) power of different applications and technologies. CAES- compressed-air energy storage, SMES- superconducting magnetic energy storage [7]. The energy can be stored in the form of chemical, thermal, electromagnetic, gravitational, electrical, and electrochemical energy forms.

Figure 1.1 shows the overview of both different energy storage technologies and applications represented in a common scale. Despite the graph provides more qualitative insight than quantitative, it gives the instructive comparative estimation of discharge duration and the power requirements of several applications. The pumped

hydro and compressed air energy storage (CAES) are superior power and energy technologies, thus suitable for high power and long duration applications, e.g., transmission services and load levelling. However, they are inappropriate technologies for applications that require a fast and milliseconds response since both are restricted to certain geographical locations. On the other hand, flywheels, superconducting magnets (SMES), batteries, and supercapacitors are high power, and medium energy storage options. They are most suitable for power quality applications (i.e., utilizing electric power successfully without interference or interruption until the charge is depleted) that require fast response in milliseconds, seconds or up to some minutes [7,8].

In this chapter, the fundamental principles, and recent development of supercapacitors including their electrolytes and electrode materials will be reviewed briefly.

1.2. Fundamental principles of Electrochemical Supercapacitors

1.2.1. Capacitor *vs*. Supercapacitor

A classical capacitor is a passive component that stores energy in an electrostatic field rather than in chemical form. It consists of two parallel electrodes (plates) separated by an insulating material (dielectric) (see Figure 1.2).

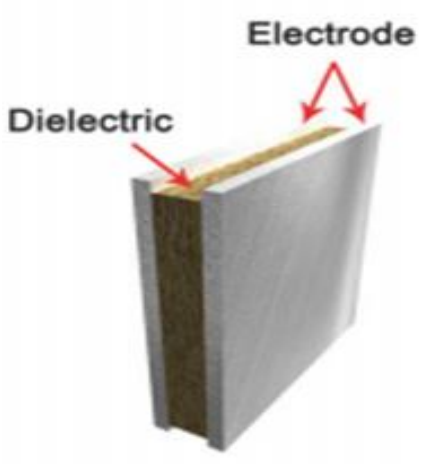

Figure 1.2. Schematic representative of electrostatic capacitor.

The capacitor is charged by applying voltage across the electrodes, which causes positive and negative charges to migrate towards the surface of electrodes of opposite polarity. When two plates are charged, a capacitor connected in a circuit will act as a voltage source and current will flow until a complete charge balance is achieved. As a result, its capacitance (C), which is measured in farads (F), is the ratio of electric charge

on each electrode (Q) to the potential difference between them (V), and expressed as eqn. 1.1 [9].

$$C = \frac{Q}{V} \qquad 1.1$$

For a typical parallel plate capacitor (see Figure 1.2), capacitance is proportional to the area of each electrode and the permittivity of free space (vacuum) and inversely proportional to the distance between the electrodes [10]:

$$C = \varepsilon_0 \frac{A}{d} \qquad 1.2$$

Where, C is the capacitance in farad (F), is the permittivity of free space ($8.9*10^{-12}Fm^{-1}$), A is the area of the plate in square meter (m^2), and d is the distance between the two parallel plates in meter (m). On the other hand, if the free space between two plates is filled with a dielectric material (see Figure 1.2), the capacitance C can be calculated as follow [10]:

$$C = \varepsilon\varepsilon_0 \frac{A}{d} \qquad 1.3$$

Where, ε is the permittivity of dielectric material. The common values of ε is 1 for air, 2 for polypropylene, and 3 for polyester. Therefore, the three main factors that determine the capacitance of a capacitor are plate area (common to the two electrodes), separation distance between the electrodes, and properties of the dielectric (inductor) used.

The two primary attributes of a capacitor are its energy and power densities, both of which can be express as a quantity per weight (usually called specific energy or power) or per unit volume. The energy stored in a capacitor is related to the charge, Q (coulomb), at each interface and the potential difference (V), and therefore, directly proportional to its capacitance, which is expressed as $E=1/2CV^2$. On the other hand, generally power (P) is the rate of energy delivery per unit time. Nevertheless, the equivalent series resistance (ESR) of internal components of a capacitor such as current collectors, electrode materials, and dielectric need to be taken in to account in order to determine P for a certain capacitor. In this case maximum power (P_{max}) can be expressed as $P_{max} = V^2/4ESR$. The ESR, by introducing the voltage drop, determines that maximum energy and power of a capacitor.

Supercapacitors (SCs), also known as electrochemical double layer capacitors (EDLCs), are special type of capacitors based on charging and discharging at the electrode-electrolyte interface of high surface area of materials such as porous carbons or some metal oxides. They are governed by the same basic principles as conventional

capacitors and are ideally suited to the rapid storage and release of energy. However, they incorporated electrodes with much higher effective surface areas and thinner dielectrics which are defined by the thickness of *double layer*, leading to an increase in both capacitance and energy; by a factor of 10,000 than those achieved by capacitors [9].

Electric Double Layer Formation in Supercapacitor: A charged surface in contact with an electrolyte solution is expect to attract ions of opposite charge and to repel ions of similar charge, thus establishing an ion atmosphere in the immediate vicinity of the surface. In this case, two parallel layers of charge are formed- the charge on the surface itself and the layer oppositely charged ions near the surface, which are separated by an atomic distance, d. This structure is called *electric double layer* (EDL) and it was first modelled by Helmholtz [11]. Helmholtz assumed that a layer of counter ions would be immobilized on the surface by the electrostatic attraction such that the surface charge is exactly neutralized. In Helmholtz model, the electric potential falls from its surface value, Ψ_o, to zero in the bulk solution over the thickness of the layer of counter ions as shown in Figure 1.3a.

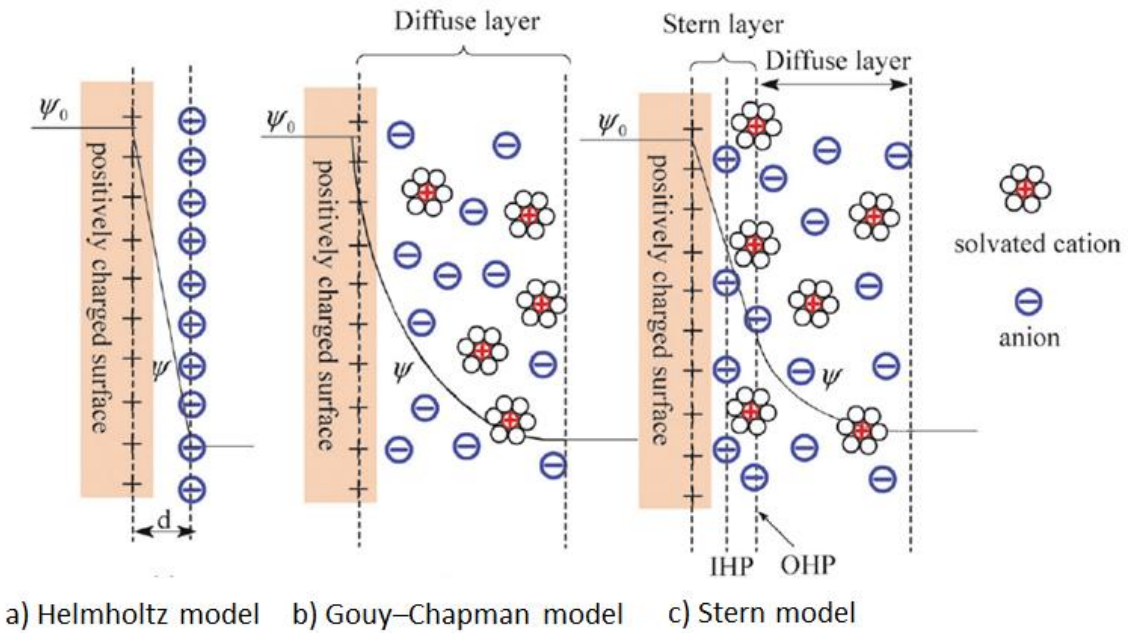

Figure 1.3. Models of the electrical double layer at a positively charged Surface [12]. *Stern model, showing the inner Helmholtz plane (IHP) and outer Helmholtz plane (OHP). The IHP refers to the distance of closest approach of specifically adsorbed ions (generally anions) and OHP refers to that of the non-specifically adsorbed ions. The OHP is also the plane where the diffuse layer begins; d is the double layer distance described by the Helmholtz model. Ψ_o and Ψ are the potentials at the electrode surface and the electrode/electrolyte interface, respectively.*

Later, the Helmholtz model was modified by Gouy and Chapman [13,14]. They pointed out that ions of electrolyte are subjected to a random and continuous thermal motion thus would not be immobilized on the surface. They suggested that the ions, which neutralize the surface charge, are spread out into the solution, forming what is called *diffuse double layer*. According to Gouy and Chapman model, the potential falls more slowly to the bulk solution (see Figure 1.3b). However, this model leads to an overestimation of the EDL capacitance. The capacitance of two separated arrays of charges increases inversely with their separation distance, hence a very large capacitance value would arise in the case of point charge ions close to the electrode surface [12].

In 19924, Stern [15] observed that neither Helmholtz model nor the Gouy-Chapman model adequately accounts for the properties of the double layer and suggested that the truth lies in a combination of the two models. Therefore, he explicitly recognizes two regions of ion distribution—the inner region called the compact layer or Stern layer and the diffuse layer (see Figure 1.3c). In the compact layer, ions (very often hydrated) are strongly adsorbed by the electrode, thus the name of compact layer. In addition, the compact layer consists of specifically adsorbed ions (in most cases they are anions irrespective of the charge nature of the electrode) and non-specifically adsorbed counter ions. The inner Helmholtz plane (IHP) and outer Helmholtz plane (OHP) are used to distinguish the two types of adsorbed ions. The diffuse layer region is as what the Gouy–Chapman model defines.

In such cases, the capacitance in the EDL (C_{dl}) can be estimated by a combination of the capacitances from the Stern type of compact double layer capacitance (C_H) and the diffusion region capacitance (C_{diff}). Thus, C_{dl} can be expressed as follow:

$$\frac{1}{C_{dl}} = \frac{1}{C_H} + \frac{1}{C_{diff}} \qquad 1.4$$

The factors that ultimately determine the capacitance of EDL include the electrode material, the electrode surface, accessibility to the electrode surface, and the electrical field across the electrode. Moreover, the types of electrolyte ions, the solvent in which the electrolyte ions are dissolved, and the chemical affinity between the adsorbed ions and the electrode surface are also significantly affect the capacitance of EDL [9].

In summary, conventional capacitors store charge on a low surface area plates and often rated in the micro-and mili-farad ranges. Whereas supercapacitors store charge in an electric double layer set up by ions at the interface between a high-surface area carbon electrode and a liquid electrolyte. Thus SCs can be rated as high as tens, hundreds, even thousands of farads per device [16].

1.2.2. Supercapacitors *vs*. Batteries

The fundamental difference between supercapacitors and batteries is their mechanisms of energy storage (*i.e.,* electrostatic/non-*faradaic vs*. chemical/*faradaic*). Batteries store energy *via* chemical reactions being placed in the electrodes that are oxidized or reduced, generating charges. Bbut supercapacitors store energy directly as electrostatic charge due to the formation of the double layer in the electrode/electrolyte inter-phase [17]. The slow kinetics of redox reaction in battery electrodes and the restricted mass transport of the reactants usually limit the power performance of batteries [10]. In supercapacitors, the formation of the double layer is a fast process, resulting in high power devices. Basic features of supercapacitors in comparison with batteries are below in Table 1.1.

Table 1.1. Features of supercapacitors in comparison with batteries [10,18]

Property	Supercapacitors	Batteries
Cyclability (cycle life)	>100,000	<1000
Specific energy	Moderate (<10 $Whkg^{-1}$)	High (30-150 $Whkg^{-1}$)
Specific power	Very high (2 $kWkg^{-1}$) at 95 % efficiency, low impedance	Moderate (0.5 $kWkg^{-1}$)
Discharge efficiency	Fast and most efficient for discharge from V to V/2	Slow and efficiency depends on internal resistance
Electrochemical reactions	Little activation polarization	Significant activation polarization
Storage mechanism	Physical	Chemical
Power limitation	Separator, ionic conductivity,	Reaction kinetics and mass transport
Energy limitation	Electrode surface area	Electrode mass
Charge rate	Very high same as discharge rate	Reaction kinetics mass transport
Cycle life limitation	Sometimes side reactions	Physical stability, chemical reversibility
Shelf life	Very long	Low

Batteries have been the common electrochemical energy storage devices used in many applications due to their high capability to store large amount of energy with a relatively small volume and weight. Nevertheless, shelf life, cycle life, and low power

density are the main problems in the battery technology. Moreover, the need for high power delivery in a short time recently increased in many applications.

Supercapacitors (SCs) or ultracapacitors with much higher power density, longer shelf life and cycle life have become as a complementary energy storage devices to batteries, especially occupying a niche position, in terms of specific power for high power applications [19]. In fact, capacitors have much lower energy density than batteries and the trade-off between energy density and high power delivery in short period of time is an important design consideration. In this case, SCs can bridge the gab between the high energy storage capability of batteries and high power capability of conventional capacitors.

Mostly of the time, energy and power densities are the main two parameters to compare various electrochemical energy devices. These can be represented by a typical graphical presentation called Ragone plot, where power and energy densities are represented in a logrithmic scale (see Figure 1.4).

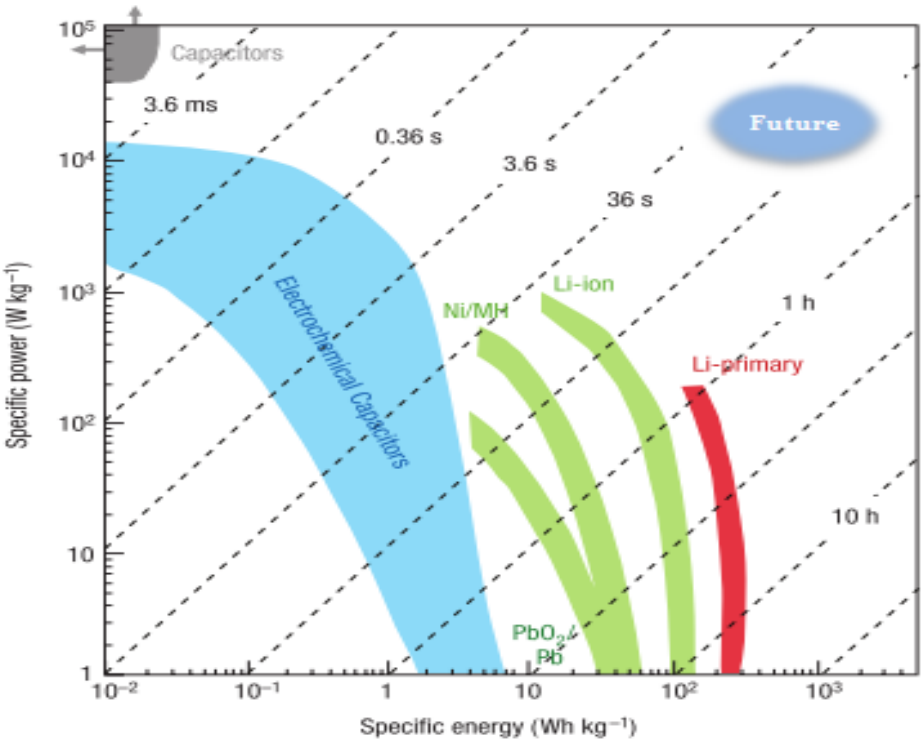

Figure 1.4. Ragone plot, specific energy density against specific power density for varies electrochemical energy storage devices [22].

According to the Ragone plot, if an electric car has a device with high energy density (*i.e.* batteries), the car can go more miles before the battery has to be recharged. Whereas if the car has a device with high power density (i.e., supercapacitors), indicating the car can accelerate faster (high power indicates how fast the car can accelerate) [20]. In general terms, batteries with higher energy density keep running

our devices for the whole day. However, the kinetic process usually acompanied by the redox reactions of the active materials in battery, resusult in volumetric changes of batteries. Such volume changes are the main cause of the limited cycle life of batteries and reduce its power delivery compared with the one in supercapacitors. Therefore, for a rapid high power delivery, recharging time (high power density), and long-life energy storage, electrochemical supercapacitors are usually preferable [21].

In Figure 1.4, the diagonal dashed lines represent time constant of charge-discharge for the represented devices. It can be calculated by dividing specific energy density to specific power density. The blue circle at the right top corner of the graph indicates the characteristic of future devices, exhibiting both high power and energy densities simultaneously.

1.2.3. Types of Supercapacitors

According to the energy storage mechanism and the nature of electrodes, electrochemical supercapacitors can be classified as electrochemical double layer capacitors (EDLC), pseudocapacitors and hybrid capacitors [17,23]

1.2.3.1. Electrochemical Double Layer Capacitors (EDLCs)

In EDLCs, the charge accumulates by electrostatic interactions at the interface between electrode surface and electrolyte when a voltage is applied across the electrodes (Figure 1.5). In order to increase the storage capacity of EDLCs, the electrode materials need to have high specific surface area. In this case, electrodes made of highly porous carbon materials generally are used (see Figure 1.5).

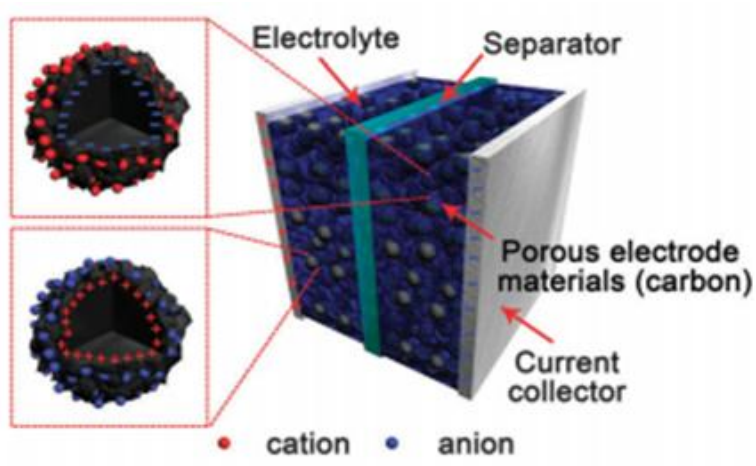

Figure 1.5. schematic representation of electrochemical double layer capacitors (EDLCs) [17]

In an EDLC, electrical energy is stored through ion adsorption (a purely electrostatic process) without Faradaic charge transfer, leading to high power densities, fast charge–discharge processes, and excellent cycling stabilities. Generally the process can be expressed according to the following equations [24,25].
On positive electrode:

$$E_{S1} + A^- \xrightarrow{charging} E_{S1}^+//A^- + e^- \qquad 1.5$$

$$E_{S1}^+//A^- + e^- \xrightarrow{discharging} E_{S1} + A^- \qquad 1.6$$

On negative electrode:

$$E_{S2} + C^+ \xrightarrow{charging} E_{S2}^+//C^+ \qquad 1.7$$

$$E_{S2}^+//C^+ \xrightarrow{discharging} E_{S2} + C^+ + e^- \qquad 1.8$$

The overall charge-discharge on process can be expressed as follow:

$$E_{S1} + E_{S2} + A^- + C^+ \xrightarrow{charging} E_{S1}^+//A^- + E_{S2}^+//C^+ \qquad 1.9$$

$$E_{S1}^+//A^- + E_{S2}^+//C^+ \xrightarrow{discharging} E_{S1} + A^- + E_{S2} + C^+ \qquad 1.10$$

Where, E_{S1} and E_{S2} are electrode surface one and two, respectively, A^- and C^+ are anion and cation, and the sign of // represents the interface between the surface of electrodes and ion of electrolytes.

The electrons travel from the negative to the positive electrode through an external load when the system is charged. Within the bulk electrolyte, cations migrate towards the negative electrode while anions move towards the positive electrode forming the double-layer in the interface electrode//electrolyte. On the other hand, the reverse processes can take place when the system is forced to discharge. In this type of process, no charge transfers across the electrode//electrolyte interface, and no net ion exchanges occur between the electrode and the electrolyte. It indicates that the electrolyte concentration remains constant during charging and discharging processes. [24,25].

1.2.3.2. Pseudocapacitors

In pseudocapacitos, energy storage relies on reversible redox reaction (faradaic process) occurring at or near the surface of an electrode material. The redox process is

so fast that the device's electrochemical features are those of a carbon-based capacitor with significantly higher capacitance (Figure 1.6).

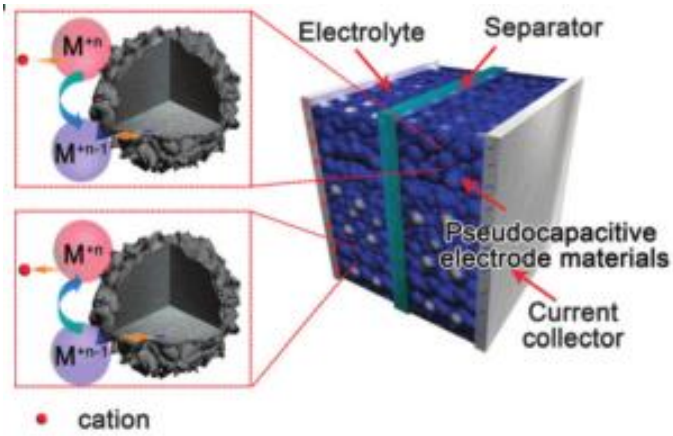

Figure 1.6. Schematic representation of Pseudocapacitors [17]

Several faradaic mechanisms that can result in pseudocapacitor features have been identified [26]. These mechanisms occur due to different physical process and with different types of materials as shown in Figure 1.7.

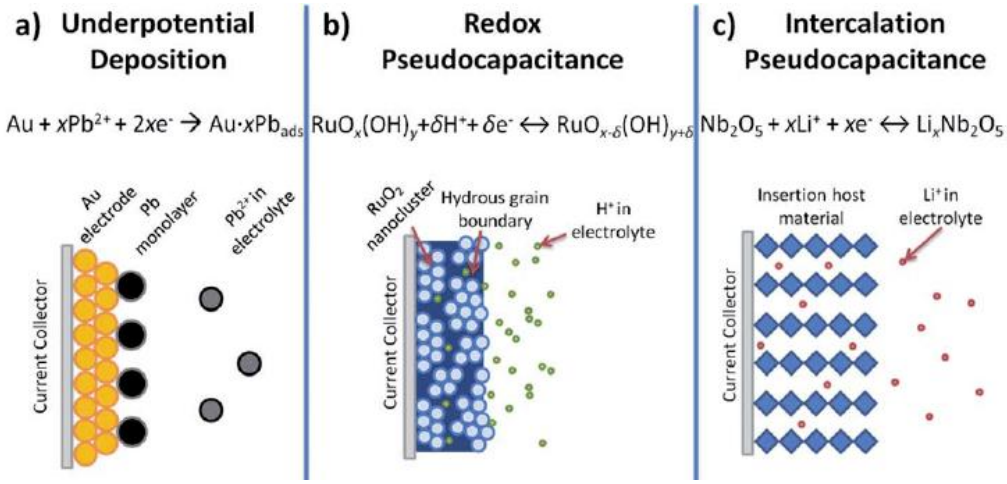

Figure 1.7. Three different types of reversible redox mechanism which give rise to pseudocapacitance [26]

The mechanisms include:

a) *Underpotential Deposition*: when metal ions form adsorbed monolayer at a different metal´s surface above their redox potential. This is the case of lead deposited on the surface of gold.

b) *Redox Pseudocapacitance*: here ions are electrochemically adsorbed onto or near the surface of electrodes with a fast faradaic charge transfers (*e.g.* storage of hydrogen with hydrated RuO_2)

c) *Intercalation Pseudocapacitance*: this occurs when ions intercalate into the tunnel or layers of a redox active electrode accompanied by a faradaic

charge transfer with no crystallographic phase separation (e.g. intercalation of Li ion on Nb_2O_5)

1.2.3.3. Hybrid Capacitors

Hybrid capacitor refers when electrostatic and faradaic energy storage mechanisms are present simultaneously in a device (see Figure 1.8).

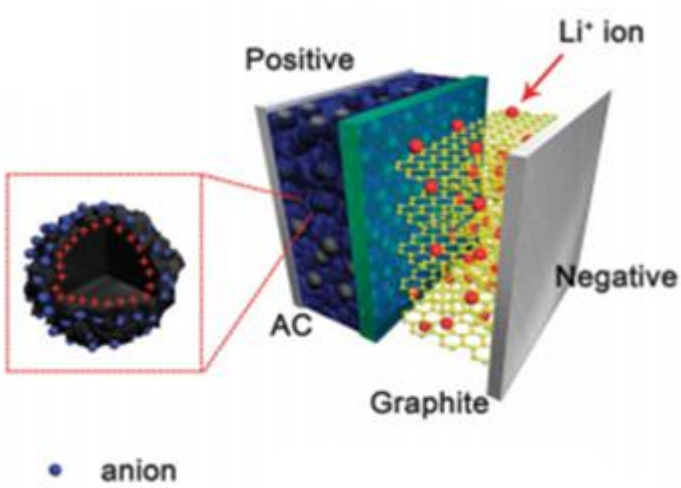

Figure 1.8. Schematic representation of hybrid or lithium ion capacitor [17].

In hybrid capacitors, the asymmetric configurations, where the anode materials are different from the cathode materials, are used, and leading to wider working potential window. This is because of the combination of two different active electrode materials that can work complementary in separately operating potential window and thereby increasing the total operating voltage of the device. Asymmetric designs generally use one EDLC electrode (mostly activated carbons) and the other being battery-type electrode (metallic lithium, PbO_2, TiO_2, $Ni(OH_2)$ etc) [17]. For instance, carbon//RuO_2/TiO_2 [27], Carbon//titania nanotubes [28], and carbon//$Ni(OH)_2$ [29] are the common hybrid capacitors built with carbon and battery-type electrodes. The latest types of hybrid capacitors are the new battery-type hybrid devices such as lithium ion capacitors (LIC) [30], and carbon//PbO_2 capacitor [31]. Moreover, asymmetrical hybrid capacitors can be designed with one pseudocapacitive positive electrode (eg, MnO_2) and the other with rechargeable battery-type electrode (eg. Li metal) [32] .

1.2.4. Principles and Evaluation Parameters for Supercapacitors

Capacitance: It is the amount of electrical charge accumulated by pure electrostatic forces. It measures the ability of a material to store an electric charge when a voltage is

applied across the electrodes. Therefore, one of the common criteria for evaluating and estimating the effective use of electrode materials, in turn, evaluating the performance of supercapacitors, is measuring the value of capacitance. The capacitance of a capacitor strongly depends on the electrode surface area, the thickness of double layer, the relative permittivity of electrolyte, and the properties of electrolytes. Therefore, the capacitance of a capacitor can be estimated by using *eqn. 1.1, eqn. 1.2, or eqn. 1.3 (*see section 1.2.1*)*.

In supercapacitors, as explained in section 1.2.1, the value of double layer capacitance is associated with the interface between electrolyte and electrodes, which varies with the types of electrolyte, porous carbon and its conditions of preparation. In a diluted solution, the diffusive part of the double layer is about 100 Å. Theoretically; the higher specific surface area of electrodes and the higher concentration of electrolyte exhibit the higher values of capacitance. The ideal surface capacitance of EDLC with porous carbon electrodes exihibits around 15-50 μFcm^{-2} [33]. Despite conventional three-electrode setups are suitable for fundamental studies on the capacitive properties of an active material, a two-electrode cell is generally recommended to estimate capacitance and evaluate the performance of full supercapacitors. Supercapacitors can be constructed in such a way that two porous carbon electrodes can be placed in opposite side of an ion permeable separator to avoid short-circuit as shown in Figure 1.9.

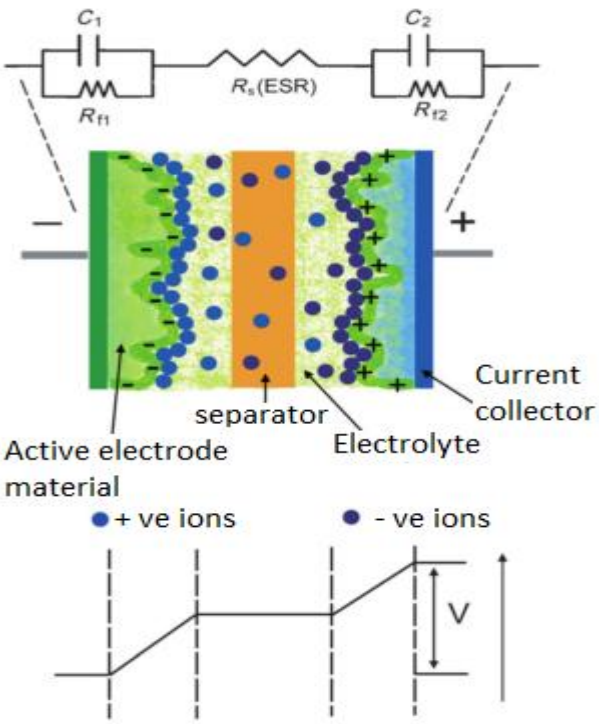

Figure 1.9. Diagram representation of two-electrode supercapacitor and its RC equivalent circuit [23].

Because two electrode cell resembles the actual supercapacitors device in real world applications and the value of capacitance would reflect the performance of a device [34].

It is worth reminding that in a charged state, the ions of electrolyte migrate towards the electrode with opposite sign to compensate the charges and forming an electrical double-layer at each of the two polarized electrode–electrolyte interfaces. Since each electrode–electrolyte interfaces represents a capacitor, the capacitance of the overall cell can be considered as two capacitors connected in series. Therefore, the cell capacitance (C_{cell}) of supercapacitor, is considered to be the sum of two capacitors connected in series and *eqn. 1.4* can be modified accordingly as follow [23,33,35].

$$\frac{1}{C_{cell}} = \frac{1}{C_{+}} + \frac{1}{C_{-}} \qquad 1.11$$

Where, C_{cell} is total capacitance of the cell, C_{+} and C_{-} are the capacitance of each electrode-electolyte interface at positive and negative electrode in farads (F), respectively.

For a symmetric device in which each electrode is made of the same type of electrode materials and contains equal amount of active materials, the capacitance of the positive electrode (C_{+}) is supposed to be equal to the capacitance of negative electrode (C_{-}). Then the capacitance of the complete cell is the half of each individual electrode and can be expressed by *eqn. 1.12* [23,35].

$$C_{cell} = \frac{C_e}{2} \qquad 1.12$$

Where, $C_e = C_{+} = C_{-}$, C_e is capacitance of a single electrode in Farads (F).

In general, capacitance, power, and energy densities are the main important parameters to evaluate the performance of supercapacitors. These parameters can be determined by the three common techniques such as cyclic voltammetry (CV), galvanostatic charge-discharge (GCD) and electrochemical impedance spectroscopy (EIS).

Cyclic Voltammetry (CV): The specific capacitance of electrode material (C_{am}) is usually obtained by cyclic voltammetry in a three-electrode configuration, which involves working electrode (WE), counter electrode (CE) and reference electrode (RE).

In carbonaceous materials where capacitance is only originated from electrostatic interactions, a CV curve is normally rectangular shape [22,23,35]. On the other hand, redox peaks with distortion usually accompany a CV curve of a pseudocapacitive or battery-like material. Generally speaking, the specific capacitance of the active material

is calculated by using the voltammetric charge integrated from the CV curve in a three electrode set-up, according to *eqn. 1.13* [19,23,35,36].

$$C_{am}(Fg^{-1}) = \frac{Q}{2mV} = \frac{1}{2mVv}\int_{v_-}^{v_+} I(V)dV \qquad 1.13$$

Where, C_{am} is the specific capacitance of the active material, Q (Coulomb, C) is the total charge obtained by integrating the positive and negative sweeps in a CV curve, m (grams, g) is the mass of active material in the working electrode. v is the scan rate (volt per second, Vs^{-1}), I is current in amper (A), and $V=V_+-V_-$ represents the potential window of the CV. If area or volume is more important than the mass of active material, from *equn.1.13*, m can be substituted by the electrode area, A or volume of the cell, V. It is worth noting that, the specific capacitance in *eqn 1.13* is normalized only by the mass of active material and doesn't include the mass of other components of supercapacitors. While CV is mostly applicable for the characterization of a single electrode with three-electrode configuration, on the other hand, two-electrode configuration is widely used to characterize the performance of a full device using a galvanostatic charg-discharge technique.

Galvanostatic Charge-Discharge (GCD): The specific capacitance of a supercapacitor cell (C_{cell}) can be calculated according to *eqn. 1.14* applied in two electrode-configuration [23]:

$$C_{sp,cell} = \frac{I}{m_t(dv/dt)} \qquad 1.14$$

Where, I (A) is the charging current, m_t (g) is the mass of active material from the two electrodes ($m_t=m_++m_-$), dv/dt (volt/second, vs^{-1}) is the slope of discharge curve. In a charge-discharge curve, the initial part of the curve is ohmic drop (IR), which is the instantaneous drop of voltage due to internal resistance when the system is changing from charge to discharge state. The rest of the discharge curve is normally linear for pure EDLC whereas a large deviation from linearity is due to faradaic contributions in pseudocapacitors and hybrid systems. As a result, for the sake of consistency, and to avoid over estimation of capacitance, the slope can usually be estimated according to *eqn. 1.15* [23,35,37]:

$$dv/dt = \frac{V_{max} - \frac{V_{max}}{2}}{T_2 - T_1} \qquad 1.15$$

Where, V_{max} is the maximum voltage after IR drop, T_2, and T_1 are the corresponding discharge times at V_{max} and $V_{max}/2$, respectively.

It is worth noting that the specific capacitance of electrode material is derived from three-electrode system, which involves working electrode (WE), counter electrode (CE) and reference electrode (RE). This value is far higher than the cell capacitance derived from two-electrode measurements. In fact, to calculate the specific capacitance for a single electrode (C_{am}) in symmetric supercapacitors using GCD technique, it is common to use *eqn. 1.16* [35,37].

$$C_{am} = 4C_{sp,cell} \qquad 1.16$$

Where C_{am} (Fg^{-1}) is the specific capacitance for a single electrode, the multiplier of 4 adjusts the capacitance of the cell and the combined mass of two electrodes to the capacitance and mass of a single electrode. Since active mass of positive and negative electrodes are equal in symmetric supercapacitors, i.e., $m_+=m_-=m$, then *eqn 1.16* can be derived from *eqn 1.11* as follow:

$$\frac{1}{C_{cell}}\left(\frac{1}{F}\right) = \frac{1}{C_+} + \frac{1}{C_-} = \frac{1}{m_+C_{+am}} + \frac{1}{m_-C_{-am}} = \frac{2}{mC_{am}}$$

i.e.

$$C_{cell}(F) = \frac{mC_{am}}{2}$$

Thus

$$C_{sp,cell}(Fg^{-1}) = \frac{C_{cell}}{m_+ + m_-} = \frac{C_{cell}}{2m}$$

$$C_{sp,cell}(Fg^{-1}) = \frac{\frac{mC_{am}}{2}}{2m} = \frac{C_{am}}{4}$$

Equivalent Series Resistance (ESR): It is the sum of different type of resistance within the cell including intrinsic resistance of electrode materials and electrolyte, mass transfer of resistance of ions, resistance of charge transfer, contact resistance between current collector and electrode material, etc [12,17]. Mostly, the resistances of bulk electrolyte and inside the pores of electrode materials are the dominant resistances in ESR. Pparticularly, when non-aqueous electrolytes (organic and ionic liquid

electrolytes) are used in supercapacitors. Therefore, it is essential to develop electrolytes with high ionic conductivity to reach high power densities of supercapacitor. Moreover, to determine the ESR from charge-discharge (CD) curve in Ωcm^2, it is common to use *eqn. 1.17*.

$$ESR\ (\Omega cm^2) = \frac{\Delta V}{2I} A \qquad 1.17$$

Where, ΔV is ohmic drop in volt, A is projected surface area of electrode in cm^2, and I is applied current in A.

Energy and Power Densities: As mentioned before, in addition to capacitance, energy and power densities are also the other two important parameters in order to evaluate the performance of supercapacitors. Both parameters can be obtainaed by galvanostatic charge-discharge (CD) in two-electrode configuration. The energy density measures the capacity to perform work while the power density is the rate of energy delivery per unit time. When supercapacitor is charged, the cell voltage will be built up across two electrodes and the standard approach to estimate the maximum energy and power densities can be experessed as follow [17,23,34,35]:

$$E_{max} = \frac{C_{sp,cell} V^2}{2} \qquad 1.18$$

$$P_{max} = \frac{V^2}{4ESR} \qquad 1.19$$

Where, E_{max} and P_{max} are the maximum energy and power densities, respectively, V is the cell voltage of supercapacitor and ESR is the equivalent series resistance of supercapacitor.

E_{max} and P_{max} are the theoretical maximum energy and power densities, respectively and they are usually overestimated. The more appropriate way to estimate the practical real energy and power densities stored in supercapacitors is as follow:

$$E_{real}(Whkg^{-1}) = \frac{I}{m_t} \int_{t_i}^{t_f} V dt \qquad 1.20$$

$$P_{real}\ (Wkg^{-1}) = \frac{E_{real}}{t_d} \qquad 1.21$$

Where, E_{real} and P_{real} are the real energy and power densities, respectively, m_t is the active mass of the two electrodes, t_i and t_f are initial and final discharge time and t_d is duration of discharge. Therefore, in order to get high energy and high power densities, the capacitance and cell operating voltage, which is determined by the electrochemical stability window of electrolyte should be high, and the ESR must be low.

For large-scale applications, other important parameters such as cycle life (cyclability), self-discharge rate, and thermal stability are normally need to be taken into consideration in order to evaluate the performance of SCs. These will be discussed briefly in the following paragraphs.

Cycle-Life: The test procedures for stabilities can be carried out by charging and discharging the SCs thousands of cycles. This will help to compare the initial capacitance and the capacitance after cycling. In EDLC where carbon electrodes are used, the cycling stability is generally high (>10,000 cycles)[12]. However, in pseudocapacitors or hybrid capacitors where redox reactions are involved, the cycle-life is reduced (800-8000 cycles)[26,38,39], due to the non-ideal electrochemical reversibility of pseudocapacitive and faradaic reactions [17,19].

Self-Discharge Rate: It is associated to the gradual loss of potential and energy across the charged supercapacitors over a certain period of time when it is kept under the open-circuit condition. Three mechanisms of self-discharge were proposed: due to a leakage-current, faradaic reactions and diffusion of ions from high ionic concentration formed during charging of the capacitors [16,40,41]:

(i) If the supercapacitor has been over charged beyond the respective (negative or positive voltage limits) decomposition limit of the electrolyte, the self-discharge is the spontaneous decline of the overcharge (over potential). This spontaneous decline of overvoltage, η, which is due to the overcharging current, occur an account of continuing discharge across the double layer until η becomes zero. The leakage process corresponds to a Faradaic, potential-dependent charge transfer reaction. Its rate, therefore, tends to progressively decreased as the self-discharge continues-exponentially with the declining potential.

(ii) If the supercapacitor electrode materials or its electrolytes contains impurities that are oxidizable or reducible over the potential range corresponds to the potential differences attained at the capacitor on charge, then supercapacitors become some extent non-polarizable. This is related to faradaic charge leakage currents that are dependent on potential. If these impurities are present in only small concentration, then the self-discharge redox process is diffusion controlled.

(iii) In some cases, self-discharge can also sometimes occur by internal redox reactions involving some of the functional groups present in the electrode materials. For instance, some of the quinonoid functional groups commonly residing on the edge of graphitic particles can trigger unwanted redox reactions in the carbon-based supercapacitors leading self-discharge.

However, since those kinds of functional groups are sparingly distributed on per gram basis of the active carbon material and their concentration is very low in the entire surface of carbon electrodes, some are not redox active. Therefore, their reaction on self-discharge could not exceed more than 2-5 % of full charge [16].

Thermal Stability: operation temperature of supercapacitors is very important for evaluation of performance of supercapacitors. Most potential applications for supercapacitors occurs over the range of temperature from -30 to 70 ^{o}C, therefore, expanding the working temperature of supercapacitors will further increase the scope of applications [9,17]. The application of working temperature can affect several parameters of supercapacitors including power and energy storages, rate performance, cyclability, and self-discharge. In most cases, the working temperature of supercapacitors is reliant on the properties of electrolyte such as, boiling point, freezing point, and viscosity. As a result, the temperature varies from one electrolyte to another.

In summary, there are always challenges to improve the performance of supercapacitors practically by using those evaluation parameters, since there will be a trade-off among those parameters. Therefore, one should design the device depending on what a specific application is looking for. For instance, since both energy and power densities are proportional to the square of the cell operating voltage, increasing the cell voltage can have a greater contribution to energy and power improvement of supercapacitor. This indicates that increasing the performance of supercapacitors in terms of energy and power densities significantly rely on the development of innovative electrolytes in order to increase the operating cell voltage. Moreover, development of novel carbon structure with highly effective specific surface area, high packing density and high conductivity is also of high relevant for supercapacitors [20]. The following sections will be focused on the overview of recent developments of different electrolytes and carbonaceous electrode materials for supercapacitors.

1.3. Electrolytes for Supercapacitors

The electrolytes (either liquid or solid electrolytes) are among the main components of supercapacitors (SCs), providing ionic conductivity, thereby facilitating ion compensation in each electrode of the cell during charge-discharge process [5,8]. The two main properties of electrolytes for supercapacitors are their ionic conductivity that can have an effect on the ESR of the SCs, and the electrochemical stability window (ESW) that will determine the operating voltage of the SCs. Thus, both power and energy densities will increases as it is discussed in the previous sections. Therefore, the electrolytes, which exhibit wider ESW and higher ionic conductivity, are the desired

choice for the better capacitive performance of supercapacitors. The electrolyte nature including the ion type and size, the ion concentration and solvent, the interaction between ions and solvent all have significant influence on the performance of supercapacitors. In addition, the interaction between electrode materials and ions of electrolyte also play a significant role in the capacitive performance of supercapacitors. For instance, the mismatching between the ions size of electrolyte and the pore size of carbon electrode materials significantly influences the capacitance stored in supercapacitors.

Electrolytes in supercapacitors play an important role in stabilizing other important parameters of supercapacitors. These include internal resistance, rate performance, operating temperature, cycle life, self-discharge, and toxicity, which need to be considered in the practical use of supercapacitors. The effects of electrolyte on different parameters, in turn, on the performance of supercapacitors are depicted in Figure 1.10.

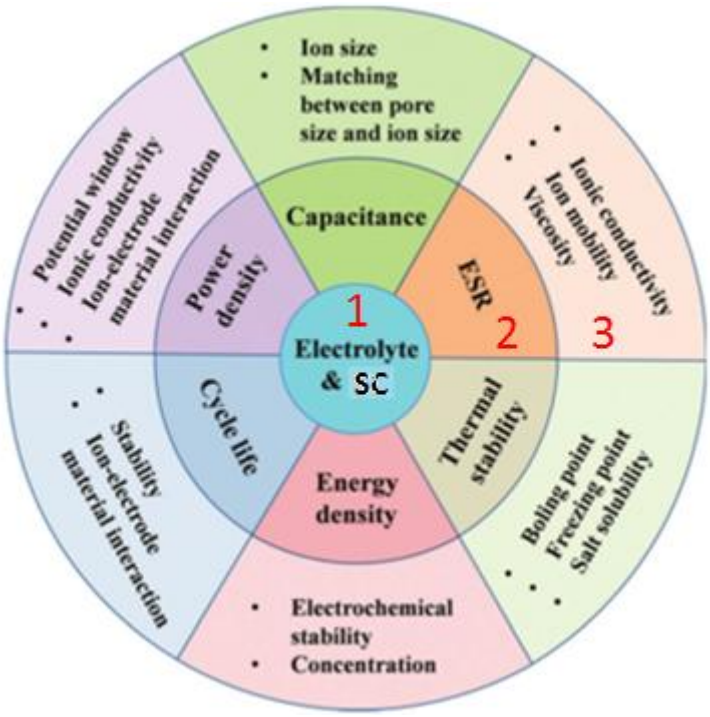

Figure 1.10. Effects of electrolyte properties on different parameters affecting the performance of supercapacitors (SC) [17].

The figure comprises three concentric circles; circle 1 consists of electrolytes and electrochemical supercapacitors (ES). Circle 2 comprises the parameters which determine the performance of supercapacitors. Circle 3 shows the properties of electrolyte (factors) that affect the parameters in (circle 2). For instance, ionic conductivity, ion mobility, and viscosity of electrolytes have a direct influence on ESR

of supercapacitors (see Figure 1.10). On the other hand, the parameters within each circle also affect each other. For instance, if the value of ESR (circle 2) is higher then, the power density of supercapacitors will be lower and so on. This shows the properties of electrolytes listed in circle 3 are very important factors for determining the performance of supercapacitors in one way or the other.

To date, several types of electrolytes have been developed for SCs and reported in literature. Electrolytes are broadly classified as liquid electrolytes and solid /quasi-solid electrolytes. Liquid electrolytes can be further categorized as aqueous electrolytes, organic electrolytes and ionic liquid electrolytes. Whereas solid or quasi-solid electrolytes can be grouped as polymer electrolytes, gel polymer electrolytes and inorganic solid electrolytes [17,42]. The general classification of electrolyte is shown in the diagram in Figure 1.11.

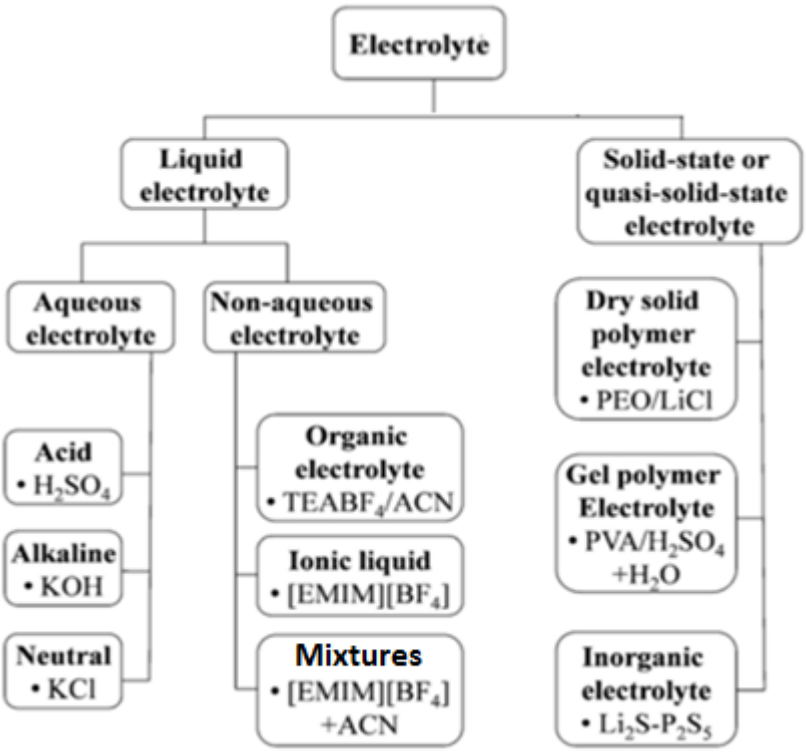

Figure 1.11. Classification of electrolytes for supercapacitors [17].

So far, there is no a single electrolyte which meets all the requirements for supercapacitors. There is always a trade-off between the two aforementioned important parameters of electrolyte; ionic conductivity and electrochemical stability window. For instance, supercapacitors with aqueous electrolytes comparatively possess high ionic conductivity and capacitance. But its ESW is limited by the narrow decomposition of electrolyte (e.g. acidic or alkaline has maximum 1V), hence resulting in low energy density devices. On the other hand, SCs with organic or ionic liquid electrolytes can be

operated at higher voltage, and will exhibit higher energy density compared with aqueous electrolytes. In addition, solid electrolytes own the advantage of avoiding leakage problem of liquid electrolytes, but they normally suffer from lower ionic conductivity. Therefore, each electrolyte has its own advantages and disadvantages.

As a result, different approaches have been carried out to develop new and high-performing electrolytes to make a wider operating potential window, higher ionic conductivity, and wide working temperature ranges. This will give an opportunity to exploite the positive effects of given electrolytes on the performance of SCs such as capacitance, energy, power density, thermal stability, and self-discharge. Herein, the following subsections will be focused on a brief review of common types of electrolytes for SCs such as aqueous, organic, ionic liquids and solid or quasi-solid state electrolytes.

1.3.1. Aqueous Electrolytes

With regard to energy density of SCs, aqueous electrolytes are relatively low choice for commercial SCs. However, aqueous electrolytes have been extensively used in research because they are inexpensive, can be easily handled thereby simplifying the fabrication and assembly process. Moreover, aqueous electrolytes relatively possess a conductivity at least one order magnitude higher than organic and ionic liquid electrolytes [30]. In general, aqueous electrolytes can be classified as acid, alkaline, and neutral solutions.

In acidic electrolyte, the most extensively used electrolyte is H_2SO_4 due to its higher ionic conductivity (0.8 Scm^{-1} at 25 ^oC), beneficial for lowering the ESR, consequently increasing power density of SCs [36]. The maximum capacitance of SCs with strong acid electrolyte (i.e., H_2SO_4) and activated carbon electrodes has been reported in the range from 100 to 300 Fg^{-1} [17,44,45]. In pseudocapacitors with H_2SO_4 electrolyte, it is reported that the specific capacitance can increased due to the fast redox reactions between some functionalities on the surface of carbon electrodes (oxygen, nitrogen and metal nitride and oxides) [17,46–48]

On the other hand, alkaline electrolytes are also frequently used for SCs investigation. Among several alkaline solutions, KOH is the most frequently used electrolyte in SCs due to its high ionic conductivity (0.6 Scm^{-1} of 6 M NaOH at 25 ^oC). Other basic electrolytes such as NaOH and LiOH have also been investigated. The maximum capacitance of activated carbon and alkaline-based SCs is similar to acid-based SCs [17].

Besides acidic and alkaline, neutral electrolytes containing salts such as NaCl, LiCl, KCl, have also been intensively investigated for SCs in the past decades. This is

due to their wider working potential window (1.5-1.6 V), and less corrosion [49] . To summarize, using neutral aqueous electrolyte in SCs is not only solve corrosion, but also it increases operating cell voltage as well as it is cost effective. The maximum specific capacitance reported for SCs based on activated carbon electrodes and 1 M Li_2SO_4 electrolyte is 180 Fg-1 [50].

1.3.2. Organic Electrolytes

Organic electrolytes are currently dominated the commercial market due to their high ESW (2.5 to 2.8 V) as shown in Table 1.2. This will significantly enhance both energy and power densities compared with aqueous electrolytes. However, there are some issues need to be considered while using organic electrolytes in SCs. They are usually associated with high cost, less specific capacitance, lower ionic conductivity, high flammability and volatility and toxicity compared to aqueous electrolytes [16,17]. In addition, organic electrolytes possess larger solvated ion size, and low dielectric constant, leading to lower capacitance in SCs compared with aqueous electrolytes. In order to have ionic conductivity, it is necessary to dissolve conducting salts in organic solvents to formulate the organic electrolyte.

For instance, the typical organic electrolyte for SCs is tetraethylammonium tetrafluoroborate ($TEABF_4$) dissolved in acetonitrile (AC) or propylene carbonate (PC). With this electrolyte, it is possible to store a maximum capacitance, maximum energy, and power densities around 150 Fg^{-1}, 25 $Whkg^{-1}$, and 25 $kWkg^{-1}$, respectively by using highly porous interconnected carbon nano-sheet based SCs at 2.7 V and 1mVs-1 [51].

The ESW of organic electrolytes is rather important as it determines energy and power densities. As the matter of fact, ESW of organic electrolyte is depend on several factors. These include the type of conducting salts (cations and anions), solvents and impurities, especially trace amount of water [53]. Recently, with the aim of increasing ESW and conductivity, F.Alloin *et.al*, reported that the ESW of organic electrolytes could be increased beyond the normal ranges (2.5 to 2.8 V) up to 3.5 and conductivity up to 5.2 $mScm^{-1}$ at 25 ^{o}C by using methoxypropionitrile (MP) as co-solvent for ethylene carbonate (EC). As a result, based on activated carbon (AC) electrodes and 1 M $TEABF_4$ in EC/PM electrolyte, SCs were able to charged up to 3.5 V and stored the maximum capacitance about 100 Fg^{-1} [54].

Table 1.2. Commercial EDLC based on organic as well as aqueous electrolytes [52]

Manufacturer	Technology	Rated data					
		V (V)	C (F)	R (mΩ)	E_{real} ($Whkg^{-1}$)	Specific Power ($kWhkg^{-1}$)	
						95%	Peak
Asahi Glass	Activated carbon/propylene carbonate	2.7	590	0.9	5	2.6	23
EPCOS	Activated carbon/ acetonitrile	2.5	220	3	3.8	1.1	10
		2.7	3400	0.45	4.3	0.8	6.7
ESMA	NiO/KOH/C hybrid	1.3	10000	0.28	1.1	0.2	1.4
LS Cable	Activated carbon	2.8	3200	0.25	3.7	1.4	12
Maxwell	Activated carbon/ acetonitrile	2.7	2885	0.38	4.2	1.7	8.8
Ness	Activated carbon/ acetonitrile	2.7	1025	2.5	3	27	
		2.7	1800	0.55	3.6	1	8.7
		2.7	5085	0.24	4.3	1	8.5
Nippol Chemcon	Activated carbon/ Propylene carbonate	2.5	2250	2.8	2.8	0.5	4
Panasonic	Activated carbon/ Propylene carbonate	2.5	1200	1	2.3	0.5	4.6
	Activated carbon/ acetonitrile	2.5	1791	0.3	3.4	1.9	17
		2.5	2500	0.43	3.7	1	9.2
Power Sys.	Activated or graphitic / Propylene carbonate	2.7	1350	1.5	4.9	0.7	5.8
		3.3	1800	3	8	0.5	4.3

Nevertheles, its intrinsic property of volatility still remains a drawback compared to IL electrolytes. However, in some cases when SCs based on organic electrolyte are charged beyond the normal ranges of ESW (2.5-2.8 V), unwanted redox reactions may happen at the electrode materials or electrolytes, causing self-discharge and gas evolution due to electrolyte degradation and carbon electrochemical oxidation. This leads to the failure of organic electrolyte based SCs considering to its long term performance and safety [55]. In this regard, ionic liquids are alternative advantageous options over organic electrolytes.

1.3.3. Ionic Liquid Electrolytes

Ionic liquids (ILs, sometimes also called as room temperature molten salts) are generally defined as those salts composed of ions (cations and anions) with melting points below 100 °C. ILs, sometimes perceived as "green solvents", usually comprise asymmetric organic cation and inorganic or organic anions and they have week interactions between ions, leading to low melting point [17,56].

It is a century ago that the triethylammonium nitrate was identified as a pure low melting salt-Ionic liquids (ILs) [57]. Then in 1940s, the first patent was documented describing the application of cellulose dissolution in a molten pyrrolidinium salt for a nuclear fuel reprocessing. Since then it has provoked the study of low-melting point chloroaluminatates [58]. Roughly in the same time, the need for new anions for polymer electrolytes based on polyethylene oxide led to the idea of a 'plasticizing anion'-an anion having a delocalized charge and multiple conformations differing only slightly in energy. The model of such anions is the bis(trifluoromethylsulphonyl)imide ($CF_3SO_2–N–SO_2CF_3$) ion, also known as TFSI, in which the extremely electron-withdrawing $CF_3SO_2^-$ groups are conjugated and linked by flexible S–N–S bonds [59]. When combined with an imidazolium cation, such as 3-ethyl-1-methylimidazolium, this anion produces a fluid ionic liquid (melting point –15 °C) with high ionic conductivity (8.8 $mScm^{-1}$) [43], comparable to the best organic electrolyte solutions. In addition, its decomposition or significant vapour pressure is as high as 300–400 °C [60].

1.3.3.1. Types and Physicochemical Properties of Ionic Liquids

Recently, the development and application of IL electrolytes in various fields have been significantly increased. This is because of their unique physicochemical properties such as high thermal, and wider electrochemical window, negligible volatility, non-flammability, low melting point, solubility affinity with many compounds, moderate viscosity, high polarity, flame retardant and high ionic conductivity [59–63] .

Depending on their composition, ILs can be classified as aprotic, protic and zwitterionic as shown in Figure 1.12. The former is suitable for lithium ion batteries and supercapacitors while the second is good for applications in fuel cells. Zwitterion ILs are more suitable for applications in electrochemical devices with addition of salt as well as ionic liquid based membrane [56,59,64]. Aprotic ILs can be prepared by the reaction of metathesis of halide salt with group 1 metal ammonium salt of the desired anion [61]. Whereas, Protic ILs are originated by the transfer of a proton from a Brönsted acid to a Brönsted base (usually an amine) [59]. On the other hand, Zwitterionic ILs can be prepared from a typical ion pair of imidazolium IL and sulfonates, dicyanide, or carboxylate mostly for proton exchange membrane applications [64].

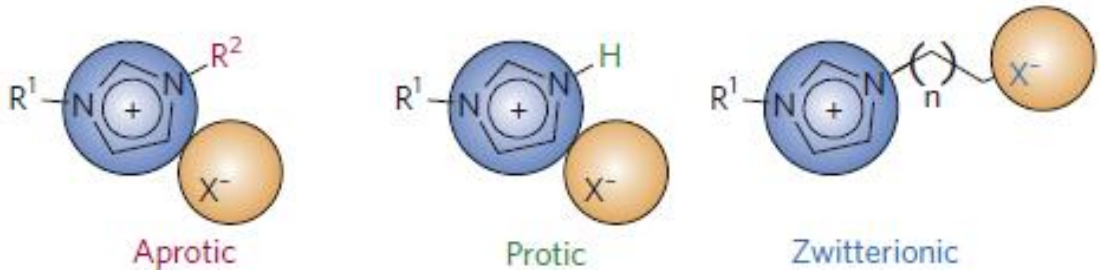

Figure 1.12. Basic types of ionic liquids

Moreover, combinations of different cations and anions give opportunities for flexibility in material design and optimization of their properties for specific applications. As shown in Figure 1.13, the common cations include among others, imidazolium, pyrrolidinium and quaternary ammonium, alkylphosphonium. The common anions cover a broad range of inorganic (e.g. halides (Cl^-, Br^-, I^-), polyatomic inorganics (PF_6^-, BF_4^-), and polyoxometallates), or more typically from organic anions such as NO_3^-, $TFSI^-$, and FSI^- [61–63].

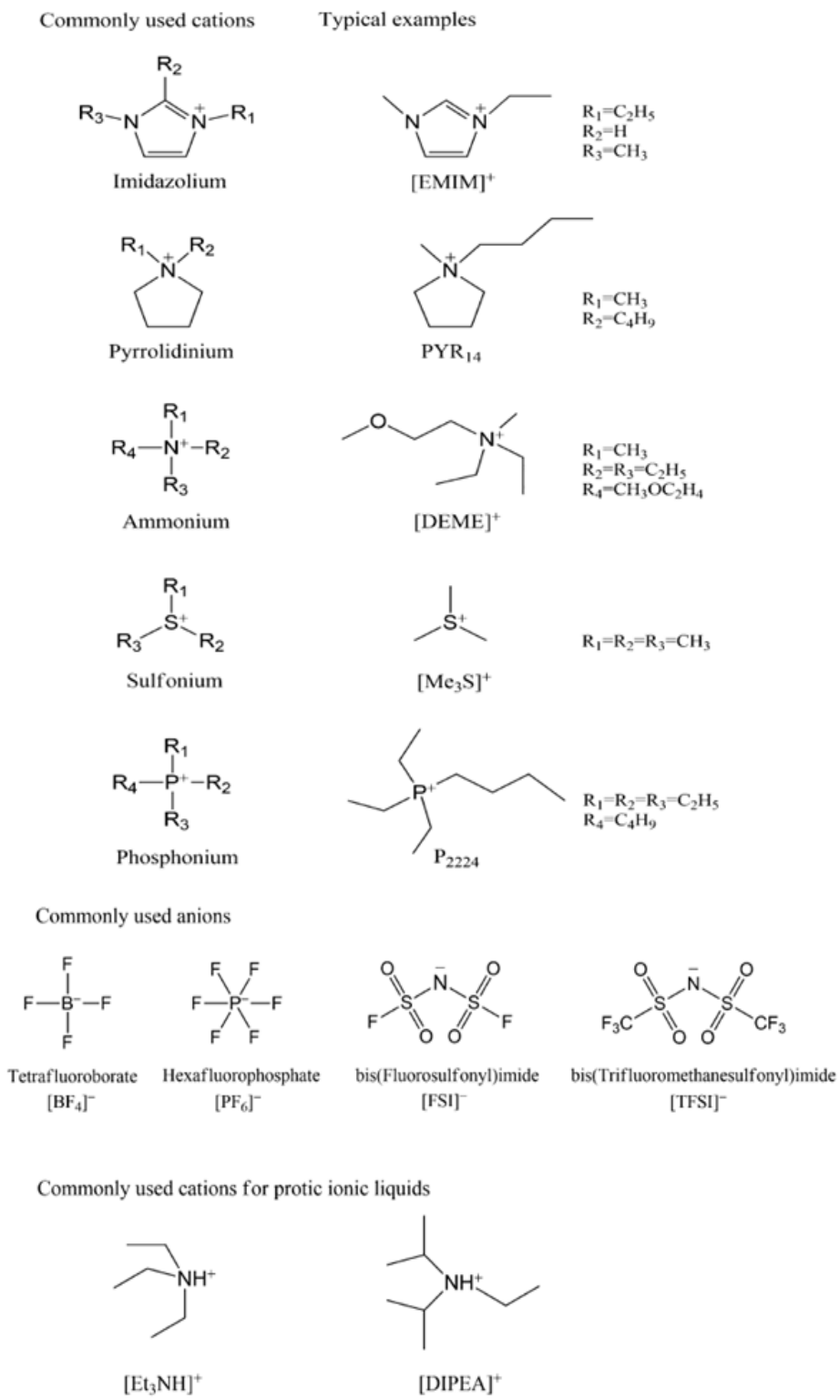

Figure 1.13. Structures of common types of cations, and anions of ionic liquids

As discussed before, conductivity and ESW of ILs are the decisive parameters for the performance of SCs. Nevertheless, they are significantly depending on the type of cation and anion of IL. Figure 1.14 depicts the ionic conductivity and ESW of different ILs, showing that EMI-based ILs displays the highest ionic conductivity reaching 10^{-2}

Scm^{-1} at RT, but their ESW values are below those of tetraalkylammonium or pyrrolidinium based ILs. This could be the main limitation in the practical use of imidazolium based ILs for high voltage batteries and supercapacitors. Furthermore, Figure 1.14 shows that both conductivity and ESW can be changed by varying not only cations but also anions of ILs.

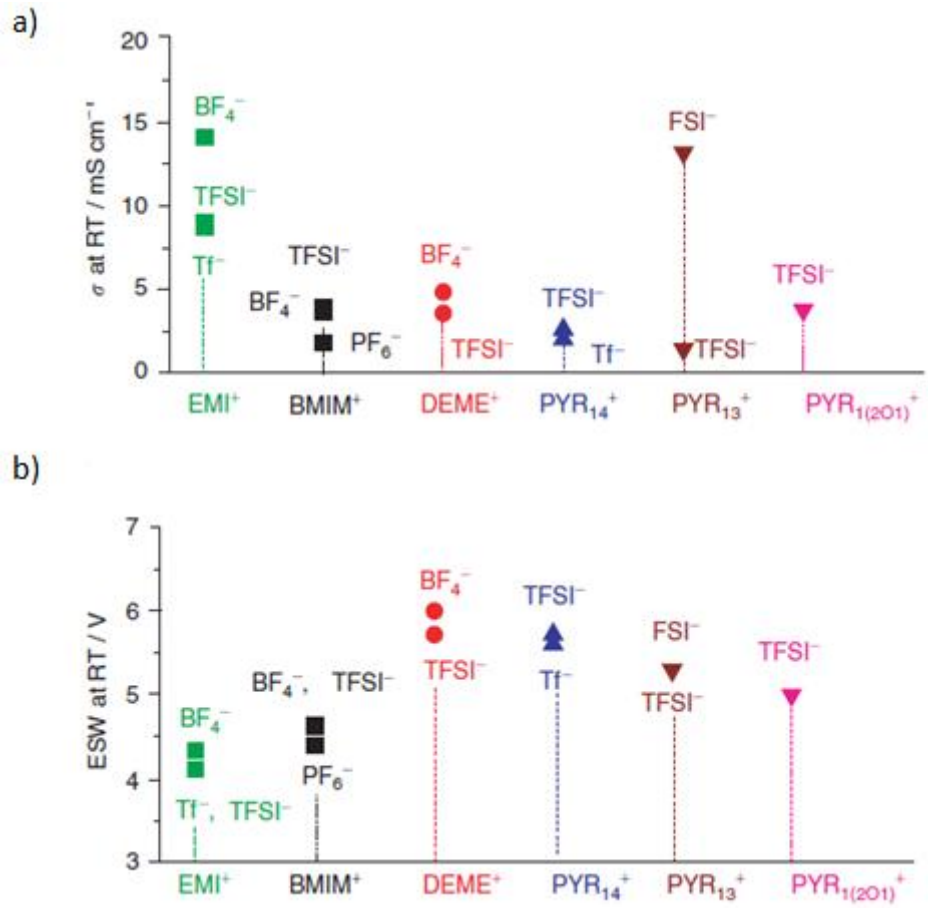

Figure 1.14. a) Conductivity (σ) and b) electrochemical stability window (ESW) of various ILs at RT [65]. EMI^+- 1-ethyl-3-methyl imidazolium, $BMIM^+$ 1-butyl-3-methylimidazolium, N-diethyl-N-methyl(2-methoxyethyl)ammonium ($DEME^+$), N-butyl- N-methyl-pyrrolidinium (PYR_{14}^+), N-methyl-N-propyl-pyrrolidinium (PYR_{13}^+), and N-methoxyethyl-N-methylpyrrolidinium ($PYR_{1(201)}$) cations with different anions.

The versatility of ILs in terms of physicochemical properties (conductivity, hydrophobicity, melting point, viscosity, solubility, and chemical and thermal stabilities) can be varied by changing the substituent group or the cation or the combined anion. In 2010, Watanabe *et.al.*,[66] has reported about ionicity of ILs, describing that the change of structure of cations or anions in ILs will result in a change in ionicity ("dissociativity"). On the other hand, ionicity is, in a certain degree, controlled by the molecular forces (inter-ionic forces), IL nature, and its structure. This

shows that the key factors for the change of properties of ILs are coulombic interactions, which increase the cohesion energy. For instance if the ion pairs (the interaction between cations and anions) of ILs are sufficiently long-lived without any dissolution, they turned out to be neutral in electric field. Thus the ion pairs will not contribute to ionic conductivity. Since ionic conductivity depends on the balance between anion–cation interactions and their respective volume, this would have important influence on most applications of ILs as electrolytes in electrochemical devices [67,68]. In fact, the coulombic interactions between anions and cations determine the quality of ILs depending on their dissociation. Figure 1.15 shows the general topology of good and poor ILs with respect to their cation-anion interactions.

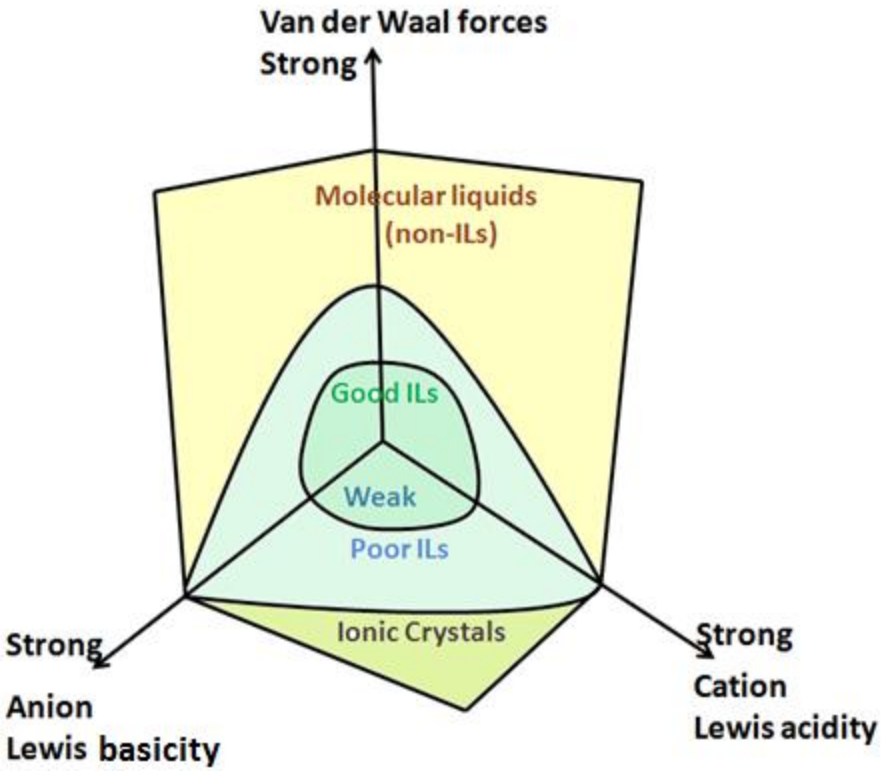

Figure 1.15. Good and poor ILs depending on the interaction strength between cations and anions of ILs (adapted from [56,66]).

In Figure 1.15 the arrows indicate the magnitude of strength of the interaction forces between cations and anions. Good IL electrolytes are in the region of week interaction forces (at the center of the figure). If the interaction forces among ions increase, the ionicity ("dissociativity") decreases resulting in poorer ILs. The strong interaction forces later result in molecular liquids or ionic crystals but not ionic liquids.

Conceptually, the salt comprising a cation and anion might be classified into one of four different groups according to the strength of interaction between anion and cation. A shown in Figure 1.16, these include Type-I that is a combination of a strongly Lewis-acidic cation with a strongly Lewis-basic anion, Type -II a weakly Lewis-acidic

cation with a strongly Lewis-basic anion. Type-III- are a combination of strongly Lewis-acidic cation with a weakly Lewis-basic anion, and Type IV- a weakly Lewis-acidic cation with a weakly Lewis-basic anion. In the Type I salts, the strong cation–anion attractions resulted in the ionic crystals that cannot be dissociated into ions at room temperature unless they are solvated with amphiphilic solvents like water, which is generally not the case with typical ILs. Salts consisting of strong Lewis acidic cations (Type II) or strong Lewis basic anions (Type III) give rise to poorer IL ionicity than in the case where the ILs (Type-IV), which contain weak Lewis acidic cations and week Lewis basic anions. Depending on their ionicity, Type-IV labelled as good ILs, while Type-II and III are poorer ILs due to their higher magnitude of cationic and anionic interactions than good ionic liquids (type-IV) (see Figure 1.16) [66].

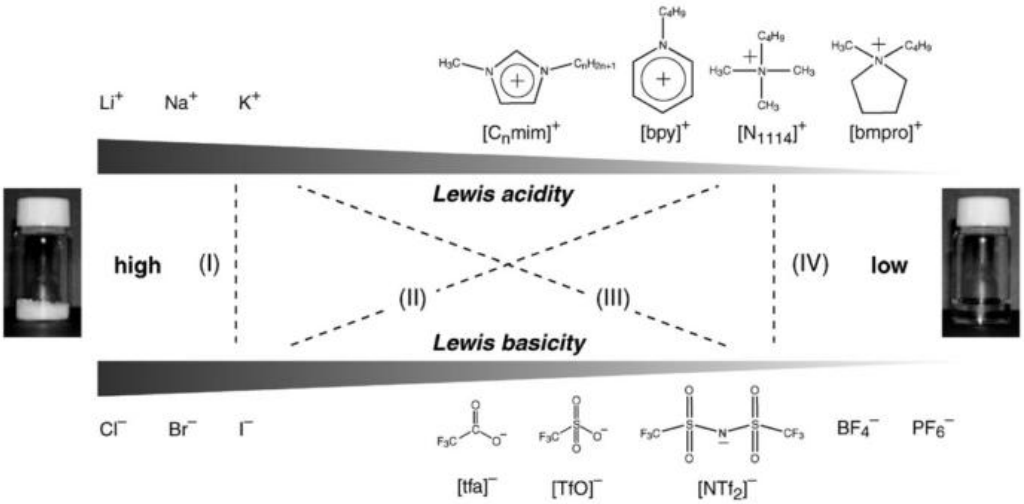

Figure 1.16. Different combinations of salts consisting of cations and anions, arranged in order of Lewis acidity for cations and Lewis basicity for anions [66]. [C_{nmim}]: 1-alkyl-3-methylimidazolium, [bpy]: N-butylpyridinium, [bmpyr]: N-butyl-N-methylpyrrolidinium, [N_{1114}]: trimethyl-butylammonium, [tfa]: trifluoroacetate, [TfO]: trifluoromethanesulfonate, [NTf_2]: bis(trifluoromethanesulfonyl)amid

In summary, the variations in the cationic and anionic structures results in different intermolecular forces in the ILs. In turn, the magnitudes and balance of the intermolecular (inter-ionic) forces control the ionicity (ionic nature or "dissociativity"). The ionic nature can be explained by anionic Lewis basicity and cationic Lewis acidity for ILs having different types of anions and cations with the same counter parts. Moreover, it can also be explained by van der Waal forces for the [$C_n$mim]-based ILs with different alkyl chain lengths, which can be found in detail in ref. [66].

1.3.3.2. Application of Ionic Liquids in Energy Storage and Production

Due to their unique physicochemical properties, the applications of ILs can be extended from energy storage and conversion (Li-ion batteries, supercapacitors, actuators, fuel cells, and dye-sensitized solar cells (DSSC)) to metal deposition, lubricants, micro-extractions for environmental analysis. They can be also used as reaction media in chemistry [69], catalysis [61], biochemistry, polymer science and even biomechanics [59,70]. Countless cation/anion combinations that exhibit low volatility, low flammability, high electrochemical and thermal stability, as well as ionic conductivity create the possibility of designing ideal tailor-made electrolytes for energy storage and productions. In this subsection, however, brief summary of ILs applications in different electrochemical energy storage devices is discussed (see Figure 1.17).

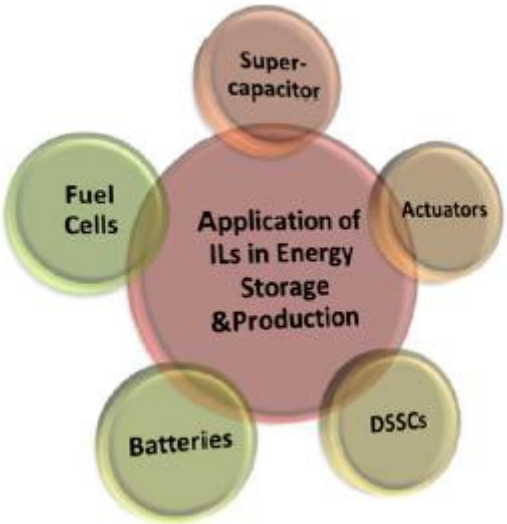

Figure 1.17. Application of ILs in energy storage and Production [71]

a) ILs as Electrolyte for Lithium-ion Batteries

The high flammability and volatility of organic electrolytes, which are derived from exothermic reactions, are the driving forces to replace the conventional organic electrolytes by ILs in lithium ion batteries. The high thermal stability and low vapor pressure of ILs insure reliabilities by preventing the intrinsic problems in organic electrolyte based batteries. Those problems include thermal runaway, pressure build up, heat evolution and sometimes explosion are all associated with organic electrolytes [59]. The use of IL as electrolytes in Li-ion batteries aims to overcome the drawbacks related to the safety aspects present with conventional organic electrolytes [72]. As a first approach, ILs were used as an additive to organic electrolytes minimizing their flammability character [73]. However, the presence of organic solvents still presents

other disadvantages such as the evaporation of the solvent and the associated pollution. Therefore, in a further approach, ILs are investigated in Li-ion batteries as solvent-free electrolytes. Selection of ILs among the vast variety is usually made by taking into account different properties of ILs including ionic conductivity, thermal stability and ESW vs Li/Li+ [59,71]. A significant number of ILs containing quaternary ammonium cations 1-ethyl-3-methylimidazolium $[EtMEim]^+$, trimethylpropylammonium $[TMePrAm]^+$, N-methyl-N-propylpyridinum, $[MePrPi]^+$, N-methyl-N-propylpiperidinium, $[MePrPp]^+$) and bis(trifluoromethanesulfonyl)imide $[N(CF_3SO_2)_2]$ anion were examined as electrolytes for lithium ion batteries. These electrolytes were tested in a $Li/LiCoO_2$ positive electrode system with a lithium-foil anode (negative electrode-battery grade). The positive electrode was prepared by mixing $LiCoO_2$, carbon black, and PVDF with the ratio of 85:7:8 w/w, respectively [74]. For instance, the $[PrMePp][N(CF_3SO_2)_2]$ electrolyte showed the best properties in the battery: the charge/discharge coulombic efficiency was 97 % at C/10 current rate at a voltage between 3.2–4.2V [74].

In some cases, there are certain problems related to their ionic conductivity while using ILs as electrolytes in lithium ion battery. Moreover, addition of lithium salt still could results a decrease in conductivity, which corresponds to a Li ion pair formation with Lewis basicity anions. Therefore, in order to prevent this problem, the reduction of Lewis basicity of the anionic center is necessary. This can be done by introducing lithium ion coordinating Lewis basic ligands such as lithium salt of borates containing penthafluorophenoxy electron-withdrawing group in to the anionic structure. In the end, the ionic conductivity of electrolyte is expected to be increased due to increasing of self-dissociation of lithium ionic liquid and enhance the lithium transfer number [75].

Due to the low cathodic stability of imidazolium-based cations, other cations such as quaternary asymmetric ammonium systems [76] pyrazolium [77], and pyrrolidinium [78] are preferred. Concerning to the anion, those bearing fluorinated imide anions such as bis(trifluoromethanesulfonyl)imide (TFSI) and very recently the bis(fluorosulfonyl) imide (FSI) become the most successful [79].

b) ILs as Electrolyte for Fuel Cells

Due to the need for proton conduction in proton exchange membrane fuel cells (PEMFC), protic ILs are mostly advantageous for this purpose. Using perfluoroalkylsulfonate membranes (Nafion) in PEMFC produces proton at the anode. Then the produced proton migrates through the electrolyte towards cathode and reacts with oxygen to produce water. This process requires humidification of the electrolyte membrane to maintain its ionic conduction. As a result, the operational temperature of

the system is limited to be below 80 °C. This means that, to operate the PEMFCs at high temperatures (100 -200 °C), the aqueous electrolyte need to be replaced by ILs due to their stability at high temperature. Furthermore, operating PEMFCs at high temperature enables the reduction in size of the cooling system and improved polarization behaviour leading to a reduction in the use of costly precious metal catalysts. Therefore, ILs containing ionic conductivity *ca.* 10^{-2} Scm^{-1}, become promising candidates to realize operation of PEMFCs at high temperatures [71,80]. Some of electrolytes for PEMFC are developed by the combination of proton conducting organic electrolytes (amine) with $HN(SO_2CF_3)_2$, or with imidazole $[ImH](CF_3SO_2)_2N$ base ILs. Imidazole-rich electrolytes exhibited higher conductivities due to proton hopping conduction mechanisms among the imidazole molecules [80,81]. Moreover, a novel binary mixture of ionic liquids, which are consisting of a zwitterionic liquid (Bim_3S) and $(CF_3SO_2)_2NH$, were tested for anhydrous proton transport. The ionic conductivity of the resulted mixture of Bim_3S (1-(1-butyl-3-imidazolio)propane-3-sulfonate) and $(CF_3SO_2)_2NH$, is found *ca.* 0.1 $mScm^{-1}$ at room temperature, and increases with temperature up to 10 $mScm^{-1}$ at 150 °C [82].

c) ILs as Electrolyte for Actuators

Actuators are structurally a three-layered configuration where the solid polymer electrolyte layer is sandwiched between two conducting polymer layers such as polyaniline (PANI), polypyrrole (PPy), and polythiophene (PT), which show dimensional changes by ion expulsion/inclusion movement during oxidation or reduction processes [83]. The relative differential expansion between conducting polymer layers results in bending. However, the low ionic conductivity of the solid polymer electrolyte leads to an intrinsically slow response system. When the solid polymer electrolyte is swollen with an electrolyte solution, the ionic conductivity is increased but the performance of this system deteriorates by the evaporation of the solvent. Moreover, another problem of present actuator systems is delamination, which limits the actuator life due to low cohesion between the conducting polymer, the metal layer, and the flexible solid polymer electrolyte. Therefore, in order to solve these problems, ILs have been used in an attempt to fabricate electromechanical actuators for their excellent physical and electrochemical properties such as non-volatility and high ionic conductivity [80]. Mostly, polymer supported gelatinous containing ILs used for actuators. For instance, polymers such as PANI, PVDF-HFP and PPy can be blended with both ILs $[BMIm]BF_4$, $[BMIm]PF_6$ and $[EMIm](CF_3SO_2)2N$ for actuators [83–85].

d) ILs as Electrolyte for Dye-Sensitized Solar Cells (DSSC)

Due to their non-volatility and non-flammability, ILs are promising candidates to resolve the loss of electrolytes at high temperature and the long-term stability problems associated with the use of conventional solvents in DSSCs. In order to facilitate the diffusion of redox species, ILs with low viscosity are usually preferable for DSSC application [71,80]. The $(CF_3SO_2)_2N$-based salts were the first ILs proved as electrolyte for DSSC in which they were used to prevent the loss of electrolyte solvent by vaporization [86].

e) ILs as Electrolyte for Supercapacitors

The current commercial SCs available in the market are mostly based on organic and aqueous electrolytes. However, the narrow ESW of these electrolytes limit the energy performance of the current SCs, in turn, hinders the wide applicability of SCs. Therefore, IL electrolytes become the promising candidate electrolytes for SCs to improve the energy density due to their broad ESW (ca 4V), conductivity at a level of 10 $mScm^{-1}$ and acceptable capacitance ca 10 μFcm^{-2} [43]. Since the maximum energy is directly proportional to the square of voltage of electrolyte ($E=1/2CV^2$), using ILs with higher operational voltage will pump up the energy storage performance of SCs. To realize high energy density and power density of SCs, IL electrolytes with high conductivity and broad ESW are required.

In some cases, the viscosity of some ILs is relatively high and it causes a decrease in ionic conductivity. To address this issue, operational temperature of SCs can be increased or ILs mixed with molecular solvents such as propylene carbonate and ethylene carbonate can be used. Despite, mixing ILs with organic solvents significantly improve physicochemical properties by reducing viscosity and increasing ionic conductivity, their ESW and safety is remained lower than the corresponding neat ILs due to the presence of organic solvents [71,87].

So far, among the vast type of ILs, mainly imidazolium and pyrrolidinium cations combined with fluorinated anions such as bis(trifluoromethanesulfonyl)imide (TFSI), bist(trifluorosulfonyl)imide (FSI), tetrafluorobarate (BF_4), and hexafluorophosphate (PF_6) have been investigated as electrolyte for SCs. SCs with these electrolytes can be charged between 3 and 3.5 V thereby increasing energy density [88]. For instance, in terms of energy and power densities, supercapacitors with aqueous electrolyte (*e.g.*, H_2SO_4) can have maximum power density (*ca.* 111 $kWkg^{-1}$), but lower energy density about 6.7 $Whkg^{-1}$. But supercapacitor with organic electrolyte (e.g., ET_4NB_4 in 1 M PC) exhibited a medium range of energy and power densities of 34 $Whkg^{-1}$ and 14 $kWkg^{-1}$,

respectively. On the other hand, the maximum power density of supercapacitors with IL (e.g. EMimTFSI) was reported about 12 $kWkg^{-1}$, which is obviously lower than that of organic electrolyte, but its energy density is higher than the one in organic electrolytes and it could be reach as high as 48 $Whkg^{-1}$ [89].

1.3.4. Solid-or Quasi-Solid State Electrolytes

As mentioned before, supercapacitors generally utilize activated carbon electrodes in combination with liquid electrolytes such as aqueous, organic, or ionic liquids (ILs). Hence, the use of separators to avoid electric contacts between electrodes and heavy encapsulation materials to prevent liquid leakage is inevitable. As a result, these devices become unsuitable to be integrated into textiles, microelectronics or lightweight energy storage systems [90]. At this stage, electrochemical energy devices based on solid electrolytes have attracted attention in recent years due to the increasing demand for fast delivering power for portable electronics, wearable electronics, microelectronics, printable electronics, and generally flexible electronic devices. The solid-state electrolytes have dual functionalities serving as the ionic conducting media as well as electrode separators. The use of solid-state electrolytes in electrochemical energy storage has advantages over their liquid counterpart. These include mechanical stability, simplification packaging and fabrication process, and liquid-leakage free thereby guarantee safety [17].

To date, most of solid-state electrolytes developed for electrochemical energy storage are polymer electrolytes. Polymer electrolytes are defined as solid ionic conductors formed by the dissolution of salts in suitable high molecular weight polymers. Generally, most polymer electrolytes classified as solid polymer electrolytes (SPE) and gel polymer electrolytes (GPE). SPE is composed of polymers (e.g. poly(ethylene oxide, PEO) and inorganic salt (e.g. LiCl) without addition of any solvent (e.g. water). In this case, the movement of salt ions through the polymer matrix enhances ionic conductivity of SPE [42]. In the following sub-sections, gel polymer electrolytes are shortly summarized.

1.3.4.1. Gel Polymer Electrolytes (GPE)

Gel electrolytes are mixed polymer-solvent-salt systems where the role of the polymer is simply to act as stiffener for the low molecular weight solvent, which operates as a medium for cation and anion motion. For instance, GPE can comprise a polymer host (e.g. poly(vinyl alcohol, PVA), salt (lithium salt), and solvent (aqueous, organic or ILs solvents). In GEP, the polymer usually serve as a reservoir, which can be swollen by the solvent [91–93] . Despite their lower mechanical strength, the conductivity of GPE is

much higher than the one in SPE. This is due to the presence of liquid in the polymer matrix of GPE. In general, there is often a trade-off between mechanical strength and conductivity of GPE.

GPE is further classified as hydrogel polymer electrolytes (HGPE), organogel polymer electrolytes (OGPE) and iongel polymer electrolytes (IGPE) depending on the solvent embedded within the polymer matrix. HGPE are usually composed of polymers (e.g. PVA) and various aqueous solution such as strong acids (e.g. H_2SO_4 and H_3PO_4), alkaline (e.g. KOH), and neutral (LiCl) [94]. Several papers have been reported demonstrating the use of HGPE in SCs [95–98]. However, there are still some drawbacks associated with hydrogel polymer electrolytes including their limited thermal stability and narrow ESW [94].

On the other hand, to increase the operating cell voltage, OGPEs, which consist of polymer host and organic solvents have been utilized as solid-state electrolyte for SCs. Various polymer hosts including PEO [99], polyvinylpyrolidine (PVP), poly (ether ether kethone) (PEEK) [100] and copolymers with different constituents such as poly(acrylonitrile)-block-(polyethylene glycol)-block-poly(acrylonitrile) (PAN-b-PEG-b-PAN) [101] have been used for synthesis of OGPE. For organic solvents in OGPE, acetonitrile (ACN), dimethyl sulfoxide (DMSO), dimethylformamide (DMF) are commonly used organic solvents [17]. In some cases, salts such as $LiClO_4$, $LiPF_6$, NaTFSI should be added as supporting of OGPE [99,101]. Nevertheless, due to the presence those organic solvents in the polymer matrix, OGPEs are associated with some disadvantages including narrow ESW, toxicity, and high volatility, thereby harmful to the environment.

At last, but not least, ionogel polymer electrolytes (IGPE), sometimes called ionic liquid based polymer electrolytes (IL-b-PE), have been intensively used as solid/quasi-solid state electrolytes in energy storage and conversions in the last decades [102]. In the case of IGPEs, instead of using organic or aqueous solvent, ILs are usually embedded in the polymer matrix (polymer host) due to the realization of their wider ESW, non-volatility and high thermal stability. The physicochemical properties of IGPE significantly rely on the intrinsic nature of ILs, host polymers and their interactions. This indicates that the selection of appropriate polymer host and ILs in order to design IGPE with high ionic conductivity and thermal stability is a crucial step. Some common examples of host polymers for IGPE include PVA [103], PEO [104], poly(vinylidene fluoride-co-hexafluoropropylene) (PVDF-HFP). For instance, ionic liquid 1-ethyl-3-methylimidazolium tris(pentafluoroethyl) trifluorophosphate (EMImFAP) embedded in PVdF-HFP copolymer host has been prepared and tested for its application as an electrolyte for solid state SCs. The prepared film shows excellent thermal stability over

the range of temperature from 5 to 90°C with wider ESW of 4.4 V (−2.2 to 2.2 V) and high ionic conductivity of 2 $mScm^{-1}$ at room temperature [105]. Due to the advantage of high ionic conductivity, some imidazolium based ILs such as ionic liquid 1-ethyl-3-methylimidazolium tetracyanoborate (EMImTCB) [106] and 1-ethyl-3-methylimidazolium thiocyanate (EMImSCN) [107] have been also used for preparing IGPE. More recently, instead of using conventional polymers, which are mentioned above, polymeric ionic liquids (PILs) have been used as a host polymer in polymer electrolytes.

1.3.4.2. Polymeric Ionic Liquids (PILs)

PILs are an extraordinary type of polyelectrolytes that contain an IL species in each of the repeating units. They can be polycations or polyanions depending on the structure of the backbones (see Figure 1.18a). PILs are usually synthesized by polymerizations of ILs monomers and present some of the unique properties of ILs (ionic conductivity, thermal stability, tuneable solution properties, and chemical stability) together with the intrinsic polymer properties [108–110]. During polymerization of ILs monomers, the properties of ILs can be translated to the synthesized PILs, but their properties are not necessarily related to each other. Despite their lower ionic conductivities, PILs are typically characterized with enhanced mechanical stability, improved process-ability, dynamic chains, durability, and spatial controllability of the IL moieties when compared to their corresponding IL monomers [111]. Compared with conventional polymers that always need addition of salt to enhance ionic conductivity (*e.g.* PEO), no additional salt needs to be added to the PILs. This is because the pendant counter-ion is free to move and responsible for the ionic conductivity. Nevertheless, for further improvement of ionic conductivity, nowadays PILs are blended with appropriate ILs, and the resulted blend is called IL-b-PE or IGPE (see Figure 1.18b). The ionic conductivity value of this blend is in between the ionic conductivity of the corresponding PILs and pure ILs itself.

The combination of PILs and ILs take some advantages. These advantages include high chemical affinity and miscibility between PILs and ILs that help to develop tailored-made ion gels. Moreover, high ion-ion interactions between the polymer matrix and IL which avoids micro-phase separation and leakage of ILs out of the polymer matrix during high load applications, and the requirement of low content of ILs to get the desire ionic conductivity suitable of a specific application are among the advantages [42,112–114].

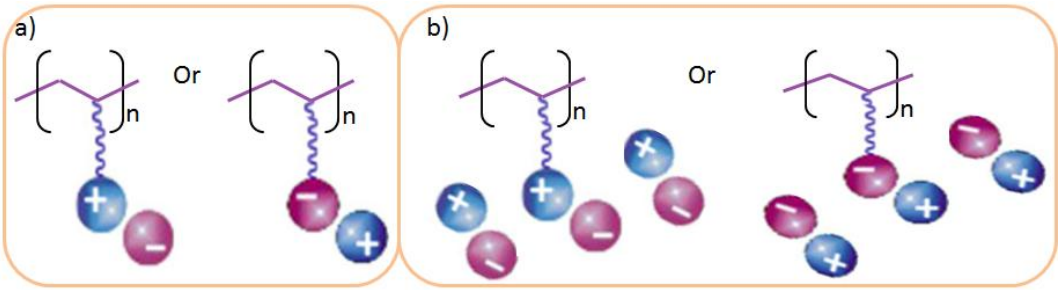

Figure 1.18. Schematic representation of a) polymeric ionic liquids (PILs) and b) iongels or ionic liquid based polymer electrolytes (IL-b-PE) using PILs as polymer matrix. Adapted from [111].

Factors Affecting Ionic Conductivity of PILs: The decisive factors that affect ion conductivity of PILs include chemical structure of the cation, anion, spacer, glass transition temperature of polymer, and external factors including humidity and purity of PILs [42]. In terms of structure of cation, to prepare PILs with high ionic conductivity, it has been proposed that one should use aprotic imidazolium cation with long preferably ethylene oxide containing, side chain at third position of heterocyclic ring. In this case, extremely bulky side substituents at the backbone of polymer will result in the decrease in inter-ion interactions (high ionicity) of the polymer which later decreases its glass transition temperature (T_g) [115].

On the other hand, considering to the structure of anion of PILs, it is revealed that the ionic conductivity of PILs is found to be significantly reliant on the delocalization's charge, its size and hydrogen bond formation with polyelectrolytes [42]. This literally indicates that in order to increase ionic conductivity of PILs, the anion should be highly mobile, smaller size with delocalized charge, and lower interactions with the spacer of the polymer backbone.

Similarly, the spacer of PILs between the main polymer chain and the attached anion significantly influences the ionic conductivity of PILs. As a rule of thumb, the spacer of PILs should be flexible in order to increase its ionic conductivity. For instance, insertion of long flexible PEO spacer enhances the conductivity form $1.1*10^{-8}$ to $1.3*10^{-5}$ Scm^{-1} [116].

In the case of glass transition temperature (T_g), the main impact of the polymer backbone on conductivity is made by its flexibility. Generally T_g of the PILs and the its ionic conductivity are inversely proportional. *i.e.*, PILs with lower T_g would exhibit higher ionic conductivity and by its interaction with ions *i.e.*, helping in ions dissociation and thus improving ions mobility. This relation can be explained in such a way that by lowering the T_g of a polymer would increase the mobility of its chain segments, improving the mobility of the side chains with the terminal ionic groups.

This mobility would lead to an increase in the ionic conductivity of the overall system. The influence of T_g on ionic conductivity is reported in [117].

Moreover, humidity is another factor that significantly influences the ionic conductivity of the PILs. It was reported that the change of humidity up to 29 % in the chamber during measurement would enhance the ionic conductivity by one order of magnitude [118]. Therefore, since PILs are hygroscopic and adsorb water easily, it is necessary to pay attention not only drying of polymers to remove its water content, but also to accurate measurement of their conductivity in dry atmosphere conditions [42]. Nevertheless, this conductivity value of PILs is so insufficient for most applications that addition of ILs is used as a strategy to enhance the conductivity of polymer electrolytes [42].

Due to the versatility nature of PILs and ILs, in principle it is possible to manipulate and tune the properties of ion gel polymer electrolyte (IL-b-PE) by designing PILs´ cationic and anionic structure or their combinations. This would give an opportunity to prepare IL-b-PE with enhanced ionic conductivity as high as 10^{-2} -10^{-3} Scm^{-1} at 25 ^{o}C [42,112]. Unlike cationic PILs and anionic PILs where the ionic conductivity is associated with only the counter-anion and counter-cation, respectively, in the case of blends of PILs with ILs, ionic conductivity is related to the migration of both anions and cations of the ionic liquid and the counter ions of the polymer matrix itself (PIL). From this point of view, Mecerreyes *et.al.* has recently reviewed in more detail and reported the main factors which influence the ionic conductivity of PILs, in turn, ion gels [42].

1.3.4.3. PILs in Combination with ILs to Prepare Ionic Liquid based Polymer Electrolyte (IL-b-PE)

The common methods to prepare IL-b-PE containing PILs as a polymer matrix are swelling of PILs in ILs, solvent casting technique, and in-situ copolymerization in the presence of ILs (Figure 1.19).

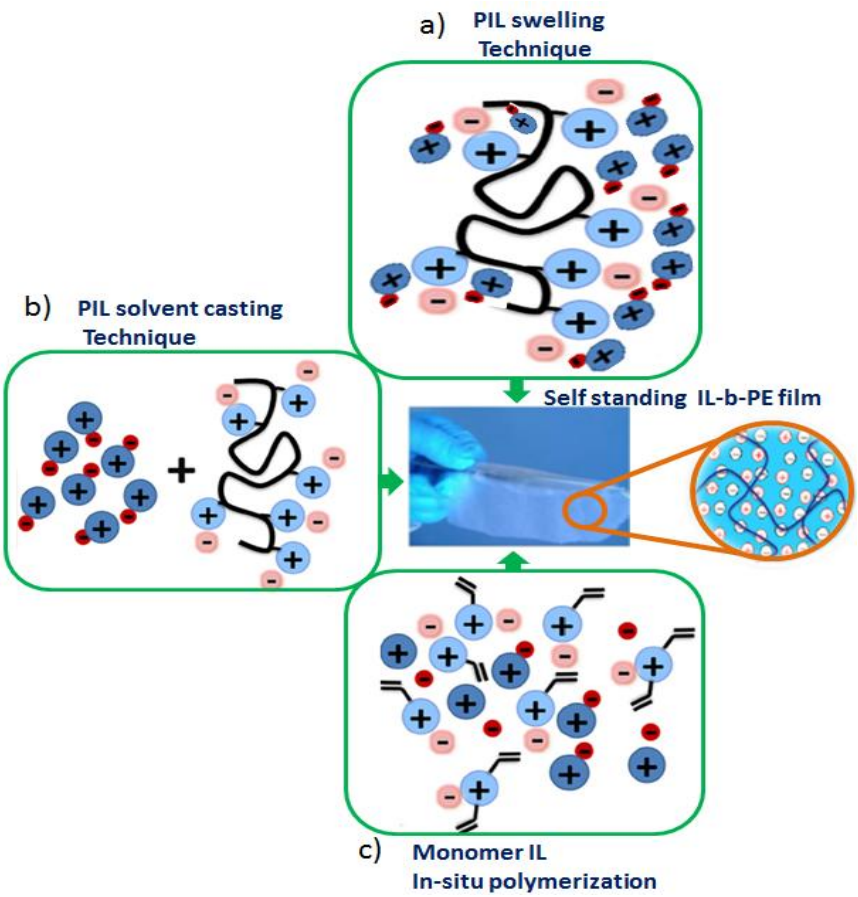

Figure 1.19. Preparation methods of iongel (IL-b-PE) a) Swelling of PIL with ILs b) solvent casting of PIL and c) monomer IL in-situ polymerization [42]. In the middle, photo showing self-standing membrane of IL-b-PE with its magnified internal structure of the membrane.

Solvent casting techniques involves dissolution of ILs and PILs in a common organic solvent (e.g. acetone) followed by casting the solution by utilizing different techniques (e.g. doctor blade technique) and drying the mixture to evaporate the solvent [113,119]. On the other hand, in swelling technique, the PIL first casted in appropriate solvent and the resulted thin film is immersed into pure ILs [120]. Nevertheless, it is complicated to control the IL content in the polymer matrix. In the third method, preparation of iongel involves in-situ polymerization of IL monomers in IL medium as a solvent [121].

Among these three methods, solvent casting method is widely used since it allows the preparation of high quality and well-controlled iongel, which can form a freestanding membrane with high content of ILs in the polymer matrix. Despite the increase in ionic conductivity of iongel with the IL content, the mechanical strength of the free standing membrane is decreasing and sometimes it is sticky when the content

of ILs in the polymer matrix increases [42]. Therefore, it is important to select compatible and appropriate PILs and ILs contents in order to have homogenous film and avoiding micro phase separations.

In-situ polymerization method has advantages over the other two methods. These include the IL content in the iongel can be increased up to 100 % by adding difunctional monomer cross-linkers. Moreoevr, IL is used as the reaction medium accelerating the polymerization of IL monomers and the blend can be formed in short period of time [42,122]. In this case, the conductivity could be increased with increasing the IL content in the iongel electrolytes. Nevertheless, the in-situ method introduces some impurities such as unreacted monomers or initiators which might limit their electrochemical performance [42].

Application in Electrochemical Devices: Generally, the application of IL-b-PE, synthesized with the combination of PILs and ILs, in electrochemical devices was not realized until R.Marcilla *et.al.* has reported the first work on the preparation of tailor-made IL-b-PE. Marcilla reported the preparation of IL-b-PE based on mixing imidazolium based PILs (poly[1-vinyl-ethyl-imidazolium]) with different ILs such as 1-butyl-3-methylimidazolium bis(trifluoromethanesulfonimide) [bmim][Tf2N] 1-butyl-3-methylimidazolium tetra- fluoroborate [bmim][BF_4] and 1-butyl-3-methylimidazolium bromide [bmim][Br], and their application in electrochromic devices [123]. Later, D. Mecerreyes *et.al.* has reported the first work on the application of iongels in lithium ion batteries based on a ternary mixture of PIL (poly (diallyldimethylammonium) TFSI), IL (N-butyl-N-methylpyrrolidinium TFSI) with the combination of lithium salt (LiTFSI as solid electrolyte for solid state lithium ion battery [114]. Since then, several reports on the application of iongels in different electrochemical devices such as DSSC [124], alkaline fuel cells [125,126], and actuators [127] have been reported. In this thesis, the application of IL-b-PE as electrolyte for supercapacitors is investigated for the first time.

1.4. Carbon Electrode Materials for Supercapacitors

The interest in porous carbon as electrode materials for supercapacitors s is recently increased. This is due to their high surface areas, possibility of tailoring their structure for particular application, good polarization, high chemical stability and low price, good electrical conductivity, environmental friendly, thermal and mechanical stabilities [128,129]. Generally, carbon based materials for supercapacitors can be classified as activated carbons [89,99,130], carbon nanotubes (CNTs) [97,131–134], carbon aerogels [135]. Furthermore, carbon nanofibers [136–138], template porous carbons [139], surface functional or heteroatom carbons such as nitrogen doped carbons/graphite

[140–143], and metal nitride doped carbon [144,145] are also different forms of carbon based materials. Some of different carbonaceous materials for supercapacitors are shown in Figure 1.20 [146]. According to IUPAC nomenclature, carbonaceous porous materials can be grouped into three classes based on their pore size: micro-porous, meso-porous and macro porous materials having pore diameter, d < 2 nm, 2 nm < d < 50 nm and >50 nm, respectively [129].

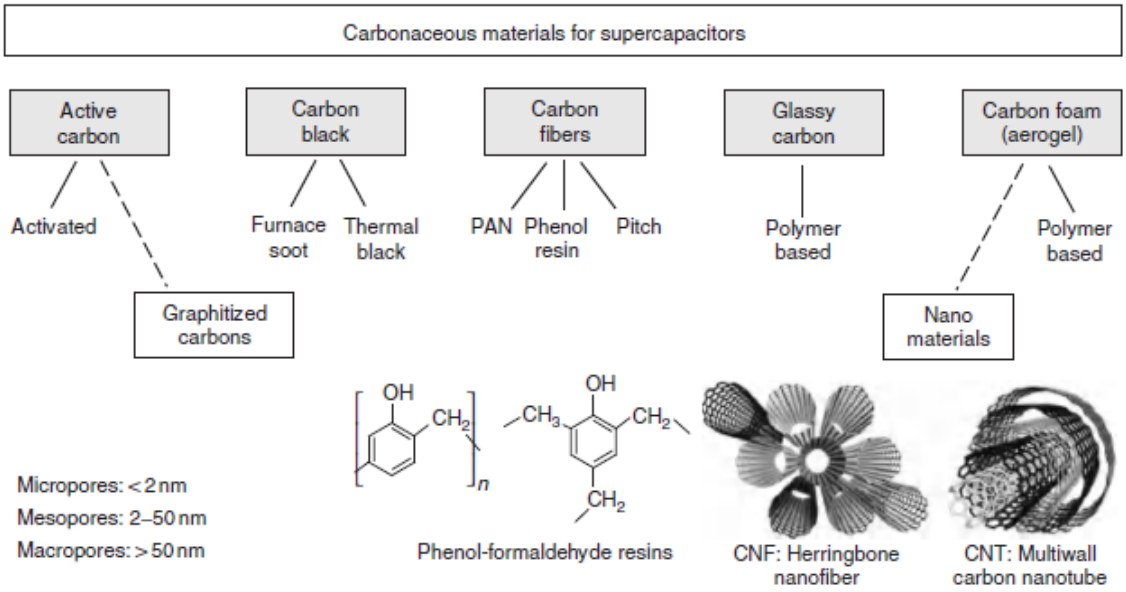

Figure 1.20 . Different types of carbonaceous materials for SCs.

Due to their versatile properties, porous carbon materials have been applied not only as electrodes for supercapacitors [33,137,147–149], and batteries [136,150–152] but also for wide range of applications such as gas separation [153,154], catalyst support [155,156], water purifications [157], absorbents [158], and fuel cells [159,160]. The selection of right carbon materials for the specific application is strongly depend on their properties such as the pore size, pore connectivity, specific surface area, and morphology of the material. These properties of porous carbon materials can be tuned by the synthesis methods, the type of precursors, and the presence of heteroatoms built in the porous carbon structure [129]. Therefore, selecting the right precursors, and using the right synthesis method would give opportunities to adjust and control the pore properties as well as the morphologies of the materials.

1.4.1. Importance of Textural Properties for the High Capacitive Performance of Supercapacitors

The capacitance of SCs is apparently depends on the textural properties of the electrode materials. Nevertheless, not all electrochemically active surface area (micro-pores) is accessible to ions of electrolyte due to the mismatch of ion size and pore size. As a result, capacitance usually doesn't linearly increase with specific surface area [161,162]. This shows that the pore size of the electrode materials plays important roles in the capacitive performance of SCs. However, from literature, there are two discrepancy views about the relationship between capacitance and pore size of electrode materials. The first view is commonly known as the "traditional view", where many researchers reported that the pore size with less than 0.5 nm [162] and 1 nm [163] were not accessible for hydrated ions and ions of organic electrolyte, respectively. As a result, the maximum specific capacitance was decreased in both electrolytes. Therefore, it was suggested that the use of electrode materials with pore size distribution ranging from 2 nm to 5 nm, which is larger than the size of two solvated ions, was the convenient way to increase the capacitive performance of supercapacitors. Nevertheless, despite great effort has been put to increase capacitive performance, not more than 200 Fg^{-1} maximum capacitance was achieved both in aqueous and organic electrolytes [22,164].

In contrast, many researchers claimed the significant capacitive contribution of electrode materials with micropores (<2 nm), even pores smaller than the solvated ion size can store high charges [165–167]. This is rather a contradictory claim to the "traditional view" discussed above. It was demonstrated with carbide derived carbon (CDC) and tetraethylammonium tetrafluoroborate (NEt_4BF_4) in acetonitrile electrolyte [22,168]. In this case, the surface normalized specific capacitance (μFcm^{-2}) was first shown to be decreased with decreasing the pore size up to 1 nm and later the trend was dramatically reversed. This shows that the specific capacitance was increased with further decreasing of pore size < 1 nm, approaching the ion size, (see Figure 1.21). It was claimed that the gravimetric and volumetric capacitance of CDC was increased by 50 % and 80 %, respectively from that of activated carbons [22]. Since the solvated ions of $NEt_4^+BF_4^-$ electrolyte was 1.3 nm and 1.16 nm for cation and anion, respectively, it was concluded that the high capacitance storage in the micropores is due to the partial or complete removal of their solvated shells thereby allowing them to access the micropores [22,168].

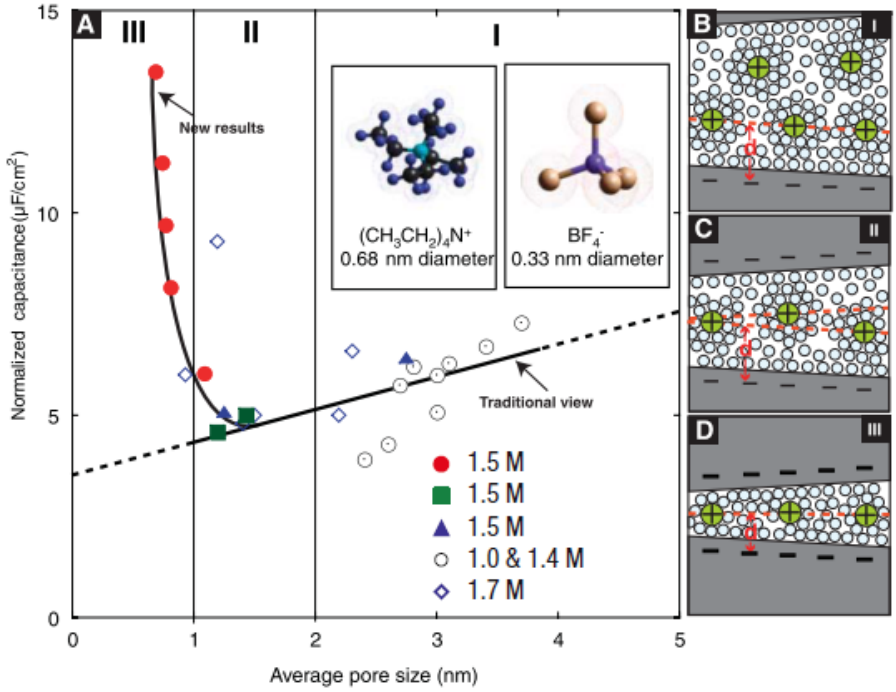

Figure 1.21. Specific capacitance normalized by the BET specific surface area of CDC carbons measured in $NEt_4^+BF_4^-$ electrolyte at different concentrations [22,168].

In Figure 1.21, (A) shows specific capacitance, normalized by BET specific surface area (SSA), decreased with decreasing pore size until a critical value was reached. This contradicts the traditional view of which it assumed that capacitance would continually decrease. (B to D) represents solvated ions residing in pores with distance between adjacent pore walls (B) > 2 nm, (C) between 1 and 2 nm, and (D) < 1 nm. Despite these two perspectives, separately hold true in their narratives, the increase in normalized capacitance of supercapacitors from synergetic effect of microporous and mesoporous contribution was totally neglected in both views, and it should be considered as a whole for the performance of supercapacitors.

1.4.2. Synthesis of Porous Carbon from Different Precursors

Porous carbon materials can be synthesized using countless carbon precursors and the search for low cost and sustainable carbon materials as electrode for supercapacitors is a vital issue. Perhaps with an eye to the future, selection of precursors, design and development of sustainable carbon-based porous materials are of high relevance [3]. So far, different porous carbon materials have been synthesized from naturally abundant low-cost renewable carbon precursors such as coconut shell [130], wood [45,169], fruit stones [170], pitch [171,172], celtuce leaves [173], and rice husk [174,175].

In most cases, porosities of carbon materials from those precursors have been mainly introduced by using template methods (either hard-, or soft templates) [176–

179], or a second activation step through either physical or chemical methods [180–182], leading micro-porous, meso-porous, or macro-porous carbon materials.

Template synthesis of porous carbon material has different sequential steps. First, mixtures/blends of template and carbon precursor need to be prepared. Second, the prepared mixtures should be carbonized at certain temperature under atmospheric or noble gas (nitrogen, helium, or argon) environment. After carbonization, the template has to be removed from the carbon matrix and leave the carbon with isolated and interconnected pore structures which were occupied by the templates [129,183]. Despite these template techniques can guarantee well controlled and designed porosity at different levels, the method is often complicated and make the synthesis highly energy intensive and expensive. Moreover, some template synthesis methods indeed accompany by certain shortcomings including use of some harmful chemicals in order to get rid of hard templates, temperature restriction for soft templates and additional post-activation steps in which pore creations is etched into carbon itself and results in a significant loss of carbon yield. Therefore, for simplification and practical application, one step approach for synthesis is highly desirable [184,185].

1.4.2.1. Salt Templating" Method

"Salt templating" is a simple mixing of a non-carbonizable inorganic salt with a carbon precursor that is condensed and scaffolded in the presence of the molten salt at elevated temperatures. The salts nano-cluster can be easily removed by simple washing with water and results in the generation of porous carbons. This method has been applied for the synthesis of highly porous carbons using different precursors and several reports can befound in literature [179,184,186–189]. The appropriate choice of cation size and counterion in the salt controls the minimal pore size as well as miscibility with the reaction medium via adjustment of the polarizability. More recently, an innovative salt template method was proposed by the group of Prof. M. Antonietti as a simple one-step and sustainable pathway for the synthesis of highly porous functional carbons from ionic liquids precursors [184]. They reported that the heteroatom doped porous carbons (boron or nitrogen doped carbon) with controlled pore volume, architecture, and high specific area up to 2000 m^2g^{-1} can be synthesized by using one step salt-templating method at high temperature. Binary eutectic mixtures of salts (LiCl, NaCl and KCl mixed with $ZnCl_2$ separately) have been used as salt porogens. Furthermore,, the ionic liquids, 1-butyl-1-methylpyrrolidinium dicyanamide ($PYR_{14}DCA$) and 1-Ethyl-3-Methylimidazolium Tetracyanoborate (EmimTCB) were used as nitrogen/carbon and boron/carbon precursors, respectively. The authors concluded that the porosity/morphology of carbon was shown to be dependent only on

the nature and type of eutectic salt mixtures. Furthermore, they suggested that the synthesized doped carbons are competent materials in catalysis and energy storage applications [184].

1.4.3. Heteroatom Doped-Porous Carbon

Introducing heteroatoms to the carbon network is one of the strategies to increase the performance of porous carbon for different applications, especially as electrode material for energy storage devices and catalytic activities. This would give opportunities to integrate high porosity and redox active materials in the electrode simultaneously [190,191]. Moreover, doping carbon with heteroatoms would increase wettability and improve the electrical conductivity of carbon materials by localizing electronic features and lowering the valence or conduction band, thereby increasing the electron density at the Fermi-level [137,192,193].

The notable heteroatoms that can be introduced into the carbon network include nitrogen [46,137], sulfur [194], phosphorus [195], metal nitride [144] and boron [196]. These doped functional groups are electrochemically active and provide high number of hydrophilic polar sites which will later increase the wettability of the material, consequently enhances the overall performances [46,197]. Nitrogen functionalities introduce Lewis base or Bronsted base character to the carbon network and oxygen presented in the carbon can also introduce electron acceptor character into the carbon surface [198].

1.4.3.1. Nitrogen-Doped Porous Carbon

Nowadays, hybridization of porous carbons with nitrogen functional materials into nanocomposites is a very appealing approach to design active electrode materials. The incorporation of nitrogen into the carbon network can be achieved by using nitrogen rich substances as precursors. These precursors include acetonitrile pyrrole or polyacrylonitrile [178,199,200], pyridine [201], chitosan [202], urea or melamine [203,204] and ionic liquids [184,205,206]. In most cases, plenty of N-containing porous carbon is prepared by thermal treatment of porous carbons with N-containing gases (ammonia) [207–210], co-carbonization of carbon with N-containing precursors [211,212] and carbonization of N-containing polymers [213]. Most of these methods involve some expensive resources like hazardous gases such as ammonia, and multi-step procedures [214]. However, biomass derivative carbohydrates [202] and phenolic compounds such as phenol-formaldehyde resin [215–217] have been used and suggested as promising carbon precursors due to its easily availability and low cost of phenolic compounds.

In fact, there are several factors, which affect the properties and the content of doped nitrogen in the carbon network. These factors include the treatment temperature, the type, and concentration of nitrogen precursors, and synthesis methods. For instance, porous nitrogen doped carbon was synthesized from nitrogen containing carbohydrates such as chitosan (medium molecular weight) and D(+)-glucosamine hydrochloride by using hydrothermal carbonization under mild temperature (180 °C) followed by carbonization at 750 °C method. In those carbons, the nitrogen content was found to be in the range from 7.7 to 9.1 % for chitosan derived carbon and from 6.3 to 6.6 % for the carbon synthesized from D(+)-glucosamine hydrochloride [202]. This indicates that the nitrogen content significantly varies according to its precursor. Recently, it has been also reported that the content of doped nitrogen varies depending on the concentration of nitrogen precursors. For instance, Wilson *et.al.,* reported that increasing the amount of nitrogen precursors (EMI-DCA) in the mixture from 25 % to 100 % results an increased content of nitrogen from 5 to 12 %, respectively [205].

1.4.3.2. Types of Nitrogen Functionalities in N-doped Porous Carbon

During thermal treatment of precursors, nitrogen atom is incorporated into the structure of carbon matrix and eventually forms different types of nitrogen functionalities. The common types of nitrogen functionalities of nitrogen doped carbons include pyridine (6-membered rings), quaternary –N (interior part of the carbon) pyridine (OH functionality is close to the nitrogen vicinity), pyridine-N-oxide (oxygen is connected to nitrogen atom), pyrrole, imide, lactam, amine and amide as shown in Scheme 1.1.

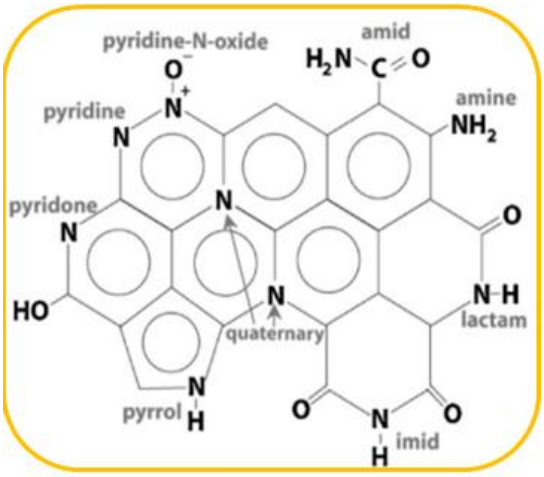

Scheme 1.1.Possible model of nitrogen containing functional groups on porous carbon, including Quaternary (N-Q), pyrrolic and pyridine (N-5), pyridinic (N-6), and pyridinic-N-oxide (N-X) [140,204].

An extensive overview of known and possible nitrogen functionalities present in nitrogen-doped carbon materials are shortly reviewed in Scheme 1.2 with their corresponding N1s nitrogen bonding energy.

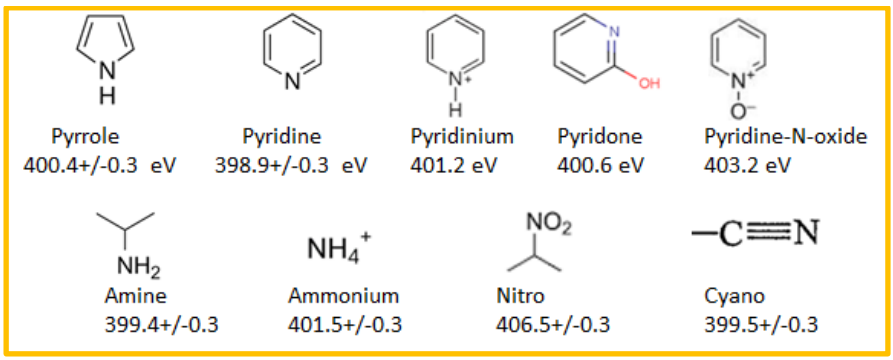

Scheme 1.2. Different forms nitrogen functionalities possibly present in nitrogen doped carbon materials with their N1s electron binding energy (BE) [218].

These nitrogen functionalities are mainly reliant on the nitrogen precursors and the treating temperatures. For instance, with regard to temperature, if a carbon is treated with urea or melamine at 400-700 °C, some functional groups such as amides, protonated amides, and aromatic amines are excessive. Whereas pyridine, pyrrol, aromatic amines protonated pyridine and quaternary nitrogen are higher if the carbon is treated at higher temperature (>650 °C) (see Scheme 1.3) [140,203,207].

Regarding the types of nitrogen precursors, if the carbon sample is treated with NH_3 at lower temperature (<400 °C), the reaction of ammonia with carboxylic sites and the ring systems of surface functionalities resulted in imides and lactams that are located within six-member rings. Moreover, additional side functionalities such as amides and amines attached to the carbon surface were also found from NH_3 treated carbons [140].

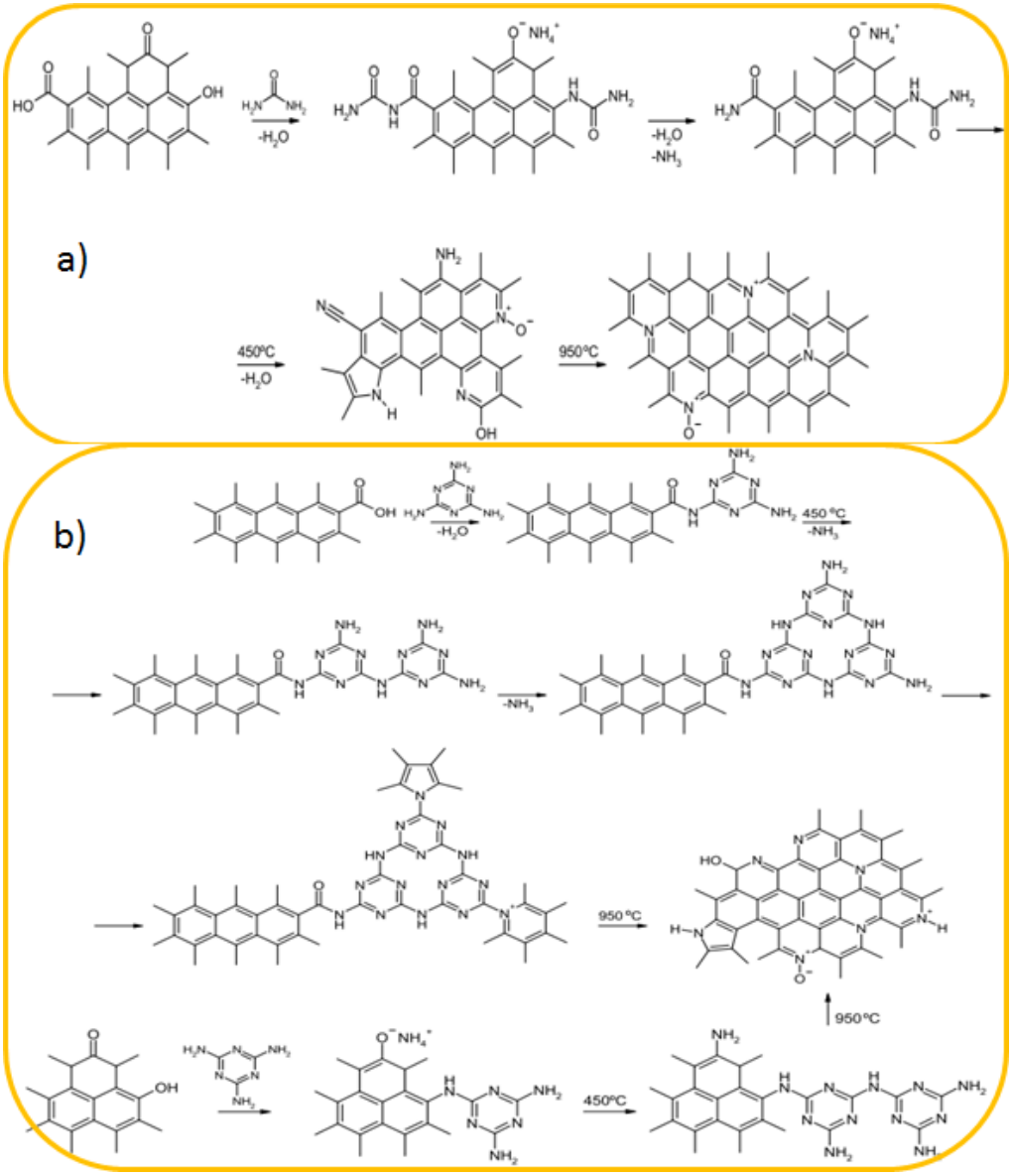

Scheme 1.3. Possible chemical reactions of carbon surface functional groups with a) urea b) melamine and thermal transformations [203]

1.4.3.3. Applications of Nitrogen Doped Carbon

Many of nitrogen rich carbons are considered as alternative promising candidate for efficient energy storage materials such as supercapacitors [46,143,205,219] and batteries [220,221]. A recent application is their use as efficient electrocatalyst for oxygen reduction reaction (ORR) in fuel cells and metal-air batteries [222,223]. Any enhancement in capacitive performance of nitrogen doped carbon is usually owned to the wettability of the electrodes, and the pseudocapacitance contribution from faradic reactions between ions of electrolyte and different nitrogen groups from the carbon network. Therefore, functional groups can be found in the form of pyrrolic, pyridinic, amine, nitro or quaternary graphitic [218,224] as explained in the previous sections.

Considering the high ion mobility and possible contribution of redox related reactions, most of the nitrogen doped carbon materials have been characterized in aqueous based electrolytes, mostly in H_2SO_4 [225,226] and KOH [137,214,226]. Capacitance of N-doped carbon electrodes in those aqueous electrolytes is quite high, in the range of 100-270 Fg^{-1}. For example, a nitrogen doped carbon synthesized from PAN was used as electrode for supercapacitor in KOH electrolyte, exhibiting high capacitance around 189-270 Fg^{-1} at 1 Ag^{-1} [214]. Moreover, the N-doped porous carbon synthesized from melamine was used as electrode material for supercapacitors in aqueous and organic electrolytes. The performance of supercapacitance with this nitrogen doped carbon electrodes showed a high capacitance, 205 Fg^{-1} in 1 M H_2SO_4, 208 Fg^{-1} in KOH, and low capacitance about 37.5 Fg^{-1} in organic electrolyte ($TEABF_4$/PC) and 74 Fg^{-1} in neutral electrolyte (3M NaCl) at 20 mAg^{-1} [46,226]. Moreover, the nitrogen-doped carbon as electrode for supercapacitors was also characterized using $TEABF_4$ electrolyte, exhibiting maximum specific capacitance as high as 114 Fg^{-1} [227]. The increment of specific capacitance with these nitrogen-doped carbon electrodes is associated with pseudocapacitance contribution of nitrogen embedded in the carbon networks. Nevertheless, the energy density of these aqueous based and organic based systems is still low due to low electrochemical stability window of electrolytes. With this regard, ionic liquid electrolytes are of high relevance in terms of high operation voltage up to 3.5 V,while benefiting from a non-volatile and temperature stable nature at the cost of low ion mobility compared to aqueous and organic electrolyte [228]. Nevertheless, only a small number of studies have been conducted in terms of characterizing nitrogen doped carbon materials in ionic liquids [142,143,205]. In those articles the range of specific capacitance has been reported about 120-240 Fg^{-1}, which is in the range of capacitance values of aqueous and organic electrolyte based supercapacitors. Specifically, the maximum capacitance of nitrogen doped carbon electrode is reported as high as 237 Fg^{-1} at 0.1 Ag^{-1} in EMIM-TFSI [205], 122 Fg^{-1} in EMIM-TFSI [142] at 1 Ag^{-1} and 170 Fg^{-1} at 2 A g^{-1} [143].

1.5. Application and Limitations of Supercapacitors

Supercapacitors are mostly used in applications requiring many rapid charge-discharge cycles rather than long term compact energy storage. However, recently the early commercialization of electrochemical capacitors for computer memory backup has now broaden into applications for transportations, and energy conservations in the large scale [10]. Within cars, buses, trains, cranes, and elevators, where they are used for regenerating braking, short term energy storage or burst mode power delivery [24].

Many large size commercial electrochemical capacitors have been recently fabricated by different companies around the globe (see photos in Figure 1.22).

Figure 1.22. Photo of different commercial electrochemical capacitors from the smallest Maxwell cells (store 1kJ) to the largest ESMA module (store around 180 kJ) [10].

From Figure 1.22, the ELIT and ECOND supercapacitors are based on aqueous electrolyte symmetric designs of bipolar construction, with many series-connected cells within the package. The ESMA capacitor, which is a larger scale, is a module consisting of a number of interconnected asymmetric cells. The Power Sys. module is composed of many individual symmetric cells externally connected and includes cell voltage-balance electronics. The figure further shows individual cells made by NESS, Nippon Chemi-Con, and Maxwell, which are of symmetric design with wound or prismatic construction [10].

Small supercapacitors (capacitance <10 F), which are a modules of two or more cells in series (4-8 V), are used in consumer electronics such as pagers, cellphones, and computer in conjunction with batteries either in power assist or battery backup mode. The requirements of small supercapacitors are usually given in terms of capacitance, RC values, volume, or thickness. The energy density of these devices is usually a secondary importance with the ability to provide periodic, multimillion second pulse being concerned [229].

Similarly, large supercapacitors (capacitance >100 F) have been recently developed for vehicle market such as hybrid electric vehicles (see Figure 1.23a) (car, bus, train), energy management/conservation applications (e.g. seaport cranes), day-night storage (see Figure 1.23b), and power tools (e.g. screwdriver).

Figure 1.23. Photo of a) electric bus powered only by ESMA asymmetric supercapacitors modules. Its 30MJ of stored energy provides 10 km of operation around a circle route. Recharging takes less than 15 min at 50 kW b) large SCs energy storage systems that provide short-time uninterruptible power. It is comprised of more than 7000 cells and is capable of delivering 2.1MW of power for 1 s. Design life is 15 years [10].

In electric and hybrid electric vehicles, supercapacitors provide the peak power for acceleration and recover energy during periods of braking. Similarly, in the day-night storage systems, supercapacitors have also been proposed for bulk energy storage to store off peak electricity from the utility grid at night, when it is abundant and low cost for use during the day, when it may be in short supply and more costly. This is particularly interesting for hot summer days, when there are heavy air conditioning loads on the grid system [229,230]. Commercial companies such as Maxwell (USA) and Panasonic (Japan) manufacture the majority of supercapacitors using symmetric activated carbon electrode materials and acetonitrile electrolytes (see Table 1. 3).

Table 1. 3.Summary of various commercial large supercapacitors [41]

Device	V rated	C(F)	R (mΩ)	RC (s)	Wh [a]	W/kg (95%)[b]	weight (kg)	volume (L)
Maxwell	2.7	2800	0.48	1.4	4.45	900	0.475	0.32
Maxwell	2.7	650	0.8	0.52	2.5	1281	0.2	0.211
Maxwell	2.7	350	3.2	1.1	4.4	1068	0.06	0.05
Ness	2.7	1800	0.55	1	3.6	975	0.38	0.277
Ness	2.7	3640	0.3	1.1	4.2	928	0.65	0.514
Ness	2.7	5085	0.24	1.22	4.3	958	0.89	0.712
Ashai Glass [c]	2.7	1375	2.5	3.4	4.9	390	0.21	0.151
Panasonic [c]	2.5	1200	1	1.2	2.3	514	0.34	0.245
Panasonic	2.5	1791	0.3	0.54	3.44	1890	0.31	0.245
Panasonic	2.5	2500	0.43	1.1	3.7	1035	0.395	0.328
EPCOS	2.7	3400	0.45	1.5	4.3	760	0.6	0.48
LS cable	2.8	3200	0.25	0.8	3.7	1400	0.63	0.47
Power sys.[c]	2.7	1350	1.5	2	4.9	650	0.21	0.151
Power sys.[c]	3.3	1800	3	5.4	8	825	0.21	0.15
ESMA-hybrid (C/NiO/aqu.)	1.3	10000	0.28	2.75	1.1	156	1.1	0.547
Fuji hybrid (C/metal oxide)	3.8	1800	1.5	2.6	9.2	1025	0.232	0.143

[a] energy density at 400 Wkg^{-1} constant power; V rated , (1/2)V rated

[b] Power is based on $P= (9/16)*(1-EF)*V^2/R$, EF-efficiency of discharge

[c] all devices use propylene carbonate and the rest use acetonitrile as the electrolyte

Current Limitations of Supercapacitors: some of the disadvantages of commercial supercapacitors include lower energy density (about 5 $Whkg^{-1}$) compared to battery (>50 $Whkg^{-1}$), high self-discharge rate and high cost. With regard to cost, supercapacitors cannot compete with batteries in terms of $/Wh, but they are highly competitive in terms of $/kW [231]. The energy density of batteries costs relatively cheaper (1-2 $/Wh) than the energy density from supercapacitors (10-20 $/Wh). On the other hand, the cost of power from supercapacitors (25-50 $/kW) is less than half of the cost of power from battery (75-150 $/kW) [230]. The high cost of energy of electrochemical capacitors has led to discouraging their acceptance in different applications. However, companies have doubled their efforts to decrease product costs and to emphasize the long term savings of longer life cycle associated to electrochemical supercapacitors [10] .

1.6. Statement of Problem

Despite great efforts have gone into developing high-performance energy storage devices (Li-ion batteries and capacitors) by using different electrode materials and liquid electrolytes, these energy storage devices suffer from slow power delivery or uptake (in the case of batteries) and low energy storage (in the case of capacitors). In this regard, a device with higher energy and power density is required in a number of applications including portable electronic device, electric vehicles, and different energy storage industries. Despite lower energy density, supercapacitors offer a promising set of characteristics such as higher power densities, higher charge-discharge rates, better cycle stability, and safer operation than batteries. Nevertheless, the main challenge in supercapacitors technology is how to improve the energy density without deteriorates its power density and safety. Moreover, the use of liquid electrolytes in conventional supercapacitors has raised concerns about safety issues and fabrication of supercapacitors based on liquid electrolytes usually accompanied with additional encapsulation materials to prevent liquid leakage and separators between electrodes to avoid short circuit. This fabrication hindered currently existing supercapacitors for flexible applications such as printed circuit and textiles. Therefore, this problem can be solved by developing solid or quasi-solid electrolytes to replace both liquid electrolytes and separator that exist in conventional supercapacitors. For these challenges, two approaches are widely considered to increase the energy density of supercapacitors in this PhD Thesis:

(I) The first approach is developing novel nitrogen doped carbonaceous based materials with high intrinsic capacitance and high electrical conductivity (low resistance).

(II) The second approach is developing innovative polymer electrolytes (IL-b-PE) with high electrochemical stability window (ESW). In this case, developing a solid-state electrolyte with high ionic conductivity and wide operating voltage (up to 3.5 V) are of high importance to address both high energy density and safety issues.

Developing both novel nitrogen-doped carbonaceous based materials as electrode and innovative polymer electrolytes with higher ESW (IL-b-PE) would both enhance capacitance and energy density of supercapacitors.

In this PhD Thesis, two main research questions are raised:

- What are the factors influencing the electrochemical performance of supercapacitors based on novel nitrogen doped carbonaceous based materials as electrodes and ionic liquid electrolytes? (Chapter 2, and 3)
- How to design innovative ionic liquid based polymer electrolytes (IL-b-PE) containing similar features of pure ionic liquid and improve electrochemical performance of all-solid state supercapacitors? (Chapter 4 & 5)

Research Approaches

To answer these research questions, two main experimental approaches corresponding to the research questions were designed.

In order to increase the capacitive performance of supercapacitors, the first experiment is focused on synthesis of highly porous nitrogen doped carbon and vanadium nitride doped carbon based nanocomposite materials as electrodes for supercapacitors. Then the electrochemical performances of supercapacitors based on as-synthesized carbon materials were characterized in different types of ILs to investigate their influence on electrochemical performance.

In the second approach, experiments were designed to develop innovative IL-b-PE based on a mixture of polymeric ionic liquids (PILs) with the different pure ionic liquids. Then, all solid state supercapacitors were assembled based on the as-synthesized IL-b-PE and activated carbon as electrodes and characterize their electrochemical performance.

For material characterizations different techniques such as isothermal analysis, BET, XPS, XRD, SEM, TGA, FTIR, 4-probe conductivity measurement, and elemental analysis were used. Furthermore, for electrochemical analysis, CV, CD, and EIS techniques were used to evaluate the performance of materials and supercapacitors.

1.7. Objectives of the Thesis

The main objective of this Thesis is to develop high performance supercapacitors based on innovative polymer electrolytes including ionic liquids and polymeric ionic liquid electrolytes (IL-b-PE) with novel carbonaceous nanocomposite electrode materials (nitrogen doped carbons and vanadium nitride doped carbons)

Specific Objectives

- To synthesize nitrogen doped carbon materials and examine the effect of synthetic parameters in electrochemical performance of supercapacitors based on those N-doped carbons using both aqueous and IL electrolytes.
- To synthesize highly porous vanadium nitride nanocomposite materials and investigate the performance of these materials as electrodes for supercapacitors in different ionic liquid electrolytes
- To characterize the electrochemical performance of all-solid state supercapacitors based on a binary mixture of polymeric ionic liquid (PIL) and its corresponding ionic liquid
- To investigate the effect of composition of ionic liquid based polymer electrolytes on the final performance of supercapacitors

1.8. References

[1] J.A.N. Zalasiewicz, M. Williams, W. Steffen, P. Crutzen, Environ. Sci. Technol. 44 (2010) 2228.

[2] W. Liao, R. Heijungs, G. Huppes, Renew. Sustain. Energy Rev. 16 (2012) 996.

[3] R.J. White, in:, R.J. White (Ed.), Porous Carbon Mater. from Sustain. Precursors, Royal Society of Chemistry, 2015, pp. 3–49.

[4] J. Ray, A. Pugliese, Gall. Poll (n.d.).

[5] F.C. Matthes, H. Hermann, W. Zimmer, The Vision Scenario for the European Union 2011 Update for the EU-27, Berlin, 2011.

[6] G. Boyel, Renewable Energy: Power for a Sustainable Future, 2nd ed., Oxford University, Oxford, UK, 2012.

[7] C. Parker, in:, J. Garche, C. Dyer, M. Pat, Z. Ogumu, D. Rand, B. Scrosati (Eds.), Encycl. Electrochem. Power Sources, Garche, Ju, 2009.

[8] P.T. Moseley, J. Garche, Electrochemical Energy Storage for Renewable Sources and Grid Balancing, Elsevier, Amsterdam, 2014.

[9] M. Lu, F. Beguin, E. Frackowoak, Supercapacitors Materials, Systems, and

Applications, John Wiley & Sons, Weinheim, Germany, 2013.

[10] J. Miller, in:, J. Garche, C. Dyer, M. Pat, Z. Ogumu, D. Rand, B. Scrosati (Eds.), Encycl. Electrochem. Power Sources, Elsevier B.V, Amsterdam, 2009, pp. 587–598.

[11] H. Helmholtz, Ann. Phys. 243 (1879) 337.

[12] L.L. Zhang, R. Zhou, X.S. Zhao, J. Mater. Chem. 38 (2009) 2520.

[13] M. Gouy, J. Phys. Théorique Appliquée 9 (1910) 457.

[14] D.L. Chapman, Philos. Mag. Ser. 6 25 (1913) 475.

[15] O. Stern, Zeitschrift Fur Elektrochemie 30 (1924) 508.

[16] B.E. Conway, Electrochemical Supercapacitors: Scientific Fundamentals and Technological Applications, Kluwer Acadamic/Plenum, New york, 1999.

[17] C. Zhong, Y. Deng, W. Hu, J. Qiao, L. Zhang, J. Zhang, Chem. Soc. Rev. (2015).

[18] P. Kurzweil, in:, J. Garche, C. Dyer, M. Pat, Z. Ogumu, D. Rand, B. Scrosati (Eds.), Encycl. Electrochem. Power Sources, Amsterdam, 2009, pp. 607–633.

[19] A. Burke, J. Power Sources 91 (2000) 37.

[20] Y. Gogotsi, P. Simon, Sci. Mag. 334 (2011) 917.

[21] J.R. Miller, P. Simon, Sci. Mag. 321 (2008) 651.

[22] P. Simon, Y. Gogotsi, Nat. Mater. 7 (2008) 845.

[23] J. Zhang, X.S. Zhao, ChemSusChem 5 (2012) 818.

[24] Guoping Wang, L. Zhang, J. Zhang, Chem. Soc. Rev. 41 (2012) 797.

[25] J.P. Zheng, J. Huang, R. Jow, J. Electrochem. Soc. 144 (1997) 2026.

[26] V. Augustyn, P. Simon, B. Dunn, Energy Environ. Sci. 7 (2014) 1597.

[27] Y.G. Wang, Z.D. Wang, Y.Y. Xia, Electrochim. Acta 50 (2005) 5641.

[28] D.W. Wang, H.T. Fang, F. Li, Z.G. Chen, Q.S. Zhong, G.Q. Lu, H.M. Cheng, Adv. Funct. Mater. 18 (2008) 3787.

[29] J.W. Long, D. Bélanger, T. Brousse, W. Sugimoto, M.B. Sassin, O. Crosnier, MRS Bull. 36 (2011) 513.

[30] M.Y. Cho, M.H. Kim, H.K. Kim, K.B. Kim, J.R. Yoon, K.C. Roh, Electrochem. Commun. 47 (2014) 5.

[31] P. Perret, Z. Khani, T. Brousse, D. B??langer, D. Guay, Electrochim. Acta 56 (2011) 8122.

[32] W. Shimizu, S. Makino, K. Takahashi, N. Imanishi, W. Sugimoto, J. Power Sources 241 (2013) 572.

[33] E. Frackowiak, F. Béguin, Carbon N. Y. 39 (2001) 937.

[34] M. Inagaki, H. Konno, O. Tanaike, J. Power Sources 195 (2010) 7880.

[35] T. Chen, L. Dai, J. Mater. Chem. A 2 (2014) 10756.

[36] M. Toupin, T. Brousse, D. Blanger, D. Be, Chem. Mater. (2004) 3184.

[37] M.D. Stoller, R.S. Ruoff, Energy Environ. Sci. 3 (2010) 1294.
[38] K. Naoi, S. Ishimoto, J. Miyamoto, W. Naoi, Energy Environ. Sci. 5 (2012) 9363.
[39] G. Yu, X. Xie, L. Pan, Z. Bao, Y. Cui, Nano Energy 2 (2013) 213.
[40] G. Xiong, C. Meng, R.G. Reifenberger, P.P. Irazoqui, T.S. Fisher, Electroanalysis 26 (2014) 30.
[41] A. Davies, A. Yu, Can. J. Chem. Eng. 89 (2011) 1342.
[42] A.S. Shaplov, R. Marcilla, D. Mecerreyes, Electrochim. Acta 175 (2015) 18.
[43] M. Galiński, A. Lewandowski, I. Stępniak, Electrochim. Acta 51 (2006) 5567.
[44] Q. Chen, Y. Hu, C. Hu, H. Cheng, Z. Zhang, H. Shao, L. Qu, Phys. Chem. Chem. Phys. 16 (2014) 19307.
[45] Z. Jin, X. Yan, Y. Yu, G. Zhao, J. Mater. Chem. A 2 (2014) 11706.
[46] D. Hulicova, M. Kodama, H. Hatori, Chem. Mater. 18 (2006) 2318.
[47] H. Oda, A. Yamashita, S. Minoura, M. Okamoto, T. Morimoto, J. Power Sources 158 (2006) 1510.
[48] J.P. Zheng, J. Electrochem. Soc. 142 (1995) 2699.
[49] L. Demarconnay, E. Raymundo-Pinero, F. Beguin, Electrochem. Commun. 12 (2010) 1275.
[50] K. Fic, G. Lota, M. Meller, E. Frackowiak, Energy Environ. Sci. 5 (2012) 5842.
[51] M. Sevilla, A.B. Fuertes, ACS Nano 8 (2014) 5069.
[52] P. Kurzweil, in:, J. Garche, C. Dyer, M. Pat, Z. Ogumu, D. Rand, B. Scrosati (Eds.), Encycl. Electrochem. Power Sources, Amsterdam, 2009.
[53] M. Ue, K. Ida, S. Mori, Jounal Electrochem. Soc. 141 (1994) 2989.
[54] E. Perricone, M. Chamas, L. Cointeaux, J.C. Leprêtre, P. Judeinstein, P. Azais, F. Béguin, F. Alloin, Electrochim. Acta 93 (2013) 1.
[55] S. Ishimoto, Y. Asakawa, M. Shinya, K. Naoi, J. Electrochem. Soc. 156 (2009) A563.
[56] Y.-S. Ye, J. Rick, B.-J. Hwang, J. Mater. Chem. A 1 (2013) 2719.
[57] P. Walden, Bull. Acad. Imp. Sci. 1800 (1914).
[58] F.H. Hurley, Electrodeposition of Aluminium, US Patent 4,446,331, 1948.
[59] M. Armand, F. Endres, D. MacFarlane, Nat. Mater. 8 (2009) 621.
[60] F. Endres, S. Zein El Abedin, Phys. Chem. Chem. Phys. 8 (2006) 2101.
[61] T. Welton, Chem. Rev. 99 (1999) 2071.
[62] J.P. Hallett, T. Welton, Chem. Rev. 111 (2011) 3508.
[63] H. Hohno, in:, J. Garche, C. Dyer, M. Pat, Z. Ogumu, D. Rand, B. Scrosati (Eds.), Encycl. Electrochem. Power Sources, Amsterdam, 2009, pp. 153–159.
[64] M. Yoshizawa, A. Narita, H. Ohno, Aust. J. Chem. 57 (2004) 139.
[65] M.. Mastragostino, F. Soavi, in:, J. Garche, C. Dyer, M. Pat, Z. Ogumu, D. Rand,

B. Scrosati (Eds.), Encycl. Electrochem. Power Sources, Amsterdam, 2009, pp. 649–657.

[66] K. Ueno, H. Tokuda, M. Watanabe, Phys. Chem. Chem. Phys. 12 (2010) 1648.

[67] D.R. MacFarlane, M. Forsyth, E.I. Izgorodina, A.P. Abbott, G. Annat, K. Fraser, Phys. Chem. Chem. Phys. 11 (2009) 4962.

[68] N. Chandrasekhar, A.-N. Unterreiner, Phys. Chem. Chem. Phys. 12 (2010) 1648.

[69] N. V Plechkova, K.R. Seddon, Chem. Soc. Rev. 37 (2008) 123.

[70] D. Mecerreyes, Applications of Ionic Liquids in Polymer Science and Technology, 1st ed., Springer-Verlag Berlin Heidelberg, Berlin Heidelberg, 2015.

[71] G.A. Tiruye, R. Marcilla, in:, D. Mecerreyes (Ed.), Appl. Ion. Liq. Polym. Sci. Technol., Mecerreyes, David, Berlin Heidelberg, 2015, pp. 199–221.

[72] A. Lewandowski, A. Świderska-Mocek, J. Power Sources 194 (2009) 601.

[73] H. Nakagawa, Y. Fujino, S. Kozono, Y. Katayama, T. Nukuda, H. Sakaebe, H. Matsumoto, K. Tatsumi, J. Power Sources 174 (2007) 1021.

[74] H. Sakaebe, H. Matsumoto, Electrochem. Commun. 5 (2003) 594.

[75] H. Shobukawa, H. Tokuda, S.I. Tabata, M. Watanabe, Electrochim. Acta 50 (2004) 305.

[76] H. Sakaebe, H. Matsumoto, K. Tatsumi, Electrochim. Acta 53 (2007) 1048.

[77] H. Sakaebe, H. Matsumoto, Electrochem. Commun. 5 (2003) 594.

[78] T. Placke, O. Fromm, S.F. Lux, P. Bieker, S. Rothermel, H.-W. Meyer, S. Passerini, M. Winter, J. Electrochem. Soc. 159 (2012) A1755.

[79] A. Guerfi, S. Duchesne, Y. Kobayashi, A. Vijh, K. Zaghib, J. Power Sources 175 (2008) 866.

[80] R. Hagiwara, J.S. Lee, Electrochemistry 75 (2007) 23.

[81] A. Noda, M.A. Bin Hasan Susan, K. Kudo, S. Mitsushima, K. Hayamizu, M. Watanabe, J. Phys. Chem. B 107 (2003) 4024.

[82] M. Yoshizawa, H. Ohno, Chem. Commun. (Camb). (2004) 1828.

[83] J. Ding, D. Zhou, G. Spinks, G. Wallace, S. Forsyth, M. Forsyth, D. MacFarlane, Chem. Mater. 15 (2003) 2392.

[84] W. Lu, A.G. Fadeev, B. Qi, E. Smela, B.R. Mattes, J. Ding, G.M. Spinks, J. Mazurkiewicz, D. Zhou, G.G. Wallace, D.R. MacFarlane, S. a Forsyth, M. Forsyth, Science (80-.). 297 (2002) 983.

[85] T. Fukushima, K. Asaka, A. Kosaka, T. Aida, Angew. Chemie - Int. Ed. 44 (2005) 2410.

[86] N. Papageorgiou, J. Electrochem. Soc. 143 (1996) 3099.

[87] R. Hagiwara, J.S. Lee, Electrochemistry 75 (2007) 23.

[88] N. Handa, T. Sugimoto, M. Yamagata, M. Kikuta, M. Kono, M. Ishikawa, J.

Power Sources 185 (2008) 1585.
[89] A. Lewandowski, A. Olejniczak, M. Galinski, I. Stepniak, J. Power Sources 195 (2010) 5814.
[90] A. Khosrozadeh, M. Xing, Q. Wang, Appl. Energy 153 (2015) 87.
[91] Y. Matsuda, K. Inoue, H. Takeuchi, Y. Okuhama, Solid State Ionics 115 (1998) 103.
[92] C. Squeira, D. Santos, Polymer Electrolytes: Fundamentals and Applications, Woodhead Publishing Limited, TJI Digital, Padstow, Cornwall, UK, 2010.
[93] C.A. Vincent, Prog. Solid State Chem. 17 (1987) 145.
[94] N.A. Choudhury, S. Sampath, A.K. Shukla, Energy Environ. Sci. 2 (2009) 55.
[95] H. Fei, C. Yang, H. Bao, G. Wang, J. Power Sources 266 (2014) 488.
[96] M. Kaempgen, C.K. Chan, J. Ma, Y. Cui, G. Gruner, Nano Lett. 9 (2009) 1872.
[97] C. Zhou, J. Liu, Nanotechnology 25 (2014) 035402.
[98] T.M. Dinh, A. Achour, S. Vizireanu, G. Dinescu, L. Nistor, K. Armstrong, D. Guay, D. Pech, Nano Energy 10 (2014) 288.
[99] C. Ramasamy, J. Palma Del Vel, M. Anderson, J. Solid State Electrochem. 18 (2014) 2217.
[100] K.-F. Chiu, S.-H. Su, Thin Solid Films 544 (2013) 144.
[101] C.-W. Huang, C.-A. Wu, S.-S. Hou, P.-L. Kuo, C.-T. Hsieh, H. Teng, Adv. Funct. Mater. 22 (2012) 4677.
[102] J.H. Shin, W.A. Henderson, S. Passerini, Electrochem. Commun. 5 (2003) 1016.
[103] C.W. Liew, S. Ramesh, a. K. Arof, Int. J. Hydrogen Energy 39 (2014) 2953.
[104] S. Ketabi, K. Lian, Electrochim. Acta 103 (2013) 174.
[105] G.P. Pandey, S.A. Hashmi, Electrochim. Acta 105 (2013) 333.
[106] G.P. Pandey, S.A. Hashmi, J. Mater. Chem. A 1 (2013) 3372.
[107] G.P. Pandeya, A.C. Rastogia, C.R. Westgatea, Electrochem. Soc. 45 (2013) 145.
[108] A.S. Shaplov, R. Marcilla, D. Mecerreyes, Electrochim. Acta 175 (2015) 18.
[109] J. Yuan, M. Antonietti, Polymer (Guildf). 52 (2011) 1469.
[110] D. Mecerreyes, Prog. Polym. Sci. 36 (2011) 1629.
[111] J. Yuan, M. Antonietti, in:, D. Mecerreyes (Ed.), Appl. Ion. Liq. Polym. Sci. Technol., Springer, Berlin Heidelberg, 2015, pp. 48–63.
[112] H. Hu, W. Yuan, H. Zhao, G.L. Baker, J. Polym. Sci. Part A Polym. Chem. 52 (2014) 121.
[113] A.-L. Pont, R. Marcilla, I. De Meatza, H. Grande, D. Mecerreyes, J. Power Sources 188 (2009) 558.
[114] G.B. Appetecchi, G.-T. Kim, M. Montanino, M. Carewska, R. Marcilla, D. Mecerreyes, I. De Meatza, J. Power Sources 195 (2010) 3668.

[115] O.A. Mel'nik, A.S. Shaplov, E.I. Lozinskaya, N.A. Popova, M. V Makarov, I.L. Odinets, K.A. Lysenko, G.I. Timofeeva, I.A. Malyshkina, Y.S. Vygodskii, Polym. Sci. Ser. B 52 (2010) 316.

[116] H. Ohno, M. Yoshizawa, W. Ogihara, Electrochim. Acta 50 (2004) 255.

[117] Y.S. Vygodskii, A.S. Shaplov, E.I. Lozinskaya, P.S. Vlasov, I.A. Malyshkina, N.D. Gavrilova, P.S. Kumar, M.R. Buchmeiser, Macromolecules 41 (2008) 1919.

[118] A.S. Shaplov, P.S. Vlasov, E.I. Lozinskaya, D.O. Ponkratov, I.A. Malyshkina, F. Vidal, O. V Okatova, G.M. Pavlov, C. Wandrey, A. Bhide, M. Sch, Y.S. Vygodskii, Macromolecules 44 (2011) 9792.

[119] G.A. Tiruye, D. Muñoz-Torrero, J. Palma, M. Anderson, R. Marcilla, J. Power Sources 279 (2015) 472.

[120] L.G. Alexander S. Shaplov, F.D. Vidal, E.I. Lozinskaya, F. Meyer, D.T. Inna A. Malyshkina, Claude Chevrot, I.L. Odinets, Y.S. Vygodskii, J. Polym. Sci. Part a-Polymer Chem. 47 (2009) 4245.

[121] H. Nakajima, H. Ohno, Polymer (Guildf). 46 (2005) 11499.

[122] Y.S. Vygodskii1, O.A. Mel'nik1, E.I. Lozinskaya, A.S. Shaplov, I.A. Malyshkina, M.Y.A. Nadejda D. Gavrilova Konstantin A. Lyssenko, D.G.G.A.A. Korlyukov, Welz-Biermann, N. Ignat'ev, U. Welz-Biermann, Polym. Adv. Technol. 18 (2007) 50.

[123] R. Marcilla, F. Alcaide, H. Sardon, J.A. Pomposo, C. Pozo-Gonzalo, D. Mecerreyes, Electrochem. Commun. 8 (2006) 482.

[124] G. Wang, L. Wang, S. Zhuo, S. Fang, Y. Lin, Chem. Commun. (Camb). 47 (2011) 2700.

[125] Y. Liu, J. Wang, Y. Yang, T.M. Brenner, S. Seifert, Y. Yan, M.W. Liberatore, A.M. Herring, J. Phys. Chem. C 118 (2014) 15136.

[126] K.J.T. Noonan, K.M. Hugar, H. a Kostalik, E.B. Lobkovsky, H.D. Abruña, G.W. Coates, J. Am. Chem. Soc. 4 (2012) 1.

[127] R. Gao, D. Wang, J.R. Heflin, T.E. Long, J. Mater. Chem. 22 (2012) 13473.

[128] F. Beguin, V. Presser, A. Balducci, E. Frackowiak, Adv. Mater. 26 (2014) 2219.

[129] J. Lee, J. Kim, T. Hyeon, Adv. Mater. 18 (2006) 2073.

[130] K. Yang, J. Peng, C. Srinivasakannan, L. Zhang, H. Xia, X. Duan, Bioresour. Technol. 101 (2010) 6163.

[131] L. and L. Dai, Wen, in:, J. Mauricio, Marulanda (Eds.), Carbon Nanotub., InTech, University Campus STeP Ri,Slavka Krautzeka 83/A,51000 Rijeka, Croatia, 2010, pp. 569–576.

[132] R. Farma, M. Deraman, Awitdrus, I.A. Talib, R. Omar, J.G. Manjunatha, M.M. Ishak, N.H. Basri, B.N.M. Dolah, Int. J. Electrochem. Sci. 8 (2013) 257.

[133] Y.J. Kang, S.-J. Chun, S.-S. Lee, B.-Y. Kim, J.H. Kim, H. Chung, S.-Y. Lee, W. Kim, ACS Nano 6 (2012) 6400.

[134] E. Senokos, V. Reguero, J. Palma, J. Vilatela, R. Marcilla, Nanoscale 8 (2016) 3620.

[135] B. Fang, L. Binder, J. Power Sources 163 (2006) 616.

[136] L. Qie, W.M. Chen, Z.H. Wang, Q.G. Shao, X. Li, L.X. Yuan, X.L. Hu, W.X. Zhang, Y.H. Huang, Adv. Mater. 24 (2012) 2047.

[137] L.F. Chen, X.D. Zhang, H.W. Liang, M. Kong, Q.F. Guan, P. Chen, Z.Y. Wu, S.H. Yu, ACS Nano 6 (2012) 7092.

[138] W. Li, F. Zhang, Y. Dou, Z. Wu, H. Liu, X. Qian, D. Gu, Y. Xia, B. Tu, D. Zhao, Adv. Energy Mater. 1 (2011) 382.

[139] C. Portet, Z. Yang, Y. Korenblit, Y. Gogotsi, R. Mokaya, G. Yushin, J. Electrochem. Soc. 156 (2009) A1.

[140] D. Hulicova-Jurcakova, M. Kodama, S. Shiraishi, H. Hatori, Z.H. Zhu, G.Q. Lu, Adv. Funct. Mater. 19 (2009) 1800.

[141] X. Yang, D. Wu, X. Chen, R. Fu, J. Phys. Chem. C 114 (2010) 8581.

[142] J.-K. Ewert, D. Weingarth, C. Denner, M. Friedrich, M. Zeiger, A. Schreiber, N. Jäckel, V. Presser, R. Kempe, J. Mater. Chem. A 3 (2015) 18906.

[143] P. Tamilarasan, S. Ramaprabhu, J. Nanosci. Nanotechnol. 15 (2015) 1154.

[144] X. Lu, T. Liu, T. Zhai, G. Wang, M. Yu, S. Xie, Y. Ling, C. Liang, Y. Tong, Y. Li, Adv. Energy Mater. 4 (2014) 1.

[145] N. Fechler, T.-P. Fellinger, M. Antonietti, Chem. Mater. 24 (2012) 713.

[146] P. Kurzweil, in:, J. Garche, C. Dyer, M. Pat, Z. Ogumu, D. Rand, B. Scrosati (Eds.), Encycl. Electrochem. Power Sources, Elsevier B.V., Amsterdam, 2009, pp. 634–648.

[147] C. Vix-Guterl, S. Saadallah, K. Jurewicz, E. Frackowiak, M. Reda, J. Parmentier, J. Patarin, F. Beguin, Mater. Sci. Eng. B Solid-State Mater. Adv. Technol. 108 (2004) 148.

[148] C. Vix-Guterl, E. Frackowiak, K. Jurewicz, M. Friebe, J. Parmentier, F. Béguin, Carbon N. Y. 43 (2005) 1293.

[149] A. Burke, Electrochim. Acta 53 (2007) 1083.

[150] A.L.M. Reddy, A. Srivastava, S.R. Gowda, H. Gullapalli, M. Dubey, P.M. Ajayan, ACS Nano 4 (2010) 6337.

[151] Y. Shao, X. Wang, M. Engelhard, C. Wang, S. Dai, J. Liu, Z. Yang, Y. Lin, J. Power Sources 195 (2010) 4375.

[152] Y.S. Hu, P. Adelhelm, B.M. Smarsly, S. Hore, M. Antonietti, J. Maier, Adv. Funct. Mater. 17 (2007) 1873.

[153] A. Ismail, L. David, J. Memb. Sci. 193 (2001) 1.
[154] S. Sircar, T.C. Golden, M.B. Rao, Carbon N. Y. 34 (1996) 1.
[155] F.B. Su, J.H. Zeng, X.Y. Bao, Y.S. Yu, J.Y. Lee, X.S. Zhao, Chem. Mater. 17 (2005) 3960.
[156] M. Uchida, J. Electrochem. Soc. 143 (1996) 2245.
[157] V. Brauch, E.U. Schlünder, Chem. Eng. Sci. 30 (1975) 539.
[158] D. Mohan, C.U. Pittman, J. Hazard. Mater. 142 (2007) 1.
[159] B.C. Steele, A. Heinzel, Nature 414 (2001) 345.
[160] H.-J. Choi, S.-M. Jung, J.-M. Seo, D.W. Chang, L. Dai, J.-B. Baek, Nano Energy 1 (2012) 534.
[161] J. Gamby, P.L. Taberna, P. Simon, J.F. Fauvarque, M. Chesneau, J. Power Sources 101 (2001) 109.
[162] H. Shi, Electrochim. Acta 41 (1996) 1633.
[163] Y.J. Kim, Y. Horie, S. Ozaki, Y. Matsuzawa, H. Suezaki, C. Kim, N. Miyashita, M. Endo, Carbon N. Y. 42 (2004) 1491.
[164] J.A. Fernández, T. Morishita, M. Toyoda, M. Inagaki, F. Stoeckli, T.A. Centeno, J. Power Sources 175 (2008) 675.
[165] M. Arulepp, J. Leis, M. Lätt, F. Miller, K. Rumma, E. Lust, A.F. Burke, J. Power Sources 162 (2006) 1460.
[166] M. Arulepp, L. Permann, J. Leis, a. Perkson, K. Rumma, a. Jänes, E. Lust, J. Power Sources 133 (2004) 320.
[167] A. Jänes, L. Permann, M. Arulepp, E. Lust, Electrochem. Commun. 6 (2004) 313.
[168] Y.G. J. Chmiola, G. Yushin, C. Portet, P.L.T. P. Simon, Sci. Mag. 313 (2006) 1760.
[169] T. Wang, S. Tan, C. Liang, Carbon N. Y. 47 (2009) 1880.
[170] A. Aygün, S. Yenisoy-Karakaş, I. Duman, Microporous Mesoporous Mater. 66 (2003) 189.
[171] P. Adelhelm, Y.-S. Hu, L. Chuenchom, M. Antonietti, B.M. Smarsly, J. Maier, Adv. Mater. 19 (2007) 4012.
[172] Z. Liu, L. Ling, W. Qiao, L. Liu, Carbon N. Y. 37 (19999) 663.
[173] R. Wang, P. Wang, X. Yan, J. Lang, C. Peng, Q. Xue, ACS Appl. Mater. Interfaces 4 (2012) 5800.
[174] Y. Gao, L. Li, Y. Jin, Y. Wang, C. Yuan, Y. Wei, G. Chen, J. Ge, H. Lu, Appl. Energy 153 (2015) 41.
[175] Y. Guo, S. Yang, K. Yu, J. Zhao, Z. Wang, H. Xu, 74 (2002) 320.
[176] E. Ramasamy, J. Chun, J. Lee, Carbon N. Y. 48 (2010) 4563.

[177] F. Goettmann, A. Fischer, M. Antonietti, A. Thomas, Angew. Chemie - Int. Ed. 45 (2006) 4467.
[178] Z. Yang, Y. Xia, X. Sun, R. Mokaya, J. Phys. Chem. B 110 (2006) 18424.
[179] B. Sakintuna, Y. Yürüm, Ind. Eng. Chem. Res. 44 (2005) 2893.
[180] B.Z. Hu, M.P. Srinivasan, Adv. Mater. (2000) 1998.
[181] Y. Zou, B.X. Han, Energy and Fuels 15 (2001) 1383.
[182] A. Ahmadpour, D.D. Do, Carbon N. Y. 34 (1996) 471.
[183] F. Schüth, Angew. Chemie - Int. Ed. 42 (2003) 3604.
[184] N. Fechler, T.-P. Fellinger, M. Antonietti, Adv. Mater. 25 (2013) 75.
[185] N. Bhandari, R. Dua, L. Estevez, R. Sahore, E.P. Giannelis, Carbon N. Y. 87 (2015) 29.
[186] X. Liu, M. Antonietti, Carbon N. Y. 69 (2014) 460.
[187] W.L. Queen, S.J. Hwu, S. Reighard, Inorg. Chem. 49 (2010) 1316.
[188] B. Fe, S.O. Cl, X. Mo, E. Ferguson, S. Hwu, C.U. V, S. Carolina, Inorg. Chem. 44 (2005) 3121.
[189] Q. Huang, M. Ulutagay, P.A. Michener, S.J. Hwu, J. Am. Chem. Soc. 121 (1999) 10323.
[190] K.R. Prasad, K. Koga, N. Miura, Chem. Mater. 16 (2004) 1845.
[191] D. Choi, G.E. Blomgren, P.N. Kumta, Adv. Mater. 18 (2006) 1178.
[192] A. Marchand, J.V. Zanchetta, Carbon N. Y. 3 (1966) 483.
[193] H.M. Jeong, J.W. Lee, W.H. Shin, Y.J. Choi, H.J. Shin, J.K. Kang, J.W. Choi, Nano Lett. 11 (2011) 2472.
[194] Z. Yang, Z. Yao, G. Li, G. Fang, H. Nie, Z. Liu, X. Zhou, X. Chen, S. Huang, ACS Nano 6 (2012) 205.
[195] Y. Zhang, T. Mori, J. Ye, A. Markus, J. Am. Chem. Soc. 132 (2010) 6294.
[196] G.M. Swain, R. Ramesham, Anal. Chem. 65 (1993) 345.
[197] M. Kodama, J. Yamashita, Y. Soneda, H. Hatori, S. Nishimura, K. Kamegawa, Mater. Sci. Eng. B 108 (2004) 156.
[198] C. Vagner, G. Finqueneisel, T. Zimny, P. Burg, B. Grzyb, J. Machnikowski, J. V Weber, Carbon N. Y. 41 (2003) 2847.
[199] P.-X. Hou, H. Orikasa, T. Yamazaki, K. Matsuoka, A. Tomita, N. Setoyama, Y. Fukushima, T. Kyotani, Chem. Mater. 17 (2005) 5187.
[200] C.O. Ania, V. Khomenko, E. Raymundo-Piñero, J.B. Parra, F. Béguin, Adv. Funct. Mater. 17 (2007) 1828.
[201] B. Xu, D. Zheng, M. Jia, G. Cao, Y. Yang, Electrochim. Acta 98 (2013) 176.
[202] L. Zhao, N. Baccile, S. Gross, Y. Zhang, W. Wei, Y. Sun, M. Antonietti, M.M. Titirici, Carbon N. Y. 48 (2010) 3778.

[203] M. Seredych, D. Hulicova-Jurcakova, G.Q. Lu, T.J. Bandosz, Carbon N. Y. 46 (2008) 1475.

[204] D. Hulicova-Jurcakova, M. Seredych, G.Q. Lu, T.J. Bandosz, Adv. Funct. Mater. 19 (2009) 438.

[205] B.E. Wilson, S. He, K. Buffington, S. Rudisill, W.H. Smyrl, A. Stein, J. Power Sources 298 (2015) 193.

[206] N. Fechler, Salts as Highly Diverse Porogens: Functional Ionic Liquid-Derived Carbons and Carbon-Based Composites for Energy-Related Applications Dissertation, University of Potsdam, 2012.

[207] C.L. Mangun, K.R. Benak, J. Economy, K.L. Foster, Carbon N. Y. 39 (2001) 1809.

[208] N.D. Kim, W. Kim, J.B. Joo, S. Oh, P. Kim, Y. Kim, J. Yi, J. Power Sources 180 (2008) 671.

[209] B. Stöhr, H.P. Boehm, R. Schlögl, Carbon N. Y. 29 (1991) 707.

[210] R.J.J. Jansen, H. van Bekkum, Carbon N. Y. 32 (1994) 1507.

[211] L. Singoredjo, F. Kapteijn, J.A. Moulijn, J.-M. Martín-Martínez, H.-P. Boehm, Carbon N. Y. 31 (1993) 213.

[212] J. Machnikowski, B. Grzyb, J. V. Weber, E. Frackowiak, J.N. Rouzaud, F. Béguin, Electrochim. Acta 49 (2004) 423.

[213] J. Lahaye, G. Nansé, A. Bagreev, V. Strelko, Carbon N. Y. 37 (1999) 585.

[214] K.T. Cho, S.B. Lee, J.W. Lee, J. Phys. Chem. C 118 (2014) 9357.

[215] A. Oya, N. Kasahara, Carbon N. Y. 38 (2000) 1141.

[216] A. Oya, S. Yoshida, J. Alcaniz-Monge, A. Linares-Solano, Carbon N. Y. 33 (1995) 1085.

[217] M.C. Huang, H. Teng, Carbon N. Y. 41 (2003) 951.

[218] J.R. Pels, F. Kapteijn, J.A. Moulijn, Q. Zhu, K.M. Thomas, Carbon N. Y. 33 (1995) 1641.

[219] B. Xu, S. Hou, F. Zhang, G. Cao, M. Chu, Y. Yang, J. Electroanal. Chem. 712 (2014) 146.

[220] W.J. Weydanz, B.M. Way, T. van Buuren, J.R. Dahn, J. Electrochem. Soc. 141 (1994) 900.

[221] X.G. Sun, X. Wang, R.T. Mayes, S. Dai, ChemSusChem 5 (2012) 2079.

[222] W. Yang, T. Fellinger, M. Antonietti, J. Am. Chem. Soc. 133 (2011) 206.

[223] L. Lai, J.R. Potts, D. Zhan, L. Wang, C.K. Poh, C. Tang, H. Gong, Z. Shen, J. Lin, R.S. Ruoff, Energy Environ. Sci. 5 (2012) 7936.

[224] F. Kapteijn, J.A. Moulijn, S. Matzner, H.P. Boehm, Carbon N. Y. 37 (1999) 1143.

[225] G. Lota, B. Grzyb, H. Machnikowska, J. Machnikowski, E. Frackowiak, Chem.

Phys. Lett. 404 (2005) 53.

[226] D. Hulicova, J. Yamashita, Y. Soneda, H. Hatori, M. Kodama, Chem. Mater. 17 (2005) 1241.

[227] E. Frackowiak, G. Lota, J. Machnikowski, C. Vix-Guterl, F. Béguin, Electrochim. Acta 51 (2006) 2209.

[228] W.-Y. Tsai, R. Lin, S. Murali, L. Li Zhang, J.K. McDonough, R.S. Ruoff, P.-L. Taberna, Y. Gogotsi, P. Simon, Nano Energy 2 (2013) 403.

[229] A. Burke, in:, J. Garche, C. Dyer, M. Pat, Z. Ogumu, D. Rand, B. Scrosati (Eds.), Encycl. Electrochem. Power Sources, Elsevier B.V, Amsterdam, 2009.

[230] J.R. Miller, A. Burke, Electrochem. Soc. 17 (2008) 53.

[231] A. Burke, H. Zhao, L. Zhengmao, Reseach Report: Review of the Present and Future Applications of Supercapacitors in Electric and Hybrid Vehicles, California, 2014.

CHAPTER II: MICROPOROUS NITROGEN-DOPED CARBON DERIVED FROM PHENOLIC AND UREA PRECURSORS AS ELECTRODE MATERIAL FOR SUPERCAPACITORS

CHAPTER II: MICROPOROUS NITROGEN-DOPED CARBON DERIVED FROM PHENOLIC AND UREA PRECURSORS AS ELECTRODE MATERIAL FOR SUPERCAPACITORS

2.1. Introduction

Nitrogen-doped carbons (N-dC) are considered as promising candidates for efficient energy storage electrode materials in supercapacitors [1–4] and batteries [5,6]. Electrochemical properties of most N-dC materials have been investigated in aqueous based electrolytes, mainly in H_2SO_4 [7,8] and KOH [8–10] and only a small number of studies have been conducted in organic electrolytes [1,7] or ionic liquids [3,4,11]. In most cases, nitrogen doped carbon present high values of capacitance due to the pseudocapacitance contribution from faradic reactions between ions of electrolyte and different nitrogen groups from the carbon network, which can be found in the form of pyrrolic, pyridinic, amine, nitro or quaternary graphitic [12–16]. A recent application of this type of N-dC is their use as efficient electrocatalyst for oxygen reduction reaction (ORR) in fuel cells and metal-air batteries [17–20].

The incorporation of nitrogen into a carbon porous network is usually achieved by co-carbonization of carbon and N-containing precursors followed by an additional step of chemical-physical activation [8,21,22]. In some cases, the high price of precursors and the need of post-treatment activation steps result in expensive materials. Therefore, the search for low cost and sustainable carbon materials as electrode for supercapacitors is a vital issue for the development of the technology. Perhaps, with an eye to the future, selection of precursors, design and development of sustainable carbon-based porous materials are of high relevance. Consequently, biomass derivative carbohydrates [22] and phenolic compounds such as phenol-formaldehyde resin have been recently used as nitrogen/carbon precursors due to their easily availability and low cost [19,23,24].

Moreover, as discussed in Chapter 1, despite the idea of “salt templating” has been proved for the synthesis of transition metal frameworks with highly micropores structures since 1999 [25], recently it has been proposed as a facile one-step method for the preparation of highly porous nitrogen and metal nitride functionalities

carbonaceous materials [26]. More recently, Fechler *et.al* [27] has reported heteroatom doped porous carbons (boron or nitrogen doped carbon) with controlled pore volume, architecture, and high specific area up to 2000 m^2g^{-1} by using one step salt-templating method. Binary eutectic mixtures of salts (LiCl, NaCl and KCl mixed with $ZnCl_2$ separately) have been used as salt porogens and the ionic liquids, 1-butyl-1-methylpyrrolidinium dicyanamide ($PYR_{14}DCA$) and 1-Ethyl-3-Methylimidazolium Tetracyanoborate (EmimTCB) were used as nitrogen/carbon and boron/carbon precursors, respectively. The authors concluded that the porosity/morphology of carbon was shown to be dependent only on the nature and type of eutectic salt mixtures. Furthermore, they suggested that the synthesized doped carbons are competent materials in catalysis and energy storage applications.

In this chapter, this salt templating method is employed to synthesize novel N-dC materials from cheap and sustainable resources. In particular, tannic acid that is a phenolic carbon precursor and urea as nitrogen precursor were used as sustainable starting materials. Tannic acid is the specific commercial name for Tannin that is a bio-mass precursor that can be extracted from Oak Bark with low cost. The main objective of this work is to synthesize highly porous N-dC from cheap and sustainable precursors by combining one-pot salt template method. Furthermore, the different parameters affecting the properties of the obtained carbons were varied systematically to evaluate the influence of concentration of nitrogen precursor, carbon precursor (urea and tannic acid, respectively) and template salts on physicochemical properties. The electrochemical performance of as-synthesized nitrogen doped carbons were characterized both in aqueous and ionic liquid electrolyte (1-butyl-1-methylpyrrolidinium bis(fluorosulfonyl)imide, ($PYR_{14}FSI$)).

2.2. Experimental Methods

2.2.1. Materials

Lithium chloride (LiCl), sodium chloride (NaCl), potassium chloride (KCl), zinc chloride ($ZnCl_2$) and H_2SO_4 each of them with 99 % purity were purchased from Sigma Aldrich and used to prepare eutectic mixtures. Tannic acid (TA) and Urea from Aldrich were also used as carbon and nitrogen precursors, respectively. Nafion perfluorinated resin solution (5 % H_2O), and absolute ethanol both from sigma Aldrich were used as binder and solvent for the preparation of carbon suspension. Polytetrafluoroethylene (PTFE 60 wt % dispersion in water, Sigma Aldrich) with 2-propanol as a solvent was used in order to get a homogeneous carbon paste to prepare carbon thin film for electrical conductivity measurement. Furthermore, 5 % of polyvinyldifluoride (PVDF) dissolved in acetone was used to prepare carbon paste for electrochemical

characterizations. Furthermore, 1-butyl-1-methylpyrrolidinium bis(fluorosulfonyl) imide, ($PYR_{14}FSI$, > 99.5%), was acquired from Solvionic and stored inside glove box.

2.2.2. Synthesis of porous N-doped Carbons (N-dC)

Salt templating method was carried out to synthesize several N-dC materials by using urea and tannic acid (TA) as nitrogen & carbon precursor, respectively in combination with 3 different eutectic salts that were used as porogens or templates. The required eutectic salts were prepared by mixing zinc chloride salt ($ZnCl_2$) with three different alkaline metal chloride salts (NaCl, LiCl, and KCl). The following three eutectic blends were prepared: $NaCl/ZnCl_2$ (29 % mol NaCl), $LiCl/ZnCl_2$ (18.7 % mol LiCl), and $KCl/ZnCl_2$ (33.7 % mol KCl).

The carbon/nitrogen precursor samples were prepared by mixing urea (nitrogen precursor) and tannin acid (TA, carbon precursor) using the following molar ratios; 0:1, 5:1, 9:1, 13:1, and 17:1 (urea:TA). In a next step, each precursor's mixture was blended with $NaCl/ZnCl_2$ eutectic salt using a mass ratio of 1:3 (urea+TA: eutectic salt) and placed in a ceramic crucible separately. As shown in Table 2.1, the as-prepared carbons were named as GT_X_NaZ where X is 0, 5, 9, 13 or 17 depending on the corresponding urea:TA molar ratio and NaZ refers to the $NaCl/ZnCl_2$ eutectic salt.

In order to evaluate the influence of concentration of eutectic salt on the physical properties of porous carbon, the ratio of urea and TA was fixed to 9:1 (urea:TA) and blended with different mass of $NaCl/ZnCl_2$. The weight ratios of precursor to $NaCl/ZnCl_2$ were 1:1, 1:3, 1:5 and 1:7. The prepared carbons were named as GT_NaZ_S, where S is 1, 3, 5 or 7 depending on the ratio of precursors (urea+TA) to $NaCl/ZnCl_2$ (see Table 2.1). Finally, in order to evaluate the influence of different nature eutectic salt, a precursor blend with a fix ratio of 9:1 (urea:TA) was blended with the other two eutectic salts; $LiCl/ZnCl_2$ and $KCl/ZnCl_2$ using a mass ratio of precursor to the eutectic salt of 1:3. For simplicity, the prepared samples were named as GT_9_LiZ, and GT_9_KZ, where 9 refer to urea:TA molar ratio and LiZ and KZ refer to $LiCl/ZnCl_2$ and $KCl/ZnCl_2$, respectively. Table 2.1 shows the different N-doped carbon with their respective nomenclature depending on the synthesis conditions: molar ratio of urea to tannic acid, mass ratio of the precursor to eutectic salt and type of eutectic salt.

All these mixtures of precursors and eutectic salts were grinded and mixed with mortar and placed in a ceramic crucible. Calcination step was performed at 800 ^{o}C under N_2 atmosphere for 1 hour. After cooling down to room temperature, the carbonized samples were washed with dilute acid (0.220 M HCl) and distilled water several times to remove the melted salts, while maintaining continuously connected micro and mesopores, which were occupied by salt clusters. Finally, the carbons were

filtered and dried in vacuum oven at 50 °C overnight. The different ratios of precursors to template salt used in this experiment and the preparation process flow chart are listed in Table 2.1, and Scheme 2.1, respectively.

Table 2.1. Different compositions and nomenclature of N-doped carbons

Molar ratio of Urea to TA	Mass ratio of precursors (urea+TA) to eutectic salt	Type of eutectic salt		
		$NaCl:ZnCl_2$	$LiCl:ZnCl_2$	$KCl:ZnCl_2$
0:1	1:3	GT_0_NaZ	-	-
5:1		GT_5_ NaZ		
9:1		GT_9_ NaZ	GT_9_ LiZ	GT_9_ KZ
13:1		GT_13_ NaZ		
17:1		GT_17_ NaZ		
9:1	1:1	GT_NaZ_1	-	-
	1:3	GT_NaZ_3	-	-
	1:5	GT_NaZ_5	-	-
	1:7	GT_NaZ_7	-	-

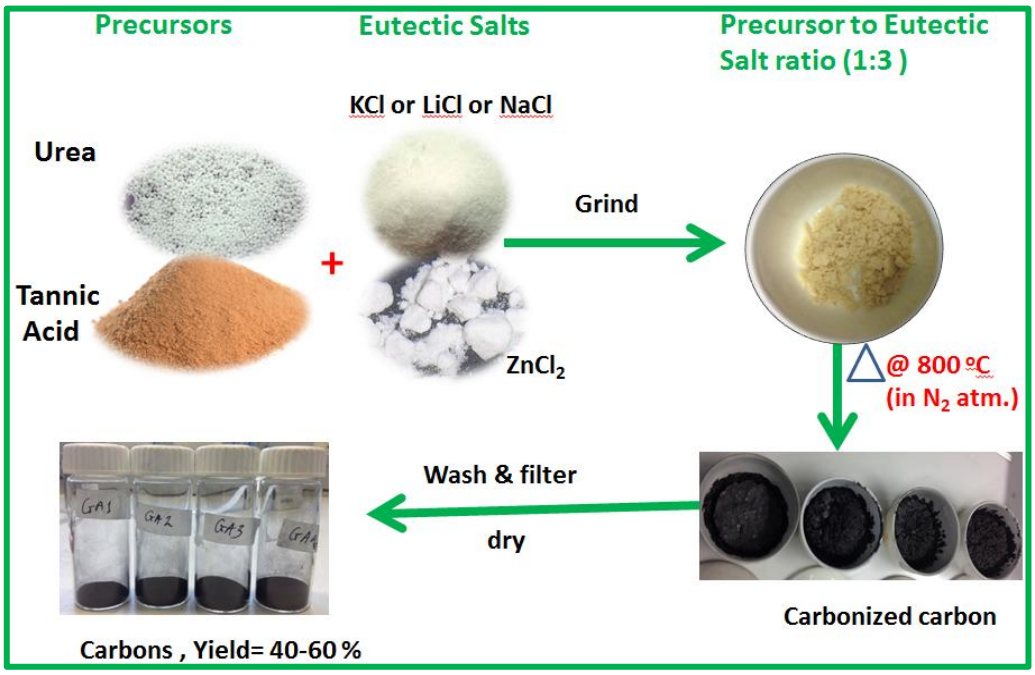

Scheme 2.1. Flow chart for preparation of precursor mixture, eutectic salts and precursor/salt mixtures and the subsequent thermal carbonization process.

2.2.3. Physical Characterization of porous N-doped Carbons (N-dC)

Argon (Ar) sorption of carbons was measured with Ar at 87 K after degassing the samples at 180 °C in vacuum for 20 hrs using a Quantachrome Instrument (Autosorb-1, version 3.01). The specific surface areas of different carbons were calculated by using DFT analysis method. For comparison, the BET surface was also calculated by BET model by using isotherm data points of adsorption in the relative pressure 0.05< p/p0 < 0.3. The pore size distributions, micro pore volume, and pore width of porous carbon were also calculated from Ar sorption data using the quenched solid density functional theory (QSDFT) equilibrium model method for slit pores. SEM images of the carbon were obtained with LEO 1550-Gemmini instrument after sputtering with platinum. XRD patterns of the porous carbon were measured by using a Brucker D8 advancing instrument with Cu-K (α) radiation (wave length =0.1542 nm). Elemental analysis of the resulting carbons was determined using a Vario Micro device in order to determine the bulk elemental composition with regard to nitrogen, carbon, hydrogen, and sulfur. The surface chemical compositions of nitrogen doped carbons were determined by X-ray photoelectron spectroscopy (XPS) using Thermo Scientific™ K-α™+ instrument , UK with monochromatic Al K-α radiation source up to 1486.86 eV and voltage of 12 KV. The sample charged was corrected using the C1s peak at 265 eV as an internal standard. The quantitative analysis of the desired element was performed with CASAXPS software after Shirley background subtraction. Peak deconvolutions and fits were obtained using Gaussian-Lorentzian line shapes at full width at half maximum (FWHM) for all fitted peaks.

2.2.4. Electrode Preparation and Electrochemical Characterizations

2.2.4.1. Electrode Preparation

In the case of aqueous electrolyte, carbon electrodes were prepared by coating a homogeneous suspension of N-dC on glassy carbon electrodes. This “modified” glassy carbon was used as working electrode in 3-electrode cell. The suspension of carbon was prepared by mixing 95 % carbon and 5 % of Nafion (binder) in ethanol (5 mg carbon + 95 µL Nafion + 350 µL ethanol). For 2 electrode set-up, electrodes were also prepared by coating a carbon slurry on coined shape Platinum current collectors (0.785 cm^2).

For N-dC materials characterized in ionic liquid electrolyte ($PYR_{14}FSI$), electrodes were prepared by coating a coin-shape stainless steel mesh current collectors (d = 1 cm) with an electrode ink prepared by mixing N-dC with Polytetrafluoroethylene (PTFE) as binder (90:10 wt.) in 2-propanol [28]. N-dC electrodes were then pressed with a uniaxial press (CARVER model 3853-0) applying a pressure of 15 tons (about 2123 kg

cm^{-2}) for 7 minutes. Finally, the coin-shaped carbon electrodes (d=1 cm) were dried at 100 °C, under vacuum overnight. The mass-loading of carbon material in the electrode was about 6 - 8 mg cm^{-2}. For electrical conductivity, the carbon paste was also rolled onto a very thin plastic film (thickness = 0.065 to 0.11 mm) in order to avoid short circuit during 4-probe conductivity measurement.

2.2.4.2. Electrochemical Characterization

Electrical Conductivity: The electrical conductivity of N-dC was determined by four-point collinear probes (SRM probe, HS code: 90241000 from Bridge Technology) using potentioamperometric techniques by applying current of 0.1, 0.2, 0.3, 0.4, and 0.5 mA. The conductivity of each carbon film was calculated by the following equation:

$$\sigma\ (Scm^{-1}) = \frac{1}{\rho}\ , \quad \rho = \frac{\pi * t * V}{I * ln2} = \frac{4.53tV}{I} \qquad 2.1$$

Where, σ is electrical conductivity, ρ is electrical resistivity, t is thickness of carbon film, V is voltage and I is current.

Cyclic Voltammetry (CV) in 3-electrode cells: CV was performed both in aqueous (H_2SO_4) and IL electrolyte ($PYR_{14}FSI$,) to determine the specific capacitance of the synthesized N-doped carbon materials. The specific capacitance (C_{am}) of the N-dC was calculated from integration of the CV curve.

Set-up in Aqueous Electrolyte: The coated glassy carbon electrode was used as working electrode while platinum wire and Ag/AgCl were used as counter and reference electrodes, respectively in 3-electrode glass electrochemical cell. CV experiments were performed over a potential range of -0.2 V to 0.8 V with 1 M H_2SO_4 electrolyte with scan rates of 100, 50, 30, 20, 10, 5 and 2 mV s-1.

Set-up in Ionic Liquid Electrolyte: Experiments were performed in a 3-electrode Swagelok cell setup. N-dC electrode, silver wire, and PICA carbon electrode with much higher mass than the working electrode were used as working electrode (WE), pseudo reference electrode (RE) and counter electrode (CE), respectively[29,30]. A 130 µm thick cellulose filter paper soaked with IL ($PYR_{14}FSI$) was used as a separator. Before assembling the cell, each electrode was impregnated with the electrolyte under vacuum at least for 1 hr. Impregnation of electrodes with electrolyte and assembling of the cell were performed inside the glove box. CV experiments were performed over a potential range of -1.75 V to 1.75 V for $PYR_{14}FSI$ at scan rates of 100, 50, 20, 10, 5 and 2 mVs^{-1}.

Galvanostatic Charge-Discharge (CD) in two electrode Swagelok cell: Symmetric supercapacitors were assembled with two equal amounts of N-dC electrodes with a projected surface area of 0.785 cm^2 using 2-electrode Swagelok® cells. Cellulose filter paper (130 µm thickness) was soaked with the electrolyte (either 1 M H_2SO_4, or

$PYR_{14}FSI$) and sandwiched between two carbon electrodes. CD experiments were conducted from 0 to 1 V in 1 M H_2SO_4 and 0 to 3.5 V in $PYR_{14}FSI$ electrolyte at different current densities such as 30, 20, 10, 5, and 2 mA cm^{-2}. From the charge-discharge experimental data, specific capacitance of the cell ($C_{sp,\,cell}$), equivalent series resistance (ESR), specific real power density (P_{real}) and real specific energy (E_{real}) of the full supercapacitor were calculated as shown below.

$$C_{sp,cell}\ (Fg^{-1}) = \frac{I}{m_{tam}\cdot(dV/dt)} \qquad 2.2$$

$$ESR(\Omega cm^2) = \frac{\Delta V\cdot A}{2\cdot I} \qquad 2.3$$

$$E_{\text{real}}(Whkg^{-1}) = \frac{I}{m_{tam}}\int_{t_i}^{t_f} V dt \qquad 2.4$$

$$P_{real}(Wkg^{-1}) = \frac{E_{real}}{t_f - t_i} \qquad 2.5$$

Here, I is the discharge current, m_{tam} is the total active mass in the supercapacitor, dV/dt is the slope of the discharge curve, ΔV is the ohmic drop when current is reversed and A is the geometric area of the electrodes. t_i and t_f are the integration limits corresponding to the time in which the discharge starts and finishes. Here, it is worth mentioning that we prefer to use "real energy" (E_{real}) values although they are lower than the maximum energy ($E_{max} = 1/2CV^2$), since it better represents the energy delivered by a real supercapacitors. In a symmetrical system, the specific capacitance referred to a single electrode (C_{am}) is related to the capacitance of the SC ($C_{sp,\,cell}$) by the following expression:

$$C_{am}\ (F\ g^{-1}) = 4C_{sp,\,cell}. \qquad 2.6$$

Electrochemical Impedance Spectroscopy (EIS) in two electrode Swagelok cell: EIS experiments were also performed over a frequency range going from 200 kHz to 10 mHz using a bias voltage of 0 V and 10 mV of amplitude. All electrochemical measurements were carried out by using a multichannel Bio-Logic Lab (model: VMP3).

2.3. Results and Discussion

2.3.1. Synthesis and Physical Characterization of porous N-doped Carbons

For the synthesis of porous N-dC, Tannic acid (TA) and urea were used as carbon and nitrogen precursors, respectively. After mixing and grinding the precursors with eutectic salts, the mixture results in a yellowish color. Carbonization of the mixtures at 800 °C for 1 hr in nitrogen atmosphere yields 40-60% yield of porous carbon. One of the main advantages of a salt template process is creating a continuous structure of conducting walls and well-ordered open pores, permitting for efficient electrolyte permeation and hence enhancing capacitance. Porosity in carbon can be tuned by splitting apart of carbon structures into layers with the presence of molten eutectic salts and results in porous N-dC. Moreover, aqueous removal of the molten eutectic salts in carbonized carbon results in a highly porous carbon materials and salts could be also recovered [27] hence closing the loop of the synthesis process.

2.3.1.1. Effect of Molar Ratio of Precursors (Urea:TA)

Several N-doped carbons were synthesized using $NaCl/ZnCl_2$ as eutectic salt at a fixed mass ratio of precursor (urea+TA) to eutectic salt of 1:3 and varying the molar ratio of urea to TA from 0 to 17 as shown inTable **2.1**. Figure 2.1 depicts Ar sorption isotherm and pore size distributions of different porous N-dCs.

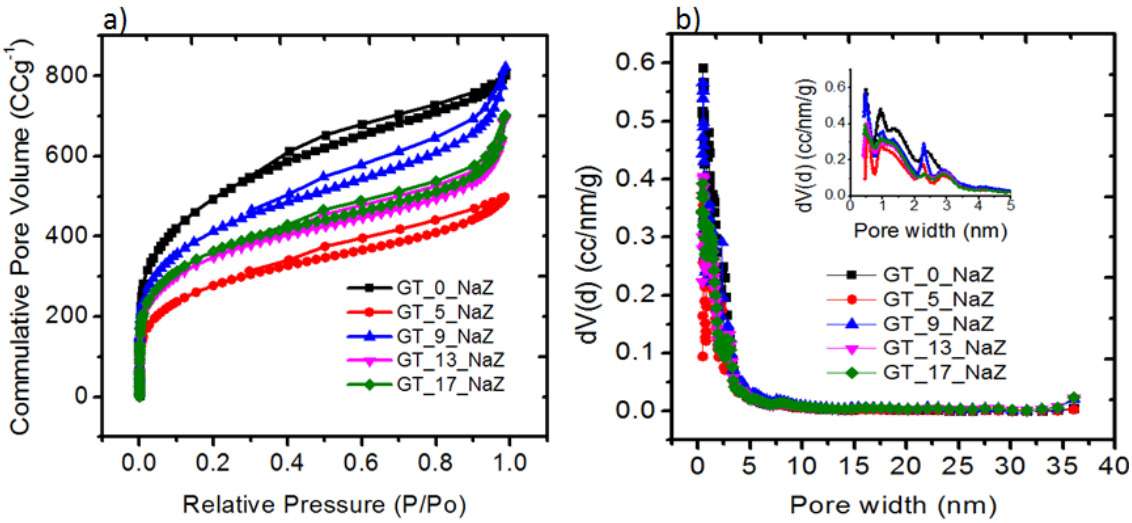

Figure 2.1. Argon (87 K) adsorption/desorption isotherms of carbon with a) ratio of urea to TA (0, 5, 9, 13, & 17) with the 1;3 ratio of precursors to $NaCl/ZnCl_2$ b) the corresponding Pore size distribution of carbons calculated by QSDFT (slit pore, QSDFT equilibrium mode)

In all cases, the isothermal graphs show a rounded knee at P/Po from 0 to 0.2, indicating the approximate location of micro monolayer formation. Moreover, within

this region at P/P_o=0-0.2 the gas adsorption is steeper, suggesting that the filing of super micropores which can be formed by the introduction of Ar within carbon structure [31]. On the other hand, low slope region in the middle of isotherm attributed to the formation of first few multi-layers during isothermal process. All carbons exhibited isothermal Type IV with a distinct hysteresis loop of type H_4 at P/P_o from 0.4 to 0.99, suggesting the presence of small mesoporous. The formation of hysteresis indicates capillary condensation in the mesoporous. The different shape of the isotherm in Figure 2.1a shows that the molar concentration of urea to tannic acid influences the textural properties of the carbons as discussed below. Figure 2.1b shows the pore size distributions of different porous carbon calculated by QSDFT (silt pore, equilibrium mode). All carbons exhibit a broad pore size distribution in the range of micropores (< 2 nm) and small mesoropores (between 2-4 nm).

Most representative textural parameters were analyzed and are included in Table 2.2.

Table 2.2. Structural parameters S_{BET} (total surface area, S_{DFT}, total pore volume V_{total}, and pore width, all are calculated by QSDFT)

Carbon	S_{BET} (m^2g^{-1})	S_{DFT} (m^2g^{-1})	[1]$S_{eff>0.533\ nm}$ (m^2g^{-1})	$S_{<2\ nm}$ (m^2g^{-1})	[2]$S_{eff.>1.1nm}$ (m^2g^{-1})	$S_{<2\ nm}/S_{DFT}$ (%)
GT_0_NaZ	1570	1557	1117	1333	600	86
GT_5_NaZ	893	806	686	652	376	81
GT_9_NaZ	1329	1326	949	1105	517	83
GT_13_NaZ	1120	1088	815	922	425	85
GT_17_NaZ	1168	1138	843	977	434	86

Carbon	V_{tot} (m^3g^{-1})	[3]$V_{eff>0.533\ nm}$ (m^3g^{-1})	$V_{<2\ nm}$ (m^3g^{-1})	[4]$V_{eff>1.1\ nm}$ (m^3g^{-1})	$V_{<2\ nm}/V_{tot}$ (%)	Pore width (nm)
GT_0_NaZ	0.98	0.88	0.59	0.67	60	0.45
GT_5_NaZ	0.61	0.58	0.32	0.45	52	0.54
GT_9_NaZ	0.97	0.89	0.48	0.72	49	0.45
GT_13_NaZ	0.81	0.75	0.41	0.59	51	0.48
GT_17_NaZ	0.83	0.76	0.43	0.59	52	0.45

[1] the $S_{eff>0.533\ nm}$ is the effective total area that can be accessed by the bivalent sulfate ($SO_4^{2-}(H_2O)_2$), ion size =0.533 nm, [2] the $S_{eff>1.1nm}$ is the area that can be accessed by the larger cation of $PYR_{14}FSI$ electrolyte (PYR_{14} cation= 1.1 nm, and FSI anion=0.32 nm), [3] the $V_{eff>0.533\ nm}$ is the total pore volume with the pore size greater than 0.533 nm, and [4]$V_{eff>1.1\ nm}$ represents the total pore volume greater than 1.1 nm pore width.

The specific surface areas of the porous carbons were characterized by Brunauer-Emmett-Teller (BET) and QSDFT analysis methods. S_{BET} and S_{DFT} as shown in Table 2.2 showing similar values. The S_{BET} of the porous carbons is in the range between 890 and 1570 m^2g^{-1} whereas the QSDFT analysis showed that the surface area ranges from 800 to 1560 m^2g^{-1}. QSDFT analysis showed that the degree of micro-porosity ($S_{<2\ nm}/S_{DFT}$) of the carbons is more than 80 % for all porous carbons as shown in Table 2.2, indicating that the synthesized carbons are mainly microporous (<2 nm pore width) with a combination of small mesopores (2 nm-50 nm).

The GT_0_NaZ porous carbon which is containing no urea in the mixture is particularly interesting. It has the higher uptake of Argon in the sorption isotherm (see Figure 2.1a), consequently it exhibits the highest specific surface area and the highest total pore volume (see Table 2.2) compared with the others. It suggests that the addition of urea into the mixture causes collapsing the wall of carbons and the primary pores within carbon walls are blocked by the doped nitrogen functional groups [14] resulting in N-dC with lower specific surface area and pore volume.

The textural properties of those N-dC materials synthesized with urea do not follow a clear trend. It was observed that the lowest 5:1 ratio of urea to tannic acid (GT_5_NaZ carbon) exhibits the lowest specific surface area (S_{DFT}) and lowest total pore volume (V_{tot}), ~850 m^2g^{-1} and 0.611 m^3g^{-1}, respectively. GT_9_NaZ carbon with an intermediate molar ratio of urea:TA (9:1), exhibited the maximum S_{DFT} around 1326 m^2g^{-1} and the maximum V_{tot} about 0.97 m^3g^{-1}. GT_13_NaZ and GT_17_NaZ present very similar isotherm and textural properties (specific surface area of about 1100 m^2g^{-1} and a total pore volume of about 0.8 m^3g^{-1}). Besides the typical parameters such as S_{BET}, S_{DFT} or V_{tot}, other parameters such as $S_{eff>0.533\ nm}$, $S_{eff.>1.1\ nm}$, $V_{eff>0.533\ nm}$ and $V_{eff.>1.1nm}$, corresponding to the "effective surface area" and "effective pore volume" for those electrolytes used in the electrochemical characterization of carbons, were estimated.

The morphology of washed porous N-dC materials was characterized by scanning electron microscopy (SEM) and the 200 nm scale images are depicted in Figure 2.2.

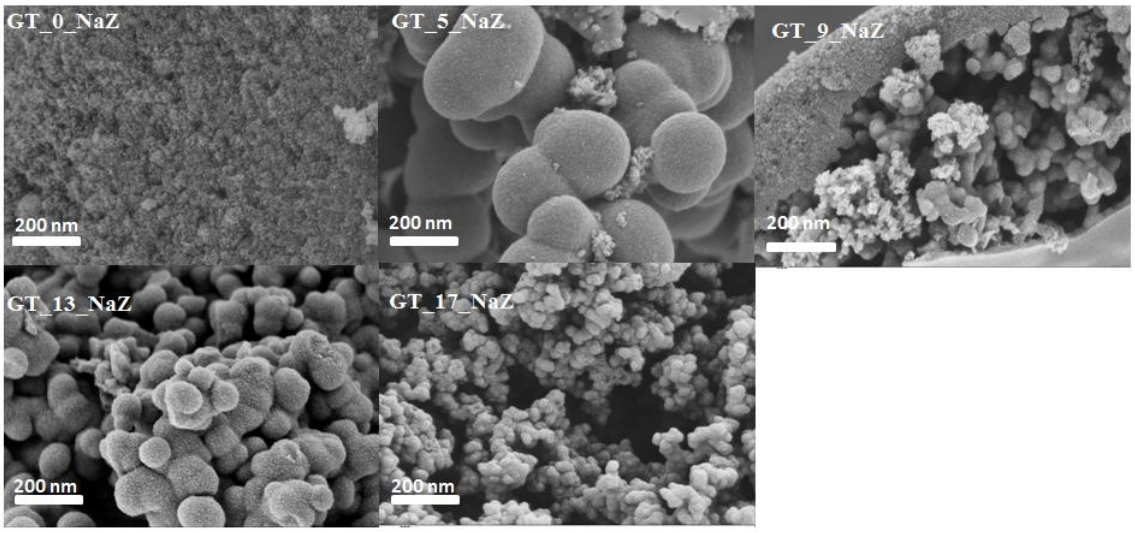

Figure 2.2. SEM images of different carbons with molar ratio of urea to TA (0:1, 5:1, 9:1, 13:1, and 17:1). The ratio of precursors (urea and tannic) to $NaCl/ZnCl_2$ template salt is 1:3.

Without adding nitrogen precursor (urea) to the mixture, the particles of GT_0_NaZ carbon are very small forming a homogeneous rough surface compared with N-doped carbons. Figure 2.2 reveals that addition of urea as nitrogen precursor results in significant change in the morphology of obtained N-dC. Morphology of those N-dCs consists of well-connected much bigger spherical particles with continuous and interconnected structure.

In the case of GT_5_NaZ N-dC which contains 5:1 ratios of urea to tannic acid, the particles are relatively bigger (~200-300 nm) and clearly visible with naked eyes throughout the sample. With further increasing of molar concentration of urea in the mixture, the N-dC particles are getting smaller and aggregated of particles are clearly observed. In some cases, large void spaces between aggregated particles are observed when the molar ratio of urea to TA increases, indicating that the additional structural collapse and lack of template replication at higher ratio of urea to TA. Particularly, in the case of GT_17_NaZ N-dC (17:1 urea to TA) wider void is visible; indicating the morphology of the carbon is generally disordered. These results demonstrate that the molar ratio of urea to TA significantly influences the morphology of carbon. Therefore, optimizing the concentration ratio of nitrogen and carbon precursors is crucial in order to get well-defined and rigid carbon structure for the reverse replication of template salt and it is very important to maintain open, continuous interconnected pores for optimal electrochemical performance [4].

The structure of porous carbons was confirmed by the X-ray diffraction (XRD) technique and the profiles of all washed porous carbons are presented in Figure 2. 3.

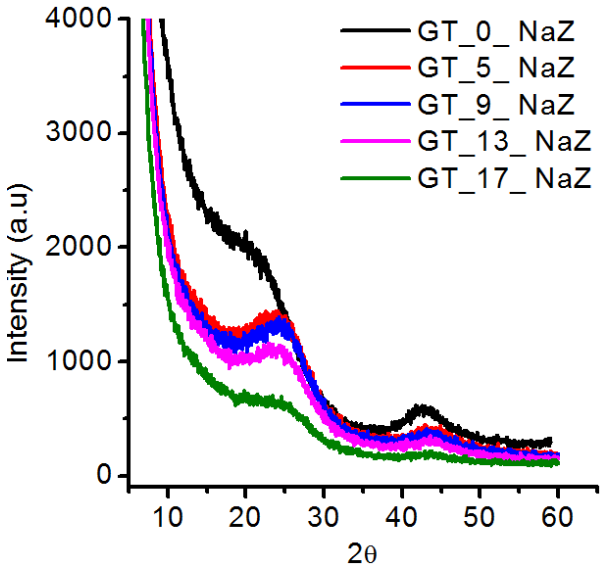

Figure 2. 3. XRD graphs of porous carbons synthesized with different ratio of urea to tannic acid (0:1, 5:1, 9:1, 13:1, and 17:1)

All carbons show a similar diffraction pattern with two broad peaks at 2θ diffraction angle of 25° and a week peak at 45°, corresponding to (002) and (100) miller indices, typically observed in graphitic layers. Therefore, the diffraction profiles show that the porous carbons have turbostratic graphitic structure, indicating that the building blocks of the synthesized N-dCs are composed of graphitic like micro-crystallites that are randomly oriented and distributed throughout the sample [32]. The low intensity and high broadness of the two peaks reveals a significant degree of disorder in all the carbons [33].

XRD pattern of N-dC materials show a clear trend with the content of urea in the precursors blend. It is clearly observed that the peaks intensity decrease when molar ratio of urea to tannic acid increases. This is particularly evidenced in GT_17_NaZ (17:1), with the highest content of urea, in which the peak intensity became relatively flat and much less prominent compared with the other carbons. This indicates that when the urea content increases in the precursors mixture, the structure of obtained carbons become more disorder and randomly oriented probably due to the higher amount of nitrogen incorporated onto the carbon matrix which was confirmed by bulk elemental and XPS analyses as explained in the next paragraphs. The absence of additional peaks indicate that the synthesized N-dC materials are free from any residual of eutectic salts as it was washed several times with distilled water after carbonization.

The direct relationship between the nitrogen content incorporated onto the carbon matrix and the molar ratio urea to tannic acid in the precursor blend was confirmed by bulk elemental analysis. It was revealed that the content of nitrogen

doped onto the N-dC matrix was increased with molar ratio of urea to tannic acid as shown in Table 2.3 The doped nitrogen content reaches maximum about 8.83 % for GT_17_NaZ carbon with 72.5 % of carbon and for the GT_5_NaZ carbon, the content of nitrogen and carbon are found to be 6.68 % and 78.4 %, respectively.

Table 2.3. Elemental Analysis for carbons synthesized with different molar ratios of urea to tannic acid and 1:3 ratio of precursors (urea and tannic acid) to template salt ($NaCl/ZnCl_2$)

Carbon	Molar ratio (urea:TA)	Elemental Analysis (wt %)				
		N	C	H	S	N/C
GT_0_NaZ	0:1	0.72	89.2	-	-	0.008
GT_5_ NaZ	5:1	6.68	78.4	2.53	1.01	0.08
GT_9_ NaZ	9:1	8.27	76.3	2.65	1	0.11
GT_13_ NaZ	13:1	8.52	73.1	2.65	1.12	0.11
GT_17_ NaZ	17:1	8.83	72.5	2.6	1	0.12

The small content of nitrogen (0.72 %) detected in the non-N-dC materials (GT_0_NaZ) is probably due to remaining nitrogen during isothermal treatment of tannic acid in N_2 atmosphere. The consistent increase in nitrogen content in the N-dC matrix with increasing molar ratio of urea to tannic acid indicates that neither urea nor tannic acid is preferentially excluded during pre-mixing the precursors and during heat treatment. This result confirms the prior research reported by A. Stein *et.al* in which it was showed that the increased content of nitrogen in the carbon matrix with increasing amount of EMI-DCA, which was served as nitrogen precursor [4].

In order to understand the role of nitrogen functionalities in the capacitive performance of supercapacitors, it is necessary to identify the types of nitrogen onto the carbon surface. In this case, only three representative carbon samples; GT_0_NaZ (non-N-dC), GT_9_NaZ and GT_17_NaZ, were selected and characterized by XPS. The XPS spectra of three carbons revealed the presence of three strong different peaks, indicating the presence of nitrogen (398-404 eV), carbon (283-290 eV) and oxygen (530 -535 eV) atoms. XPS analysis confirmed that the nitrogen content onto the surface of porous carbons increased with molar concentration of urea to tannic acid (see Table 2.4), being in good agreement with the trend of bulk elemental analysis.

Table 2.4. Surface composition of GT_0_NaZ, GT_9_NaZ and GT_17_NaZ characterized by XPS.

Carbon	Molar ratio (urea:TA)	XPS Analysis (%)				
		N	C	O	O/C	N/C
GT_0_NaZ	0:1	0.50	89.89	3.007	0.03	0.006
GT_9_ NaZ	9:1	6.50	89.19	3.55	0.040	0.07
GT_17_ NaZ	17:1	7.10	89.89	3.72	0.04	0.08

The presence of small nitrogen content in the control sample (GT_0_NaZ) is due to the introduction of nitrogen during thermal treatment of sample in N_2 atmosphere. The full XPS scan of GT_0_NaZ is presented in Figure 2.4a, showing the O1s and C1s peaks are visible, whereas the N1s peak is relatively invisible.

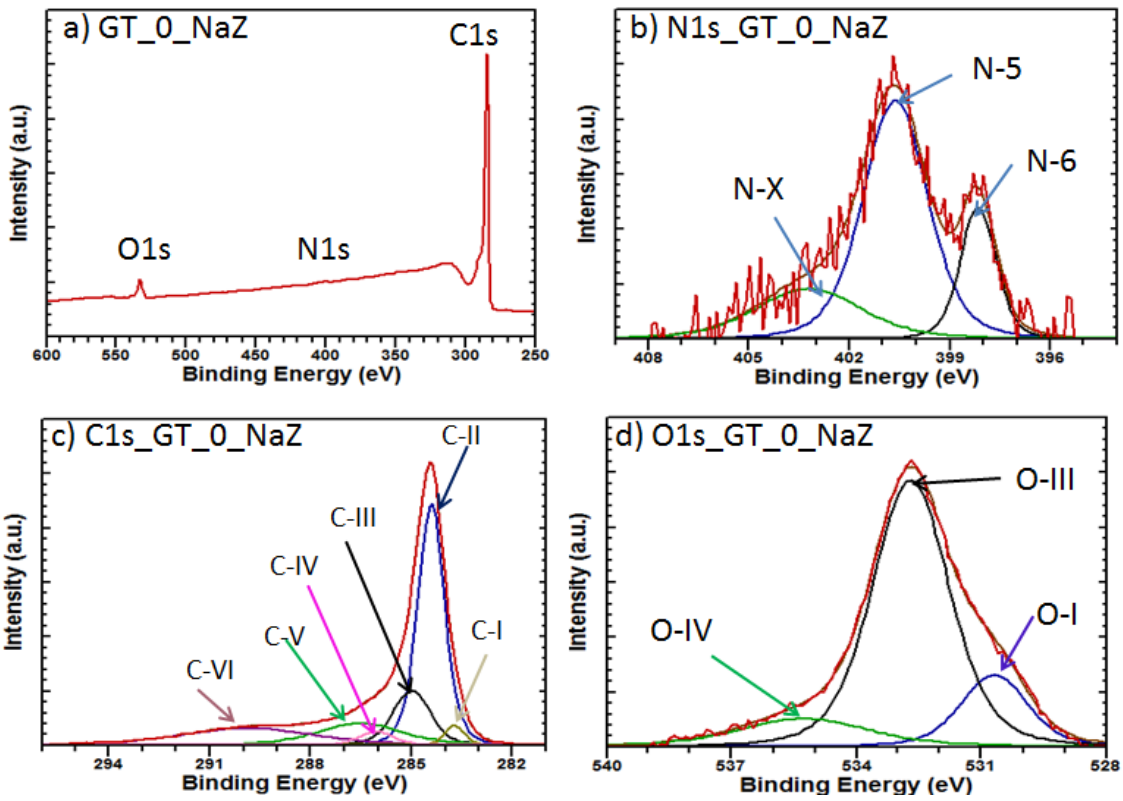

Figure 2.4. a) XPS full scan spectra of GT_0_NaZ porous **N-dC** deconvoluted at high resolution spectrum of b) N1s c) C1s and d) O1s.

According to literature, the nitrogen functionalities present in carbons include pyridinic (N-6) at about 398 eV, amine, pyrrolic or pyridine (N-5) at about 400 eV, N-quaternary, pyridinium or ammonium (N-Q) at 401 eV and pyridine-N-oxide (N-X) at about 403 eV [12,31,34–38]. Sometimes, binding energy at 398.5-400.1 eV is overlapped and assigned to lactom, amides and imid nitrogen functionalities [12,39].

Table 2.5. Composition of N, O, and C onto three **N-dCs** determined by XPS analysis.

GT_0_NaZ		GT_9_NaZ		GT_17_NaZ		Possible nitrogen functionalities on the surface of porous carbon
N1s		N1s		N1s		
BE(eV)	At. %	BE(eV)	At. %	BE(eV)	At. %	
398.14	18	398.16	33	398.18	31	N-6 (pyridinic)
400.62	60	400.02	39	400.11	45	N-5 (Pyrrolic or Pyridone, amine, or amide)
ND*	ND*	401.05	12	401.14	10	N-Q (N-quaternary, pyridinium, ammonium)
403.22	30	403.45	15.	403.82	14	N-X (Pyridine-N-Oxide)
GT_0_NaZ		GT_9_NaZ		GT_17_NaZ		Possible Carbon functionalities on the surface of porous carbon
C1s		C1s		C1s		
BE(eV)	At. %	BE(eV)	At. %	BE(eV)	At. %	
283.8	3	283.98	6.8	284.11	10.	C-I (C*-C (sp^2))
284.41	48	284.58	37	284.64	35	C-II (C*-C (sp^3))
284.99	15	285.14	14	285.25	14	C-III (C*-N)
286	3.52	285.86	12	286.02	13	C-IV (C*-O-C*, C-OH, or C=N)
286.53	13	286.92	13	287.27	11	C-V (C*=O, amide/aldehyde/ketone)
289.87	16	289.92	16	290.0	14	C-VI ($\pi \rightarrow \pi^*$ transitions), C*=O (carboxylic/ester groups)
GT_0_NaZ		GT_9_NaZ		GT_17_NaZ		Possible oxygen functionalities on the surface of porous carbon
O1s		O1s		O1s		
BE(eV)	At. %	BE(eV)	At. %	BE(eV)	At. %	
530.68	16	530.65	24	530.74	27	O-I (-C=O, quinone type)
ND	ND	531.0	12	531.0	15	O-II(-C-O (carbonyl groups)
532.69	71	532.56	63	532.6	58	O-III (C=O, C-OH phenol, C-O-C-)
535.26	12	535.54	12	535.72	14	O-IV (-COOH, H_2O)

*Not detected

The deconvolution of the N1s spectra of non-N-dC shows three different peaks (N-X, N-5 and N-6), indicating the presence of three different nitrogen functionalities (Figure 2.4b). [34]. Among these nitrogen functionalities, the majority of nitrogen in GT_0_NaZ N-dC is presented in the form of N-5 (about 61 %) (see Table 2.5 in the next page). The peak corresponding to N-Q at about 401 eV is not present in this carbon.

Fitting the C1s spectrum of GT_0_NaZ can be resolved into six individual component peak as shown in Figure 2.4c. C-I (BE=283.7 eV) corresponds to carbon C-C (sp^2 hybridaztion), C-II (BE=284.41 eV) to graphitic carbon (sp^3 hybridization), C-III (BE=284.99 eV) to carbon in amine (C-N), C-IV (BE=286 eV) to carbon presents in the form of alcohol or ether, C-V (BE=286.53 eV) to carbon either in ketone, aldehyde or amide and C-VI (BE=289.87 eV) to carbon in carboxylic, ester or $\pi \rightarrow \pi^*$ transitions in the aromatic ring [34,36,40]. The majority form of carbon in the GT_0_NaZ is the C-C in the form of sp^3 hybridization that comprises 48 % out of 90 % of carbon content.

Moreover, deconvolution of O1s spectrum reveals the presence of three peaks at 530.68 corresponding to C=O groups in quinone or urea (O-I), at 532.69 eV (O-II) corresponding to carbonyl oxygen atoms esters, amides, anhydrides, and oxygen atom in C-OH (carboxyl or phenol), C-O-C (ether) (O-III) and at 535.26 eV corresponding to oxygen in carboxylic or chemisorbed water (O-IV) [31,34–37]. The majority content of oxygen existing in GT_0_NaZ porous carbon is in the form of C-OH, phenolic or C-O-C (ether groups) which comprise about 71 % from the total of carbon as shown in Table 2.5.

Similarly, the high resolution N1s spectra of carbons synthesized with 9:1 and 17:1 molar ratios of urea to tannic acid (GT_9_NaZ and GT_17_NaZ, respectively) were deconvoluted and shown in Figure 2.5b and Figure 2.6b. In addition to N-5, N-6 and N-X, both GT_9_NaZ and GT_17_NaZ porous N-dC materials revealed additional quaternary nitrogen (N-Q) which was not detected in GT_0_NaZ (control sample without urea). It is important to mention here that N-Q peak corresponds to the structural nitrogen that is densely incorporated into the graphitic backbone of the carbonaceous material. The structural incorporation of the nitrogen into the carbon matrix will cause lowering the balance band due to the electron richness of the nitrogen. As a result it would increase the electron density at the fermi-level, consequently increasing the electrical conductivity of the N-doped carbon material [41]. This is very important effect for the application of N-dC materials in electrochemical devices. Result in Table 2.5 indicates that the major content of nitrogen in both carbons (GT_9_NaZ and GT_17_NaZ) was found in the form of N-5 (pyrrolic, amide, amine, or pyridone nitrogen). This value increase with increasing molar ratio of urea to tannic acid with 39 % for GT_9_NaZ and 45 %, for GT_17_NaZ (see Table 2.5). The content of

both N-6 and N-X decreased from 33 % of N-6 and 15 % of N-X in GT_9_NaZ to 31 % of N-6 and 14 % of N-X in GT_17_NaZ with increasing molar ratio of urea to TA. Similarly, the content of N-Q also decreased from 12 % in GT_9_NaZ carbon to 10 % in GT_17_NaZ. The decreasing trend of N-6, N-Q and N-X with increasing ratio urea:TA are in a contrary to the trend of N-5 groups whose concentration increased with increasing ratios (Table 2.5). This indicates that when the molar concentration of nitrogen precursor (urea) increased, the carbon surface is dominated by N-5 nitrogen functionalities (amine, amide, pyrrolic, or pyridine nitrogen functions).

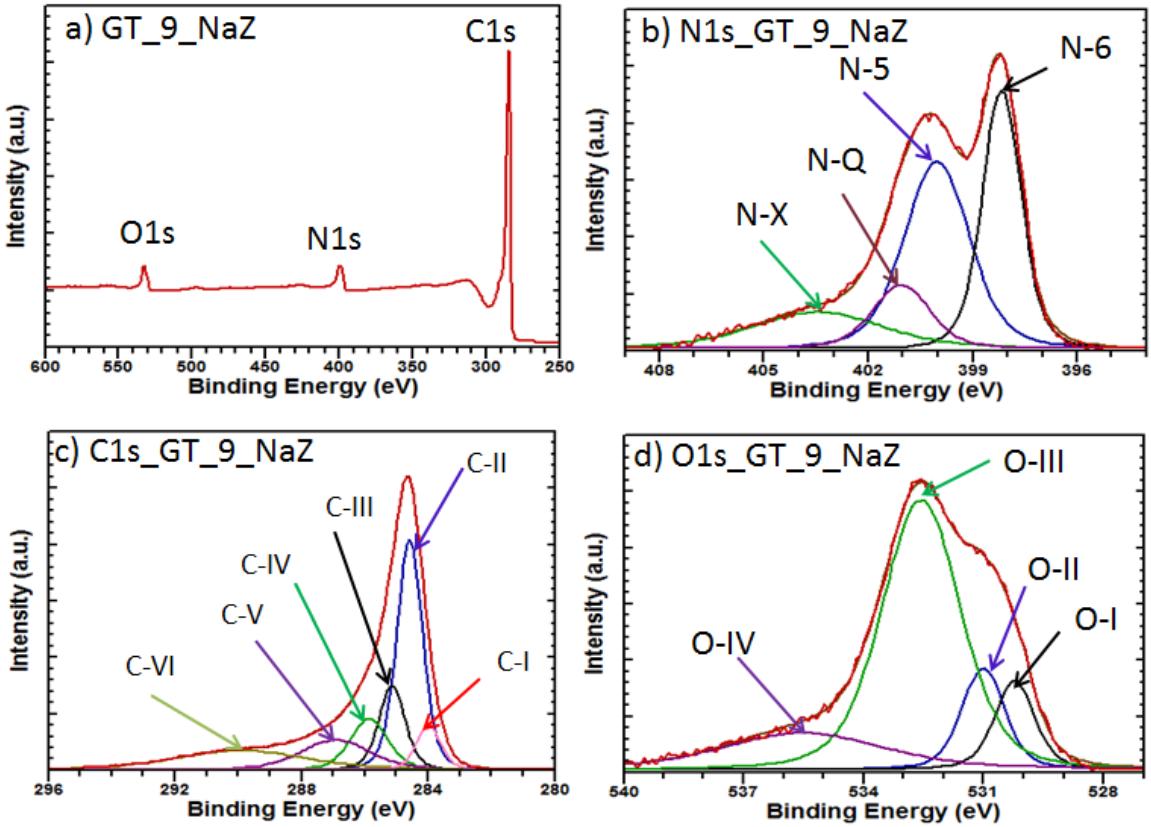

Figure 2.5. a) XPS full scan spectra of GT_9_NaZ porous carbon b) deconvoluted high resolution spectrum of b) N1s c) C1s and d) O1s

Moreover, the deconvoluted C1s spectra of both GT_9_NaZ and GT_17_NaZ carbons are shown in Figure 2.5c and Figure 2.6c, respectively and revealed the same six different peaks described for GT_0_NaZ. The majority of C1s in both GT_9_NaZ and GT_17_NaZ carbons is found in the form of C-C (sp^3) which comprises 37 % and 35 %, respectively. Table 2.5 shows that the content of C-I and C-IV functional groups are higher in GT_9_NaZ and GT_17_NaZ N-dC materials compared with the non-doped carbon (GT_0_NaZ), indicating that the favourable incorporation of graphitic carbon (sp^2) and C=N functionalities at higher concentration of urea to tannic acid. Finally, the high resolution of O1s spectra of GT_9_NaZ and GT_17_NaZ porous N-dC materials

also deconvoluted and fitted into four different Gaussian-Lorentzian peaks as shown in Figure 2.5d and Figure 2.6d. Those peaks are assigned to oxygen O-I (C=O quinone type groups) at 530.65-530.74 eV, O-II groups (C-O carbonyl groups) at 531 eV, O-III groups (C=O carbonyl oxygen atoms in esters, amides, anhydrides, and oxygen atoms in C-OH, hydroxyls, phenol or C-O-C ether groups) at 532.56-532.6 eV and O-IV oxygen groups (carboxylic or chemisorbed water) at 535.54-535.74 eV [14,31,37]. In all three N-dC materials (GT_0_NaZ, GT_9_NaZ, and GT_17_NaZ) the maximum content of oxygen is found to be in the form of O-III (phenol, C-OH, and C=O).

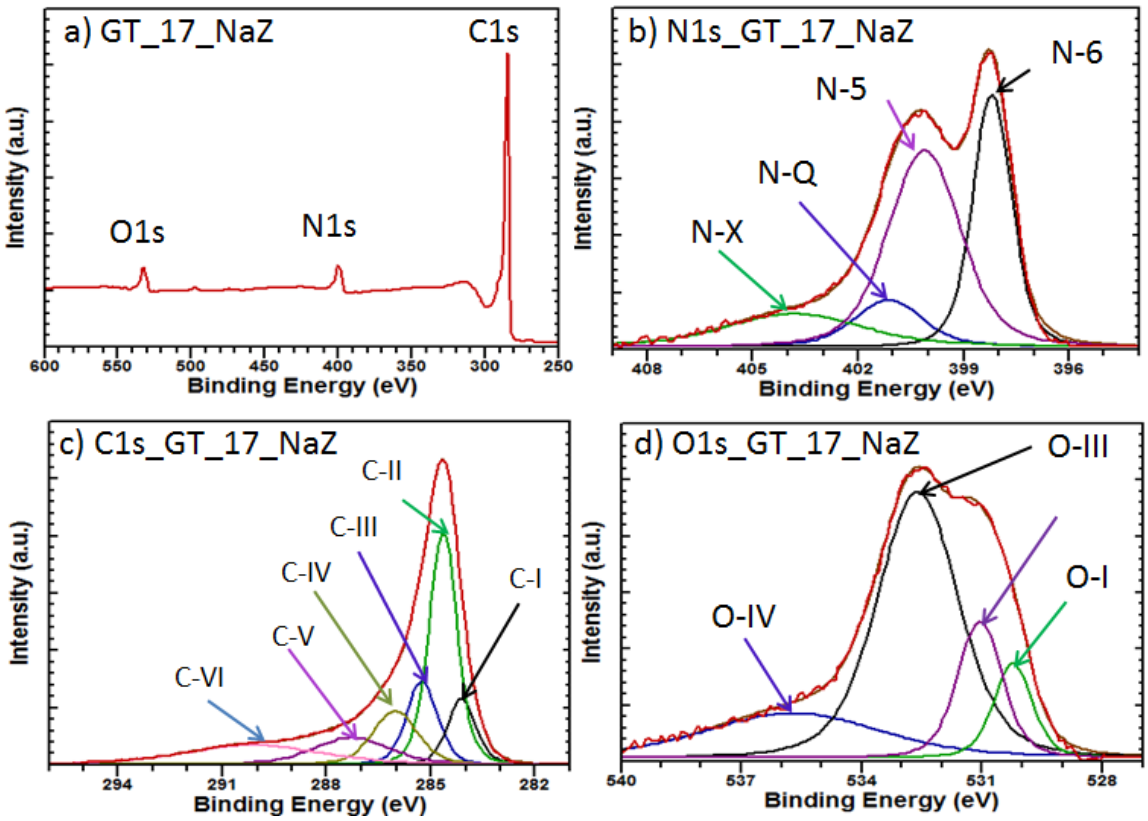

Figure 2.6. a) XPS full scan spectra of GT_17_NaZ N-dC materials deconvoluted high resolution spectrum of b) N1s c) C1s and d) O1s

2.3.1.2. Effect of Mass Ratio of precursors (urea+TA) to eutectic salt

In order to evaluate the influence of concentration of template eutectic salt on the physical properties of porous carbon, the ratio of urea and TA was fixed to 9:1 (urea:TA) and blended with different mass of $NaCl/ZnCl_2$. The molar ratio of urea to TA was fixed to 9:1 because it exhibited N-dC materials (GT_9_NaZ) with the best textural properties as shown in previous section. The mass ratios of precursors (urea+TA) to $NaCl/ZnCl_2$ include 1:1, 1:3, 1:5 and 1:7. The prepared N-dC materials were named as GT_NaZ_S, where S is 1, 3, 5 or 7 depending on the mass ratio of precursors to salt (see Table **2.1**).

Figure 2.7a shows Ar sorption isotherm for different porous carbons. GT_NaZ_1 , which was prepared with the lowest ratio of precursors to template salt (1:1), shows the lowest gas uptake and it reaches plateau at P/P_o = 0.1, indicating an isothermal type I. However, when the ratio of precursors to template salt was increased 3 times (1:3), additional gas uptake was also observed. This is probably due to development of macro textures between sheets in addition to delamination of carbon structures at higher eutectic salt. Nevertheless, there is no further increase in gas uptake at higher ratios of precursors to template salt (1:5 or 1:7). N-dC with ratio of 1:3, 1:5 and 1:7 present isothermal type IV with sharp increased uptake of Ar below P/P_o=0.1, ascribing the presence of micro-pores (<2 nm) and small hysteresis in the region of relative pressure from 0.4 to 0.9, confirming the presence of small meso-pores (2-50 nm). Figure 2.7b shows the pore size distribution of different carbons indicating that the porosities of carbons are dominated by micropores (< 2 nm) and small mesopores (between 2-3 nm).

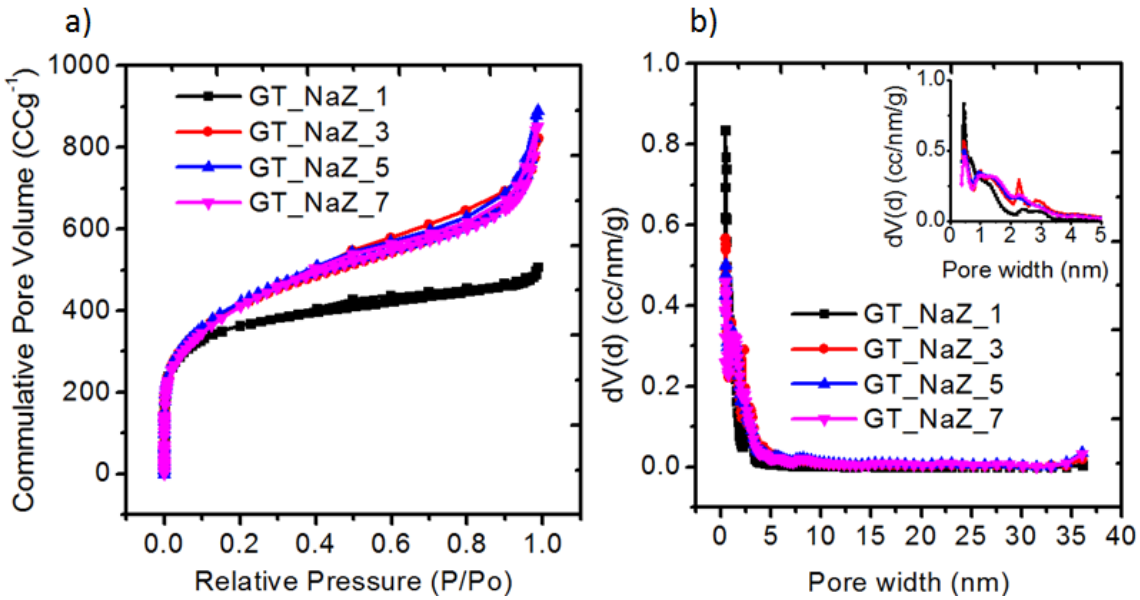

Figure 2.7. Argon (87 K) adsorption/desorption isotherms of carbon with a) ratio of precursors (urea and TA) to template salt ($NaCl/ZnCl_2$)(1:1, 1:3:, 1:5, and 1:7) with the 9:1 ratio of urea to TA b) the corresponding Pore size distribution of carbons calculated by QSDFT (slit pore, QSDFT equilibrium mode)

Different structural parameters of the synthesized carbons are presented in Table 2.6. Both specific surface areas estimated using BET and DFT methods were calculated and presented in the table showing similar values. Increasing ratio from 1:1 to 1:5 promotes formation of small mesopores as shown small hysteresis in Ar sorption (see Figure 2.7a), contributing small increase in S_{BET}, S_{DFT} and V_{tot}, whereas further increasing eutectic salt content in the mixture to 1:7, decreases its S_{BET}, S_{DFT} and V_{tot} ,

probably due to the lack of template replication at higher content of $NaCl/ZnCl_2$, and promotes high degree of mesopority ($S_{>2nm}/S_{DFT}$=16 %). The GT_NaZ_1 carbon exhibits 94 % degree of micro-porosity indicating that the carbon is mainly microporous. Increasing the template salt concentration decreases the degree of micro-porosity from 94 % to 83-85 %, confirming formation of mesopores at higher ratios as shown in Table 2.6. Similarly, the contributions of micropores volume ($V_{<2nm}$) to the total pore volume (V_{tot}) also decreased with increasing mass ratio of $NaCl/ZnCl_2$. For example, the degree of micro-pore volume ($V_{<2nm}/V_{tot}$) decreased from 74 % for GT_NaZ_1 to 48-49 % for GT_NaZ_3, GT_NaZ_5 and GT_NaZ_7. It is worth mentioning here that GT_NaZ_1 presents a $S_{eff>1.1\,nm}$ value of 289 m^2g^{-1} which was calculated based on the bigger cation size of $PYR_{14}FSI$ electrolyte used for further electrochemical characterization in this work. In fact, $S_{eff>1.1\,nm}$ is significantly lower than for the other N-dC, contributing values higher than 500 m^2g^{-1} (see Table 2.6) This might have an significant effect on the electrochemical properties of this carbon in ionic liquids with big ions.

Table 2.6. Structural parameters total surface area,v $S_{DFT,}$ total pore volume V_{tot}, and pore width, all are calculated by QSDFT).

Carbon	S_{BET} (m^2g^{-1})	S_{DFT} (m^2g^{-1})	$S_{eff>0.533\,nm}$ (m^2g^{-1})	$S_{<2\,nm}$ (m^2g^{-1})	$S_{eff.>1.1\,nm}$ (m^2g^{-1})	$S_{<2\,nm}/S_{DFT}$ (%)
GT_NaZ_1	1197	1267	800	1185	289	93
GT_NaZ_3	1329	1326	949	1105	517	83
GT_NaZ_5	1353	1338	958	1138	518	85
GT_NaZ_7	1314	1272	932	1071	534	84
Carbon	**V_{tot} (m^3g^{-1})**	**$V_{>0.533nm}$ (m^3g^{-1})**	**$V_{<2\,nm}$ (m^3g^{-1})**	**$V_{eff>1.1nm}$ (m^3g^{-1})**	**$V_{<2\,nm}/V_{tot}$ (%)**	**Pore width (nm)**
GT_NaZ_1	0.61	0.50	0.45	0.30	74	0.45
GT_NaZ_3	0.98	0.89	0.48	0.72	49	0.45
GT_NaZ_5	1.03	0.95	0.50	0.77	48	0.48
GT_NaZ_7	0.99	0.92	0.49	0.76	49	0.48

Figure 2.8 represents the SEM images of N-dC materials prepared with different ratio of precursors (urea+TA) to $NaCl/ZnCl_2$. SEM image of GT_NaZ_1 shows a rough flat surface whereas the morphology of the other 3 samples are granular-shape. GT_NaZ_3 is mainly formed by spherical particles of about 50-100 nm. Figure 2.8 shows that GT_NaZ_5 and GT_NaZ_7 have very similar morphology with smaller carbon particles with irregular shapes and interconnected particles forming aggregates.

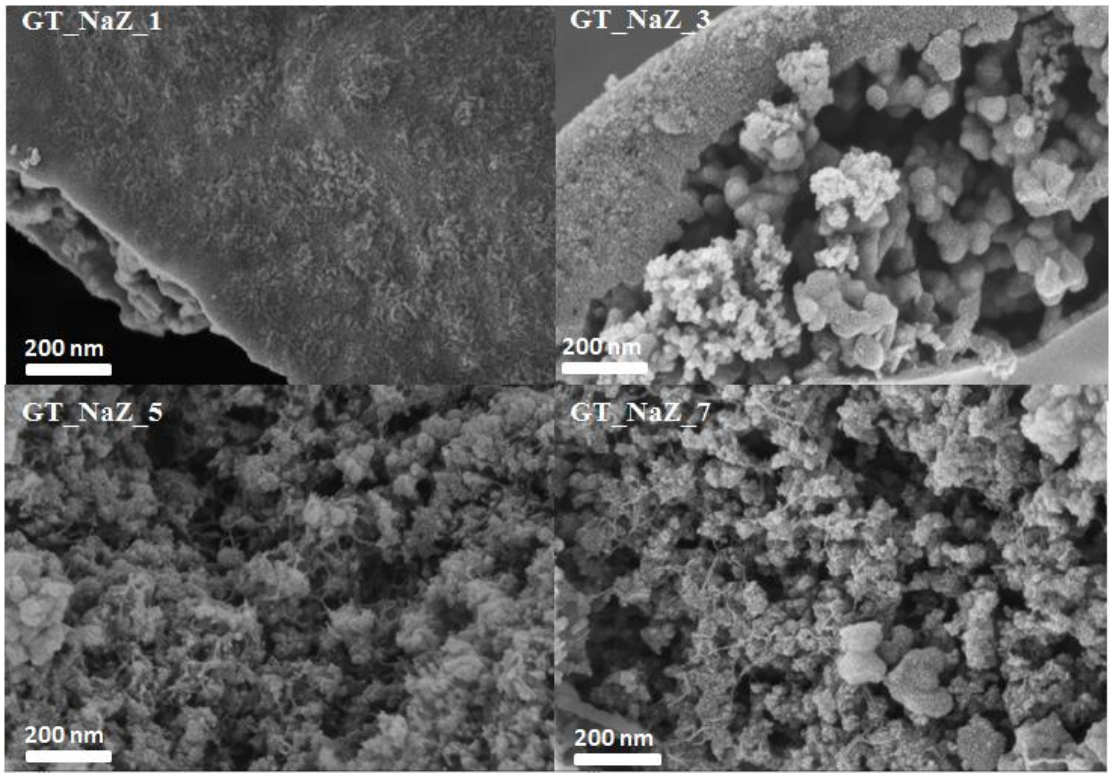

Figure 2.8. SEM images for different carbons with different ratio of precursors (urea+TA) to NaCl/$ZnCl_2$ (1:1, 1:3, 1:5, and 1:7). 9:1 ratio of urea to TA in all N-dC.

The characteristic XRD patterns are represented in Figure 2.9 being similar to those depicted in Figure 3.3 for previous carbons.

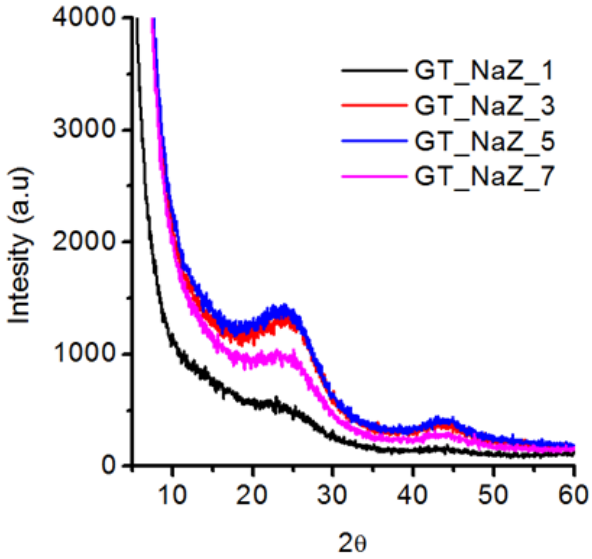

Figure 2.9. Characteristic XRD patterns for different porous carbons. 9:1 ratio of urea to TA and different ratio of precursors (urea+TA) to NaCl/$ZnCl_2$ (1:1, 1:3, 1:5, & 1:7).

XRD patterns show a broad diffraction peak at 2θ diffraction angle of 25° and a week peak at 45°, corresponding to (002) and (100), respectively, confirming the graphitic like structure. Moreover, the broad peaks and their low intensity suggest that those porous carbons are highly disordered materials in the form of amorphous carbon [33], especially in the case of GT_NaZ_1 that exhibits very low intense peaks. Despite the high amount of template salt that was increased from 1:1 to 1:7, no additional peaks were shown in the XRD pattern, confirming the total salt removal during washing step.

Table 2.7 shows the elemental composition of the different N-dC materials. It is observed that except GT_NaZ_3 that exhibits nitrogen content of 8.3 %, all N-dCs show similar nitrogen content *ca.* 7 %, despite the ratio of urea to TA was fixed to 9:1 for all compositions while increasing the content of salt as porogen. Since the ratio of urea (nitrogen precursor) to TA (carbon precursor) was kept constant at 9:1 for all the carbons, the N/C ratio in the obtained N-dC materials was practically the same.

Table 2.7. Bulk elemental analysis for N-dC materials synthesized with different ratio of precursors to $NaCl/ZnCl_2$ (1:1, 1:3, 1:5, & 1:7).

Carbon	Mass ratio (precursor:salt)	Elemental Analysis (wt %)				
		N	C	H	S	N/C
GT_NaZ_1	1:1	6.9	62.81	2.8	0.66	0.11
GT_NAZ_3	1:3	8.3	76.26	2.65	1	0.11
GT_NaZ_5	1:5	7	67.62	2.3	0.63	0.10
GT_NaZ_7	1:7	6.8	67.4	2.05	0.7	0.10

2.3.1.3. Effect of the Type of Eutectic Salt

In this section, properties of N-dC materials with different eutectic salts ($NaCl/ZnCl_2$, $LiCl/ZnCl_2$ and $KCl/ZnCl_2$) synthesized in similar conditions as explained before were compared. A precursor blend with a fix ratio of 9:1 (urea:TA) was blended with the selected eutectic salt using a fixed mass ratio of precursor (urea+TA) to the respective eutectic salt of 1:3. As-prepared N-dC materials were named as GT_9_NaZ, GT_9_LiZ, and GT_9_KZ where 9 refer to urea:TA molar ratio and NaZ, LiZ and KZ refer to $NaCl/ZnCl_2$, $LiCl/ZnCl_2$ and $KCl/ZnCl_2$, respectively.

Figure 2.10(a-b) shows the Ar sorption isotherm and the pore size distribution of the three N-dC materials. Differences found in isotherms indicate that textural properties of N-doped carbons are dependent on the intrinsic nature of eutectic salt. Although the three N-dC materials show a Type IV isotherm typical from mesoporous carbons, GT_9_KZ present much lower gas uptake than GT_9_NaZ and GT_9_LiZ.

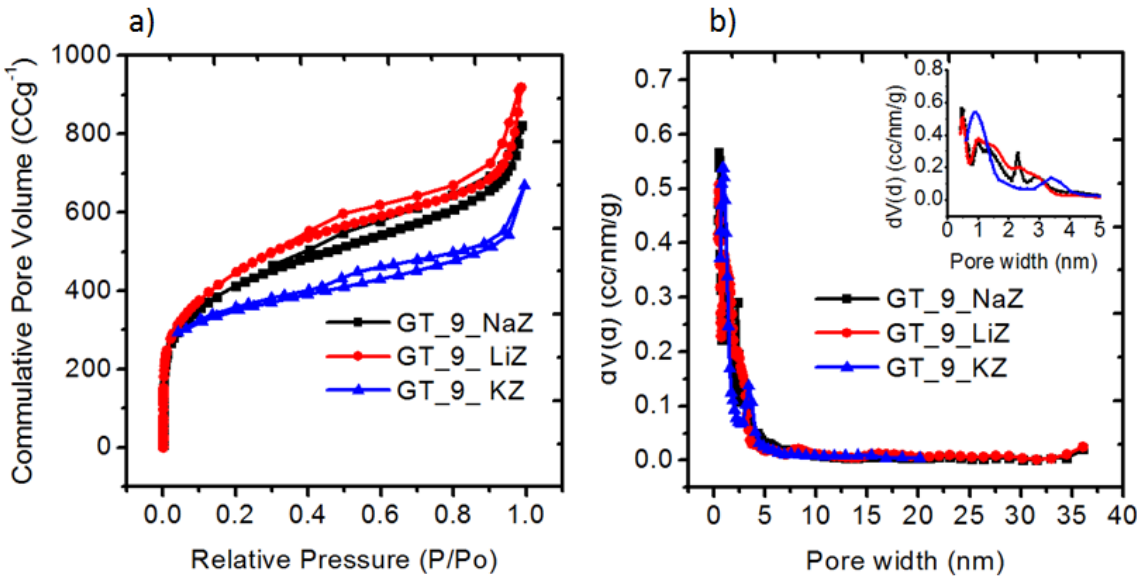

Figure 2.10. Argon (87 K) adsorption/desorption isotherms of carbon with a) 9:1 ratio of urea to TA and 1:3 ratio of precursors to eutectic salt b) the corresponding Pore size distribution of carbons calculated by QSDFT (slit pore, QSDFT equilibrium mode)

Table 2.8 shows the textural properties of carbons synthesized with different template salts. GT_9_KZ has the lowest specific surface area (S_{DFT}=1149 m^2g^{-1}), the lowest "effective surface areas" and lowest total pore volume (0.801 m^3g^{-1}) whereas GT_9_NaZ and GT_9_LiZ carbons present higher surface area of 1326 and 1382 m^2g^{-1}, respectively. The degree of micro-porosity ($S_{<2nm}/S_{DFT}$) is around 80-83% in all the cases.

Table 2.8. Structural parameters S_{BET} (total surface area, S_{DFT}, total pore volume V_{tot}, and pore width, all are calculated by QSDFT).

Carbon	S_{BET} (m^2g^{-1})	S_{DFT} (m^2g^{-1})	$S_{eff>0.533\ nm}$ (m^2g^{-1})	$S_{<2\ nm}$ (m^2g^{-1})	$S_{eff.>1.1\ nm}$ (m^2g^{-1})	$S_{<2\ nm}/S_{DFT}$ (%)
GT_9_NaZ	1329	1326	949	1105	517	83
GT_9_LiZ	1409	1382	1013	1158	583	84
GT_9_KZ*	1251	1149	1149	996	399	79
Carbon	**V_{tot} (m^3g^{-1})**	**$V_{>0.533nm}$ (m^3g^{-1})**	**$V_{<2\ nm}$ (m^3g^{-1})**	**$V_{eff>1.1nm}$ (m^3g^{-1})**	**$V_{<2\ nm}/V_{tot}$ (%)**	**Pore width (nm)**
GT_9_NaZ	0.977	0.89	0.48	0.72	49	0.45
GT_9_LiZ	1.087	1.00	0.53	0.83	48	0.48
GT_9_KZ*	0.801	0.80	0.47	0.51	58	0.85

*The isothermal analysis of GT_9_KZ carbon was characterized by N_2 sorption isotherm

Representative morphologies were obtained for those N-dC materials derived from 9:1 ratio of urea to TA and different template salts (see Figure 2.11). Changing from $NaCl/ZnCl_2$ salt to $LiCl/ZnCl_2$ to $KCl/ZnCl_2$ salts shows an increase in aggregation of carbon particles, indicating the morphology of the porous N-dC materials significantly influenced by the nature of the eutectic salt.

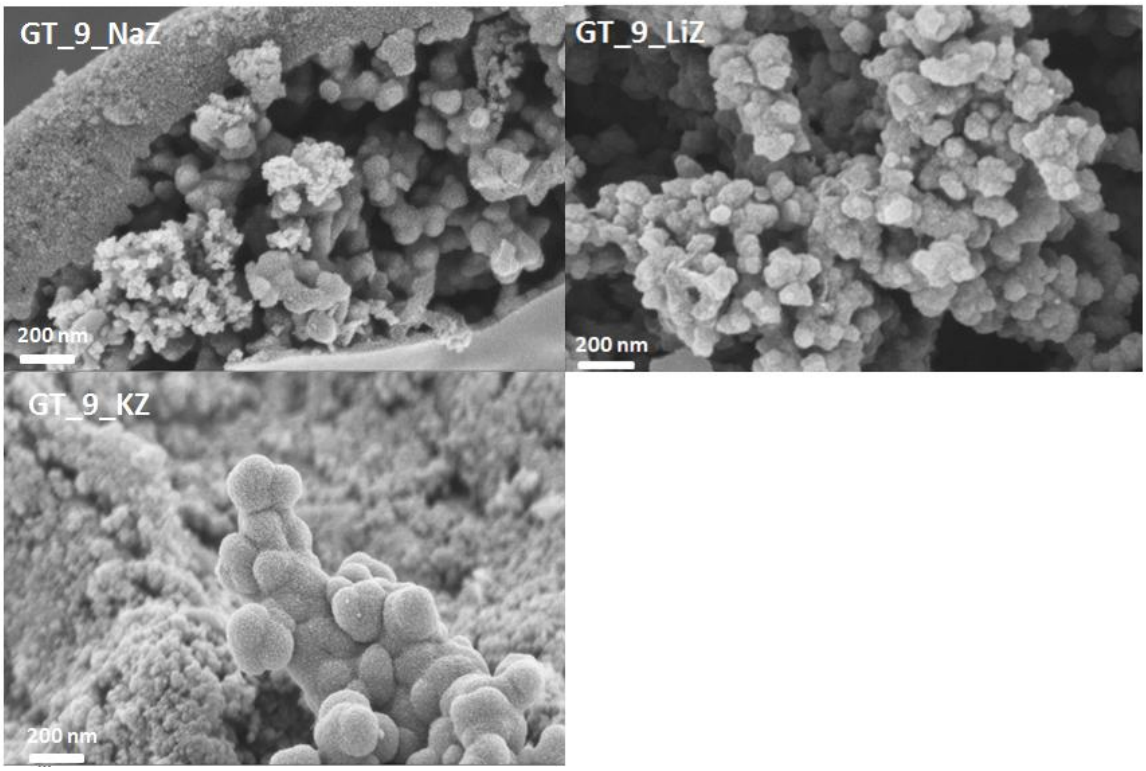

Figure 2.11. SEM images for different carbons with different template salts (9:1 ratio of urea to tannic acid and 1:3 ratio of precursors to the respective template salt)

The representative XRD pattern peaks of the washed powder carbons are shown in Figure 2.12. All porous carbons exhibited peaks at 2θ 25° (002) and 44.5° (100), characteristic of slightly disorder porous graphitic carbons.

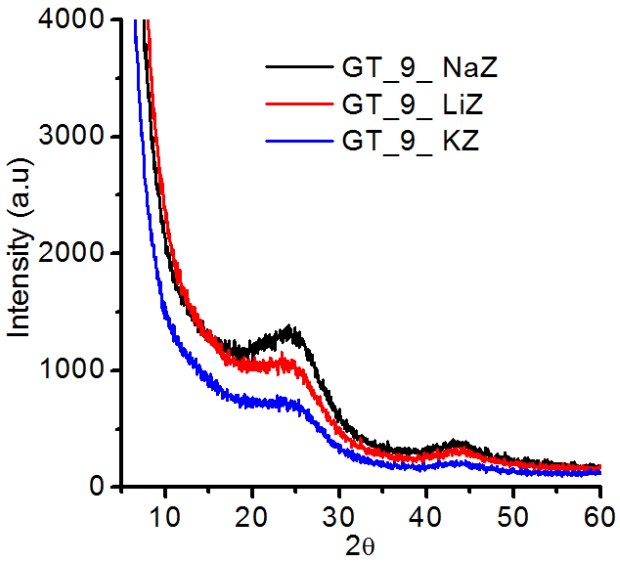

Figure 2.12. Characteristics patterns of XRD peaks for different carbons synthesized with different template salts

Table 2.9 shows the bulk elemental composition of different N-dC materials. It is observed that N-dC synthesized with $NaCl/ZnCl_2$ exhibited the highest content of nitrogen and carbon compared with the carbons synthesized with $LiCl/ZnCl_2$ and $KCl/ZnCl_2$. However, since the ratio of urea (nitrogen precursor) to tannic acid (carbon precursor) was kept constant (9:1), the N/C ratio was practically the same in the obtained carbons.

Table 2.9. Bulk elemental analysis of different carbons synthesized with different template salts.

Carbon	Elemental Analysis (wt %)				
	N	C	H	S	N/C
GT_9_ NaZ	8.3	76	2.65	1	0.11
GT_9_ LiZ	7.06	68	2.2	6.12	0.10
GT_9_ KZ	6.43	69	2.33	0.72	0.09

2.3.2. Electrochemical Characterization

2.3.2.1. Electrical Conductivity of Synthesized Carbons

One of the particular problems in the development of multifunctional materials for application in energy storage devices is the poor electrical conductivities of porous materials. It is generally accepted that the incorporation of structural hetroatoms into the carbon may distort a perfectly ordered carbon matrix leading to a possible

modification of electronic properties of the doped carbon materials at Fermi level. This, in turn, would lead to an increase in electrical conductivity of the doped carbon, ascribing a direct relationship between electrical conductivity of porous carbons, and doped nitrogen. To investigate the effectiveness of doped nitrogen on electrical conductivity of porous N-dC materials, each porous N-dC was measured with four-probe after pressing the thin carbon film by using uniaxial pressing machine. The thickness of carbon film was in the range between 0.065 and 0.11 mm.

Figure 2.13 shows the electrical conductivity and the N/C content of carbons synthesized with different molar ratios of urea to TA with $NaCl_2/ZnCl_2$ as porogen. It is observed that the electrical conductivity of GT_0_NaZ (control sample synthesized without urea) (about 10 Scm^{-1}) was surpassed by all the N-dC, indicating the electronic properties due to the presence of much higher amount of nitrogen in the carbon structure as proved by elemental analysis. In fact, Figure 2.13 also shows that nitrogen content was gradually increased with increasing molar ratio of urea to TA in precursors blend.

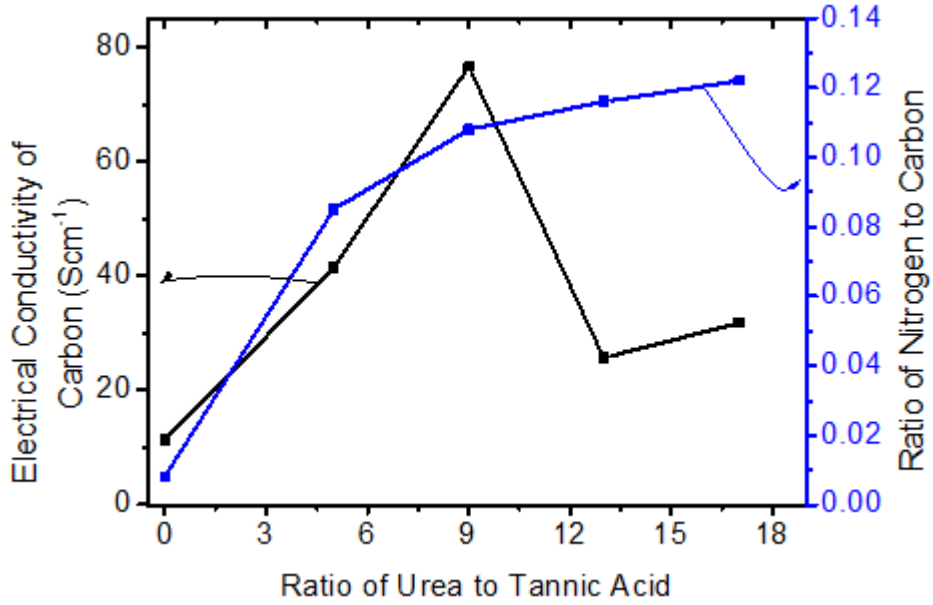

Figure 2.13.Electrical conductivity of N-dC with different ratios of urea to TA with 1: 3 mas ratio of precursors (urea+TA) to $NaCl/ZnCl_2$; GT_0_NaZ, GT_5_NaZ, GT_9_NaZ, GT_13_NaZ, and GT_17_NaZ.

It was shown that the electrical conductivity does not follow an increasing trend with increasing nitrogen content. Electrical conductivity increased with ratio of urea to TA reaching a maximum value of 76 Scm^{-1} for GT_9_NaZ (molar ratio of urea:TA of 9:1). Despite the higher nitrogen content at higher ratio of urea to tannic acid (>9:1), the electrical conductivity of porous N-dC was decreased for GT_13_NaZ and GT_17_NaZ. In order to explain this behaviour, XPS experiments of GT_0_NaZ

(control sample), GT_9_NaZ and GT_17_NaZ were analyzed in detailed. Table 2.5 showed that contribution of different forms of nitrogen associated to N-6, N-Q and N-X functionalities decrease from 33%, 12% and 15% in GT_9_NaZ to 31%, 10% and 14% in GT_17_NaZ. As discussed before, these three nitrogen functionalities are ascribed to the structural nitrogen incorporated into the graphitic backbone (ring of the carbon). Those functionalities can able to lower the energy of the valence band increasing the electron density at the Fermi-level and consequently, the electrical conductivity of the N-dC material [41]. Therefore, the highest conductivity for GT_9_NaZ carbon might be explained by the highest content of these three nitrogen functionalities in GT_9_NaZ. The higher net nitrogen content in GT_17_NaZ is due to the higher contribution of N-5 that includes amine, amide, pyrrolic, or pyridine nitrogen functionalities, some of which (amine and amide) are covalently attached to the carbon surface and barely influence the electrical conductivity of carbons. This result confirms the same trend previously reported in literature [1,4]. Hulicavo *et.al.*, confirmed that the electrical conductivity of melamine templated porous carbon was decreased at high content of doped nitrogen onto the carbon surface [1]. Similarly, recent study also demonstrated that the electrical conductivity was increased in carbon containing up to 8 % of nitrogen, but then decreased in carbon containing higher than 8 % of nitrogen [4].

Figure 2.14 represents the electrical conductivity of carbons synthesized with different mass of $NaCl/ZnCl_2$ eutectic salt (GT_NaZ_X (X=1, 3, 5 and 7)).

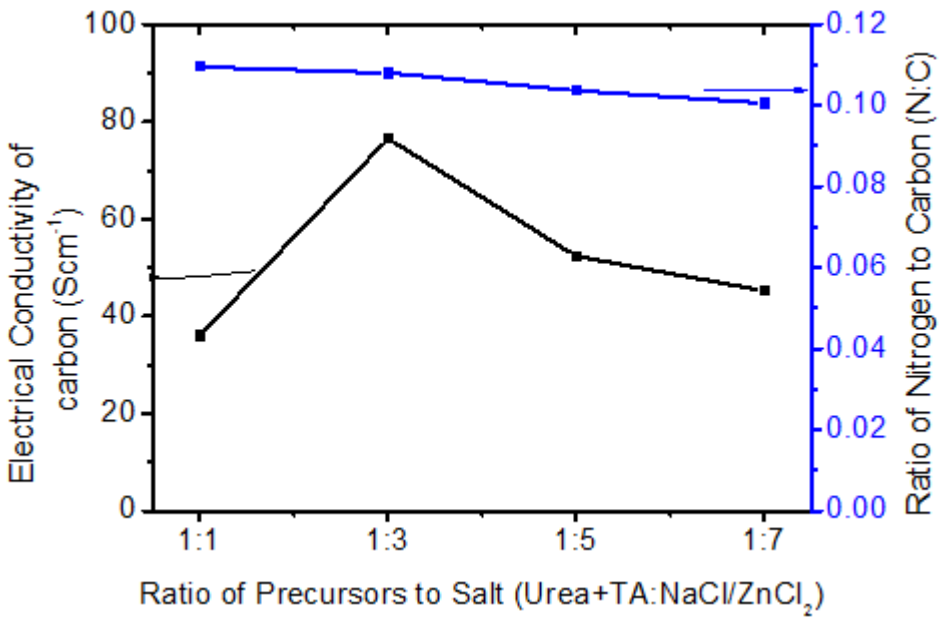

Figure 2.14. Electrical conductivity of N-doped carbons with different ratios of precursors (9:1 ratio of urea to tannic acid) to template salt ($NaCl/ZnCl_2$): GT_NaZ_1, GT_NaZ_3, GT_NaZ_5 and GT_NaZ_7.

In this case, the ratio of urea to TA was kept at 9:1. As expected, the ratio of nitrogen to carbon (N/C) is more or less constant and independent of the content of template salt. The values of electrical conductivities are in a range between 35 to 76 Scm^{-1} and no clear trend was observed. Since the N-dC synthesized with the mixture of 9:1 ratio of urea to TA and 1:3 ratio of precursors (urea+TA) to $NaCl_2/ZnCl_2$ exhibit the higher electrical conductivity, we systematically select this composition for further analysis of electrical conductivity N-dC synthesized with different types of eutectic salts such as $KCl/ZnCl_2$ and $LiCl/ZnCl_2$.

Comparison of electrical conductivities among carbons synthesized with $NaCl/ZnCl_2$, $KCl/ZnCl_2$ and $LiCl/ZnCl_2$ salts are discussed here. Despite the nitrogen content in GT_9_NaZ (8.3 %) was higher than the one in GT_9_LiZ and GT_9_KZ N-dC (6.4-7 %) as shown in Table 2.9, Figure 2.15 reveals that the ratio of nitrogen to carbon (N/C) in the matrix does insignificantly change. However, Figure 2.15 shows that the electrical conductivity of carbons decreases from 76 Scm^{-1} to about 30 Scm^{-1} when $KCl/ZnCl_2$ and $LiCl/ZnCl_2$ salt are used. This decrease is probably due to the different type of nitrogen functionalities incorporated on the carbon that should be corroborated by XPS.

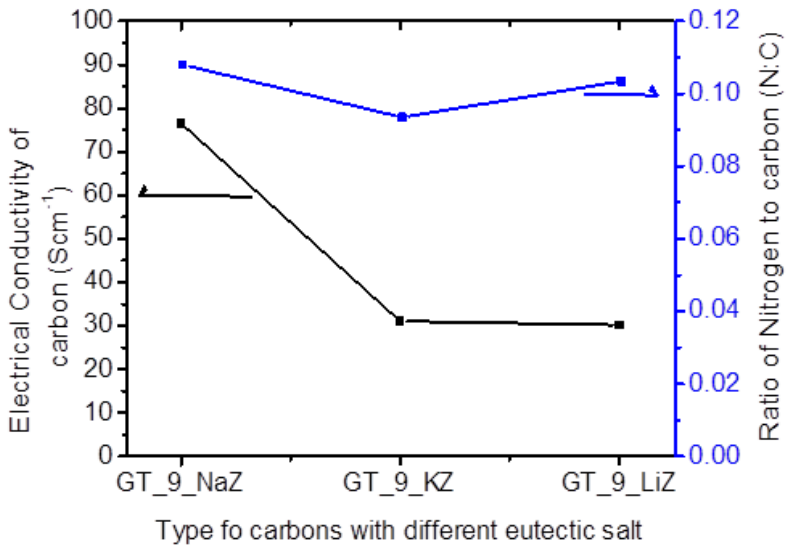

Figure 2.15. Electrical conductivities of carbons with 9:1 ratio of urea to TA and different eutectic salt (1:3 ratios of precursors to eutectic salt).

2.3.2.2. Capacitive Performance of N-dC for Supercapacitors using 1 M H_2SO_4 Aqueous Electrolyte

a) Effect of Molar Ratio of Precursors (Urea:Tannic Acid)

To investigate the properties of porous N-dC as electrode for supercapacitors, we first carried out cyclic voltammetry measurements with a 3-electrode glass cell at different

scan rates using 1 M H_2SO_4 as electrolyte as shown in Figure 2.16. N-dC were synthesized using NaCl/$ZnCl_2$ as porogen at a fixed mass ratio of precursor (urea+TA) to eutectic salt of 1:3 and varying the molar ratio of Urea to TA from 0 to 17.

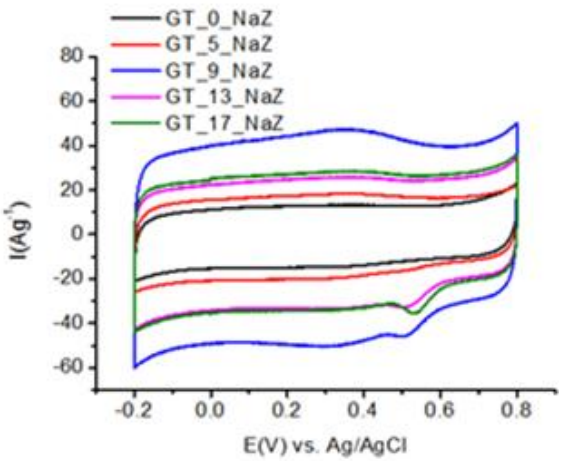

Figure 2.16. Cyclic voltammetry for different porous N-doped carbons at 5 mVs^{-1}

The area under the curves is corresponds to the capacitance stored by the carbon electrodes in supercapacitors. The notable difference in electrochemical surface activity among carbons can be clearly recognized. It was confirmed that, despite the highest specific surface area (S_{BET}~1570 m^2g^{-1}), the non-doped carbon (GT_0_NaZ) exhibits the smallest capacitance performance compared with other nitrogen doped carbons due to the absence of doped nitrogen in the carbon matrix. The higher capacitance of N-doped carbons can be associated to combined effect of electric double layer capacitance and pseudocapacitance contribution of nitrogen and oxygen functionalities present in N-doped carbons [9,15,16]. According to Figure 2.16, the specific capacitance follows this order: GT_9_NaZ > GT_13_NaZ ~ GT_17_NaZ > GT_5_NaZ > GT_0_NaZ that is in good agreement with the textural properties (S_{BET}, S_{DFT} and $S_{eff>0.533nm}$) of those N-doped carbons as shown in Table 2.2.

Interestingly, CV curves of some of the N-dC present a hump at 0.5 V vs. Ag/AgCl reference electrode in the reduction sweep. This hump has been attributed by some authors to the catalytic activity of N-dC towards the oxygen reduction reaction (ORR)[20]. In order to confirm this, CV experiments were performed in acid electrolyte saturated with O_2 and in acid electrolyte saturated with N_2. Figure 2.17 depicts cyclic voltammetry (CV) of one N-dC (GT_9_NaZ) and non- doped carbon (GT_0_NaZ) in presence and absence of nitrogen. CV curves of GT_0_NaZ carbon, which was synthesized without urea, are exactly the same in both O_2 and N_2 saturated electrolytes, and no peak is detected. This indicates the lack of catalytic ability of non-doped carbon towards ORR. As mentioned above, CV of GT_9_NaZ shows a hump at 0.5 V vs.

Ag/AgCl reference electrode in presence of oxygen. This peak completely disappears when oxygen is removed from the electrolyte confirming that the origin of that peak is the catalytic ability of N-doped carbon towards ORR [20]. Although this interesting finding is out of the scope of this thesis, it is worth mentioning here that salt templating method might be a proper facile synthetic method to develop N-dC with catalytic properties.

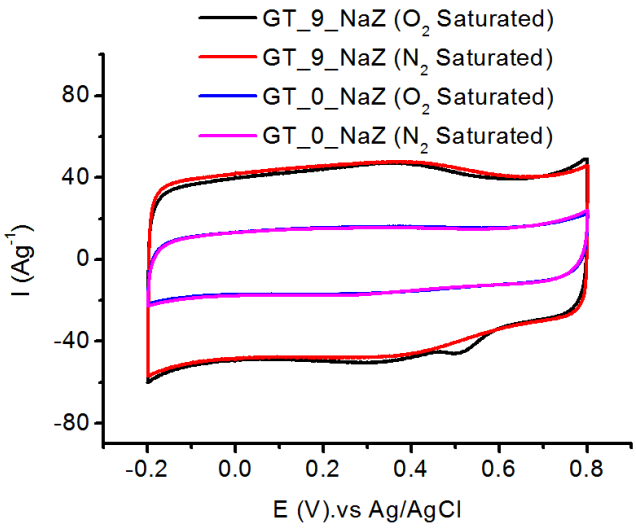

Figure 2.17. CV of N-dC and non-doped carbon in N_2 and O_2 saturated in 1M H_2SO_4 at 5 mV s^{-1}.

After experiments in 3-electrode cells, supercapacitors (SC) were assembled in 2-electrode Swagelok® cells. Cellulose filter paper was soaked with 1 M H_2SO_4, and sandwiched between two carbon electrodes. Figure 2.18 shows the Nyquist plot of SCs assembled with those carbons. The imaginary impedance approaches to zero at high frequencies (200 kHz) and dramatically increases when frequency decreased to 10 mHz, suggesting the storage of double layer capacitance at the interfaces. The maximum equivalent series resistance (ESR) is found to be 1.5 Ω from non-N-dC (GT_0_NaZ), whereas the rest of carbons exhibit ESR values in the same rage from 0.6 to 1.2 Ω. The ESR is composed of intrinsic resistance of the electrodes, interface resistance at the electrolyte-electrodes and at active material-current collector, and resistance of electrolyte. The decrease of internal resistance in N-dC might be attributed to the higher electrical conductivity of N-dC (25-76 Scm^{-1}) compared with GT_0_NaZ (10 Scm^{-1}) as shown in Figure 2.13).

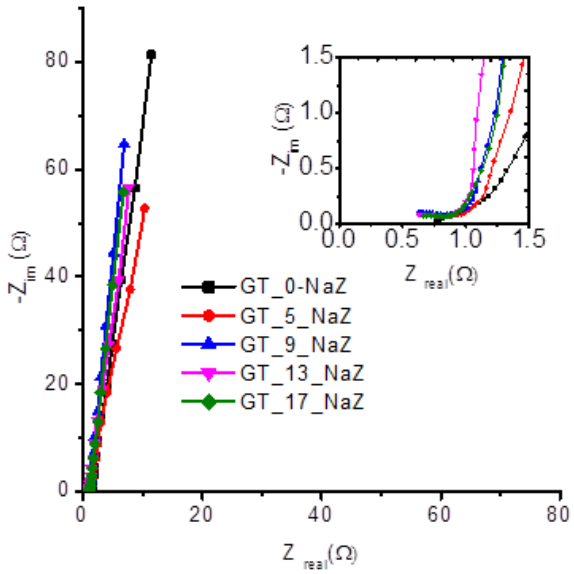

Figure 2.18. Nyquist plot for carbons synthesized with different ratios of urea to TA with NaCl/ZnCl2 porogen salt (1:3 ratio of precursors to NaCl/ZnCl2). Measurements were done with 2-electrode Swagelok cell.

The electrochemical performances of SCs were also characterized by galvanostatic charge-discharge. Figure 2.19a shows the representative CD voltage profiles of different SCs charged from 0 V to 1 V at 5 $mAcm^{-2}$. The discharge curves of SCs revealed a linear slope and very low ohmic drop with clear differences depending on the type of carbon. The specific capacitance of single electrode (C_{am}), the equivalent series resistance (ESR), the specific real energy (E_{real}) and the specific real power (P_{real}) of the SCs were obtained by applying *eqn.2.2-2.6* to the discharge profiles (Figure 2.19b-d). Figure 2.19b indicates that GT_9_NaZ carbon exhibits lower ESR values (0.6 to 1.2 Ω cm2), being in a good agreement with its highest electrical conductivity as explained above. On contrary, non-doped carbon (GT_0_NaZ) presents the highest values of ESR (1.6-4 Ω cm^2) in good agreement with impedance spectroscopy results.

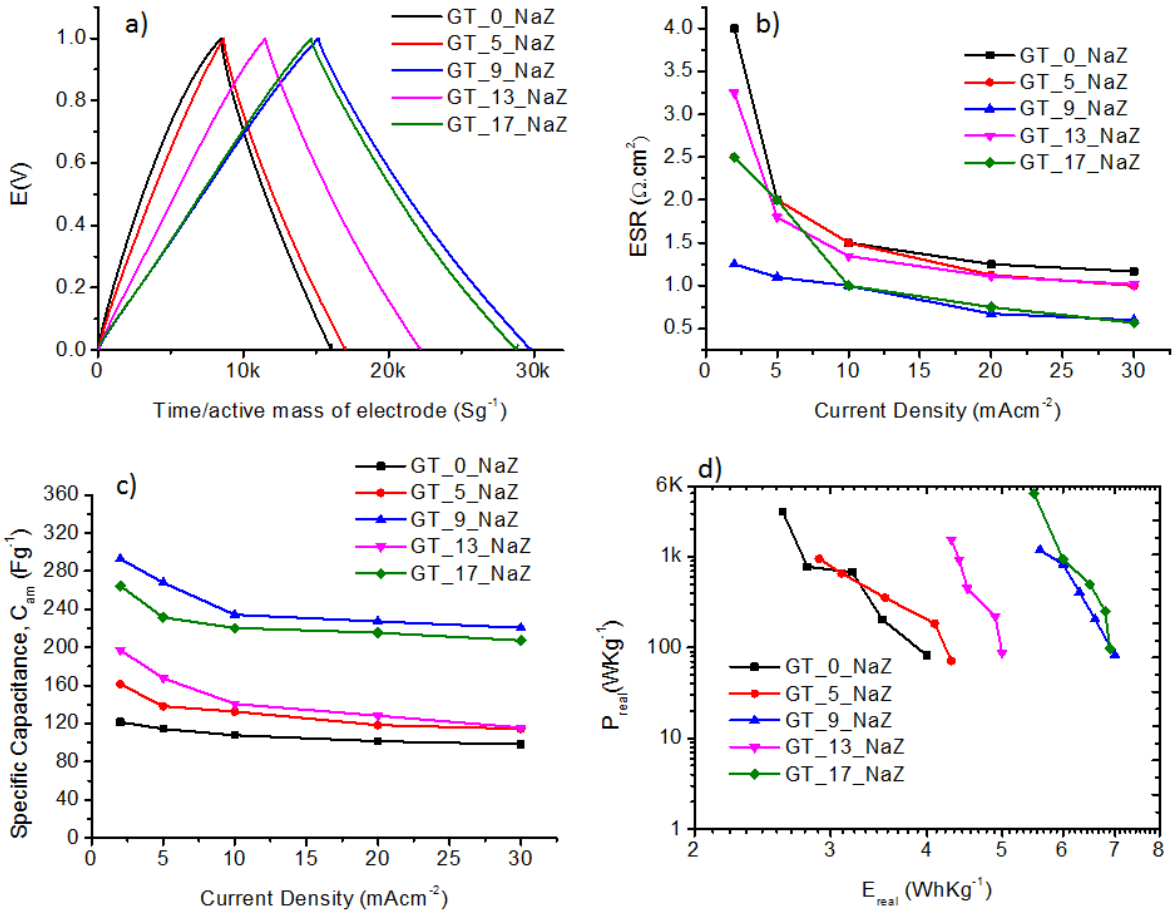

Figure 2.19. Electrochemical performance of carbons synthesized with different ratios of urea to TA with $NaCl/ZnCl_2$ porogen salt (1:3 ratio of precursors to $NaCl/ZnCl_2$) a) CD at 5 $mAcm^{-2}$, b) ESR, d) C_{am} d) Ragone plot at different current densities.

Figure 2.19c indicates the specific capacitance of SCs charged from 0 to 1 V at different current densities. In all cases, N-dCs outperformed non-doped carbon (GT_0_NaZ), confirming the enhancement of electrochemical performance of SCs using N-dC. Those results are consistent with the CV results discussed above and the same trend was observed. The enhancement of capacitance is directly linked to the content of doped nitrogen in the carbon matrix. Presence of nitrogen functionalities might contribute to the enhancement of capacitance in two different ways; first through the additional contribution of pseudocapacitance and second, due to the improved wettability of porous carbon. Wettability of carbon surface by doped nitrogen might be improved due to the increasing number of hydrophilic polar sites that might also promote the accessibility of ions of electrolyte into the pores [7].

In order to investigate how the electrochemical performance is influenced by the textural properties of carbons, specific surface and also "effective surface area" are considered. In these experiments 1 M H_2SO_4 was used as electrolyte and their corresponding adsorbed ions are bivalent sulfate, $SO_4^{2-}(H_2O)_{12}$ and hydronium (H_3O^+)

ions with the corresponding ion size to be 0.533 and 0.42 nm, respectively [14,42]. Two "effective surface areas (S_{eff})" may be calculated, one for each type (size) of ion. However, for simplicity, only the effective surface area related with the bigger ion (Seff>0.533nm) was calculated and used in the discussion (see Table 2.2).

Among N-dC, the GT_9_NaZ carbon outperforms the others due to the synergetic effect of: highest effective surface area ($S_{eff>0.533nm}$ = 949 m^2g^{-1}) which can be easily accessed by negatively and positively charged ions, and the highest value of electrical conductivity (76 Scm^{-1}). The C_{am} of GT_9_NaZ is as high as 295 Fg^{-1} at 2 $mAcm^{-2}$, which is more than twice the capacitance of non-foped carbon electrode (GT_0_NaZ) (120 Fg^{-1} at 2 $mAcm^{-2}$). Other N-dCs (GT_5_NaZ, GT_13_NaZ and GT_17_NaZ) also possess high C_{am} ranging from 160 to 260 Fg^{-1} at 2 $mAcm^{-2}$. The general trend of C_{am} of electrode materials is: GT_9_NaZ > GT_17_NaZ > GT_13_NaZ > GT_5_NaZ > GT_0_NaZ that fits perfectly with the values of S_{DFT} and $S_{eff>0.533\ nm}$ included in Table 2.2. It is important to mention here, that the capacitive performance of some of these N-dC are better than carbon synthesized from coconut shell modified with urea (200 Fg^{-1} at 0.01 Ag^{-1} in 1 M H_2SO_4)[14] and others reported in [1,10]. Figure 2.19d shows the Ragone plot that depicts energy and power densities of SCs in logarithmic scale. Since the voltage is very low in aqueous electrolyte, it is obvious that the energy density is comparatively low compared with non-aqueous electrolytes. Since energy is directly proportional to capacitance ($E=1/2CV^2$) the energy values follow the same trend than those in capacitance for the different carbons: GT_9_NaZ ≥ GT_17_NaZ > GT_13_NaZ > GT_5_NaZ > GT_0_NaZ. GT_9_NaZ and GT_17_NaZ exhibit the highest value of energy density in the range of 6-7 $WhKg^{-1}$ at a power density that goes from 0.1 to 6 $kWkg^{-1}$ depending on the current density.

b) Effect of Mass ratio of precursors (urea+TA) to eutectic salt

The carbons synthesized with different ratios of precursors (urea+TA, with 9:1) to $NaCl/ZnCl_2$ (1:3, 1:5, and 1:7) were tested in order to evaluate the influence of template salt on electrochemical performance of supercapacitors. Among those N-dCs, GT_NaZ_3 outperforms other N-dC which is associated to the combined synergetic effect of its highest nitrogen content and electrical conductivity as well as high $S_{eff>0.533nm}$ as discussed before. According to Figure 2.20, that shows the CV in 3-electrode cell, the C_{am} follows the order: GT_NaZ_3 > GT_NaZ_5 > GT_NaZ_7. Since the textural properties (S_{BET}, S_{DFT} and $S_{eff>0.533nm}$) of these carbons are (see Table 2.6) present insignificant difference, the better performance of GT_NaZ_3 might be attributed only to its highest electrical conductivity.

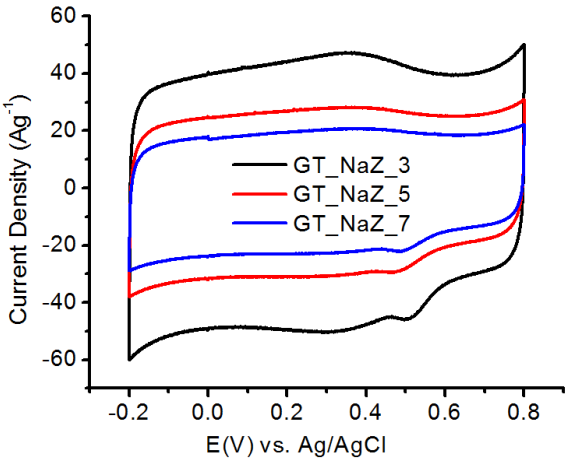

Figure 2.20. Cyclic voltammetry for different porous N-doped carbons at 5 mVs^{-1}

After experiments in 3-electrode cells, supercapacitors (SC) were assembled in 2-electrode Swagelok® cells. The impedance spectroscopy results in Figure 2.21 showed that the ESR value of each carbon electrode was slightly increased with the ratio of eutectic salt used. GT_NaZ_7 carbon has the highest ESR which is in good agreement with the lowest value of conductivity (σ~45 Scm^{-1})

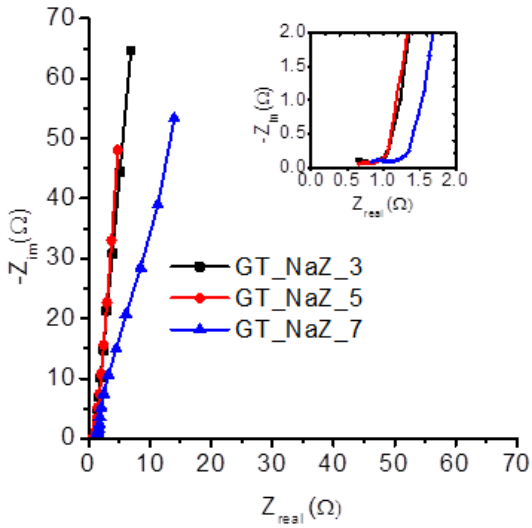

Figure 2.21. Nyquist plot for carbons synthesized with 9:1 ratios of urea to TA and different molar concentrations of $NaCl/ZnCl_2$ template salt.

Figure 2.22 (a-d) represents the charge-discharge electrochemical performance of GT_NaZ_3, GT_NaZ_5, and GT_NaZ_7 N-dC electrodes. Figure 2.22a shows the representative charge-discharge profiles of carbons recorded with potential range from 0 to 1V at 5 mA cm^{-2} in 1 M H_2SO_4 electrolyte. It can be clearly observed that the symmetrical CD profiles reflect good capacitance performance with very low ohmic ranging from 0.01 to 0.017 Ω drop in all tested carbons. Furthermore, Figure 2.22b

shows constantly increasing values of ESR with ratio of precursors to template salt, being in good agreement with Nyquist plot and values of electrical conductivity of carbons (see Fig Figure 2.21 and Figure 2.14).

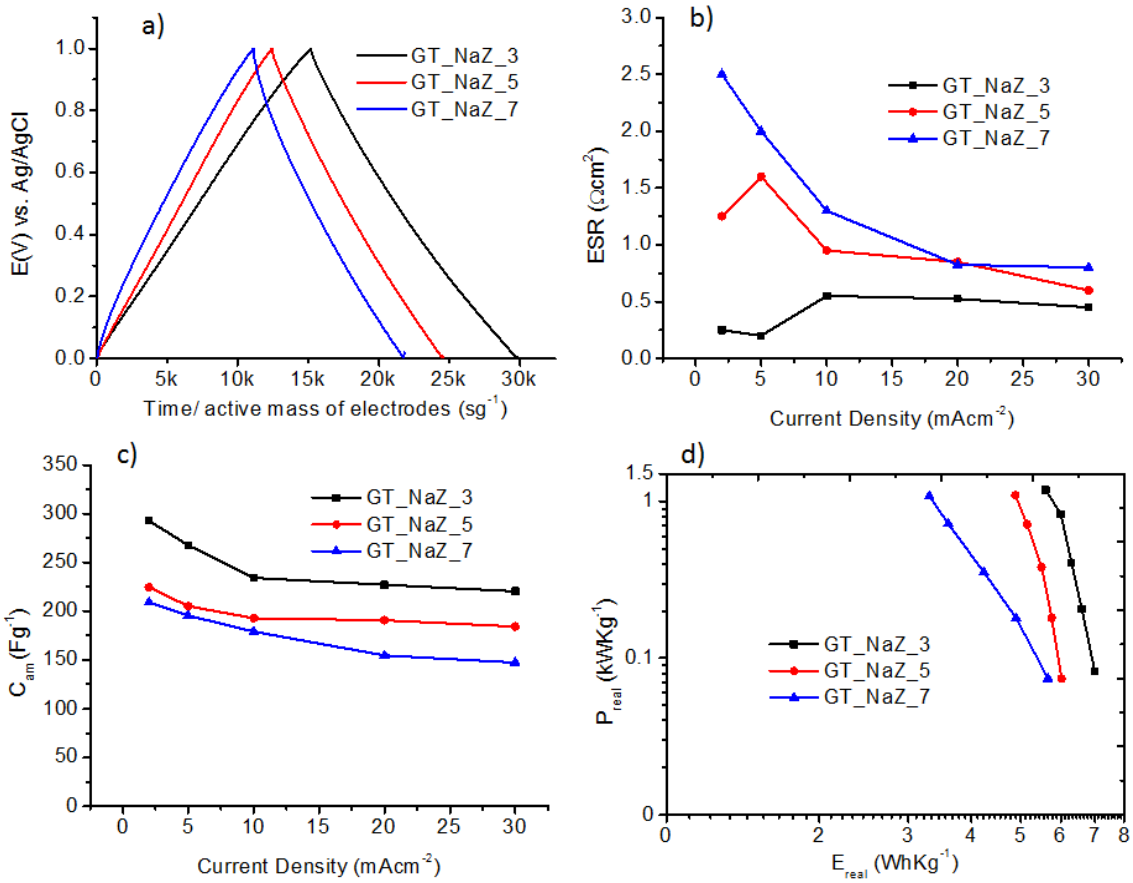

Figure 2.22. Electrochemical performance of carbons synthesized with different ratios of precursors (urea:TA= 9:1) to NaCl/$ZnCl_2$ porogen salt a) CD at 5 mAcm^{-2}, b) ESR, d) C_{am} d) Ragone plot at different current densities.

Figure 2.22c depicts the C_{am} of GT_NaZ_3, GT_NaZ_5 and GT_NaZ_7 at different current densities. The trend in capacitance is the same as in CV: GT_NaZ_3 > GT_NaZ_5 > GT_NaZ_7. Since textural properties are more or less the same (see Figure 2.7b) these differences might be significantly attributed to the differences in electrical conductivity (see Figure 2.14). Figure 2.22d shows the logarithm representation of real energy (E_{real}) vs. real power (P_{real}) densities of as-synthesized carbons. Power densities are similar for all the carbons. However, clear differences can be observed in energy values that follows the same trend as for capacitance values: GT_NaZ_3 > GT_NaZ_5 > GT_NaZ_7. It was shown that the electrochemical performance is not enhanced by increasing the ratio of salt template in the mixture. In this case, the 1:3 ratio of precursors (urea and TA) to eutectic salt (NaCl/$ZnCl_2$) was found to be the optimum ratio.

c) Effect of the Type of Eutectic Salt

Here the influence of different eutectic salts ($NaCl/ZnCl_2$, $LiCl/ZnCl_2$ and $KCl/ZnCl_2$) on the electrochemical performance of N-dC is evaluated. The 9:1 ratio of urea to tannic acid and the 1:3 ratios of precursors (urea+TA) to $NaCl/ZnCl_2$, were found to be the optimum ratios between precursors and $NaCl/ZnCl_2$. In this section, the best performing carbon (GT_9_NaZ) will be compared with carbons synthesized with $LiCl/ZnCl_2$ or $KCl/ZnCl_2$. In this case, the influence of different type of template eutectic salts on the electrochemical performance is investigated. (Please note that GT_9_NaZ and GT_NaZ_3 are the same carbons as they were synthesized with the same compositions of precursors and eutectic salt)

According to Figure 2.23, that shows the CV in 3-electrode cell, the trend of C_{am} of those N-dC follows as GT_NaZ_3 > GT_NaZ_5 > GT_NaZ_7, being in a good agreement with the nitrogen content (see Table 2.9) and the electrical conductivity (see Figure 2.15) of those carbons

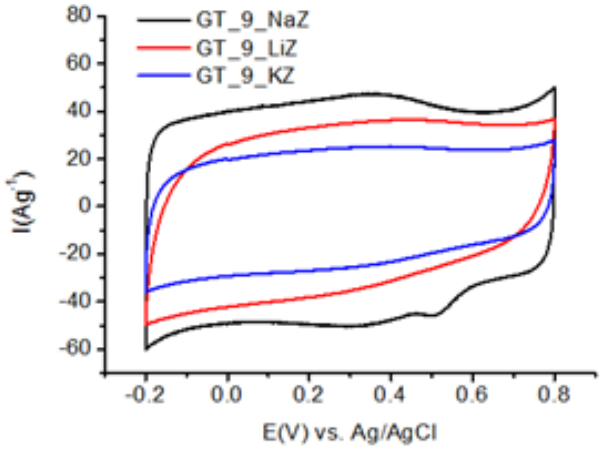

Figure 2.23. Cyclic voltammetry for different porous N-dC at 5 mVs^{-1}

After experiments in 3-electrode cells, supercapacitors (SC) were assembled in 2-electrode Swagelok® cells. Figure 2.24(a-d) shows the comparative electrochemical performance of SC assembled with $NaCl/ZnCl_2$, $LiCl/ZnCl_2$ or $KCl/ZnCl_2$, respectively.

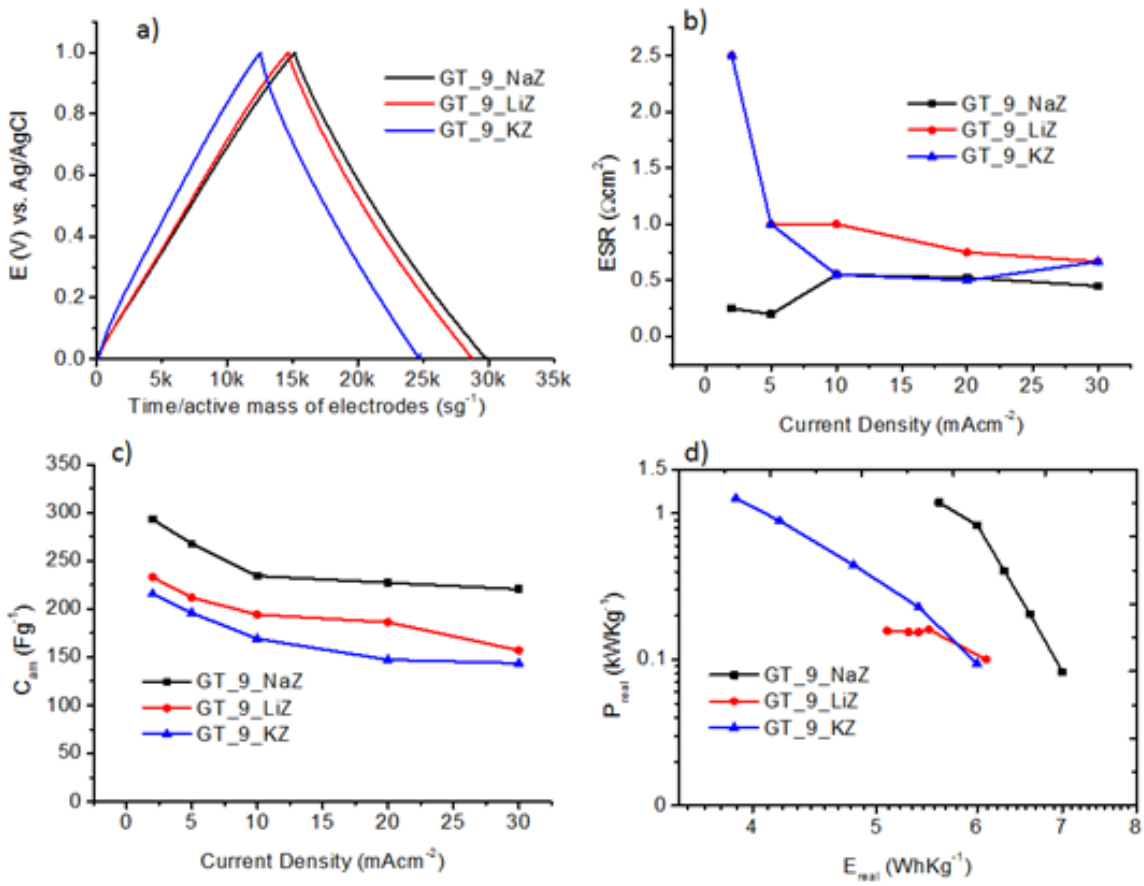

Figure 2.24. Electrochemical performance of SCs based on N-dCs synthesized with different types of eutectice salts ($NaCl/ZnCl_2$, $LiCl/ZnCl_2$ and $KCl/ZnCl_2$) a) charge-discharge profile at 5 $mAcm^{-2}$, b) ESR c) C_{am} and d) Ragone plot at different current densities.

Figure 2.24a shows the representative charge-discharge profiles at 5 $mAcm^{-2}$. All carbons exhibit symmetrical linear curves indicating the storage of double layer capacitance. Despite very low ohmic drop for each carbon electrode, there is still difference among different N-dC attributed to the different nature of template salts which determines porosity of carbons during thermal treatment. Figure 2.24b shows the following order of ESR: GT_9_LiZ > GT_9_KZ > GT_9_NaZ with values ranging 0.25 to 2.5 Ωcm^{-2}. Figure 2.24c shows the C_{am} of the GT_9_NaZ, GT_9_KZ, and GT_9_LiZ at different current densities with values in the range of 200-295 Fg^{-1}. Although textural properties of GT_9_LiZ are slightly better than for GT_9_NaZ the latter carbon presented the best performance. This is probably due to the highest electrical conductivity of this carbon in comparison with the other two (see Figure 2.15). GT_9_KZ presents the poorest performance probably attributed to the lowest specific surface area (S_{BET}, S_{DFT} and $S_{eff>0.533\ nm}$), the lowest nitrogen content (Table 2.9) and electrical conductivity (see Figure 2.15). Figure 2.24d represents the Ragone plot in a

logarithmic scale of real energy vs. real power densities. The real energy density of GT_9_NaZ carbon is found to be the best compared with other N-dCs. All in all, the electrochemical results show that the carbons synthesized with $NaCl/ZnCl_2$ show the best performance in all aspects. In general, it was shown in previous section that the physical properties of nitrogen doped carbon are affected by the ratio of urea to tannic acid, the ratio of precursors to template salt and the nature of template salts. This in turn, affects the electrochemical performance of supercapacitors in aqueous electrolytes, as discussed above.

2.3.2.3. Capacitive Performance of N-dC in Supercapacitors using Ionic Liquid Electrolyte ($PYR_{14}FSI$)

To complete the investigation, herein, some porous N-dC were selected and electrochemically characterized in ionic liquids (ILs) based supercapacitors. The CV characterizations were carried out using 3-electrode T-shaped Swagelok cell over a potential range -1.75 V to +1.75 V in 1-butyl-1-methylpyrrolidinium bis(fluorosulfonyl) imide ($PYR_{14}FSI$) and at different scan rates: 100, 50, 20, 10, 5, and 2 mVs^{-1}. In this configuration, porous N-dC were used as working electrode, PICA carbons with double mass as counter electrode and silver wire as pseudo reference. The supercapacitor prototypes were assembled in 2-electrode Swagelok cell as explained in previous section. These 2 and 3 electrode configurations in Swagelok cell are very convenient for testing materials in expensive and air/water sensitive electrolytes since it makes use of small amount of electrolyte and could be assembled inside the glove box. After assembling, the Swagelok cell can be hermetically closed and taken out the glove box for ordinary electrochemical characterization avoiding electrolyte contamination during measurement.

a) Effect of Molar Ratio of Precursors (Urea:TA)

To evaluate the performance of novel N-dC electrodes synthesized with different ratios of urea to TA were selected. The selected N-dC were GT_0_NaZ, GT_9_NaZ, and GT_17_NaZ, which were systematically synthesized with molar ratio of urea to TA; 0:1, 9:1 and 17:1, respectively. The representative CV in 3-electrode electrochemical cell at 5 mVs^{-1} and the scan rate dependent specific capacitance for these three N-dC electrodes are shown in Figure 2.25.

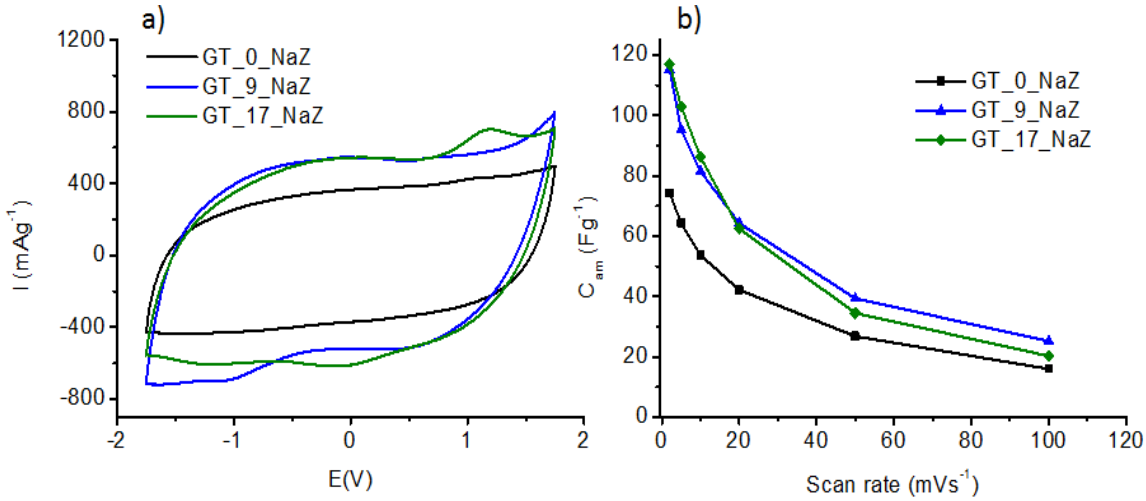

Figure 2.25. a) Cyclic voltammetry for different porous N-dCs at 5 mVs^{-1} b) specific capacitance at different scan rates.

Coulombic efficiency of the system in all scan rates is higher than 95 % confirming the reversibility of the energy storage process. Similarly to results in aqueous electrolyte, the CV curves in IL also indicate that N-dCs (GT_9_NaZ and GT_17_NaZ) outperform the carbon synthesized non-doped carbon (GT_0_NaZ). In addition, Figure 2.25a exhibits nearly rectangular shape with humps, indicating that the N-dC electrodes contribute pseudocapacitance attributed to the interaction between nitrogen functionalities and ions of electrolyte [43,44]. Figure 2.25b displays the specific capacitance (C_{am}) of different porous N-dCs electrodes at different scan rates. The C_{am} fades with increasing scan rate in all N-dC electrodes, demonstrating the higher ion diffusion limitation at higher scan rates. In all cases, N-dC electrodes stored higher C_{am} compared with non-doped carbon electrode (GT_0_NaZ) in $PYR_{14}FSI$ electrolyte confirming the dependence of capacitance with the content of doped nitrogen in the carbon. In order to investigate how the electrochemical performance is influenced by the textural properties of carbons, "effective surface area" of each carbon is considered. $S_{eff>1.1nm}$ was calculated and used in the discussion (seeTable 2.2). Note, despite the highest effective specific surface area ($S_{eff>1.1\,nm}$ = 600 m^2g^{-1}) which can be accessed by the big PYR_{14} cation (1.1 nm diameter [45]), the GT_0_NaZ exhibits the lowest capacitance compared to GT_9_NaZ with $S_{eff>1.1\,nm}$ = 517 m^2g^{-1} or GT_17_NaZ with $S_{eff>1.1\,nm}$ = 434 m^2g^{-1} (see Table 2.2). Exactly the same trend was observed in aqueous electrolyte (1 M H_2SO_4). This might be probably due to the beneficial effect of N-doping to electrical conductivity and especially, to the pseudocapacitive contribution that result in N-doped carbons with better capacitances than non-doped carbon. Small difference in capacitance between GT_9_NaZ and GT_17_NaZ was also observed especially at higher scan rates. It turns out that the GT_9_NaZ carbon electrodes with

higher $S_{eff\ >1.1\ nm}$ = 517 m^2g^{-1} and $V_{eff\ >1.1\ nm}$ = 0.72 m^3g^{-1} outperforms the GT_17_NaZ ($S_{eff\ >1.1\ nm}$ = 434 m^2g^{-1} and $V_{eff\ >1.1\ nm}$ =0.59 m^3g^{-1}) at higher scan rates as shown in Figure 2.25b. Nevertheless, the maximum capacitance of the nitrogen doped electrodes in $PYR_{14}FSI$ was found to be 119 Fg^{-1} at 2 mVs^{-1} as shown in Figure 2.25b.

After experiments in 3-electrode cells, supercapacitors (SCs) were assembled in 2-electrode Swagelok® cells. Figure 2.26 represents the frequency dependence impedance spectroscopy of carbons synthesized with different molar ratio of urea to TA. The capacitance behaviour of N-dC is confirmed by the steep rising line parallel to imaginary impedance ($-Z_{im}$) at low frequencies.

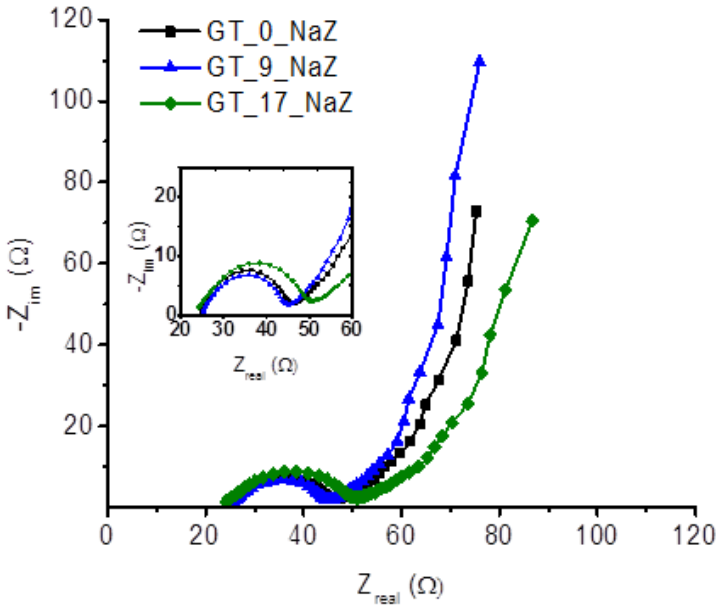

Figure 2.26. Nyquist plot for SCs based on carbons synthesized with different ratios of urea to TA with NaCl/ZnCl2 porogen salt (1:3 ratio of precursors to NaCl/ZnCl2).

Equivalent series resistance (ESR) for different SCs are in the range of about 45-50 Ω with slightly higher ESR value for GT_17_NaZ, probably due to the lower electrical conductivity of this carbon (see Table 2.3). Higher ESR values in this electrolyte in comparison with those in aqueous electrolyte (see Figure 2.19) is attributed to the much higher viscosity and bulk resistance of $PYR_{14}FSI$ in comparison with 1 MH_2SO_4 aqueous electrolyte.

The electrochemical performance of SCs was also characterized by galvanostatic charge-discharge. Figure 2.27a represents CD voltage profiles for different symmetric SCs assembled with different N-dC electrodes charged from 0 to 3.5 V at 5 $mAcm^{-2}$. All CD curves exhibited triangular-shaped profile, indicating the typical double layer capacitance behaviour with coulombic efficiency greater than 95 %. The CD profiles display different ohmic drop (IR) when the current changes from positive (charging mode) to negative (discharging mode). This has an effect on Figure 2.27b that shows

the equivalent series resistance (ESR) for the three SCs with different N-dC electrodes. The increasing order of ESR is: GT_9_NaZ < GT_17_NaZ < GT_0_NaZ that is in good agreement with the electrical conductivity of carbons as shown in Figure 2.13.

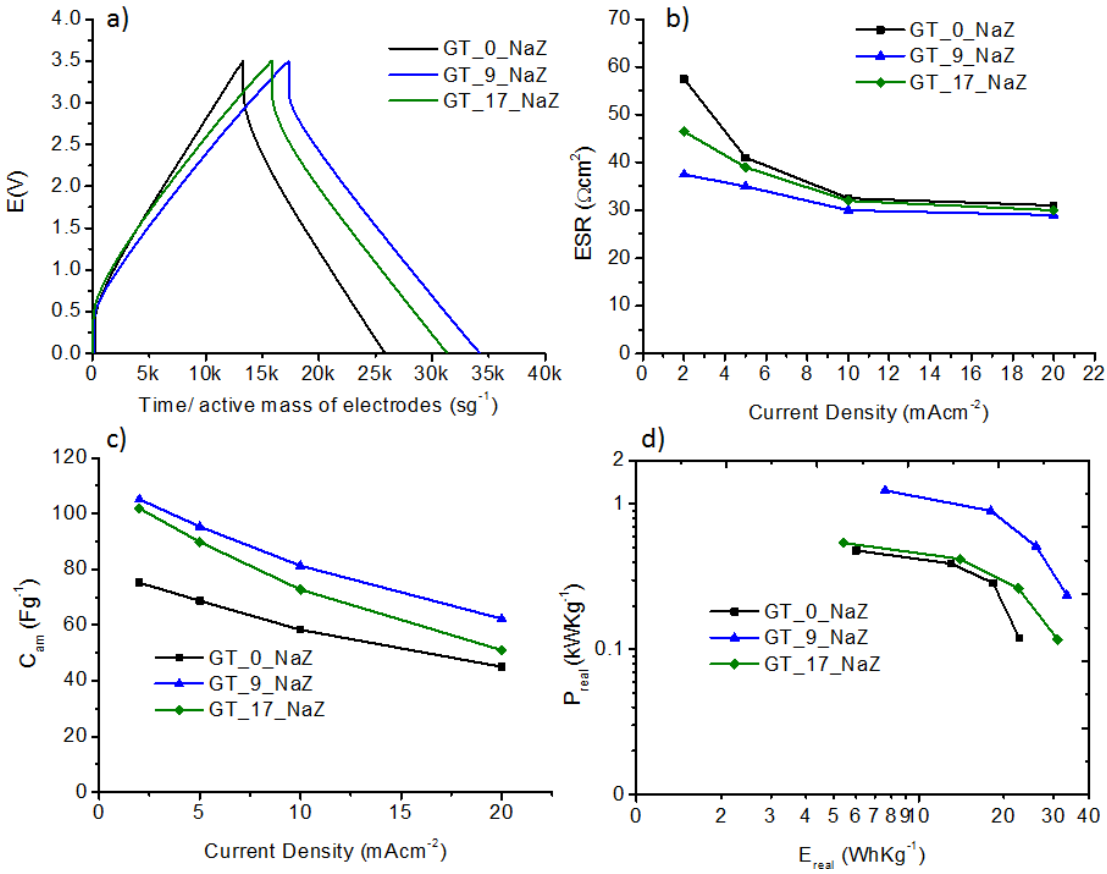

Figure 2.27 .Electrochemical performance of SCs assembled with N-dC synthesized with different ratios of urea to TA with NaCl/$ZnCl_2$ porogen salt in $PYR_{14}FSI$ as electrolyte a) CD at 5 mAcm^{-2}, b) ESR, c) C_{am} d) Ragone plot at different current densities.

Figure 2.27c displays the specific capacitance (C_{am}) of different porous N-dC electrodes calculated from CD voltage profiles at different current densities. The C_{am} fades with increasing current density in all cases due to the insufficient time for the ions to diffuse into the pores of carbon electrodes and increases polarization resistance [3]. In all cases, N-dC outperform non- doed carbon (GT_0_NaZ), confirming the enhancement of electrochemical performance of SCs using N-dCs. Those results are consistent with the CV results discussed above and the same trend is observed also in aqueous electrolyte in previous sections: GT_9_NaZ > GT_17_NaZ > GT_0_NaZ.

Figure 2.27d represents the Ragone plot for SCs using $PYR_{14}FSI$ electrolyte and different carbons. Since energy is directly proportional to capacitance, the energy values follow the same trend as those for capacitance showing that N-dC electrodes

exhibit higher real energy and power densities than non-doped carbon electrode. It is obvious that the power density of N-dCs in aqueous electrolytes is higher (see Figure 2.19d) compared with the power in $PYR_{14}FSI$. But the real energy of N-dC is 6 times higher than the energy desnity of N-dC in aqueous electrolytes as shown in Figure 2.27d. The maximum real energy density stored by GT_9_NaZ is about 33 $Whkg^{-1}$ at 2 $mAcm^{-2}$. This energy value would correspond to a specific real energy of 10 $WhKg^{-1}$ in a commercial style (package-device) which is typically containing 30 % of active materials. This real energy value is twice higher than the energy value in commercial carbon/carbon based supercapacitors, which normally exhibit the energy density and power density of 4-5 $Whkg^{-1}$ and 0.156-1.8 $kWkg^{-1}$, respectively [46]. This is due to combination of appropriate values of capacitance and very high values of voltage (3.5 V) in comparison with 1 V or 2.5-2.7 V maximum voltage used for commercial SCs using aqueous or organic electrolytes, respectively. It is worth noting that the real energy density is still as high as 8 $Whkg^{-1}$ corresponding to the highest specific power density about 1.4 $kWkg^{-1}$ at higher current density, 20 $mAcm^{-2}$.

b) Effect of Mass ratio of precursors (urea+TA) to eutectic salt

To investigate the influence of concentration of eutectic salt ($NaCl/ZnCl_2$) with fixed ratio of urea to TA (9:1), three porous carbon electrodes with increasing molar concentration of template salt ($NaCl/ZnCl_2$) (GT_NaZ_3, GT_NaZ_5 and GT_NaZ_7) were also investigated. Figure 2.28a shows representative CV curves of three different carbons performed in 3-electrode T-shaped Swagelok cells using $PYR_{14}FSI$ electrolyte. All N-dC electrodes display nearly rectangular CV shape with small humps, indicating the combination effect of double layer and pseudocapacitive behavior of the materials. No significant difference in specific capacitance of the GT_3_NaZ and GT_7_NaZ N-dC electrodes was observed. This might be due to the same range of effective specific surface area accessible by PYR_{14} cation ($S_{eff>1.1\,nm}$ = 517 -530 m^2g^{-1}) (see Table 2.6). The C_{am} of at different scan rates can be seen in Figure 2.28b, showing decreasing of capacitance with increasing of scan rate in all cases. It implies the insufficient time for ions to diffuse into the pores of electrodes at higher scan rate, thereby increasing mass diffusion resistance which results in less capacitance. The maximum C_{am} stored by GT_NaZ_3 and GT_NaZ_7 is about 119 Fg^{-1} while the GT_NaZ_5 stored about 90 Fg^{-1} at 2 mVs^{-1}.

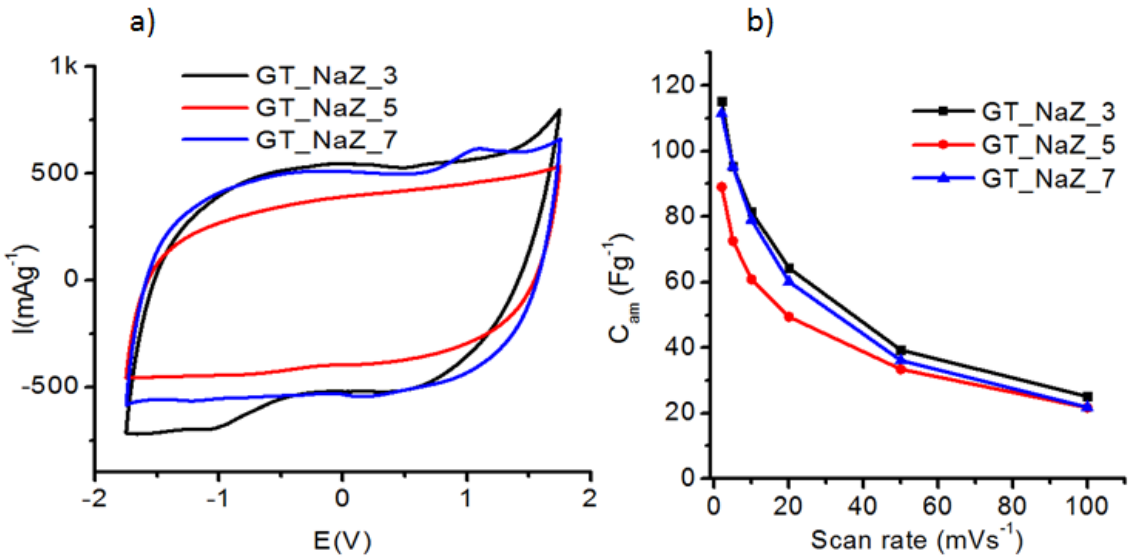

Figure 2.28. a) Cyclic voltammetry for different porous N-doped carbons at 5 mVs^{-1} b) specific capacitance at different scan rates.

The influence of amount of eutectic salt on capacitive performance in $PYR_{14}FSI$ electrolyte was also investigated in supercapacitors using 2-electrode Swagelok set-up. Figure 2.29 shows the Nyquist plot for supercapacitors using porous N-dC as electrodes and $PYR_{14}FSI$ as electrolyte.

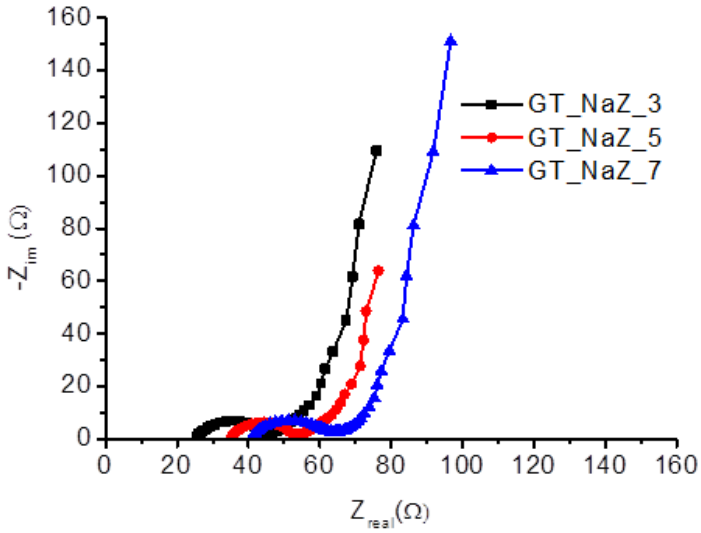

Figure 2.29. Nyquist plot for SCs based on different porous N-doped carbon electrodes (GT_NaZ_3, GT_NaZ_5 and GT_NaZ_7).

This frequency dependence plot featured a vertical line parallel to imaginary impedance, ascribing capacitance behaviour of porous N-dC electrodes. The general trend of ESR values in SCs with different porous N-doped carbons is: GT_NaZ_3 (45 Ω) < GT_NaZ_5 (55 Ω) < GT_NaZ_7 (65 Ω). This trend is in good agreement with the

values of electrical conductivity exhibited for GT_NaZ_3, GT_NaZ_5, and GT_NaZ_7 about 76 Scm^{-1}, 53 Scm^{-1}, and 45 Scm^{-1}, respectively (see Figure 2.14).

The electrochemical performance of SCs was also characterized by galvanostatic charge-discharge experiments. Figure 2.30a shows the representative charge-discharge voltage profile of the three different supercapacitors at 5 $mAcm^{-2}$.

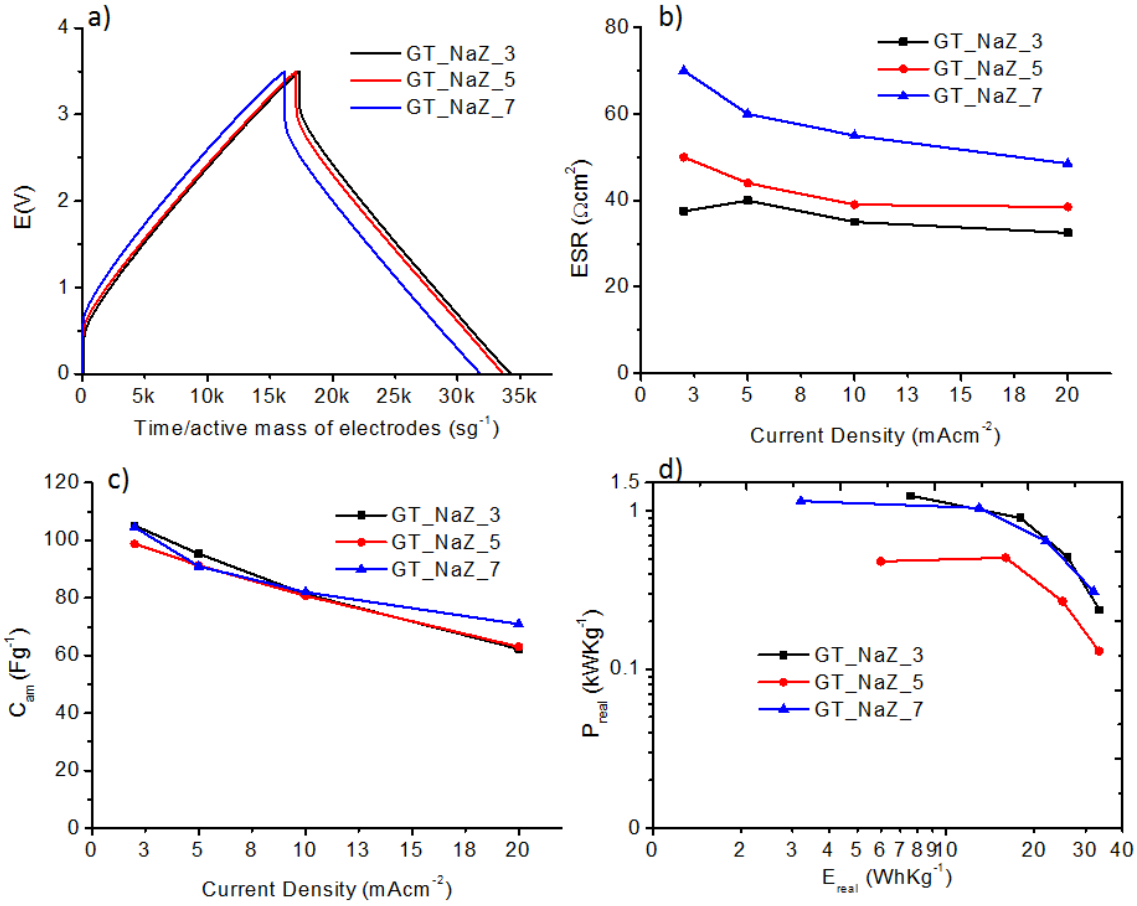

Figure 2.30. Electrochemical performance of SCs assembled with N-dC in $PYR_{14}FSI$ as electrolyte a) CD at 5 $mAcm^{-2}$, b) ESR, c) C_{am} d) Ragone plot at different current densities.

It was realized that the ohmic drop of SCs increased as follow: GT_NaZ_3 (0.4 V) ≤ GT_NaZ_5 (0.45 V) < GT_NaZ_7 (0.6 V). This is clearly reflected in the Figure 2.30b that depicts the ESR values that vary from 40 Ωcm^2 for GT_NaZ_3 to 50 Ωcm^2 for GT_NaZ_5 and to 70 Ωcm^2 for GT_NaZ_7 at 2 $mAcm^{-2}$. Those values are in good agreement with Nyquist plot and might be attributed to the different electrical conductivity of the 3 N-doped carbons. Figure 2.30c shows the specific capacitance of different N-dC electrodes at different current densities. It was initially intended to compare the capacitive performance of N-dC electrodes synthesized with different ratios of template salt ($NaCl/ZnCl_2$). However, no significant difference in specific capacitance of N-dC was observed, probably due to their similar textural properties (see

overlapping isotherms in Figure 2.10 and Table 2.6). The specific capacitances for these carbons varied from 110 Fg^{-1} at 2 $mAcm^{-2}$ to 70 Fg^{-1} at 20 $mAcm^{-2}$. In order to complete CD characterizations, the real energy and real power densities are also estimated on the basis of charge-discharge voltage profiles over the range of current densities from 2 to 20 $mAcm^{-2}$. Figure 2.30d depicts the Ragone plot which demonstrates that the maximum real energy density was as high as 33 $Whkg^{-1}$ at 2 $mAcm^{-2}$. The increasing trend of real energy density is as follow: GT_NaZ_7 < GT_NaZ_5 < GT_NaZ_3. A significant decrease in power density is observed for GT_NaZ_5 but this behavior cannot be explained according to textural properties or conductivity values so the possible reasons are still under discussion.

c) Effect of the Type of Eutectic Salt

Furthermore, in order to evaluate the influence of the nature of eutectic salt on electrochemical properties, GT_9_NaZ, GT_9_KZ, and GT_9_LiZ, synthesized with $NaCl/ZnCl_2$, $KCl/ZnCl_2$ and $LiCl/ZnCl_2$ were electrochemically characterized in $PYR_{14}FSI$. Figure 2.31a displays the rectangular-like shape curves, confirming the capacitive behaviour of the carbons.

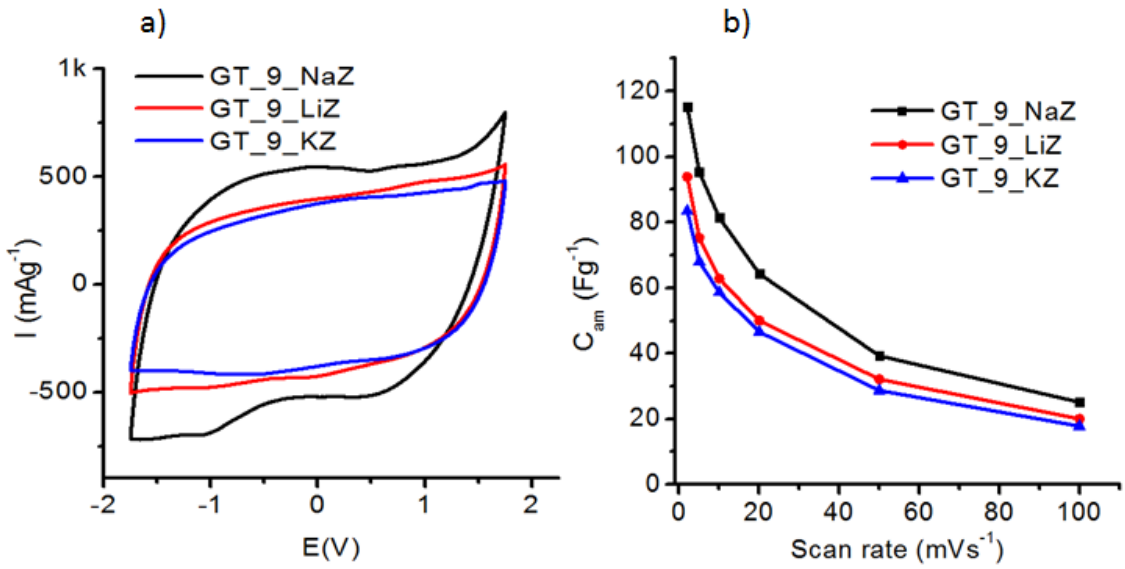

Figure 2.31. a) Cyclic voltammetry for different porous N-doped carbons at 5 mVs^{-1} b) specific capacitance at different scan rates.

In addition, CV of GT_9_NaZ exhibited a significant hump, indicating the pseudocapacitance contribution due to its high content of doped nitrogen (8.3 %) compared with the other carbons, 7 % N for GT_9_LiZ and 6.43 % N for GT_9_KZ, which was affected by the nature of eutectic salts. Figure 2.31b represents the specific capacitance for different N-dC electrodes calculated from CV curves at different scan

rates. The GT_9_NaZ carbon electrode exhibits the maximum specific capacitance of 119 Fg^{-1}, whereas the GT_9_LiZ and GT_9_KZ carbons stored the maximum capacitance about 93 Fg^{-1} and 82 Fg^{-1}, respectively at 2 mVs^{-1}. This trend is similar to the one found in SCs based on the same carbons in aqueous electrolyte (see Figure 2.23). As explained in the section dedicated to aqueous electrolyte, GT_9_NaZ presents the best performance despite having slightly poorer textural properties ($S_{eff>1.1nm}$=517 m^2g^{-1} vs 583 m^2g^{-1} for GT_9_LiZ). This was attributed to the higher electrical conductivity of GT_9_NaZ in comparison with the other two carbons (see Figure 2.15) although other combined effects such as the nature of the nitrogen functionalities and the wettability of the carbons might also affect.

After experiments in 3-electrode cells, supercapacitors (SC) were assembled in 2-electrode Swagelok® cells. Figure 2.32 illustrates the Nyquist plot of three different porous nitrogen doped carbon electrodes in $PYR_{14}FSI$ electrolyte. Similarly, the appearance of vertical line of the plot parallel to imaginary impedance ascribes the capacitance behavior of each carbon electrodes. The lowest ESR value (~45 Ω) was obtained for SCs with GT_9_NaZ carbon which exhibited the highest electrical conductivity (76 Scm^{-1}). GT_9_LiZ and GT_9_KZ with lower values of conductivity (~30 Scm^{-1}) result in SCs with higher values of ESR.

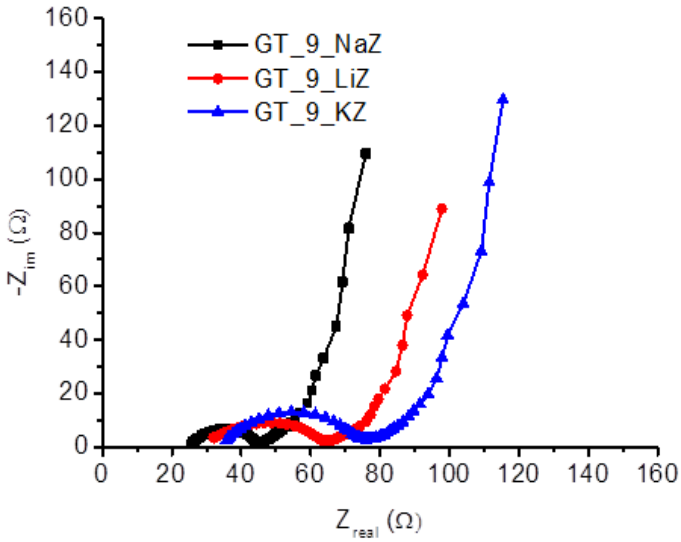

Figure 2.32. Nyquist plot for SCs based on carbons synthesized with different eutectic salts (GT_9_NaZ, GT_9_LiZ and GT_9_KZ).

Figure 2.33a shows the representative charge-discharge voltage profiles of SCs based on GT_9_NaZ, GT_9_LiZ and GT_9_KZ porous N-dC electrodes at 5 $mAcm^{-2}$. As anticipated by impedance spectroscopy, the ohmic drop of GT_9_NaZ carbon electrode is lower (~0.4 V) than the ohmic drop of GT_9_LiZ and GT_9_KZ carbons

(~0.8 V). This is evidenced in Figure 2.33b that represents ESR of each nitrogen doped carbon electrode at different current densities. The ESR values of GT_9_NaZ carbon electrode were relatively lower (35-40 Ωcm²) compared with GT_9_LiZ and GT_9_KZ carbon electrodes (50-70 Ωcm² at current range of 2-20 mAcm⁻²). This demonstrates that the internal resistance of SCs significantly influenced by the electrical conductivity of the N-doped carbons that depend on several factors including the type of template salt.

Figure 2.33c shows that The GT_9_NaZ exhibits the maximum specific capacitance ca. 110 and 60 Fg^{-1} at 2 and 20 $mAcm^{-2}$, respectively. Regarding to the type of eutectic salts, the increasing order of specific capacitance is: GT_9_KZ < GT_9_LiZ < GT_9_NaZ as shown in Figure 2.33c.

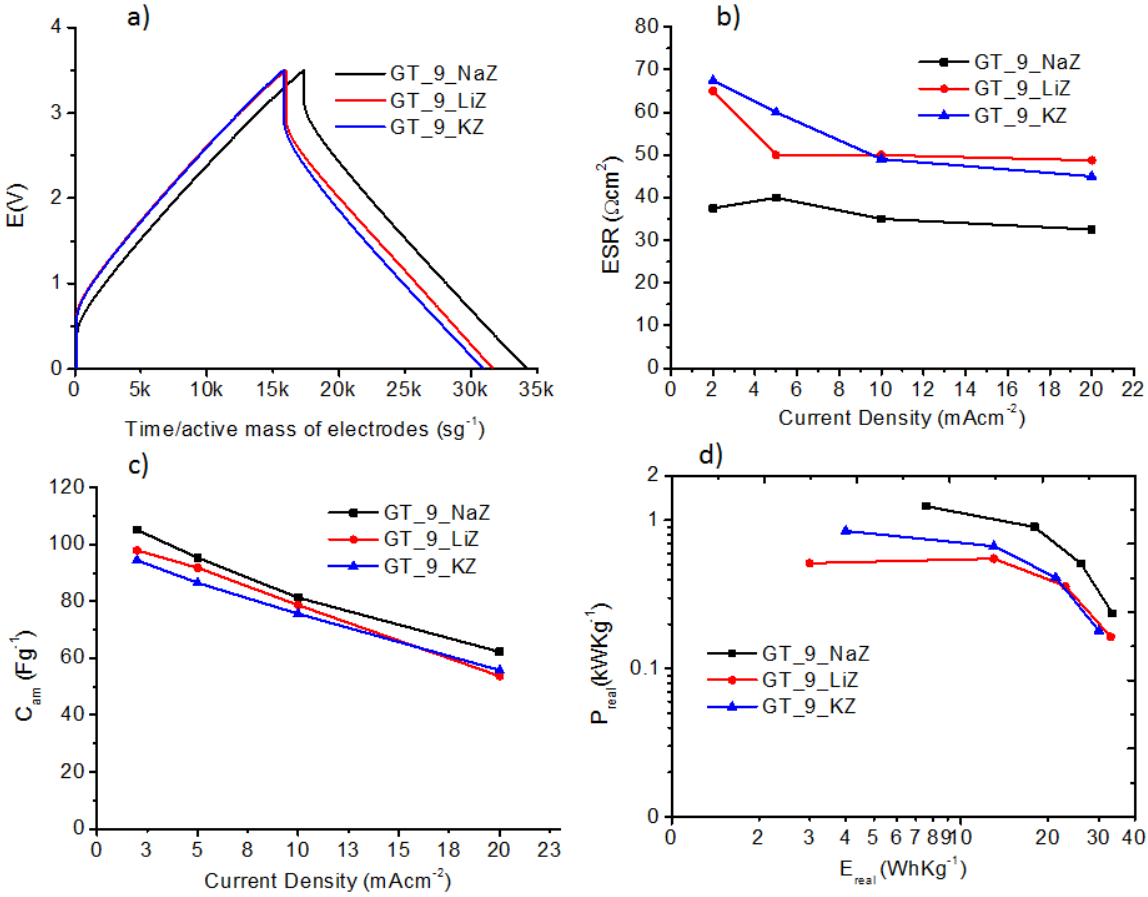

Figure 2.33. Electrochemical performance of SCs based on carbon electrodes synthesized with different salt templates ($NaCl/ZnCl_2$, $NaCl/ZnCl_2$ and $NaCl/ZnCl_2$) (GT_9_NaZ, GT_9_LiZ, and GT_9_KZ) in $PYR_{14}FSI$ at RT a) charge-discharge profile

The N-dC with $KCl/ZnCl_2$ template salt exhibits slightly less capacitive performance compared with the N-dC synthesized with $NaCl/ZnCl_2$ and $LiCl/ZnCl_2$ eutectic salts. Moreover, the Ragone plot for these N-dC electrodes demonstrates that the GT_9_NaZ (*ca.* 33 $Whkg^{-1}$) stored the highest real energy and power densities

compared with GT_9_LiZ and GT_9_KZ electrodes as shown in Figure 2.33d. This is in a good agreement with cyclic voltammetries (CV) performed in 3-electrode configuration and with the behavior of these N-dC in 1M H_2SO_4 aqueous electrolyte.

2.4. Conclusion

Novel nitrogen enriched micro-porous carbons have been synthesized from cheap and sustainable precursors, tannic acid and urea, using a combination of facile one-step thermal treatment and eutectic salts ($NaCl/ZnCl_2$, $LiCl/ZnCl_2$ or $KCl/ZnCl_2$) methods. After heating the mixture at 800 ^{0}C for 1 hr followed by aqueous removal of the molten salts, N-doped carbons (N-dC) with high micro-meso porosity as well as high nitrogen content up to 8.8 % were obtained.

Analysis of textural properties reveals that addition of nitrogen precursor to the precursor mixture decreases the specific surface area of N-dCs by 10-40 % compared with the non-doped carbon porous carbon. This is due to the incorporation of nitrogen functionalities into the carbon matrix which results in the block of some micro pores of the carbons, in turn, decreases the total specific surface area and total pore volume of the carbon. Profound investigation of textural properties indicates that the pore volume, surface area, and pore size of N-dC are adjusted by the synthetic conditions: molar ratio of urea to tannic acid, mass ratio of precursors to eutectic salts as well as the nature of eutectic salt.

Moreover, the content of nitrogen incorporated onto the carbon networks and their electrical conductivity was also found to be highly reliant on the concentration of nitrogen precursor (urea), the amount and the nature of eutectic salt which was used during thermal synthesis. For instance, bulk elemental and XPS analyses confirmed that the nitrogen content in the carbon matrix was increased with the amount of nitrogen precursor (urea) whereas decreased with increasing amount of eutectic salt. It was confirmed that the electrical conductivity of all N-dC outperforms the non-doped carbon, indicating the change of electronic properties of porous carbons by the doped nitrogen in the carbon matrix. Despite the nitrogen content was increased with the amount of nitrogen precursor, it was also observed that the electrical conductivity of the carbon decreased at the highest content of nitrogen. Deconvoluted N1s spectra in XPS demonstrated that in those carbons, the contribution of N-Q, N-X and N-6 functionalities, associated to structural nitrogen that has been proved to increase the electrical conductivity, decreased significantly resulting in carbons with lower conductivity. All of these variations in porosity, morphology, and content of doped nitrogen are affected by the concentration of precursors, nature of eutectic salts, as well as the amount of eutectic salts used during thermal synthesis.

In order to investigate the potential application of these N-dC materials in supercapacitors, the electrochemical performance of these carbons was investigated in 1 M H_2SO_4 aqueous electrolyte and in $PYR_{14}FSI$ ionic liquid. It was demonstrated that the physical properties of N-dC affects their electrochemical performance both in 1 M H_2SO_4 aqueous and in ionic liquid ($PYR_{14}FSI$) electrolytes. In fact, similar trends (with respect to the synthetic parameters of the carbons) were observed for aqueous electrolyte and $PYR_{14}FSI$. Among different N-dC, GT_9_NaZ electrode exhibits the best capacitive performance compared with other carbons due to the combined synergetic effect of textural properties (high effective surface area, and high pore volume), high nitrogen content that enhances pseudocapcitance and electrical conductivity (76 Scm^{-1}). The maximum specific capacitance of this carbon was 295 Fg^{-1} and 110 Fg^{-1} at 2 $mAcm^{-2}$ in 1 M H_2SO_4 and $PYR_{14}FSI$, respectively. It is worth mentioning that the values of specific capacitance in $PYR_{14}FSI$ were about half of the values obtained in aqueous electrolyte for most carbons. Since capacitance is directly proportional to the surface area these results might be explained by the different "effective surface area" of the carbons in the two electrolytes. Two different "effective surface areas" were calculated according to the size of the biggest ion in each electrolyte. In most of the carbons, effective surface area for $PYR_{14}FSI$ ($S_{eff>1.1nm}$) were less about half than the effective surface area for 1M H_2SO_4 aqueous electrolyte ($S_{eff>0.51nm}$) being in good agreement with the values of capacitance in both electrolytes. Despite the lower values of capacitance, the real energy of SCs with GT_9_NaZ carbon in $PYR_{14}FSI$ electrolyte was as high as 33 $Whkg^{-1}$ at 2 $mAcm^{-2}$ due to the possibility to operate up to 3.5 V. The electrochemical performance of these N-dC electrodes both in 1M H_2SO_4 and ionic liquid electrolyte surpass the performance of N-dC in acid electrolyte [7,8], and ionic liquid [11] reported in literature. Moreover, comparing the capacitive performance of N-dC, synthesized from TA acid and urea, outperform activated carbon in IL reported in literature [45,47], confirming that N-dC synthesized from very cheap precursors are an alternative materials as electrode for supercapacitors in high power applications.

In conclusion, here novel N-dC materials from sustainable precursor synthesized using a facile one-step method is presented. By fine-tuning of synthetic parameters it is possible to obtain N-dC with excellent combination of textural properties, nitrogen functionalities, and good electrical conductivity. Those N-doped carbons presented excellent electrochemical properties both in aqueous electrolyte and in ionic liquids due to the synergetic effect of high specific surface area, high degree of microporesity and high content of nitrogen in the carbon matrix. This suggests that the opportunity of fine-tuning morphology and porosity of N-doped carbons relies on optimization of

synthetic parameters. This optimization will pave the way for the development of novel nitrogen doped carbon material as electrode material for supercapacitors.

2.5. References

[1] D. Hulicova, M. Kodama, H. Hatori, Chem. Mater. 18 (2006) 2318.

[2] B. Xu, S. Hou, F. Zhang, G. Cao, M. Chu, Y. Yang, J. Electroanal. Chem. 712 (2014) 146.

[3] P. Tamilarasan, S. Ramaprabhu, J. Nanosci. Nanotechnol. 15 (2015) 1154.

[4] B.E. Wilson, S. He, K. Buffington, S. Rudisill, W.H. Smyrl, A. Stein, J. Power Sources 298 (2015) 193.

[5] W.J. Weydanz, B.M. Way, T. van Buuren, J.R. Dahn, J. Electrochem. Soc. 141 (1994) 900.

[6] X.G. Sun, X. Wang, R.T. Mayes, S. Dai, ChemSusChem 5 (2012) 2079.

[7] G. Lota, B. Grzyb, H. Machnikowska, J. Machnikowski, E. Frackowiak, Chem. Phys. Lett. 404 (2005) 53.

[8] D. Hulicova, J. Yamashita, Y. Soneda, H. Hatori, M. Kodama, Chem. Mater. 17 (2005) 1241.

[9] L.F. Chen, X.D. Zhang, H.W. Liang, M. Kong, Q.F. Guan, P. Chen, Z.Y. Wu, S.H. Yu, ACS Nano 6 (2012) 7092.

[10] K.T. Cho, S.B. Lee, J.W. Lee, J. Phys. Chem. C 118 (2014) 9357.

[11] J.-K. Ewert, D. Weingarth, C. Denner, M. Friedrich, M. Zeiger, A. Schreiber, N. Jäckel, V. Presser, R. Kempe, J. Mater. Chem. A 3 (2015) 18906.

[12] J.R. Pels, F. Kapteijn, J.A. Moulijn, Q. Zhu, K.M. Thomas, Carbon N. Y. 33 (1995) 1641.

[13] F. Kapteijn, J.A. Moulijn, S. Matzner, H.P. Boehm, Carbon N. Y. 37 (1999) 1143.

[14] D. Hulicova-Jurcakova, M. Seredych, G.Q. Lu, T.J. Bandosz, Adv. Funct. Mater. 19 (2009) 438.

[15] M. Seredych, D. Hulicova-Jurcakova, G.Q. Lu, T.J. Bandosz, Carbon N. Y. 46 (2008) 1475.

[16] L. Zhao, L.-Z. Fan, M.-Q. Zhou, H. Guan, S. Qiao, M. Antonietti, M.-M. Titirici, Adv. Mater. 22 (2010) 5202.

[17] W. Yang, T. Fellinger, M. Antonietti, J. Am. Chem. Soc. 133 (2011) 206.

[18] L. Lai, J.R. Potts, D. Zhan, L. Wang, C.K. Poh, C. Tang, H. Gong, Z. Shen, J. Lin, R.S. Ruoff, Energy Environ. Sci. 5 (2012) 7936.

[19] M.C. Huang, H. Teng, Carbon N. Y. 41 (2003) 951.

[20] K.R. Lee, K.U. Lee, J.W. Lee, B.T. Ahn, S.I. Woo, Electrochem. Commun. 12 (2010) 1052.

[21] B. Xu, D. Zheng, M. Jia, G. Cao, Y. Yang, Electrochim. Acta 98 (2013) 176.

[22] L. Zhao, N. Baccile, S. Gross, Y. Zhang, W. Wei, Y. Sun, M. Antonietti, M.M. Titirici, Carbon N. Y. 48 (2010) 3778.

[23] A. Oya, N. Kasahara, Carbon N. Y. 38 (2000) 1141.

[24] A. Oya, S. Yoshida, J. Alcaniz-Monge, A. Linares-Solano, Carbon N. Y. 33 (1995) 1085.

[25] Q. Huang, M. Ulutagay, P.A. Michener, S.J. Hwu, J. Am. Chem. Soc. 121 (1999) 10323.

[26] N. Fechler, Salts as Highly Diverse Porogens: Functional Ionic Liquid-Derived Carbons and Carbon-Based Composites for Energy-Related Applications Dissertation, University of Potsdam, 2012.

[27] N. Fechler, T.-P. Fellinger, M. Antonietti, Adv. Mater. 25 (2013) 75.

[28] S. Vaquero, R. Díaz, A. Anderson, J. Palma, R. Marcilla, Electrochim. Acta 86 (2012) 241.

[29] S. Vaquero, R. Díaz, M. Anderson, J. Palma, R. Marcilla, Electrochim. Acta 86 (2012) 241.

[30] M.M. Jaramillo, A. Mendoza, S. Vaquero, M. Anderson, J. Palma, R. Marcilla, RSC Adv. 2 (2012) 8439.

[31] L. Li, E. Liu, H. Shen, Y. Yang, Z. Huang, X. Xiang, Y. Tian, J. Solid State Electrochem. 15 (2011) 175.

[32] R. Farma, M. Deraman, Awitdrus, I.A. Talib, R. Omar, J.G. Manjunatha, M.M. Ishak, N.H. Basri, B.N.M. Dolah, Int. J. Electrochem. Sci. 8 (2013) 257.

[33] B. Manoj, A.G. Kunjomana, Int. J. Electrochem. Sci. 7 (2012) 3127.

[34] S. Biniak, Carbon N. Y. 35 (1997) 1799.

[35] J.. Figueiredo, M.F.. Pereira, M.M.. Freitas, J.J.. Órfão, Carbon N. Y. 37 (1999) 1379.

[36] U. Zielke, K.J. Huttinger, W.P. Hoffman, Carbon N. Y. 34 (1996) 983.

[37] M. Seredych, D. Hulicova-Jurcakova, G.Q. Lu, T.J. Bandosz, Carbon N. Y. 46 (2008) 1475.

[38] N. Dwivedi, R.J. Yeo, N. Satyanarayana, S. Kundu, S. Tripathy, C.S. Bhatia, Sci. Rep. 5 (2015) 7772.

[39] D. Hulicova-Jurcakova, M. Kodama, S. Shiraishi, H. Hatori, Z.H. Zhu, G.Q. Lu, Adv. Funct. Mater. 19 (2009) 1800.

[40] Y. Xie, P.M.A. Sherwood, Chem. Mater. 2 (1990) 293.

[41] D. Kim, C. Lin, T. Mihalisin, Chem. Mater. 67 (1991) 686.

[42] M. Endo, T. Maeda, T. Takeda, Y.J. Kim, K. Koshiba, H. Hara, M.S. Dresselhaus, J. Electrochem. Soc. 148 (2001) A910.

[43] V. Sahu, S. Grover, B. Tulachan, M. Sharma, G. Srivastava, M. Roy, M. Saxena, N. Sethy, K. Bhargava, D. Philip, H. Kim, G. Singh, S.K. Singh, M. Das, R.K. Sharma, Electrochim. Acta 160 (2015) 244.

[44] P. Iamprasertkun, A. Krittayavathananon, M. Sawangphruk, Carbon N. Y. 102 (2016) 455.

[45] A. Balducci, R. Dugas, P.L. Taberna, P. Simon, D. Plée, M. Mastragostino, S. Passerini, J. Power Sources 165 (2007) 922.

[46] A. Burke, Electrochim. Acta 53 (2007) 1083.

[47] N. Handa, T. Sugimoto, M. Yamagata, M. Kikuta, M. Kono, M. Ishikawa, J. Power Sources 185 (2008) 1585.

CHAPTER III: VANADIUM NITRIDE@NITROGEN-DOPED CARBON AS ELECTRODE MATERIAL FOR ILs BASED SUPERCAPACITORS[2]

[2] Most of the results included in this chapter are published as: "N. Fechler, G.A. Tiruye, R. Marcilla, M. Antonietti. Vanadium Nitride@N-Doped Carbon Nanocomposites: Tuning of Pore Structure and Particle Size Through Salt Templating and Its Influence on Supercapacitance in Ionic Liquid Media. RSC Advances.4, 214, 26981-26989."

CHAPTER III: VANADIUM NITRIDE@NITROGEN-DOPED CARBON AS ELECTRODE MATERIAL FOR ILs BASED SUPERCAPACITORS

3.1. Introduction

The importance of the need to develop supercapacitors has been recently realized. This has led to the development of various interesting electrode materials such as graphene [1], transition metal nitride [2], transition metal oxide [3], heteroatoms doped carbon [4], conductive polymers [5], and others. Great effort has been placed into tailoring the architecture of the electrode materials on the nanometer scale *via* composition and morphology to retain high energy density at high rates. A prominent example is carbon which can possess a broad variety of properties depending on the actual nanostructure. The right combination of different materials into nanocomposites or nano-hybrids results in combined or even enhanced properties through synergistic interactions. This approach turned out to be especially attractive for the design of energy materials for supercapacitors [6–8], batteries [9] and applied as catalysts for fuel cell [10]. Nanocomposites used in supercapacitors mostly combine a high porous carbon matrix with a redox active species [6,11–13]. While porosity contributes a high specific surface area and provides the electrical conduction pathways for storing energy in the electrical double layer, redox active species add Faradaic reactions, *e.g.,* reversible redox processes between the electroactive electrode material and the electrolyte ions [3,14,15]. Here, metal oxides such as RuO_2 [16], MnO_2 [3] and V_2O_5 [17,18], poly(pyrrole) [5], and nitrogen doped carbons [19] are the most examined candidates as electrode materials. Until recently, one of the most favorable electrode materials is RuO_2, nevertheless, its high cost essentially hinder their commercial application [6,14,16]. Vanadium oxides (V_xO_y) also exhibit a variety of oxidation states [18,20] potentially advantageous for the performance in pseudocapacitors, but the poor electronic conductivity of V2O5 is a prohibitive drawback [18].

Vanadium nitride (VN) is found to be a promising electrode material due to its low cost and significantly enhanced electronic conductivity compared to V_2O_5 [20]. The high capacitance was attributed to a thin oxide layer on top of the surface of the VN [20]. However, the rate capability is still rather limited which can be ascribed to insufficient electronic contact in between the single VN particles. Eventually, this

problem can be solved by forming a nanocomposite, most favorably with carbon from a concurrent synthesis approach that generates and controls all synthetic components at the same time.

Up to now, various methods have been developed to synthesize nanocomposite materials as electrode for supercapacitors. Among different synthesis methods, a facile one-pot synthesis towards nanocomposite is widely used. For instance, F_2O_3 nanoparticle on nitrogen doped graphene [21] and metal nitride nanoparticle on nitrogen doped carbon [22] have been synthesized using one-pot synthesis method.

Recently, N. Fechler *et. al.* reported a one-pot synthesis approach towards metal nitride nanoparticles within a porous nitrogen-doped carbon matrix (MN@N-dC) using an ionic liquid (IL) as the nitrogen as well as carbon source [22]. However, those composites were not appropriate for supercapacitor applications as the surface area was low (550 m^2g^{-1} for VN@N-dC and 350 m^2g^{-1} for TiN@N-dC nanoparticles) and the area depends on the metal amount used in the initial precursor solution. Furthermore, the materials were entirely microporous, and larger pores, which are important for high rate transport, were not accessible. To solve this problem, the combination of one-pot synthesis and salt-templating methods can be used as a good strategy for the synthesis of highly efficient electrode materials with high specific surface area and hierarchically pore size distribution. A simple salt-templating is a well-known method to synthesize carbons with micro- as well as mesopores [23–25]. If miscibility between the molten salt and the carbonizing material is retained over the main part of the reaction pathway, the resulting carbon would exhibit a high specific surface area with the pore size corresponding to salt clusters and their percolation structures. Then, the molten salt phase can be easily removed by simple washing with water, while the carbon is not etched as such. Ultimately, this method can be considered as a simple closed-loop process including salt recycling which results in the demanded high surface area carbons in high yields with structural and chemical functionality [23,26].

Herein, we present the possibility to synthesize vanadium nitride in nitrogen doped carbon (VN@N-dC) composites where besides drastically increased surface areas (2400 $m^2 g^{-1}$ vs. 550 m^2g^{-1}) and pore volumes (1.65 cm^3g^{-1} vs. 0.2 cm^3g^{-1}), it is possible to tune the vanadium nitride (VN) particle size as well as the pore size in the nanometre regime even independently through a simple “salt templating method”. By adding Cesium acetate (CsAc) and zinc acetate ($ZnAc_2$) as salt porogens, separately into the mixture of precursors, porous composites of vanadium nitride nanoparticles in nitrogen-doped carbon (VN@N-dC) with unusually high surface areas of up to 2400 m^2g^{-1} were synthesized. The salts were chosen as they homogeneously mix with the precursor solution, thus they can act *in-situ* as templates during the carbonization process. Additionally, we demonstrate that a rational control over synthetic parameters

allows fine tuning of the composite properties such as porosity and particle size. The usefulness of those nanocomposites is demonstrated by the investigation of their electrochemical properties in ionic liquids and their application as active material in electrodes for supercapacitors based on ionic liquids. Variation of the solvent ion size in those media allows quantifying the accessibility of redox active sites in a variety of diversely structured storage materials.

This chapter was the first result of an on-going and fruitful collaboration between the group of Prof. Markus Antonietti at Max Planck Institute for Colloids and Interfaces (MPI), Postdam, Germany and the IMDEA Energy Institute, Madrid Spain within the framework of the RENAISSANCE-ITN European Project (http://www.renaissance-itn.eu/home). The MPI group was focused on the synthesis of VN@N-dC with controllable surface area, pore size, pore volume and particle size through "salt templating" in one-step synthesis. IMDEA Energy was responsible for the complete electrochemical characterization of different carbons and their application as electrode materials for supercapacitors.

3.2. Experimental Methods

3.2.1. Materials

Ethyl methylimidazolium dicyanamide (Emim-dca) was purchased from IoLiTec with a purity of > 98%. 1-butyl-1-methylpyrrolidinium bis(fluorosulfonyl)imide, ($PYR_{14}FSI$, > 99.9 %), 1-butyl-1-methylpyrrolidinium bis(trifluorosulfonyl)imide, ($PYR_{14}TFSI$, > 99.9 %), were acquired from Solvionic and stored inside glove box. The vanadium precursors $VOCl_3$ (99%), NH_4VO_3 (99%) as well as salts (porogens) cesium acetate (99.9%) and Zinc acetate dihydrate (> 98%) were acquired from Sigma Aldrich. Carbon black (Alfa Aesar GmbH & Co KG, Germany), activated carbon (Picactif BP 10, PICA), Polytetrafluoroethylene (PTFE 60 wt. % dispersion in water), and 2-propanol both from Sigma Aldrich were used to prepare homogeneous carbon ink. Stainless steel mesh from Goodfellow was also used as a current collector. All chemicals were used without further purification.

3.2.2. Synthesis of vanadium nitride in nitrogen doped carbon (VN@N-dC) composites

In a typical reaction, $VOCl_3$ (50 mg) or NH_4VO_3 (35 mg), as metal precursor, was dissolved in Emim-dca (1 g). Varying concentrations of CsAc (max. 1 g), $ZnAc_2$ (1.162 g) or an equimolar (1:1) of CsAc/$ZnAc_2$ mixture were subsequently added. For reasons of comparison, the molar ratio of acetate cation and ionic liquid was kept identical for both porogens. A pure reference nitrogen-doped carbon was produced by mixing

Emim-dca (1 g) with CsAc (340 mg). All precursors were thoroughly mixed by gentle heating prior to the calcination process. The resulting solutions were placed in a ceramic crucible and heated to 800 °C with a heating rate of 10 $Kmin^{-1}$ in a Nabertherm N7/H Chamber Oven. After holding this temperature for 1 h the samples were allowed to cool to room temperature. All steps were carried out under a flow of nitrogen. In order to remove the residual porogen, the materials were grinded and washed in water (the sample solely prepared with $ZnAc_2*(H_2O)_2$ was additionally washed with 1 M HCl) for several hours and finally filtered off and dried in vacuum.

The resulting composites are named VN@N-dC-x-y-z, where x indicates the salt amount in mg (notation expressed in amount CsAc), y the type of salt, and z the type of Vanadium precursor used for the synthesis, respectively. The composite synthesized with 200 mg instead of 50 mg of $VOCl_3$ is labeled VN@N-dC-x-y-z-200.

3.2.3. Physical Characterization

Wide angle X-ray scattering (WAXS) patterns were measured on a Bruker D8 Advance instrument using Cu-Kα-radiation. Nitrogen sorption measurements were accomplished with N_2 at 77 K after degassing the samples at 150 °C under vacuum for 20 hours using a Quantachrome Quadrasorb SI porosimeter. The surface area was calculated by applying the BET model to the linear part of the isotherm data points of the adsorption branch in the relative pressure range $p/p_0 < 0.11$ for the microporous and $p/p_0 < 0.3$ for the mesoporous materials. The pore size distribution was calculated from N_2 sorption data using the nonlocal density functional theory (NLDFT) equilibrium model method for slit pores provided by Quantachrome data reduction software QuadraWin Version 5.05. TEM images were obtained using a Zeiss EM 912 Ω instrument. Elemental analysis was accomplished as combustion analysis using a Vario Micro device. ICP OES analysis was carried out using an ICP OES Optima 2100 DV (Perkin Elmer). XPS-measurements were made with a Kratos Axis 165 system using Al-K_α-radiation. SEM images were obtained on a LEO 1550-Gemini instrument after sputtering with platinum.

3.2.4. Electrochemical Characterization

Electrode Preparation: As a standard procedure for electrode preparation, each electrode was prepared by thoroughly stirring the mixture of each respective carbon composite (VN@N-dC-1000-CsAc-$VOCl_3$, VN@N-dC-1000-CsAc-NH_4VO_3, or VN@N-dC-1000-$ZnAc_2$-NH_4VO_3) and Polytetrafluoroethylene (PTFE 60 wt. % dispersion in water, Sigma Aldrich) with 2-propanol as a solvent in order to get a homogeneous paste [27,28]. The final composition of the paste was 90 wt. % of respective carbon composite

and 10 wt. % of PTFE as a binder. For the reason of comparison, electrodes were also prepared with the commercial activated carbon Picactif BP 10 (PICA). In the case of PICA electrode, the percentage composition was 80 wt. % PICA, 10 wt. % binder (PTFE) and 10 wt. % black carbon that was added to enhance the electrical conductivity of PICA carbon. Next, the paste was rolled up onto a coin-shaped stainless steel mesh current collector (d = 1 cm). The coated electrodes were then pressed with a uniaxial press (CARVER model 3853-0) applying a pressure of 15 tons (about 2123 kg cm^{-2}) for 7 minutes and dried at 130 °C under vacuum overnight. The mass-loading of the dried electrodes was about 6 - 8 mg cm^{-2} of active mass.

3-Electrode Set-Up: Cyclic Voltammetry (CV) was carried out on a multichannel Bio-Logic Lab (model: VMP3) by using a three-electrode Swagelok® cell (half-cell set-up). In this set-up, each carbon composite electrode (VN@N-dC-1000-CsAc-$VOCl_3$, VN@N-dC-1000-CsAc-NH_4VO_3, VN@N-dC-1000-$ZnAc_2$-NH_4VO_3) and PICA was used as a working electrode, a silver wire was used as a pseudo reference electrode and an additional PICA electrode having much higher mass than the working electrode (WE) was used as the counter electrode (CE). A 130 μm thick cellulose filter paper soaked with the IL (N-butyl-N-methylpyrrolidinium bis(trifluoromethylsulfonyl)imide ($PYR_{14}TFSI$, 99.9%, Solvionic, France) or N-butyl-N-methylpyrrolidinium bis(fluorosulfonyl)imide ($PYR_{14}FSI$, 99.9%, Solvionic, France) was used as a separator. Before assembling the cell, each electrode was impregnated with the electrolyte under vacuum and kept at least for 1 h before assembling. Impregnation and assembling of the cell were performed inside the glove box. CV experiments were performed at room temperature, over a potential range of -1.75 V to 1.75 V and at scan rates of 100, 50, 20, 10, 5 mVs^{-1}. The specific capacitance (C_{am}) of the single electrode was calculated from integration of the CV curve over different ranges of scan rates.

2-Electrode-Setup: Symmetric supercapacitors were assembled using two-electrode Swagelok® cells where the separator soaked with the ILs ($PYR_{14}TFSI$ or $PYR_{14}FSI$) was sandwiched between two electrodes (same carbon and same mass). Electrochemical Impedance spectroscopy (EIS) experiments were performed over a frequency range of from 200 kHz to 10 mHz using a bias voltage of 0 V and 10 mV in amplitude. Galvanostatic charge-discharge experiments were conducted at room temperature from 0 to 3.5 V at different current densities: 50, 20, 10, and 5 mA cm^{-2}. From the charge-discharge experimental data, specific capacitance ($C_{sp,\,cell}$), equivalent series resistance (ESR) and real specific energy (Ereal) of the full supercapacitor were calculated using *egn.2.2 to eqn.2.6*, in chapter 2.

3.3. Results and Discussion

3.3.1. Synthesis of VN@N Doped Carbon Composites

As stated above, simultaneous control of the composite properties within a single step is synthetically highly appealing. Generally, the synthesis of materials starts with dissolving the metal precursor and the template salt in the IL. Two different metal precursors ($VOCl_3$ and NH_4VO_3) and two different porogen salts (CsAc and ZnAc) were used in the synthesis, as detailed below.

$VOCl_3$ as Metal Precursor: In order to evaluate the influence of the salt porogen amount, a series of composites was prepared with a fixed amount of $VOCl_3$, the IL (Emim-dca) and varying concentrations of CsAc. Mixing $VOCl_3$ with Emim-dca results in a homogeneous green solution which indicates that the initial oxidation state V^{5+} is already reduced to V^{3+} before any heat treatment (Figure 3.1a). Further addition of CsAc gives a liquid green salt solution after gentle heating, which turns more viscous at low and gelatinous/glassy at high salt concentrations after being cooled back to room temperature (Figure 3.1b).

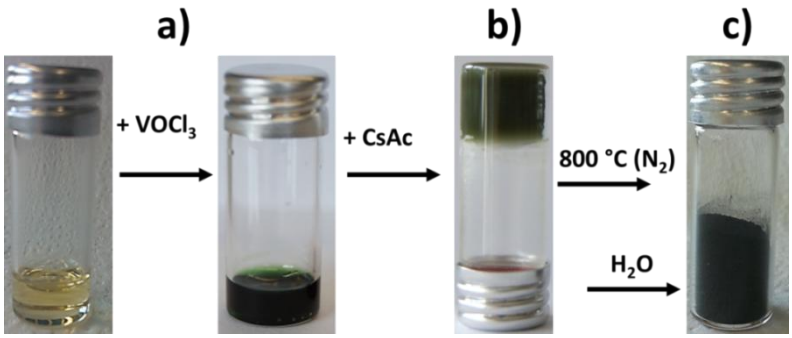

Figure 3.1. a) Preparation of the composite precursor solution by dissolution of $VOCl_3$ in Emim-dca. b) Precursor solution with CsAc of VN@N-dC-1000-CsAc-$VOCl_3$ before and c) after calcination at 800 °C and aqueous porogen removal.

The gel/glass can reversibly be liquefied by re-heating, indicating the formation of a physical network where the CsAc salt ions cross-link the IL solvent clusters *via* strong solvent coordination. The heat-treatment of this easy-to-process liquid precursor solution under inert atmosphere and aqueous removal of the salt porogen finally results in highly porous composites which are isolated as voluminous black powders (Figure 3.1c).

NH_4VO_3 as Metal Precursor: To investigate a possible influence of the metal precursor as well as the template salt, $VOCl_3$ was replaced by NH_4VO_3 and zinc acetate ($ZnAc_2$) chosen as second porogen. Two composites were prepared with the pure porogens CsAc and $ZnAc_2$ and, for proof of principle, a third one with an equimolar

(1:1) CsAc/$ZnAc_2$ mixture of both salts, all at the highest amount of salt. For better comparison, the molar metal and salt concentrations were kept equal to the $VOCl_3$/CsAc system.

In contrast to the $VOCl_3$/Emim-dca system, the initial precursor mixture of NH_4VO_3/Emim-dca forms a dark black solution and the addition of CsAc leads to beige solid (Figure 3.2a&b). This points to the formation of V_2O_3 and $[V(O_2)]^{3+}$ or $H_3[VO_2(O_2)]$ species from NH_4VO_3, respectively. However, exchange of CsAc for $ZnAc_2$ leads to a green gel (Figure 3.2c), again indicative for V^{3+} ions. The formation of a gel is attributed to the stronger coordination ability of zinc compared to Cesium which eventually results in a more homogeneous network.

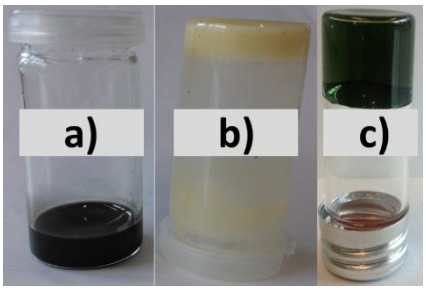

Figure 3.2. a) Dissolution of NH_4VO_3 in Emim-dca, b) precursor solution of VN@N-dC-1000-CsAc-NH_4VO_3 and c) VN@N-dC-1000-$ZnAc_2$-NH_4VO_3.

3.3.2. Physical Characterization of the Composites

$VOCl_3$ as Metal Precursor: A representative transmission electron microcopy (TEM) picture of VN@N-dC-340-CsAc-$VOCl_3$ is shown in Figure 3.3a.

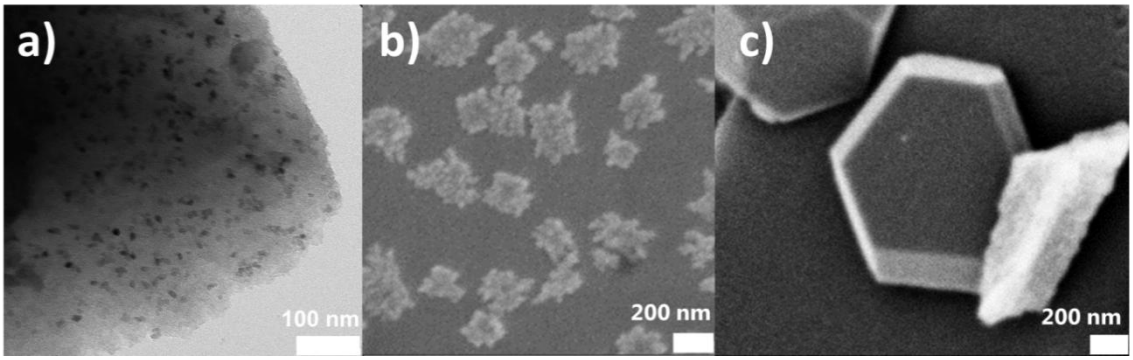

Figure 3.3. a) TEM images of VN@N-dC-340-CsAc-$VOCl_3$. SEM images of b) VN@N-dC-340-CsAc-$VOCl_3$ and c) VN@N-dC-1000-CsAc-$VOCl_3$, characterizing growth of non-hybridized outer VN particle species as a defect structure.

It reveals nanoparticles with an average particle size of around 10 nm in diameter, embedded within a porous carbon matrix. This is very different from previous works where only carbon materials were prepared [23,26]. Scanning electron

microcopy (SEM) images of VN@N-dC-340-CsAc-$VOCl_3$ and VN@N-dC-1000-CsAc-$VOCl_3$ show additional larger particles on the outer surface of the final material as coexisting species, which grow bigger with higher porogen salt concentrations (Figure 3.3b&c).

Wide angle X-ray scattering (WAXS) patterns of the washed products can be assigned to pure VN (see Figure 3.4a). At a fixed $VOCl_3$ concentration, the diffraction peaks turn narrower with increasing CsAc concentration, i.e. the nanoparticles become larger. On the one hand, this probably arises from a decrease in viscosity at reaction temperature. Moreover, high amounts of salt might lower the solubility within the precursor solution at the reaction temperature. The crystallite sizes were calculated using the Scherrer equation (see Figure 3.4b), which however came out smaller than depicted in scanning electron microscopy. Here, it is worth mentioning that the Scherrer equation is only applicable to spherical particles and solely corresponds to primary crystallite size. Thus, the results from TEM/SEM and WAXS can deviate, yet a general trend of increased structural size with the porogen amount is observed in all cases.

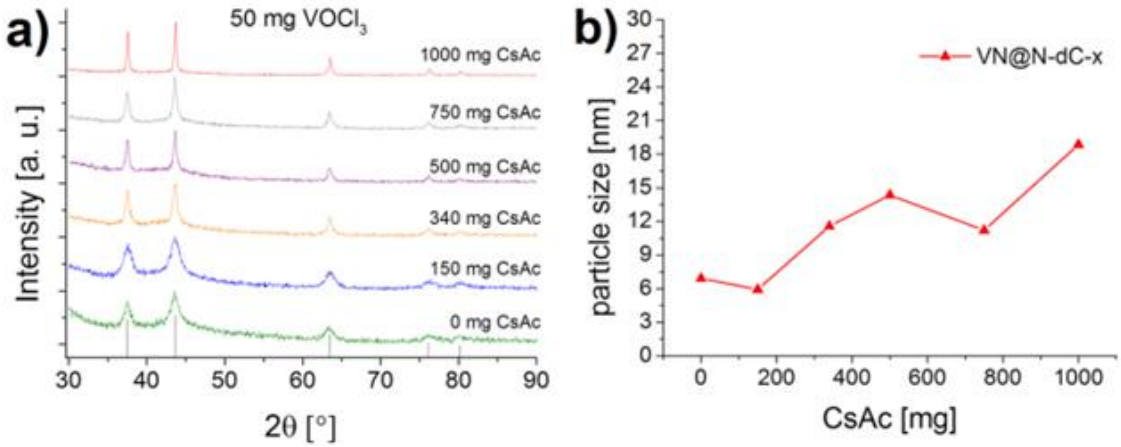

Figure 3.4.a) WAXS patterns of calcined, washed VN@N-dC-x-CsAc-VOCl3 and b) calculated particle size using Scherrer equation at different CsAc concentrations.

Figure 3.5 shows the N_2 adsorption-desorption isotherms and the corresponding specific surface areas of the composites at different CsAc concentrations. It is known that carbonized Emim-dca without any salt template shows no porosity [29,30]. This is also observed if only small amounts of $VOCl_3$ (50 mg) are added (VN@N-dC-0-$VOCl_3$, Brunauer-Emmett-Teller (BET) evaluation 20 m^2g^{-1}), which is in accordance with the previous report (Figure 3.5) [22]. However, through the addition of the salt CsAc, the surface area of the composite increases significantly (Figure 3.5b).

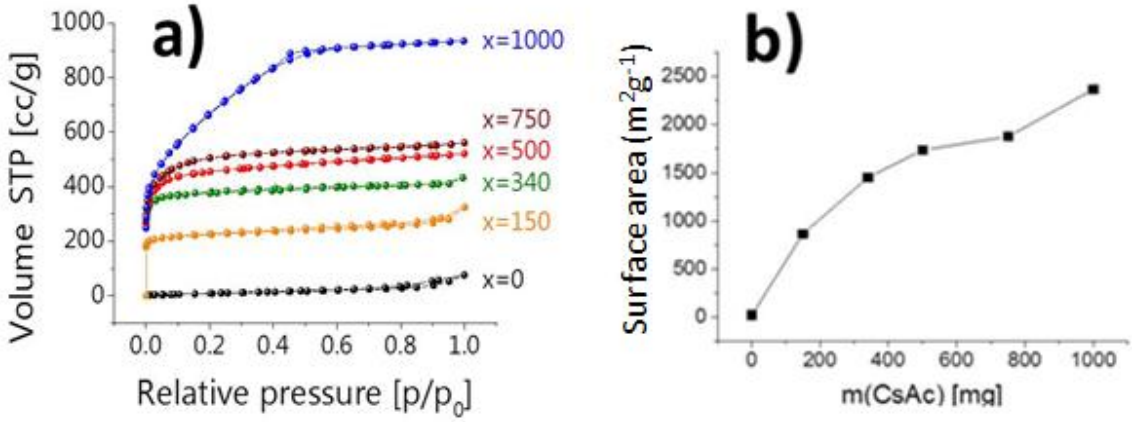

Figure 3.5.a) Nitrogen sorption isotherms of VN@N-dC-x-CsAc-$VOCl_3$ at different CsAc concentrations x. b) Trend of the apparent surface areas of the same series of composite materials.

At a fixed $VOCl_3$ amount, the isotherms are of type I for 0 to 500 mg CsAc which implies a solely microporous structure of the composites, i.e. the salt presumably acts as a "molecular template". At 750 mg CsAc, the sorption isotherm shows a further uptake of N_2 in the medium relative pressure region, reflecting a contribution of additional supermicropores and small mesopores which are attributed to small salt clusters in the 2 nm range now acting as template. Finally, for the highest CsAc concentration, a small hysteresis at P/Po= 0.4-0.6 is observed in the isotherm, underlining that the content of small mesopores has significantly been increased (Figure 3.5a).

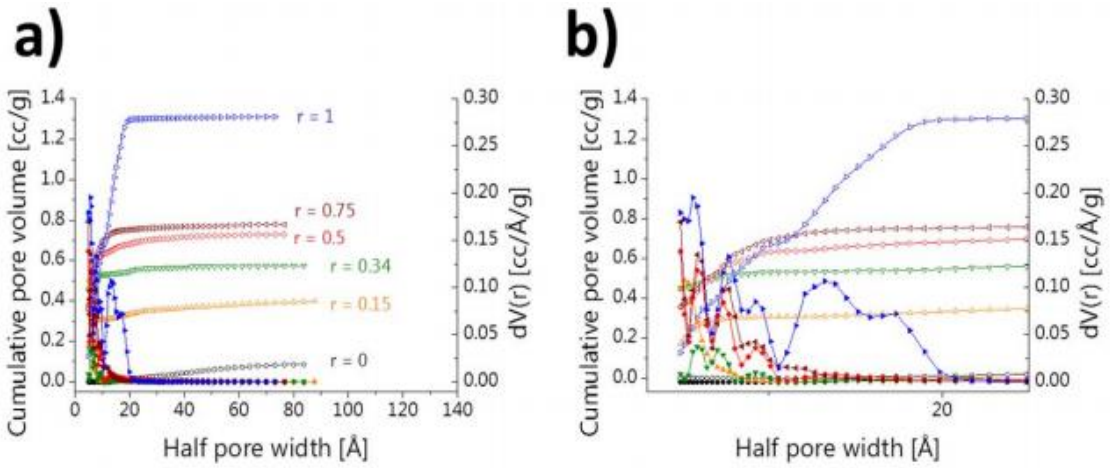

Figure 3.6. a) PSDs of VN@N-dC-x-CsAc-VOCl3, r is the amount of CsAc in gram b) magnification of half pore width from 0 to 30 Å.

Figure 3.6 shows the pore size distribution (PSD) curve calculated by DFT method for the different composites. While for VN@N-dC-340-CsAc-$VOCl_3$ (r=0.34 g of CsAc in figure) a high contribution of pores around 1 nm in diameter can be

observed, additional pores of around 3 nm are found for VN@N-dC-1000-CsAc-$VOCl_3$ (r=1 in figure) (see Figure 3.6).

The apparent surface area increases about linearly with increasing CsAc concentrations (see Figure 3.5b), which means that the salt indeed mainly acts as molecular or nanoclustered template, with the larger pores created by percolation effects setting in at high salt concentrations. Here, it is noted that an apparent surface area of 2400 m^2g^{-1} is much higher than that of any zeolite [31], approaching the theoretical value of molecularly dispersed single layer graphene [32] and it is the range of the highest surface areas found for activated carbons [33]. Taking into account the simplicity of the applied one step synthetic process, this is a remarkable result. As a reference experiment to demonstrate the importance of added metal precursor, a pure nitrogen-doped carbon N-dC-340-CsAc was prepared without adding vanadium precursor. The nitrogen sorption of the calcined and washed product reveals only a moderate apparent surface area of 200 m^2g^{-1} compared to 1600 m^2g^{-1} for the respective metal containing composite VN@N-dC-340-CsAc-$VOCl_3$. In the pure hybrid VN@N-dC-0-$VOCl_3$, we assumed that porosity originates from a cohesive delamination at the material interfaces caused by the growth of the metal nitride nanoparticles in between the forming carbon layers. In the pure salt melt system N-dC-340-CsAc, entrapped salt is present in the final carbon as even medium amounts of salt are not sufficient to create percolating, accessible pores: the mixing of carbon and salt is very homogeneous. Obviously, nanoparticles promote the entry to those salt pores by creating additional pores via interfacial delamination. This is supported by the measurement of residual Cs content in the reference carbon of 3 wt%, compared to 0.1 wt% in the composite as determined by inductively coupled plasma optical emission spectrometry (ICP-OES). In VN@N-dC-1000-CsAc-$VOCl_3$, the very high apparent surface area of 2400 m^2g^{-1} could be generated even at low metal nitride concentrations. The overall pore volume of the material nicely coincides with expectation based on the relative salt porogen content. Etching processes by the base CsOH cannot be excluded, but are not necessary to describe the pore volume of the material. In addition, the carbon yield is too high for a major contribution of classical activation.

The amount of vanadium within the composites determined by ICP-OES was found to be ca. 7 wt % which is similar to the value obtained for the composite produced without salt (see Table 3.1). Thus, the metal nitride content is simply controlled by the amount of initial metal precursor and does not depend on added salt. Furthermore, elemental analysis reveals an average composition of 70 wt% carbon, 7.5 wt% nitrogen, and slightly varying amounts of oxygen with the highest content of 10.5 wt % for the microporous composite (340 mg CsAc, see Table 3.1). Oxygen terminated

surfaces are in fact beneficial for the desired application: V_xO_y was reported to be responsible for high capacitances observed for VN in form of a thin oxide layer on top of the nitride, and additional oxygen within the carbon increases the capacitance in a similar fashion, but also by improved solvent wetting [34].

Table 3.1. Composition of the composites VN@N-dC-x-CsAc-$VOCl_3$.

CsAc	Elements (wt%)				
X (mg)	Elemental analysis			ICP OES	XPS
	N	C	H	V	O
0	12.29	69	1.04	7	8.4
150	7.61	70	1.79	-	-
340	7.6	69	1.58	5.6	11
500	5.95	65	2.78	-	-
750	6.96	60	1.05	-	-
1000	11.18	62	0.9	7.8	5.4

To confirm the presence of structural nitrogen, X-ray photoelectron spectroscopy (XPS) was performed and shown in Figure 3.7. N1s spectra show the nature of the nitrogen to be mainly pyridinic (398.6 eV), quaternary-graphitic (400.4 eV) and oxidic nitrogen within graphitic micro domains (402.2 eV), respectively [33,35,36] (see Figure 3.7a). The V2p peaks reveal, in addition to signals assigned to VN (513.6 eV), the presence of V_xO_y (514.9 to 518.9 eV) [17,20,37] (Figure 3.7b).

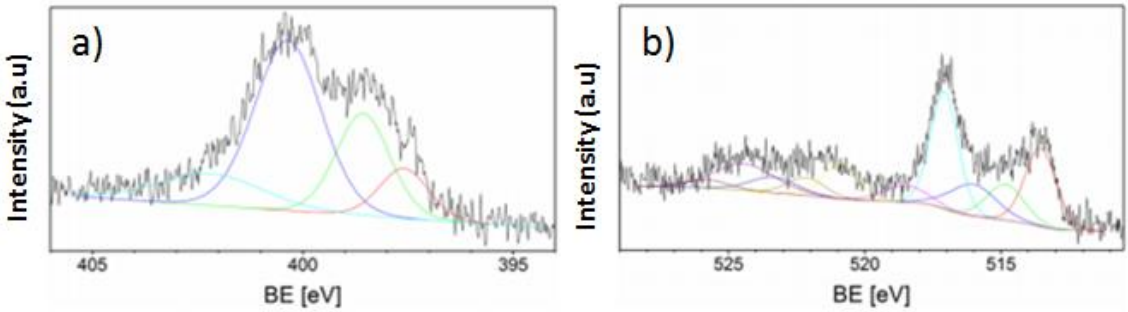

Figure 3.7. XPS-spectra: a) N1s and b) V2p orbitals of VN@N-dC-340-CsAc-$VOCl_3$.

NH_4VO_3 as Metal Precursor: To investigate the influence of the metal precursor and the template salt in the composite properties, $VOCl_3$ was replaced by NH_4VO_3 and zinc acetate ($ZnAc_2$) chosen as second porogen. Two composites were prepared with the pure porogens CsAc and $ZnAc_2$ and a third one with an equimolar (1:1) of CsAc/$ZnAc_2$ mixture of both salts, all at the highest amount of salt (1000) and with NH_4VO_3 as metal precursor. For better comparison, the molar metal and salt concentrations were kept equal to the $VOCl_3$/CsAc system. TEM pictures of the final products are shown in

Figure 3.8(a-c) reveal the biggest VN nanoparticles for CsAc, followed by the 1:1-CsAc/$ZnAc_2$ mixture and finally very small VN nanoparticles in the case of $ZnAc_2$. This already indicates the possibility to influence the particle size through the nature or composition of the salt template. WAXS patterns of the composites shown in Figure 3.8d still give reflections ascribed to vanadium nitride, thus the nitride formation is not influenced as such. The peaks become narrower from $ZnAc_2$ over the CsAc/$ZnAc_2$ mixture to CsAc which reflects an increase in the crystallite size and supports the results obtained from TEM. The smaller crystallite size for the $ZnAc_2$-containing systems is attributed to the more homogeneous precursor structure and the stronger complexation of the ILs to the zinc ions.

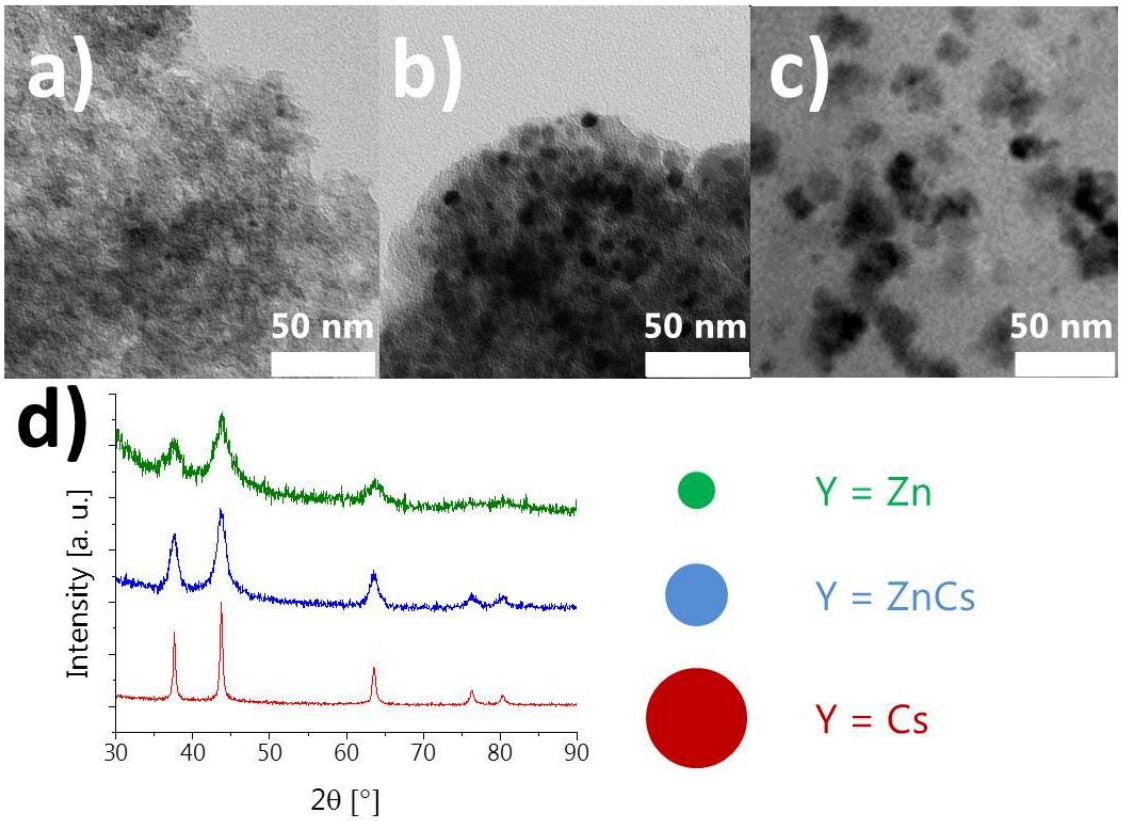

Figure 3.8. a-c) TEM pictures and d) WAXS patterns of VN@N-dC-1000-$ZnAc_2$-NH_4VO_3 (a), green), VN@N-dC-1000-1:1CsAc/$ZnAc_2$-NH_4VO_3 (b), blue) and VN@N-dC-1000-CsAc-NH_4VO_3 (c), red).

Nitrogen sorption measurements of the composites in Figure 3.9a show that also the surface area, pore size and pore volume can be tuned simply by the nature of the porogen salt.

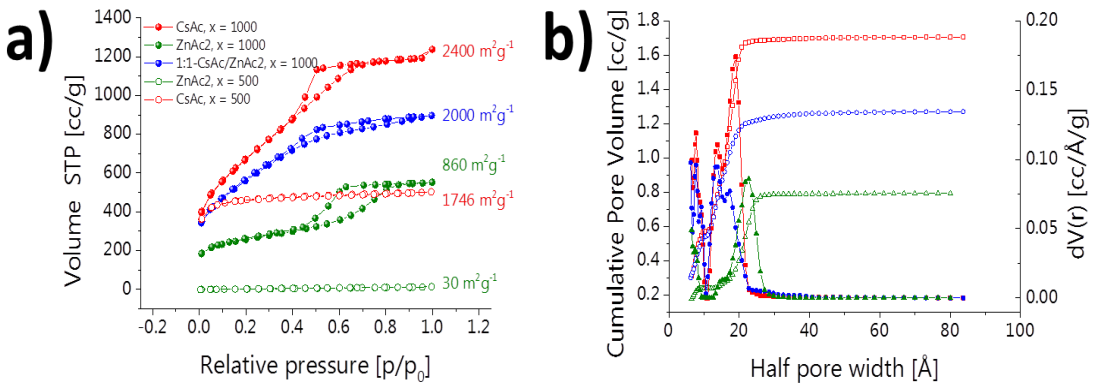

Figure 3.9. a) Nitrogen sorption isotherms and b) PSD of VN@N-dC-1000-$ZnAc_2$-NH_4VO_3 (green), VN@N-dC-1000-1:1CsAc/$ZnAc_2$-NH_4VO_3 (blue) and VN@N-dC-1000-CsAc-NH_4VO_3 (red).

While VN@N-dC-1000-CsAc-NH_4VO_3 solely prepared with CsAc reveals again an isotherm with a small hysteresis loop indicative of small mesopores (about 3.5 nm), the Zn-based material VN@N-dC-1000-$ZnAc_2$-NH_4VO_3 shows a type IV isotherm with a pronounced hysteresis typical for bigger mesopores. The corresponding pore size distribution (PSD) quantifies this behavior with an average pore diameter of 5 nm (Figure 3.9b). The low amount of micropores in VN@N-dC-1000-$ZnAc_2$-NH_4VO_3 is probably due to the smaller VN nanoparticles with their decreased ability to form delamination cracks (thus giving access to the micropores), but the presence of a remainder of zinc oxide structures to block the pores can neither be excluded. Both effects result in an overall lower total pore volume and surface area than the corresponding CsAc-materials. As shown in Figure 3.9 the porosity of a composite prepared with the 1:1-CsAc/$ZnAc_2$ mixture is finally in between the respective values of the pure salt systems. The comparison with composites produced with half the amount of porogen salt is very different to the salt mixture and thereby exclude that the porosity only results from one salt component (Figure 3.9). In general, this orthogonality offers the opportunity to tune the particle size and pore architecture independently by using different amounts and compositions of a porogen salt mixture. Based on these results, a schematic model of the ongoing structural processes during the carbon and composite formation can be drawn (Scheme 3. 1).

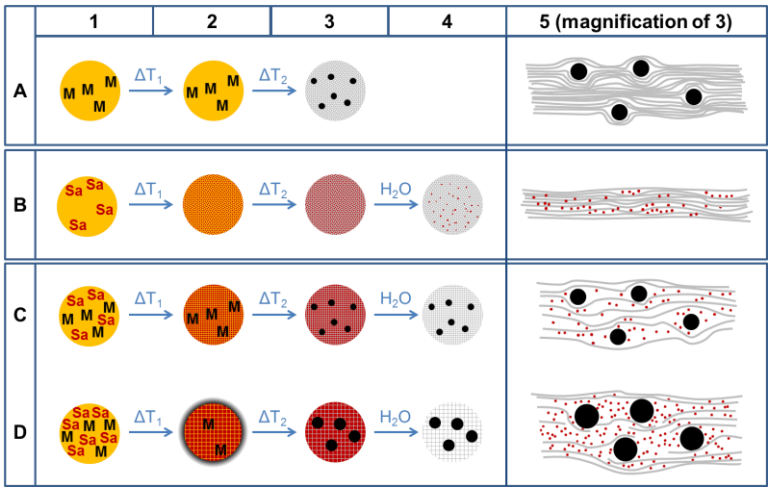

Scheme 3. 1. Stages of product formation using an IL (yellow), a metal precursor (M, black) and salt templating (Sa, red). Precursor mixtures at room temperature (column 1), low heating-temperature (column 2), high/final heating-temperature (column 3, 5 magnification) and after washing (column 4). Salt free composite (row A), salt templated carbon (row B), salt templated composite at low salt concentration (row C) and salt templated composite at high salt concentration (row D).

3.3.3. Electrochemical Characterization of VN@N-dC Composites as Electrode for Ionic Liquid based Supercapacitors

The composites were then tested as electrode materials for supercapacitor in IL electrolyte. Because the synthesis approach offers the possibility to tune the composite porosity simply by the salt amount x, it enables the conduction of a systematic study. Here, water is a very well examined case, but it's naturally restricted operation window prohibits the full utilization of such composites which can in principle also be operated at higher voltage/higher energy density supercapacitors. So, to get a picture of the specific area requirements of such an electric energy storage process, samples were therefore tested in the ionic liquid (IL) electrolytes N-butyl-N-methyl-pyrrolidinium bis(trifluoromethylsulfonyl)imide ($PYR_{14}TFSI$) and N-butyl-N-methyl-pyrrolidinium bis(fluorosulfonyl)imide ($PYR_{14}FSI$), respectively. This gives the opportunity for direct comparison of two differently size counter ions and molecular insights into the energy storage process. In some cases, measurements in ILs are known to rely on bigger pores, due to mass transport properties for the larger ions, the three composites synthesized at the highest amount of salt, i.e. VN@N-dC-1000-CsAc-$VOCl_3$ (S_{BET}~2400 m^2g^{-1}, pore size ~ 1 nm for micro pores and 3 nm for meso pores), VN@N-dC-1000-CsAc-NH_4VO_3 (S_{BET}~2400 m^2g^{-1}, pore size ~ 1 nm for micro pores and 3.5 nm for meso-pore) and VN@N-dC-1000-ZnAc-NH_4VO_3 (S_{BET}~860 m^2g^{-1}, pore size ~ 5 nm), were chosen. One of the best performing commercial activated carbon (PICA)

(S_{BET}~2411 m^2g^{-1}, pore size ~ 1.4 nm) was also used for the sake of comparison [28]. In order to investigate the electrochemical properties of single electrodes, specific capacitance of materials were obtained by cyclic voltammetry (CV) experiments which were performed at room temperature in 3-electrode electrochemical cell. The CV curves at 10 mVs^{-1} as well as the scan rate dependent specific capacitances of the three composites and Pica as the reference material in $PYR_{14}TFSI$ are shown in Figure 3.10. The CVs of VN@N-dC-1000-CsAc-$VOCl_3$ and VN@N-dC-1000-CsAc-NH_4VO_3 are similar to the CV for PICA carbon but show very small humps which are characteristic for pseudocapacitive contributions (Figure 3.10a). This together with high surface areas contributes to very high capacitances (going from ~100 Fg^{-1} at 5 mVs^{-1} to ~30 Fg^{-1} at 100 mVs^{-1}), which are in the range of PICA as one of the best commercial carbons.

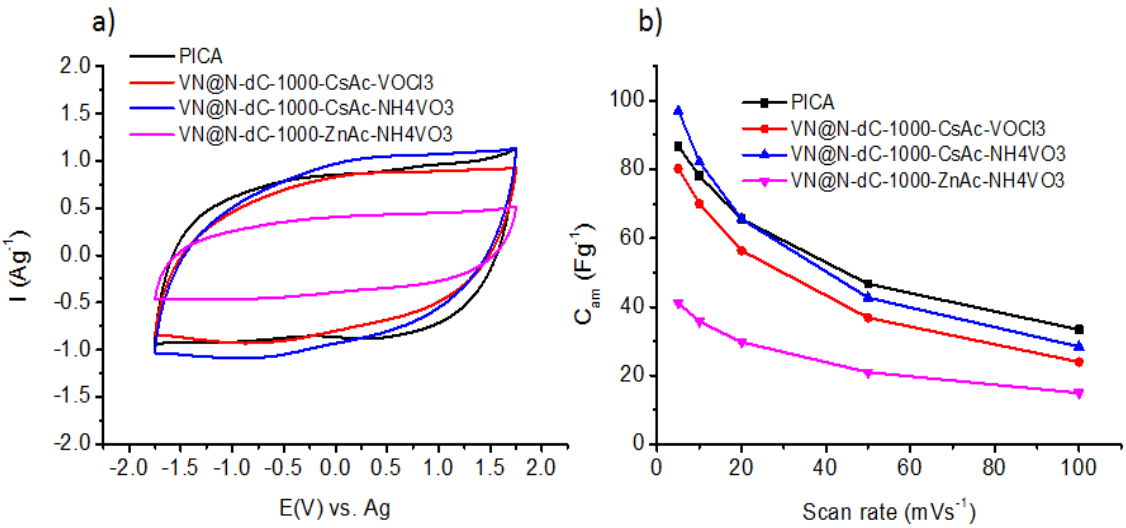

Figure 3.10. a) CVs of VN@N-dC-1000-CsAc-$VOCl_3$ (red), VN@N-dC-1000-CsAc-NH_4VO_3 (blue), VN@N-dC-1000-ZnAc-NH_4VO_3 (pink), and Pica (black) from -1.75 to +1.75 V at 10mVs^{-1} scan rate. b) Specific capacitances vs. the scan rate calculated from CVs performed from -1.75 to +1.75 V in $PYR_{14}TFSI$.

Furthermore, it was confirmed that, even though bigger pores should increase mass transport and guarantee better access of the IL to the surface, the composite with the largest pore size, i.e. VN@N-dC-1000-ZnAc-NH_4VO_3, possesses the lowest capacitance (40 Fg^{-1} at 5 mVs^{-1} and 20 Fg^{-1} at 100 mVs^{-1}). This is probably due to the lower surface area (860 m^2g^{-1}) and the absence of humps in VN@N-dC-1000-ZnAc-NH_4VO_3 indicating a lower accessibility of the nitride nanoparticles by the ionic liquid. This lower accessibility is attributed to the surface effects on the very small VN particles present in this composite (Figure 3.8). The surface redox sites of this composite might

be rather quickly blocked by the comparably big IL ions compared with other composites with relatively bigger VN particles.

Moreover, symmetric supercapacitors were assembled in 2-electrode Swagelok setup in order to evaluate the performance of different composite materials as electrode in full cell supercapacitors. Electrochemical impedance spectroscopy of different supercapacitors using $PYR_{14}TFSI$ as electrolyte is shown in Figure 3.11. In real supercapacitors, the steep rising of the imaginary impedance (y-axis) at lower frequencies accompanied with a semi-circle at the higher frequencies region indicates the formation of double layer capacitance (see Figure 3.11). The semi-circle in the x-axis corresponds to the equivalent series resistance (ESR) which comprises resistance of the electrolyte, resistance of interfaces between the electrolyte and the electrode materials, and charge transfer resistance. The increasing impedance resistance of the composite materials shows the following trend: PICA≤VN@N-dc-1000-CsAc-NH_4VO_3<VN@N-dc-1000-CsAc-$VOCl_3$<VN@N-dc-1000-ZnAc-NH_4VO_3 as shown in Figure 3.11.

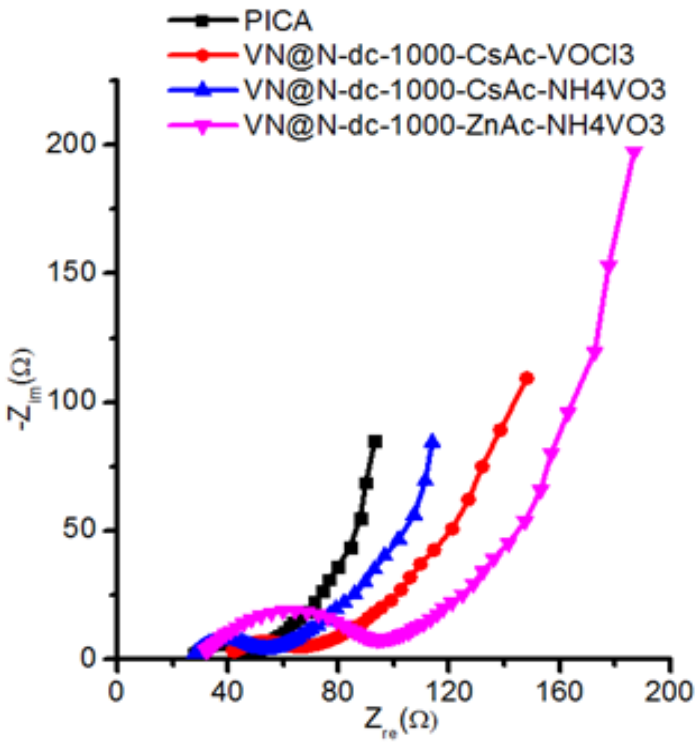

Figure 3.11. Nyquist plot for different supercapacitors assembled with different composite electrode materials at RT and $PYR_{14}TFSI$.

Figure 3.12 show the galvanostatic charge-discharge (CD) profiles for the different symmetric supercapacitors and the values of the resulting electrochemical parameters (ESR, C_{am}, and E_{real}). The representative charge-discharge voltage profile at 10 $mAcm^{-2}$ is shown in Figure 3.12a. All composites show nearly triangular shaped, indicating double layer capacitance behaviour. The two composites, *i.e.* VN@N-dC-1000-CsAc-$VOCl_3$ and VN@N-dC-1000-CsAc-NH_4VO_3 showed comparable

ohmic drop (≈0.5 V) as the commercial carbon probably due the biggest VN ananoparticles of those carbons which migh improve the electrical conductivity of the composite compared to the smaller VN presented by VN@N-dC-1000-ZnAc-NH_4VO_3 composie. Figure 3.12b indicates the ESR of different composite electrodes at different current densities. It shows that the composites with cesium acetate salt exhibit lower range of ESR values (from 15 to 25 Ωcm²) over different current ranges, while the composite with zinc acetate presents the maximum ESR values. Despite the deviation of the values of resistance of composite materials between frequency dependent impedance measurement and current dependent charge-discharge measurement, yet the same trend of resistance is observed in both cases.

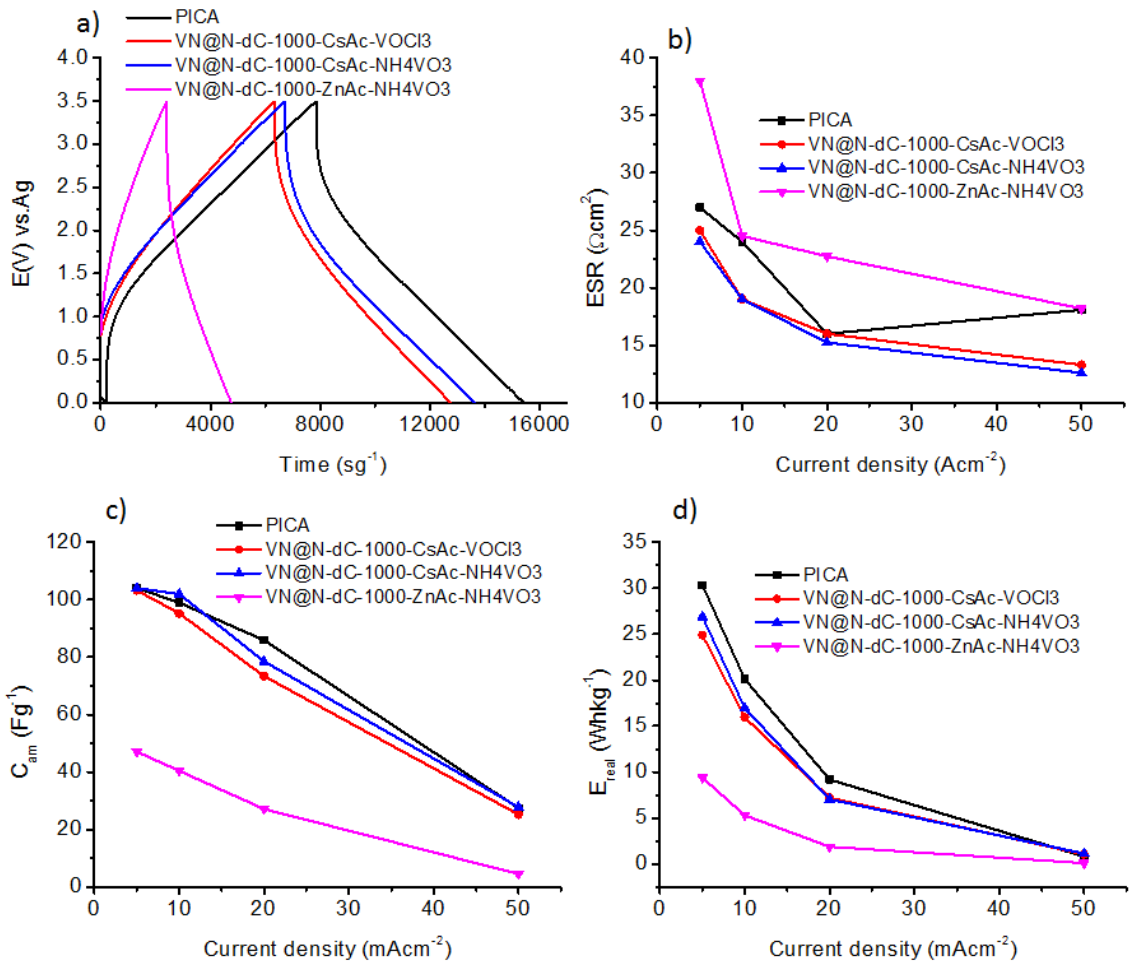

Figure 3.12. a) Galvanostatic charge-discharge profiles of different supercapacitors cycled from 0 V to 3.5 V at 10 mA cm⁻². b) ESR c) Specific capacitances (C_{am}) and d) specific real energy (E_{real}) vs. current density calculated from charge-discharge. Measurements were conducted in 2-electrode setup in $PYR_{14}TFSI$ at RT.

The specific capacitance of each composite electrode calculated at different current densities is displayed in Figure 3.12c. A comparable trend of capacitance as cyclic voltamogram is also observed in the galvanostatic charge-discharge profiles. It

shows that VN@N-dC-1000-CsAc-$VOCl_3$ and VN@N-dC-1000-CsAc-NH_4VO_3 exhibited nearly similar capacitive performance as the commercial carbon electrode (PICA), indicating the synergetic effect of high specific surface area and VN nanoparticles in the carbon structure enhances the capacitance. Infact, these composites with smaller pore sizes but high surface area (2400 m^2g^{-1}), i.e. VN@N-dC-1000-CsAc-$VOCl_3$ and VN@N-dC-1000-CsAc-NH_4VO_3, show superior performance with high real specific energy values of about 27 $Whkg^{-1}$ at low discharge current (5 $mAcm^{-2}$) in PYR_{14}TFSI electrolyte (Figure 3.12d) as compared to the mesoporous and lower surface area (840 m^2g^{-1}) of VN@N-dC-1000-ZnAc-NH_4VO_3.

Figure 3.13 shows CV results in 3-electrode electrochemical cells in PYR_{14}FSI electrolyte. Moving from the bigger anion in PYR_{14}TFSI (0.8 nm TFSI anion) [38] to the smaller anion in PYR_{14}FSI (0.30 nm FSI anion) [39,40], superior electrochemical performance was observed for all composites.

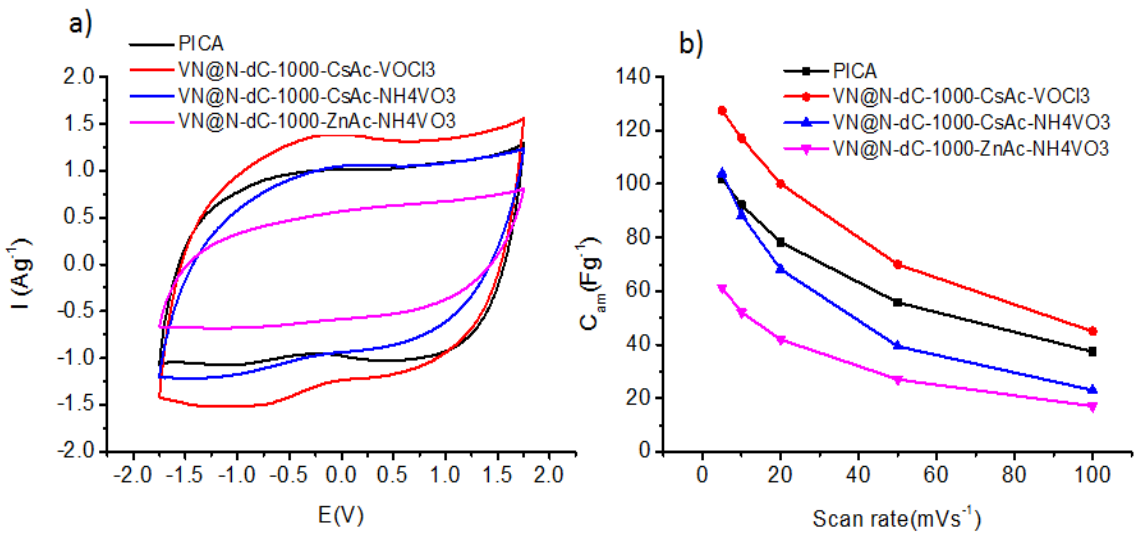

Figure 3.13. a) CVs of VN@N-dC-1000-CsAc-$VOCl_3$ (red), VN@N-dC-1000-CsAc-NH_4VO_3(blue), VN@N-dC-1000-ZnAc-NH_4VO_3 (pink) and Pica (black) from -1.75 to 1.75 V at 10mVs^{-1} scan rate. b) Specific capacitances vs. the scan rate calculated from CVs performed from -1.75 to 1.75 V in PYR_{14}FSI at RT.

With regard to this, the capacitance of composite electrodes in PYR_{14}FSI electrolyte is increased by *ca.* 30 % compared with the capacitance in PYR_{14}TFSI electrolyte. This is probably due to the lower size of FSI anion (0.3 nm) and the higher ionic conductivity of PYR_{14}FSI (4.1 $mScm^{-1}$) compared with ionic conductivity of PYR_{14}TFSI (1.8 $mScm^{-1}$) [41]. In the particular case of VN@N-dC-1000-CsAc-$VOCl_3$, the capacitance is increased from 80 Fg^{-1} in PY_{14}TFSI to 130 Fg^{-1} in PYR_{14}FSI at 5 mVs^{-1}. As the result, the specific capacitance of this composite exceeded by more than 23 % (130

Fg^{-1}) of the capacitance obtained with the commercial PICA carbon (105 Fg^{-1}) as shown in Figure 3.13b.

Symmetric supercapacitors were also assembled in a 2-electrode Swagelok using $PYR_{14}FSI$ as electrolyte. Electrochemical impedance spectroscopy in Figure 3.14 showed that the supercapacitors exhibit lower resistance with $PYR_{14}FSI$ electrolyte compare with the one in $PYR_{14}TFSI$. Comparatively, the resistance of SCs with $PYR_{14}FSI$ electrolyte is decreased by more than 50 % from the resistance in the $PYR_{14}TFSI$ electrolyte, indicating the high diffusion of ions in the bulk electrolyte and in the pores of electrodes. The general trend of resistance of the full supercapacitors in $PYR_{14}FSI$ electrolyte is: VN@N-dc-1000-CsAc-$VOCl_3$<PICA<VN@N-dc-1000-CsAc-NH_4VO_3<VN@N-dc-1000-ZnAc-NH_4VO_3 as shown in Figure 3.14.

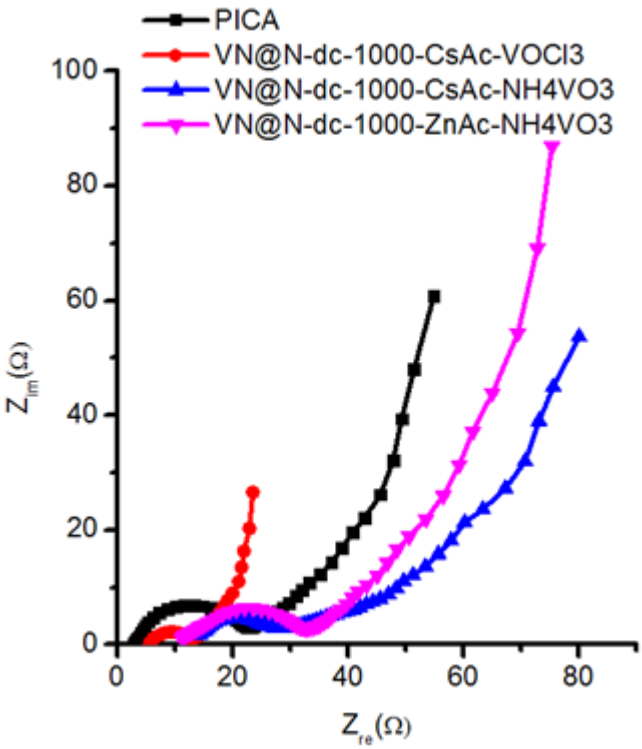

Figure 3.14. Nyquist plot for different supercapacitors assembled with different composite electrode materials at RT and $PYR_{14}FSI$

To complete the full electrochemical characterization, supercapacitors were also subjected to charge-discharge at different current densities (Figure 3.15). The representative charge-discharge voltage profiles at 10 mVs^{-1} indicate the smaller ohmic drop (0.4 V) for VN@N-dc-1000-CsAc-$VOCl_3$ composite while the VN@N-dc-100-ZnAc-NH_4O_3 exhibits the maximum ohmic drop around 1 V (Figure 3.6a). Furthermore, Figure 3.15b shows the value of ESR exhibiting the same trend as the result of impedance spectroscopy analysis (Figure 3.14), as follow: VN@N-dc-1000-CsAc-$VOCl_3$< PICA <VN@N-dc-1000-CsAc-NH_4VO_3< VN@N-dc-1000-ZnAc-NH_4VO_3.

The specific capacitance of each composite and the commercial PICA carbon is shown in Figure 3.15c. It shows that the VN@N-dc-100-CsAc-$VOCl_3$ and VN@N-dc-100-CsAc-NH_4O_3 exhibit the maximum capacitance more than 25 % (125 Fg^{-1}) and 19 % (119 Fg^{-1}), respectively compared with the capacitance stored by PICA carbon (100 Fg^{-1}) at 5 $mAcm^{-2}$, consistent with CV results.

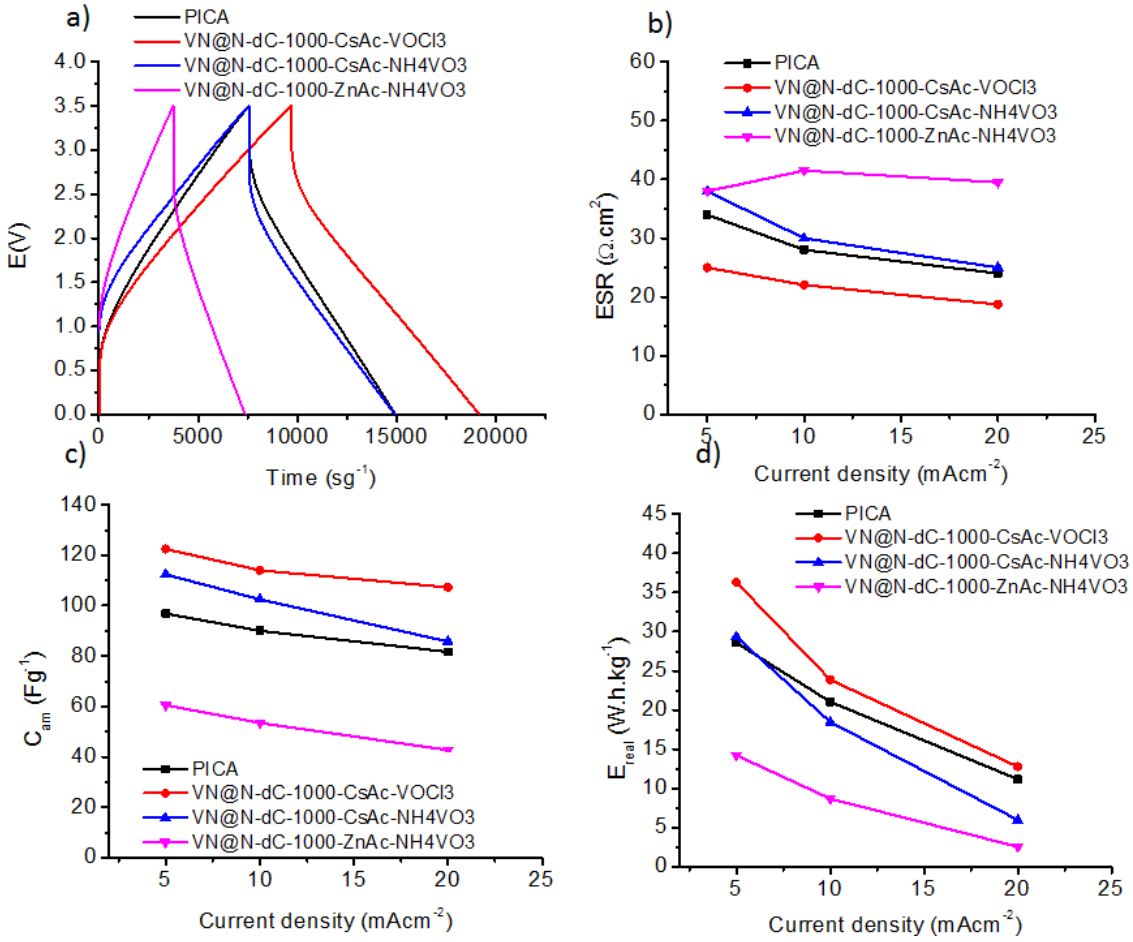

Figure 3.15.a) Galvanostatic charge-discharge profiles of supercapacitors cycled from 0 V to 3.5 V at 10mA cm^{-2}. b) ESR c) Specific capacitances (C_{am}) and d) specific real energy (E_{real}) vs. current density calculated from charge-discharge in $PYR_{14}FSI$.

Interestingly, these composites maintain the capacitive retention as high as >90 % if the charging current increases 4 folds from that of 5 $mAcm^{-2}$. On the other hand, similar to the result in $PYR_{14}TFSI$, the VN@N-dc-100-ZnAc-NH_4O_3 shows the poorest capacitive performance in $PYR_{14}TFSI$ compared with other composites probably due to the lowest value of specific surface area.

Likewise, a further increase in real energy densities can be reached for all composites by using $PYR_{14}FSI$ electrolyte, indicating the improvement of electrode-electrolyte interfaces probably due to the good match between pores of composite and ions of electrolyte. (Figure 3.15d). The maximum real energy density in $PYR_{14}FSI$ is increased by 37 % (37 $Whkg^{-1}$) compared with the one in $PYR_{14}TFSI$ electrolyte, even

exceeding the high performance commercial PICA. Remarkably, the energy storage properties of the PICA carbon seem not to be significantly affected by different IL electrolytes, which hint to the absence of critical steric effects at the redox active sites.

3.4. Conclusion

The facile one-step synthesis of highly porous carbon/metal nitride nanocomposites is presented by calcining a mixture of an ionic liquid as nitrogen/carbon source, a metal precursor and simple salts, i.e. cesium and zinc acetate, as porogen. This technique was illustrated with the preparation of VN nanoparticles embedded in a nitrogen-doped carbon matrix where the surface area, pore volume, pore size, and nanoparticle size can be tuned by the porogen salt amount and salt nature. Additionally, the composite properties can be further adjusted through salt mixtures. The main advantages of the synthesis approach are the formation of a homogeneous starting solution, which can be easily shaped and processed, the simultaneous control of several parameters in just one step and a simple aqueous removal of the porogen after carbonization. This offers the opportunity of tuning the morphologies of the composites from micro- to mesoporous with apparent surface areas up to 2400 m^2g^{-1}.

To describe the effectiveness of the approach, the composites were tested as electrodes in supercapacitors using two different ionic liquid electrolytes: $PYR_{14}TFSI$ and $PYR_{14}FSI$. Since the synthesized composite materials possess widely variable structures, pore sizes, and hybrids, it is important to compare the capacitive performance in two different ionic liquids within the same materials systems. The VN@N doped carbon composites synthesized with the cesium acetate porogen salt (VN@N-dC-1000-CsAc-$VOCl_3$ & VN@N-dC-1000-CsAc-NH_4VO_3) showed better performance than VN@N-dC synthesized with zinc acetate porogen salt (VN@N-dC-1000-ZnAc-NH_4VO_3), indicating that the porogen salt significantly influences the pore properties of as-synthesized composite, in turn, affects their electrochemical performances. Without further optimization, the materials revealed very high capacitances and energy density in both electrolytes, attributable to the higher driving voltage in IL. Generally, the composites with smaller pore sizes (VN@N-dC-1000-CsAc-$VOCl_3$ & VN@N-dC-1000-CsAc-NH_4VO_3) showed a better performance than the material with the higher pore size and smaller specific surface area (VN@N-dC-1000-ZnAc-NH_4VO_3). The high performance of VN@N-dC-1000-CsAc-$VOCl_3$ & VN@N-dC-1000-CsAc-NH_4VO_3) composites resulted from synergistic combination of a high surface area, good electronic conductivity due to the nitrogen-doped carbon matrix, and an intimate contact between VN nanoparticles and the carbon. The VN@N-dC-1000-CsAc-$VOCl_3$ exhibited as high as 125 Fg^{-1} and 37 $Whkg^{-1}$ of specific capacitance

and real energy density, respectively in $PYR_{14}FSI$ electrolyte, which is improved by 23-25 % compared with the capacitive performance of the commercial carbon electrode (PICA) at 5 $mAcm^{-2}$. Since the metal precursors and porogen salts can be varied, the present scheme is expected to be a rather general approach also towards other highly porous carbon/metal nitride composites. This enables future designed custom-made synthesis of materials optimizing their performance both in the field of catalysis or energy storage systems.

3.5. References

[1] G. Xiong, C. Meng, R.G. Reifenberger, P.P. Irazoqui, T.S. Fisher, Electroanalysis 26 (2014) 30.

[2] X. Lu, T. Liu, T. Zhai, G. Wang, M. Yu, S. Xie, Y. Ling, C. Liang, Y. Tong, Y. Li, Adv. Energy Mater. 4 (2014) 1.

[3] X. Lang, A. Hirata, T. Fujita, M. Chen, Nat. Nanotechnol. 6 (2011) 232.

[4] L.F. Chen, Z.H. Huang, H.W. Liang, H.L. Gao, S.H. Yu, Adv. Funct. Mater. 24 (2014) 5104.

[5] P.A. Mini, A. Balakrishnan, S. V. Nair, K.R. V. Subramanian, Chem. Commun. 47 (2011) 5753.

[6] Y. Zhang, H. Feng, X. Wu, L. Wang, A. Zhang, T. Xia, H. Dong, X. Li, L. Zhang, Int. J. Hydrogen Energy 34 (2009) 4889.

[7] Guoping Wang, L. Zhang, J. Zhang, Chem. Soc. Rev. 41 (2012) 797.

[8] P. Jampani, A. Manivannan, P.N. Kumta, Electrochem. Soc. Interface 19 (2010) 57.

[9] X.M. Liu, Z. dong Huang, S. woon Oh, B. Zhang, P.C. Ma, M.M.F. Yuen, J.K. Kim, Compos. Sci. Technol. 72 (2012) 121.

[10] E.S. Steigerwalt, G.A. Deluga, D.E. Cliffel, C.M. Lukehart, J. Phys. Chem. B 105 (2001) 8097.

[11] Z. Chen, J. Wen, C. Yan, L. Rice, H. Sohn, M. Shen, M. Cai, B. Dunn, Y. Lu, Adv. Energy Mater. 1 (2011) 551.

[12] L.L. Zhang, R. Zhou, X.S. Zhao, J. Mater. Chem. 38 (2009) 2520.

[13] R.F. Service, Mater. Sci. 313 (2006) 902.

[14] Y. Zhai, Y. Dou, D. Zhao, P.F. Fulvio, R.T. Mayes, S. Dai, Adv. Mater. 23 (2011) 4828.

[15] H.M. Jeong, J.W. Lee, W.H. Shin, Y.J. Choi, H.J. Shin, J.K. Kang, J.W. Choi, Nano Lett. 11 (2011) 2472.

[16] C. Sassoye, C. Laberty, H. Le Khanh, S. Cassaignon, C. Boissière, M. Antonietti, C. Sanchez, Adv. Funct. Mater. 19 (2009) 1922.

[17] C.M. Ghimbeu, E. Raymundo-Piñero, P. Fioux, F. Béguin, C. Vix-Guterl, J. Mater. Chem. 21 (2011) 13268.

[18] S.D. Perera, B. Patel, N. Nijem, K. Roodenko, O. Seitz, J.P. Ferraris, Y.J. Chabal, K.J. Balkus, Adv. Energy Mater. 1 (2011) 936.

[19] L. Zhao, L.-Z. Fan, M.-Q. Zhou, H. Guan, S. Qiao, M. Antonietti, M.-M. Titirici, Adv. Mater. 22 (2010) 5202.

[20] D. Choi, G.E. Blomgren, P.N. Kumta, Adv. Mater. 18 (2006) 1178.

[21] Z. Ma, X. Huang, S. Dou, J. Wu, S. Wang, J. Phys. Chem. C 118 (2014) 17231.

[22] N. Fechler, T.-P. Fellinger, M. Antonietti, Chem. Mater. 24 (2012) 713.

[23] N. Fechler, T.-P. Fellinger, M. Antonietti, Adv. Mater. 25 (2013) 75.

[24] J. Zhu, K. Sakaushi, G. Clavel, M. Shalom, M. Antonietti, T.P. Fellinger, J. Am. Chem. Soc. 137 (2015) 5480.

[25] S. Zhu, J. Li, C. He, N. Zhao, E. Liu, C. Shia, M. Zhanga, J. Mater. Chem. A 3 (2015) 22266.

[26] P. Kuhn, M. Antonietti, A. Thomas, Angew. Chemie Int. Ed. 47 (2008) 3450.

[27] S. Vaquero, R. Díaz, A. Anderson, J. Palma, R. Marcilla, Electrochim. Acta 86 (2012) 241.

[28] M.M. Jaramillo, A. Mendoza, S. Vaquero, M. Anderson, J. Palma, R. Marcilla, RSC Adv. 2 (2012) 8439.

[29] B.J.P. Paraknowitsch, J. Zhang, D. Su, A. Thomas, M. Antonietti, Adv. Mater. 22 (2010) 87.

[30] J.P. Paraknowitsch, A. Thomas, M. Antonietti, J. Mater. Chem. 20 (2010) 6746.

[31] J. Pérez-Ramírez, C.H. Christensen, K. Egeblad, C.H. Christensen, J.C. Groen,

Chem. Soc. Rev. 37 (2008) 2530.

[32] C.N.R. Rao, A.K. Sood, K.S. Subrahmanyam, A. Govindaraj, Angew. Chemie Int. Ed. 48 (2009) 7752.

[33] J. Lee, J. Kim, T. Hyeon, Adv. Mater. 18 (2006) 2073.

[34] W. Li, F. Zhang, Y. Dou, Z. Wu, H. Liu, X. Qian, D. Gu, Y. Xia, B. Tu, D. Zhao, Adv. Energy Mater. 1 (2011) 382.

[35] Y. Shao, X. Wang, M. Engelhard, C. Wang, S. Dai, J. Liu, Z. Yang, Y. Lin, J. Power Sources 195 (2010) 4375.

[36] J.P. Paraknowitsch, Y. Zhang, A. Thomas, J. Mater. Chem. 21 (2011) 15537.

[37] X. Zhou, C. Shang, L. Gu, S. Dong, X. Chen, P. Han, L. Li, J. Yao, Z. Liu, H. Xu, Y. Zhu, G. Cui, ACS Appl. Mater. Interfaces 3 (2011) 3058.

[38] P. Simon, Y. Gogotsi, Nat. Mater. 7 (2008) 845.

[39] S. Seki, T. Kobayashi, Y. Kobayashi, K. Takei, H. Miyashiro, K. Hayamizu, S. Tsuzuki, T. Mitsugi, Y. Umebayashi, J. Mol. Liq. 152 (2010) 9.

[40] H.-B. Han, S.-S. Zhou, D.-J. Zhang, S.-W. Feng, L.-F. Li, K. Liu, W.-F. Feng, J. Nie, H. Li, X.-J. Huang, J. Power Sources 196 (2011) 3623.

[41] P. Johansson, L.E. Fast, A. Matic, G.B. Appetecchi, S. Passerini, J. Power Sources 195 (2010) 2074.

CHAPTER IV: IONIC LIQUID BASED POLYMER ELECTROLYTE FOR ALL-SOLID STATE SUPERCAPACITORS[3,4]

Most of the results included in this chapter are published as :

[3] "G.A. Tiruye, D. Muñoz-Torrero, J. Palma, M. Anderson, R. Marcilla: All-solid state supercapacitors operating at 3.5 V by using ionic liquid based polymer electrolytes. J Power Sources 2015;279:472–80"

[4] "G. A. Tiruye, D.M. Torrero, J. Palma, M. Anderson, R. Marcilla, 2015: "Desarrollo de Supercondensadores Sólidos mediante el uso de Electrolitos Poliméricos basados en Líquidos Iónicos". REVISTA DE PLÁSTICOS MODERNOS, 2015,109, 702".

CHAPTER IV: IONIC LIQUID BASED POLYMER ELECTROLYTE FOR ALL-SOLID STATE SUPERCAPACITORS

4.1. Introduction

As discussed in chapter I, Electric double-layer capacitors (EDLC) are one promising electrochemical energy storage devices that meet the requirements for applications where high power values and high number of charge-discharge cycles are needed. Despite lower specific energy, SCs exhibit a promising set of characteristics such as higher power density, higher charge-discharge rates, better cycle stability and safer operation than batteries [1–3].

The properties of electrode materials, electrolytes and electrode-electrolyte interfaces significantly determine the performance of SCs [4]. In particular, electrolytes constitute one of the most determining factors for controlling maximum operating voltage, energy density, and safety issues. The main drawback associated with aqueous and organic electrolytes in energy storage devices is their lower electrochemical stability window (ESW), 1 V for aqueous and 2.7 V for organic electrolytes, which results in the lower energy density according to the equation of $E=1/2CV^2$. As discussed in chapter II and III of this PhD Thesis, this problem can be partially solved by using ionic liquid electrolytes (ILs) in supercapacitors whose main advantage is the higher operating voltage (3.5V) and the corresponding energy density that they can achieve in comparison with conventional electrolytes (aqueous and organic electrolytes) [5]. However, the issues associated with the liquid nature of electrolyte such as leakage of electrolyte due to packaging damage and lack of integration among different components (such as separator, electrolytes and electrodes) are still arise serious safety issue [6]. Unless there is a high-standard safety encapsulation material inside the device, leakage of liquid electrolytes will result in poor supercapacitor performance, damage of electrical circuits, environmental and health impacts. Therefore, the need of additional encapsulation materials for liquid based SCs is an inevitable. However, on the other side, the lack of integration between supercapacitor components limit the flexibility and integration of supercapacitors' components in printed circuits or textiles [7].

Nevertheless, these limiting factors can be solved by developing solid or quasi-solid polymer electrolytes that can create opportunities for easily packing and handling,

flexibility, compact, and thin configuration devices. Moreover, devices using these kind of polymer electrolytes can also be volumetrically stable during cell operations, have a long shelf life (storage of supercapacitors in non-operational conditions at constant temperature) due to low internal corrosion, and environmentally safer as there is no leakage of liquid electrolytes [1,3,7,8].

In the past years, different types of polymer or gel electrolytes containing PVA, Chitosan, nafion, etc, have been investigated since they provide high values of conductivity [9–12]. However, due to the water present in the electrolyte, the operating voltage does not exceed 1 V, so that the specific energy was not particularly high. In order to further improve the performance of polymer electrolytes-based SCs, an increase of the operating voltage is a must. In the field of polymer electrolytes, the most recent and promising result are achieved by embedding ILs in a polymer matrix. Several polymer matrices including conventional PAN [13] PVdF-HFP [14,15] PEO [16–18] PVA [19] and PMMA [19] have been investigated in combination with imidazolium ionic liquids (EMImTf, EMImFAP, EMImTFSI, or $EmImBF_4$) to develop solid supercapacitors. For instance, Ramaprabhu, S. *et. al.* assembled all-solid-state SCs by using hydrogen exfoliated graphene (HEG) electrodes and gel like electrolyte composed of 1-butyl-3-methylimidazolium bis(trifluoromethylsulfonyl)imide (BMIMTFSI) incorporated into polyacrylonitrile (PAN/BMImTFSI) with 1:2 weight ratio. The performance of all-solid state SCs was very promising and the result shows specific capacitance (C_{am}), maximum energy density (E_{max}) and power density of 98 Fg^{-1}, 30 $Whkg^{-1}$, and 15 $kWkg^{-1}$, respectively, during charge-discharge at 3 V and specific current of 10 Ag^{-1} [6]. Those results were better than those obtained for supercapacitors using polymer electrolytes using PVdF-HFP or PTFE embedded with similar IL [20,21].

In order to increase the conductivity of the polymer electrolytes, Lewandowski A. *et. al* has investigated the ternary mixture of PAN, $EMImBF_4$ and TSM (Sulpholane, plasticizer and conductivity enhancer) (12:48:40 wt.%) as polymer electrolyte for supercapacitors. It was showed that SCs based on this ternary mixture and activated carbon electrodes stored a maximum capacitance of 200 Fg^{-1} at 1V cell potential [13]. However, the low operating voltage limited the energy density and estimated to be 7 $Whkg^{-1}$ Moreover, other conventional polymers blended with different ratios of imidazolium-based ILs (such as 1-ethyl-3-methyl- imidazolium triflate, $EMImCF_3SO_3$ (EMImTf)) were also used as ionic liquid based polymer electrolyte (IL-b-PE) in solid state SCs with activated carbon electrodes. These IL-b-PE include PAN/EMImTf/TSM (13:56:31), PVA/EMImTf (30:70), PEO/EMImTf (45:55), PMMA/EMImTf (30:70) and (PVDF-co-FHP)/EMImTf (58:42)[22]. Among these polymer electrolytes, the highest conductivity was obtained for PAN/EMImTf/TSM (12:56:32), about 16 $mScm^{-2}$, and

the performance of SCs based on this composition stored a maximum of 230 Fg^{-1} at 0.8 $mAcm^{-2}$ and maximum energy density about 10.5 $Whkg^{-1}$) during charge-discharge at 3 V [22]. The higher capacitance stored in this system is probably due to the smaller ion size of triflate (CF_3SO_3), that could improve its mobility during charge-discharge compared with TFSI ($N(CF_3SO_2)_2$) ion which has the bigger ion size.

In spite of the great effort trying to develop better IL-b-PE for the last decades, only few of the aforementioned examples showed a specific capacitance and rate capability close to the corresponding pure ionic liquid itself. The reason behind is presumably owing to their lower ionic conductivity, less compatibility of the polymer matrix and the ILs embedded in the polymer which can end up with agglomeration, and hence hindering the free movement of ions in the polymer matrix. Moreover, the compatibility of the polymer matrix with the electrode materials, either pore size of the electrode materials or the effective ion size of the polymer electrolytes, also matters for the performance of SCs. More recently, very promising results have been obtained by Ishikawa *et. al.* in which $EMImBF_4$ was successfully incorporated into different polysaccharide matrixes such as alginate and chitosan. In this work, C_{am} was about 131 Fg^{-1} at 2,5 $mAcm^{-2}$ and 2,5V, which is nearly similar to the C_{am} obtained from SCs based on pure $EMImBF_4$ IL electrolyte. The authors concluded that the higher C_{am} stored by SCs with IL based polysaccharides polyelectrolyte was due to the high affinity of polysaccharides for the activated carbon electrodes that leads to a decrease in the electrode/electrolyte interfacial resistance [23–25]. This shows that the compatibility of the electrode materials with the polymer electrolyte itself is significantly important in energy storage devices.

The development of Polymeric Ionic Liquids (PILs), polymers bearing ionic liquids features in their structure, have attracted a growing interest in polymer science [26]. Although PILs already have ionic conductivity due to their ionic character, the conductivity values (10^{-5} S/cm at 30°C) are usually too low for application in devices. Due to the chemical affinity between Polymeric Ionic Liquids (PILs) and ionic liquids (ILs), PILs presents some advantages compared with other conventional polymer matrix to encapsulate-solidify-gelify ILs and to develop tailor-made ionic liquid based polymer electrolytes (IL-b-PE). In general, those IL-b-PE have intermediate ionic conductivity values between pure PILs and pure ILs which depend on the composition but they may be up to 10^{-3} Scm^{-1} at 30°C. In fact, the main advantage is the excellent compatibility between PIL and ILs where phase separation and leakage is minimized as compared to other polymeric matrixes. The formulation of these PILs with their ILs counterparts have been investigated by different authors and applied in different electrochemical devices such as Li-ion batteries [27,28] field-effect transistors [29],

electrochromic devices [30], fuel cells [31] and dye sensitized solar cells [32]. For instance, just to mention few examples, R.Marcilla *et. al.*, reported a promising IL-b-PE by blending PIL (pDADMATFSI) with pure IL ($PYR_{14}TFSI$) and lithium salt (LiTFSI) showing conductivity values about 10^{-4} Scm^{-1} at room temperature. This ternary IL-b-PE was successfully used in all-solid state Li-ion battery showing good capacity values of 140 mAh g^{-1} with very good capacity retention [28]. The reason of selecting that particular PIL/IL couple having both the same anion and similar cation is to create compatible, stable, and homogeneous polymer electrolytes.

It is worth mentioning that most of the IL-b-PEs reported in literature are prepared by blending polymers with imidazolium based ILs. This is due to the higher conductivity of imidazolium ILs which results in high conductivity of IL-b-PE compared with other ILs. Despite the higher conductivity of imidazolium based IL-b-PE, their lower electrochemical stability window (ESW=3V with activated carbon electrodes) limits the operating voltage compared with other ILs such as those based on more stable quaternary ammonium or pyrrodilinium based cations. As a result, the overall capacitive performance of electrochemical energy storage devices using imidazolium ionic liquid based polymer electrolytes will likely to be less appealing in terms of their energy density. Recently, other ILs such as pyrrolidinium based cations have been used to prepare IL-b-PE having a wider range of ESW and being more suitable for applications where high voltages is required such as Li-ion batteries [33].

In this chapter, the performance of all-solid state supercapacitors based on a binary mixture of a pyrrolidinium-based PIL (poly(diallyldimethylammonium)bis(trifluoromethanesulfonyl)imide (pDADMTFSI)) and its corresponding ionic liquid (N-butyl-N-methylpyrrolidinium bis(trifluoromethylsulfonyl)imide ($PYR_{14}TFSI$)) is investigated. Selection of the PIL and IL, both bearing pyrrolidinium cation and TFSI anion, was based on the wide electrochemical stability window of both ions. PICA carbon is a widely used commercial activated carbon that was selected as active material for the preparation of electrodes. The electrochemical performance of all-solid state supercapacitors containing different ratios of IL-b-PE to the active mass of electrodes (IL-b-PE:active mass of electrodes) is also investigated. Although the performance of pyrrolidinium based IL-b-PE in Li-ion battery has been reported in literature, this is the first work in which a polymeric ionic liquid (PILs) is used as a polymer matrix in all-solid state SCs. Especially, the remarkable innovation is the selection of PIL and IL, both bearing pyrrolidinium cation with the final goal of increasing the operating voltage and maximizing the energy density of all-solid SCs.

4.2. Experimental Methods

4.2.1. Materials

Lithium bis(trifluoromethanesulfonyl)imide (LiTFSI, ≥99%) and N-methyl-N-butylpyrrolidinium bis(trifluoromethanesulfonyl)imide, $PYR_{14}TFSI$ (high purity, >99.5%) were purchased from Solvionic and stored in the glove box. Poly(diallyldimethylammonium) chloride solution (pDADMAC) (average Mw 400,000–500,000, 20wt.% in H_2O) was obtained from Aldrich. Acetone (purity >99%) was used for solution preparation. NMP (N-methyl-2-pyrrolidone, analytical grade), polyvinylidenefluoride (PVDF, solution in water, from Aldrich), carbon black (Alfa Aesar GmbH & Co KG, Germany) and activated carbon (Picactif BP 10, PICA) were used to prepare carbon ink. Aluminum foil (25 µm thickness and 99 % purity) from Goodfellow was also used as a current collector.

4.2.2. Synthesis of poly(diallyldimethylammonium) bis(trifluoromethanesulfonyl)imide (pDADMATFSI) and preparation of ionic liquid based polymer electrolyte (IL-b-PE)

Poly(diallyldimethylammonium) bis(trifluoromethanesulfonyl)imide (pDADMATFSI) was prepared by a simple ion exchange reaction from the commercially purchased polymer precursor poly(diallyldimethylammonium)chloride (pDADMAC) and lithium bis(trifluoromethanesulfonyl)imide (LiTFSI) according to the procedure reported elsewhere [34] in more details. First, 8.5 g of LiTFSI salt was dissolved in 10 ml of distilled water. Second, 20 g of a commercial 20 % pDADMAC solution was diluted in 100 ml of distilled water. The stoichiometric excess of salt to polymer of 1.7 ratio was used. Finally, these two solutions were mixed in a 250 ml round bottom flask and stirred for 5 min at room temperature and the resulting white precipitate was filtered and dried at 130 ^{o}C in vacuum overnight and a constant weight is obtained (around 90 % of yield). Finally, the ionic liquid based polymer electrolyte (IL-b-PE) was prepared by dissolving 1.4 g of PIL (pDADMATFSI) in 4 ml of acetone and the mixture was stirred with magnetic stirrer until the polymer dissolves completely. Then 2.1 g of IL ($PYR_{14}TFSI$) was added to the solution drop by drop in order to get a ratio of ionic liquid to polymeric ionic liquid (IL:PIL) of 60:40 by weight. As shown in Figure 4.1, Doctor blade technique was used for casting this solution (IL-b-PE) to obtain self-standing transparent membranes of about 60 µm thickness. The membrane was used for physico-chemical characterization and ionic conductivity measurement. It was dried at 130 ^{o}C under vacuum overnight before characterization. This 60:40 ratio was initially selected because it provided self-standing membranes with an optimum

balance between mechanical stability and ionic conductivity that have been successfully used lithium-ion batteries [28].

4.2.3. Preparation of Carbon Electrodes

PICA carbon being the active material, carbon black and PVDF (80:10:10) were mixed with 25 ml of N-methyl-2-pyrrolidone (NMP) and added into a ball mill grinder operated at 250 rpm for 30 minutes to obtain homogeneous carbon ink. Carbon electrodes were prepared by casting the carbon ink on the aluminum current collector (25 µm thickness and 99 % purity) using doctor blade technique. Finally, the electrodes were dried at 80 °C overnight and cut in to a coin-like shape (diameter=12 mm). The final carbon electrodes have a thickness of about 100-160 µm corresponding with a carbon mass loading of about 2-4 mg cm^{-2}.

4.2.4. Electrode Impregnation and All-Solid State Supercapacitors Assembling

It is worth noting that the typical procedure of assembling all-solid solid state supercapacitors is sandwiching a free standing membrane between two carbon electrodes. Nevertheless, this procedure was not suitable since the effective area of carbon electrode was limited to only the projected surface area of the membrane and the micropores of electrodes were not filled with polymer electrolytes and this situation doesn't contribute to the double layer formation. Therefore, to solve this problem, IL-b-PE solution was prepared by dissolving 1.4 g of pDADMATFSI in 4 g of acetone. Next, 2.1 g. of $PYR_{14}TFSI$ were added to the solution in order to obtain a ratio of 60:40 (IL:PIL in weight). Then carbon electrodes were impregnated with polymer electrolytes in such a way that different amount (from 20 µl to 80 µl) of IL-b-PE solution was added with a micropipette onto the surface of carbon electrode to obtain electrodes with different ratios of IL-b-PE to active material (ratios from 5 to 18). The IL-b-PE solution was easily seeped through porous carbon electrode and hence the pores of carbon electrode could be filled with IL-b-PE, and at the same time the surface of the electrode was covered with thin film of IL-b-PE. In order to facilitate the impregnation process the impregnated electrodes were kept under vacuum for 1 hour. Then, the impregnated electrodes were dried at 130° C under vacuum overnight.

After drying, the impregnated electrodes were weighted in order to calculate the mass ratio of IL-b-PE to activated carbon presented in each carbon electrode by measuring the weight of carbon electrodes before and after impregnation. Electrodes having different IL-b-PE to active mass ratios (5, 7, 13, 15, and 18) were prepared. Finally, all-solid state symmetric supercapacitors were assembled by facing two impregnated electrodes, which have equal active mass and impregnation ratios, in 2-

electrode Swagelok® cell. Since the IL-b-PE thin layer on the electrode surface is served both as solid electrolyte and as separator, there is no need to add further separator in between two electrodes. Five SCs were assembled having different ratios of IL-b-PE to active mass (5, 7, 13, 15, and 18).

The general flow chart from synthesis of PIL and IL-b-PE to assembling of all solid state SCs is shown in Figure 4.1 below.

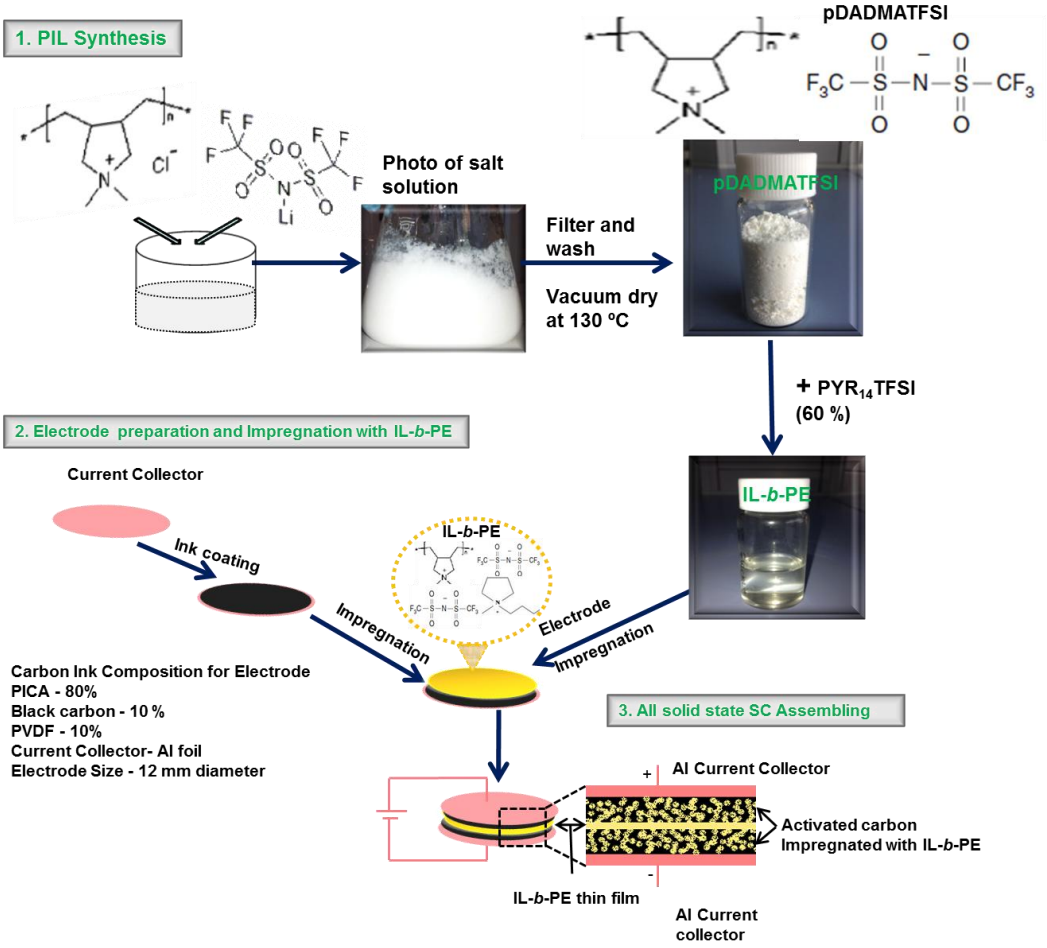

Figure 4.1. Block diagram of PIL synthesis, electrode preparation, impregnation, and all-solid state assembling used in this work.

4.2.5. Physico-Chemical Characterizations

Thermogravimetric analysis (TGA) of IL-b-PE and individual components were performed with DSC-TGA equipment (T.A. Instrument, model SDT Q600) by heating the samples from 30 to 650 °C (heating rate 5 °C min^{-1}) under air flow rate of 100 ml min^{-1}. Scanning electron microscopy (SEM) images of the carbon electrodes (both impregnated and non-impregnated electrodes) were taken by using Table Top Microscope (Hitachi TM-1000) at 15 KV accelerating voltage under vacuum. Both

horizontal and cross-sectional images of the samples were obtained. Moreover, to determine the presence of IL-b-PE in the cross-section of impregnated electrode, EDX analysis, coupled to SEM microscopic, was performed. Fourier transform infrared (FTIR) spectra were measured in a Thermo scientific instrument (Thermo NICOLET 6700) operating in a diffuse reflectance mode (DRIFT). The FTIR spectrum was collected after 128 scans at a resolution of 4 cm−1 in the range of 4000-500 cm−1.

Ionic conductivities (σ) of IL-b-PE membrane at different temperatures (from -30 to 120 ºC) were obtained by Electrochemical Impedance Spectroscopy (EIS) using a Bio-logic VMP3 multi-channel potentiostatic-galvanostatic system with an impedance module. The experiment was carried out with 2-electrode Swagelok® cell in which a coin-like shaped membrane (0.785 cm^2 area and 60 µm thickness) was sandwiched in between two stainless steel pistons. Different temperatures were programmed by environmental chamber (BINDER, Model MK 53 (E2)) interfaced with APTCOM3 software. Each temperature was stabilized for at least 1h before each measurement begins. The frequency range was varied from 1 MHz to 10 mHz at the bias voltage of 0 V with a potential amplitude of 10 mV. Ionic conductivity (σ) for each temperature was calculated using the following expression; $\sigma\ (Scm^{-1}) = t/R{\cdot}A$, where, t is the thickness of the membrane (cm), A is geometrical area of the membrane (cm^2) and R is the resistance calculated by the intercept of the curve with the real axis on a Nyquist plot (Ω).

4.2.6. Electrochemical Characterization of All-Solid State Supercapacitors

Electrochemical behavior of all-solid state supercapacitors was determined by Impedance Spectroscopy followed by galvanostatic charge-discharge (CD) experiments using a multichannel Bio-Logic VMP3 at room temperature (RT) and at 60 ºC. Impedance experiments were performed over a frequency range of from 200 kHz to 10 mHz at the bias voltage of 0 V with 10 mV amplitude. CD experiments were conducted from 0 to 3.5 V at different current densities: 5, 2, 1 mA cm^{-2}. From CD experimental data, specific capacitance (C_{am}), equivalent series resistance (ESR), and real specific energy (E_{real}) for full supercapacitor were calculated as shown in *eqn.2.2 to eqn.2.6 in* Chapter II.

4.3. Results and Discussion

4.3.1. Characterization of the Ionic Liquid based Polymer Electrolyte (IL-b-PE)

The anion exchange reaction for the synthesis of pDADMATFSI polymer matrix was confirmed by FTIR. Figure 4.2 shows that the spectra of hygroscopic precursor pDADMAC displays a strong peak around 3400 cm-1 corresponding to OH group from

water. However, after blending the polymer matrix with pure ILs, FTIR spectra of pDADMATFSI shows the disappearance of strong peak at higher wave number (3400 cm^{-1}) and new peaks at 1050, 1140, 1180 and 1350 cm^{-1} appeared. These new peaks are attributed to the exchanged TFSI anion confirming the successful anion exchange reaction during the synthesis of the polymer [34]. FTIR spectra of pure IL ($PYR_{14}TFSI$) and IL-b-PE show the same peaks corresponding to the TFSI anion also present in those compounds.

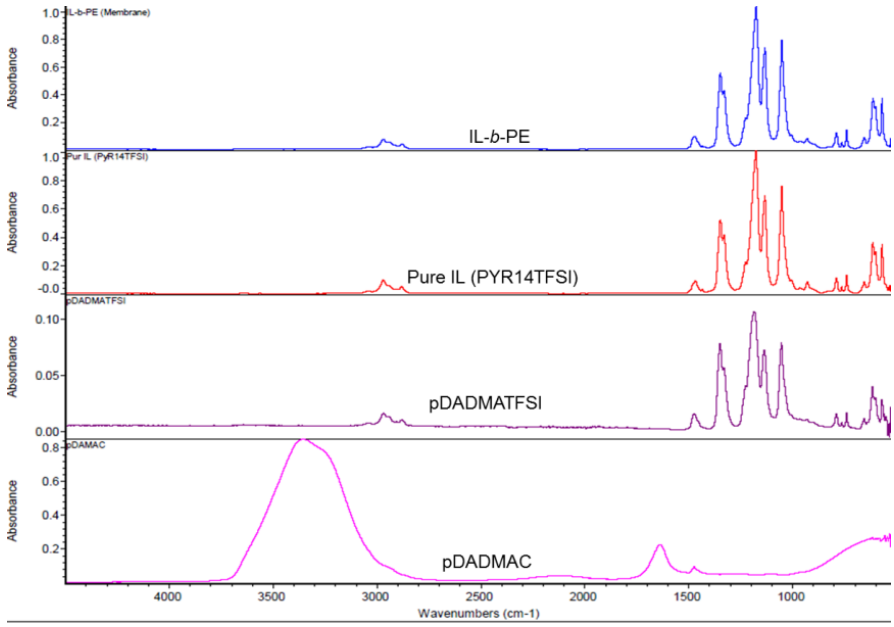

Figure 4.2. FTIR graph for the precursor (pDADMAC), pure PIL (pDADMATFSI), pure IL ($PYR_{14}TFSI$) and IL-b-PE.

Thermal properties of the precursor pDADMAC, polymer matrix (pDADMATFSI), pure ionic liquid $PYR_{14}TFSI$ and formulated IL-b-PE are illustrated in Figure 4.3. TGA of precursor pDADMAC showed a weight loss of about 15 % below 200 ºC probably due to evaporation of adsorbed water. A much more significant weight loss was observed beyond 300 ºC corresponding to thermal degradation of the polymer. Figure 4.3 also shows that thermal stability of pDADMATFSI outperforms its precursor pDADMAC since weight loss is observed only beyond 350ºC [26,34]. The pure IL ($PYR_{14}TFSI$) presents the higher thermal stability (about 400 ºC) and the IL-b-PE presents an intermediate stability between pDADMATFSI and $PYR_{14}TFSI$. Moreover, all the samples containing the TFSI anion exhibit no weigh loss at low temperatures being good evidence for the non-hygroscopic nature of those materials. This is particularly convenient for electrolytes since the presence of water can result in inferior electrochemical performance.

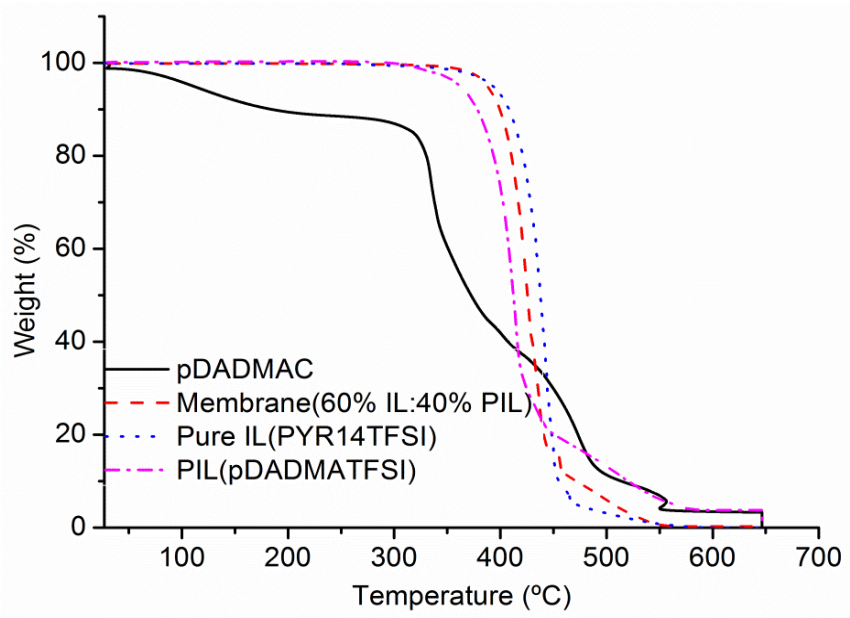

Figure 4.3. TGA of Pure IL ($PYR_{14}TFSI$), precursor pDADMAC, pDADMATFSI, and IL-b-PE (60 % w/w of $PYR_{14}TFSI$) (heating rate: 5 °C min-1 under air).

The ionic conductivity of the free-standing IL-b-PE (PYR14TFSI 60 % w/w) was determined by impedance spectroscopy. Figure 4. 4 depicts the conductivity values of the membrane at different temperatures showing values from 10^{-7} Scm^{-1} at low temperatures (-30 °C) to 27 $mScm^{-1}$ at high temperatures (120 °C). The values at 25 °C and 60 °C are $5*10^{-4}$ Scm^{-1} and $3*10^{-3}$ Scm^{-1}, respectively. The slight curvature observed in the Arrhenius plot is in good accordance with the Vogel-Tamman-Fulcher (VTF) model. This feature is commonly seen in amorphous polymer electrolytes being in good agreement with the amorphous nature of the polymer matrix and with the plasticity provided by the $PYR_{14}TFSI$. The conductivity values obtained in this work are in good agreement with the conductivity values reported in literature for similar IL-b-PE [34].

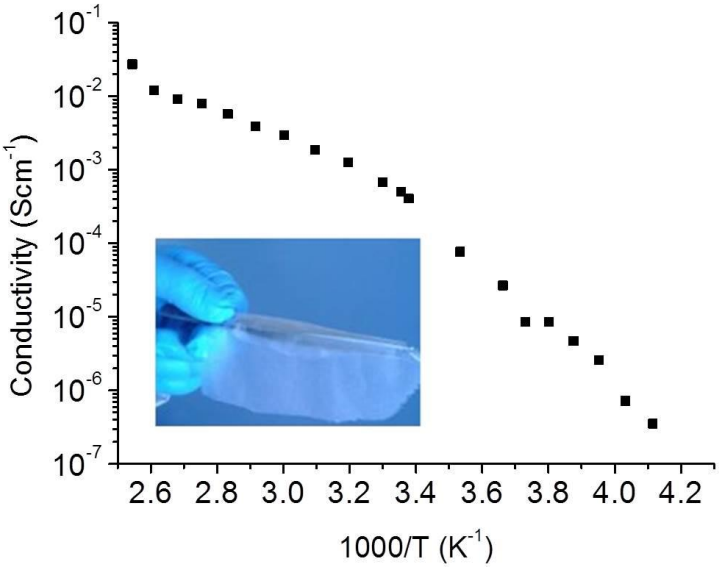

Figure 4. 4. Arrhenius plot of ionic conductivity (σ) of IL-b-PE membrane (60 % wt. of $PYR_{14}TFSI$) and photo of free standing membrane (inset).

4.3.2. Impregnation of Carbon Electrodes with IL-b-PE

First, porous carbon electrodes using PICA carbon (S_{BET}~2000-2400 m^2g^{-1}) were prepared on an Al current collector. Impregnated carbon electrodes were then prepared by spreading an acetone solution of IL-b-PE on the top surface of carbon electrodes, letting the solvent to evaporate. Schematic representation of zoomed layers in the structure of impregnated carbon electrode is presented in Figure 4.5.

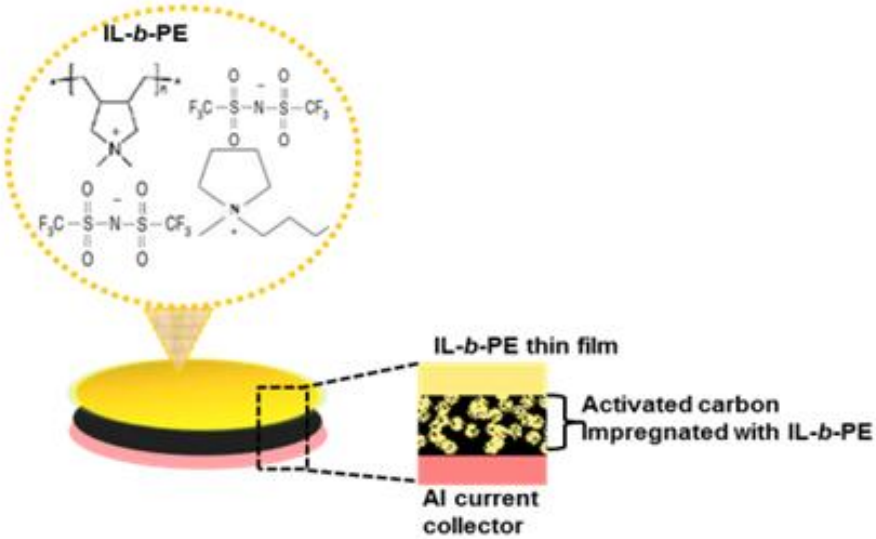

Figure 4.5. Schematic representation of impregnated carbon electrode including the chemical structure of IL-b-PE.

Figure 4.5 illustrates how the IL-b-PE should fill the pores of activated carbon and also remain as a thin film on the top surface of carbon electrode. Electrodes with different weight ratio of IL-b-PE to active mass of electrodes ranging from 5 to 18 were obtained by varying the amount of electrolyte solution.

To analyze the morphology of impregnated carbon electrodes and to evaluate the feasibility of the method, SEM images were taken at horizontal (Figure 4.6) and cross-sectional views (Figure 4.7).

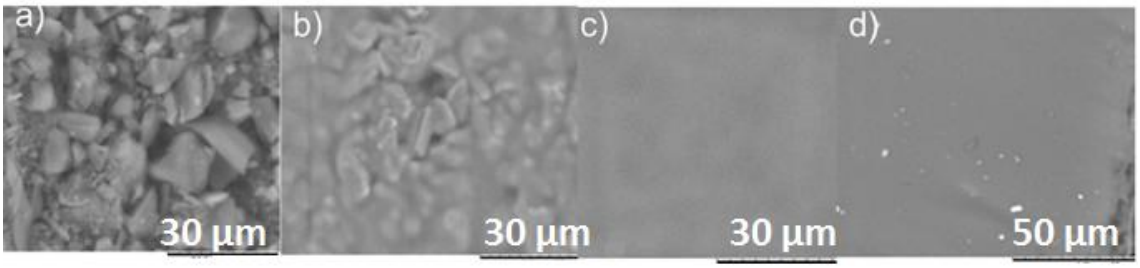

Figure 4.6. Horizontal (top) SEM images for carbon electrodes with different impregnation ratios a) non-impregnated, b) ratio ≤5, c) ratio 7, and d) ratio 15.

Horizontal (top) view images were used to determine whether the IL-b-PE covers the electrode surface homogeneously at different impregnation ratios. The surface of non-impregnated carbon electrode is also presented in Figure 4.6a, showing the presence of PICA carbon particles about 15-20 µm diameter. Figure 4.6b shows the SEM image of the electrode with the lower impregnation ratio (≤5) where carbon particles, resembling the non-impregnated electrode, are visible underneath a very thin layer of IL-b-PE. Thus, an impregnation ratio lower than 5 was not enough to cover homogeneously the surface of carbon electrodes. In Figure 4.6c & d a homogeneous layer of IL-b-PE was observed demonstrating that impregnation ratios of 7 and 15 perfectly coat the electrode surface with a thin film of IL-b-PE. As a result, carbon particles underneath were not observed as the case of electrode impregnated with lower ratio. It is worth noting that this outer IL-b-PE compact layer is necessary to avoid short-circuits during all-solid state supercapacitor operation. Figure 4.7 shows the cross-sectional view of SEM images used to determine the thickness of the outer layer of IL-b-PE with different impregnation ratios. For the sake of comparison, SEM of non-impregnated carbon electrode is also shown in Figure 4.7a.

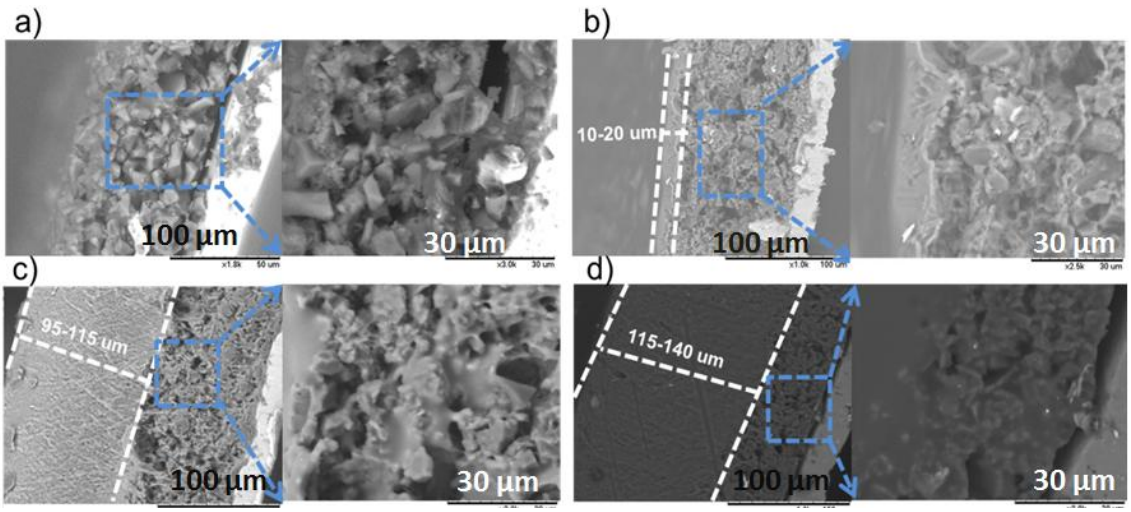

Figure 4.7. Cross-sectional SEM images of a) non-impregnated carbon electrode, and electrodes with different impregnation ratios b) ratio ≤5, c) ratio 7 and d) ratio 15. Zoom images of cross-section view are included right next to the corresponding impregnation ratios.

As expected, the thickness of the outer film of IL-b-PE increases with increasing impregnation ratios of IL-b-PE to active mass of the electrode. Figure 4.7b shows that with impregnation ratio equal or lower than ≤5, the thickness of IL-b-PE thin film was not higher than 15-20 µm (in some parts of the electrode this layer was not even visible). Moreover, magnified image also confirmed that the carbon particles within the electrode were not completely covered by IL-b-PE. Figure 4.7c and d show a polymer outer layer thickness about 95-115 µm for impregnation ratio of 7 and 115-140 µm for impregnation ratio of 15. By using these impregnation ratios, one could see that the electrodes were very well impregnated and internal carbon particles and carbon pores were completely covered by polymer electrolyte. This was confirmed by mapping elemental sulfur (S) using EDX (coupled to the SEM microscope) detecting the presence of sulfur (S)IL-b-PE all along the thickness of electrodes.

Using EDX analysis, sulfur, S atom, which is only present in TFSI anion from IL-b-PE, was detected in the cross-section view of impregnated electrodes and confirmed well impregnation in which the electrolyte is seeped deep into the pores of carbon. The weight percentage peak of S atom in the-impregnated carbon electrodes is as high as 92 % as shown in Figure 4.8. This shows that the IL-b-PE are well seeped into the porous carbon electrodes and results in well impregnated carbon electrodes. It is worth mentioning that since symmetric supercapacitors were assembled in 2-electrode Swagelok® cell by facing two impregnated electrodes, the outer IL-b-PE layer of each impregnated electrode will contribute to the resistance of the whole device.

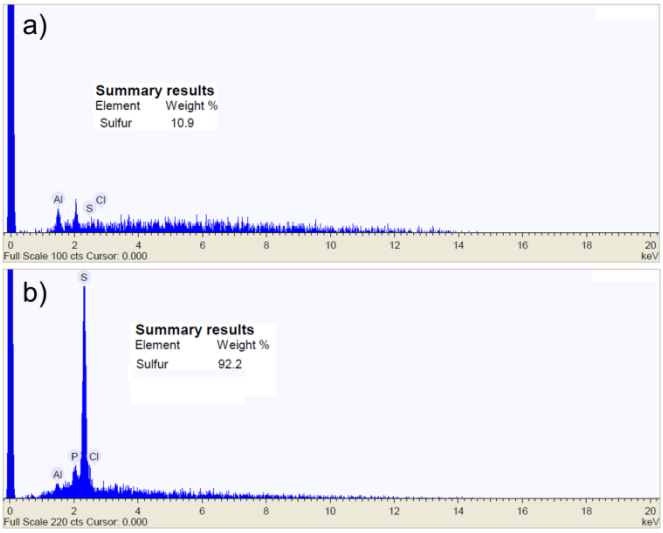

Figure 4.8. EDX analysis of sulfur atom at the cross-section of electrodes a) for non-impregnated b) impregnated electrode with IL-b-PE

4.3.3. Electrochemical Characterization of All-Solid State Supercapacitors

Here, it is worth reminding that at the beginning, solid state SCs prototypes were assembled by sandwiching a self-standing IL-b-PE membrane in between two non-impregnated carbon electrodes. However, the performance of those all-solid state SCs was very poor since the micro pores of PICA carbon were not filled with polymer electrolytes. In this case, the carbon-electrolyte interface, which is proportional to the double layer capacitance, is limited only to the geometric or projected surface area of the electrode, consequently results in very low capacitance storage. In other words, the area of the electrode accessible to the ions of electrolyte is negligible compared with convectional SCs in which carbon pores are flooded with liquid electrolyte where the carbon–electrolyte interface is almost equal to the specific surface area of the carbon itself. Therefore, to increase charge storage in solid state SCs, it is quite clear that the carbon-electrolyte interface need to be improved [4] . As a result, in order to improve the carbon electrode-electrolyte interface, each carbon electrode was impregnate with IL-b-PE solution before assembling SCs, as explained in experimental section. Then, all-solid state SCs were assembled by facing two impregnated carbon electrodes in 2-electrode Swagelok® cell. Here, it is important to keep in mind that the thickness of IL-b-PE layer in the final device is the sum of the thickness of outer layer (thickness of thin film on the electrode surface) from both electrodes.

All-solid state supercapacitors with different ratios of IL-b-PE to active mass (5, 7, 13, 15, and 18) were assembled and characterized by impedance spectroscopy and galvanostatic charge discharge (CD) techniques. From now on, the term SCX, where SC

stands for supercapacitors and X stands for different impregnation ratios (5, 7, 13, 15 or 18) will be used in the text for the sake of clarity.

4.3.4. Electrochemical Impedance Spectroscopy (EIS)

Nyquist plots of all-solid SCs with different impregnation ratios were obtained both at RT and at 60 ºC. Nyquist plot at RT are presented in Figure 4.9.

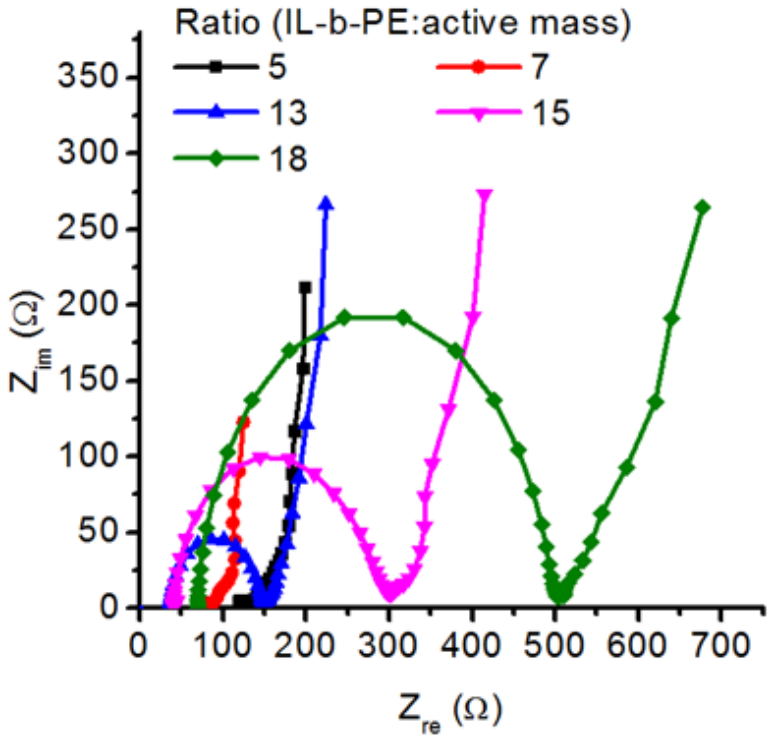

Figure 4.9. Nyquist plots for all solid-state supercapacitors having different impregnation ratios (SC5, SC7, SC13, SC15 and SC18) at RT, and Equivalent circuit of the system in this study, where Rs solution or bulk resistance, Rct charge transfer resistance, Zw Warburg diffusion element Cdl double layer capacitance and CL limiting capacitance at lower frequencies.

In ideal double layer capacitors, the Nyquist plot is a straight line parallel to y-axis (imaginary axis, $-Z_{im}$). But in the case of real supercapacitors, the steep rising impedance behavior is observed at lower frequencies accompanied with semi-circle at higher frequencies. The intersection of the semi-circle with X axis (Z'_{real}) corresponds to the equivalent series resistance (ESR) that are associated to different resistances including R_s - solution or bulk electrolyte resistance and R_{ct} interfacial charge transfer resistance. As it can be seen from Figure 4.9 in all cases, capacitive behavior of SCs was detected by the steep increasing vertical line of impedance plots in the low frequency

region. Figure 4.9 shows that ESR increases with increasing impregnation ratios with the lowest value of 95 Ω cm^2 for SC7 having an IL-b-PE average thickness (t) of about 210 µm. ESR for SC13 (t = 240 µm), SC15 (t= 255 µm) and SC18 (t= 300 µm) were 170, 340 and 500 Ωcm^2, respectively. This is in good agreement with the increasing thickness of the intermediated layer that causes higher resistance in the final device. Therefore, maintaining the optimum ratios of IL-b-PE to active material of the electrode is very important in all-solid state SCs.

4.3.5. Galvanostatic Charge-Discharge (CD)

In order to further investigate the electrochemical performance of impregnated electrodes, all-solid state supercapacitors were also characterized by galvanostatic charge-discharge (CD) from 0 to 3.5 V at different current densities. The electrochemical parameters (C_{SC}, C_{am}, ESR and E_{real}) for all solid-state SCs were calculated from CD profiles according to *eqn.2.2 to eqn.2.6*. It is worth noting that it was possible to perform CD in solid state SCs at an operating voltage as high as 3.5 V reversible, with coulombic efficiency ≥ 95 % in all cases.

Figure 4.10a shows the typical CD voltage profiles from 0 to 3.5V at 1 mAcm-2 for different SCs assembled in a 2-electrode Swagelok® cell. All SCs exhibit a triangular shape corresponding to an electrical double layer capacitor (EDLC). The charge-discharge profiles reveal that ohmic drop increases with increasing impregnation ratios (corresponding to increasing thickness of IL-b-PE between electrodes). In fact, ESR derived from CD profiles (Figure 4.10b) shows the following trends: SC7 < SC5 ≤ SC13 < SC15< SC18 which is in good agreement with impedance results discussed above. Figure 4.10c depicts the specific capacitance (C_{am}) of all solid state SCs for different impregnation ratios at different current densities. Similar to conventional SCs with liquid electrolytes, C_{am} decrease when current density increases in all cases. This is due to ion diffusion limitation in IL-b-PE at higher current density which results in less accommodation of ions in the pores of carbon electrodes. In other words, at higher current density, ions, which are expected to create polarization followed by accommodation of charges at the surface of carbon electrodes, get less time to diffuse into the pores of carbon electrodes. The highest and the lowest C_{am} at 1 mA cm^{-2} were found to be 100 Fg^{-1} (ratio 7) and 80 Fg^{-1} (ratio 5), respectively. These maximum values are similar to C_{am} values obtained from SCs based on Pica carbon electrodes and pure IL, $PYR_{14}TFSI$ electrolyte (105 Fg^{-1}) at 5 $mAcm^{-2}$ and 3.5 V, as depicted in Chapter III. These results provide additional evidence that the impregnation of IL-b-PE was successful and most of the pores were completely covered by IL-b-PE contributing the formation of electrode-electrolyte double layer formation. Even though, C_{am} values

were not very different for several impregnation ratios, the following trend was found: SC7 > SC13 > SC15> SC18 > SC5.

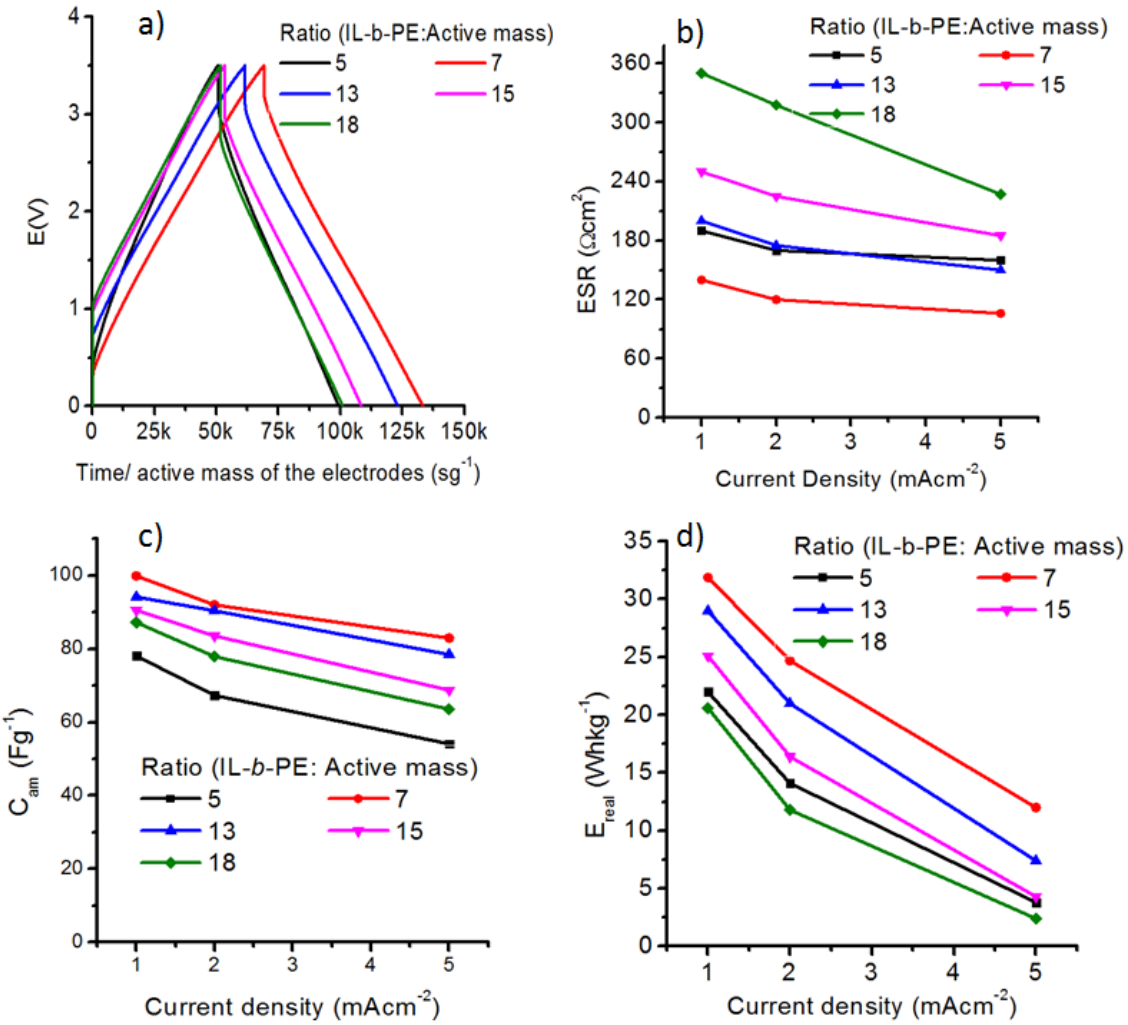

Figure 4.10. Electrochemical characterization of a full all-solid state Supercapacitors with different impregnation ratios at RT a) representative of Charge-discharge (CD) for full SCs at 1mAcm^{-2} b) ESR c) specific capacitance (C_{am}) and d) real energy (E_{real}) at different current densities

Figure 4.10d represents the real energy density (E_{real}) for different all-solid state SCs with different impregnation ratios at different current densities. It shows that, in all cases, the E_{real} values, which are proportional to the area under CD profile curves, rapidly decreased with increasing current densities. This is due to the observed increasing of ohmic drop that reduces the area under the curve at higher current densities. All-solid state SCs with 7 impregnation ratio (SC7) stores a maximum E_{real} of 32 Whkg^{-1} , which corresponds to the maximum $C_{am,}$(100 Fg^{-1}) at 1 mAcm^{-2} being equivalent to the E_{real} obtained from SCs based on the PICA carbon electrodes and pure $PYR_{14}TFSI$ electrolyte (E_{real} ≈30 Whkg^{-1} at 5 mAcm^{-2} and 3.5 V), as detailed in Chapter

III. The E_{real} for all solid state SCs with different impregnation ratios is as follow: SC7 > SC13 > SC15 > SC5 > SC18. As it has been discussed above, it is obvious that the higher impregnation ratios will ensure a homogeneous impregnation in the pores of carbon electrodes; however, it might also create a very thick intermediate IL-b-PE layer increasing the resistance in the supercapacitor, thus decreasing their electrochemical performance.

In this sense, we highlight here that the lowest capacitance value is obtained with SC5 due to the less coverage of carbon particles by IL-b-PE. Since the electrode is not well impregnated with IL-b-PE, it might be difficult for the ions to diffuse through the pores even at the lower current density in which the ions can have enough time to diffuse into pores of electrode. As a result the capacitance of SC5 is decreased compared with higher impregnation ratios. Moreover, it is worth reminding that the values C_{am} and E_{real} are normalized by the total mass of active material of electrodes. So, part of carbon in the electrode might not be used for charge storage due to poor impregnation with IL-b-PE but it is considered in the total mass of the electrode for calculation of specific capacitance and real energy density. In the case of SC5, the values of C_{am} and E_{real} are lower because some parts of the carbon in the electrode might not be in contact with electrolyte so it does not contribute to the charge storage. Therefore, especially in the case of all solid state SCs, in addition to other factors the values of C_{am} and E_{real} will depend on how the electrodes were well impregnated.

To grasp clearly this idea, the schematic representation of lower and higher impregnation ratios of IL-b-PE to active materials is schematically depicted in Figure 4.11. The schematic representation is exactly mimicked from the impregnated electrodes shown by SEM microscopy. It represents the comparative illustration of the carbon electrodes impregnated with IL-b-PE at low and high impregnation ratios. With a low impregnation ratio (ratio ≤5), not all part of the carbon electrode was impregnated by IL-b-PE which is represented by the arrows pointing downwards in the carbon pores (Figure 4.11a). Even the layer of IL-b-PE at the surface of electrode is not coated homogeneously, showing that a very thin layer of IL-b-PE wrinkled on the rough surface of carbon electrode and this will not be good as it could create a short circuited during supercapacitors operations. On the other hand, with high impregnation ratios (Figure 4.11b), the IL-b-PE electrolyte is well distributed deep into the pores of carbon electrodes showing that pores of carbon are being effectively impregnated with IL-b-PE electrolyte which is good for CD process. However, impregnating carbon electrodes with very high amount of IL-b-PE electrolyte also has a drawback in the sense that the thickness of film on the carbon surface will be very high resulting in a large resistance which is undesirable in any electrochemical energy storage devices. Therefore, for all

solid state SCs one has to make sure that the impregnation ratio must be optimized accordingly; both very low and very high impregnation ratios significantly limit the capacitive performance of all-solid state SCs.

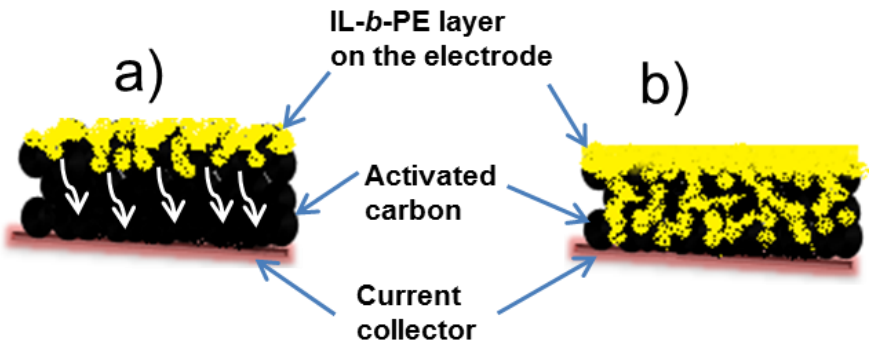

Figure 4.11. Schematic representation of impregnated carbon electrodes with IL-b-PE a) lower impregnation ratio (5), showing less amount of IL-b-PE in the pores of carbon and wrinkled thin film of IL-b-PE on the top surface of carbon b) higher impregnation ratio (ratio 7, 13, 15, or 18), depicting carbon pores are completely impregnated with IL-b-PE and stable thin film of electrolyte also perfectly covered the surface of carbon.

4.3.6. Effect of Operating SCs at Higher Temperature

In order to further improve the electrochemical performance of all-solid state supercapacitors, the temperature was increased up to 60 °C. This strategy is commonly used in SCs using pure ionic liquids because the ion transportation of electrolytes improves with increasing temperature. Since ionic conductivity of IL-b-PE membrane also increased with temperature (see Figure 4. 4), it is a good strategy to evaluate the effect of increasing temperature on the performance of all-solid state SCs with different impregnation ratios as well. Figure 4.12 represents the Nyquist plot for all-solid state SCs with different impregnation ratio at 60 °C. Similarly to results obtained at RT, Figure 4.9 also shows a capacitive behavior reflected by steep increasing of the Nyquist plot at low frequency region. When the operating temperature was increased up to 60 °C, the ESR, R_s R_{ct} & Z_w values for all-solid state SCs decreased almost by half compared to RT due to the ionic conductivity of the IL-b-PE increased from $3*10^{-3}$ Scm^{-1} at 25 °C to $5*10^{-4}$ Scm^{-1} at 60 °C.

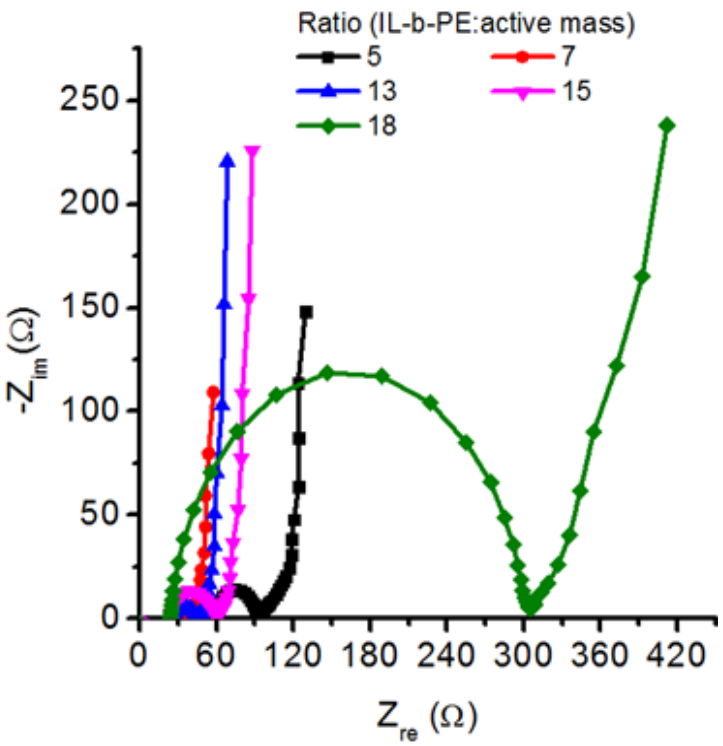

Figure 4.12.Nyquist plots for all solid-state supercapacitors having different impregnation ratios (SC5, SC7, SC13, SC15 and SC18) at 60 °C.

The representative charge-discharge (CD) voltage profiles for different all-solid state SCs with different impregnation ratios at 60 °C are shown in Figure 4.13a. It shows that charge-discharge profiles exhibited relatively small omhic drop which is improved by the ionic mobility of the massive electrolyte at higher temperature. Electrochemical performance of all-solid state SCs follows the same trend as that of RT. However, differences in performance among different impregnation ratios are diminished at 60 °C except for SC5 which still shows the higher ohmic drop and a distorted profile, indicating the poor performance of this SC even at higher temperature due to less amount of IL-b-PE.

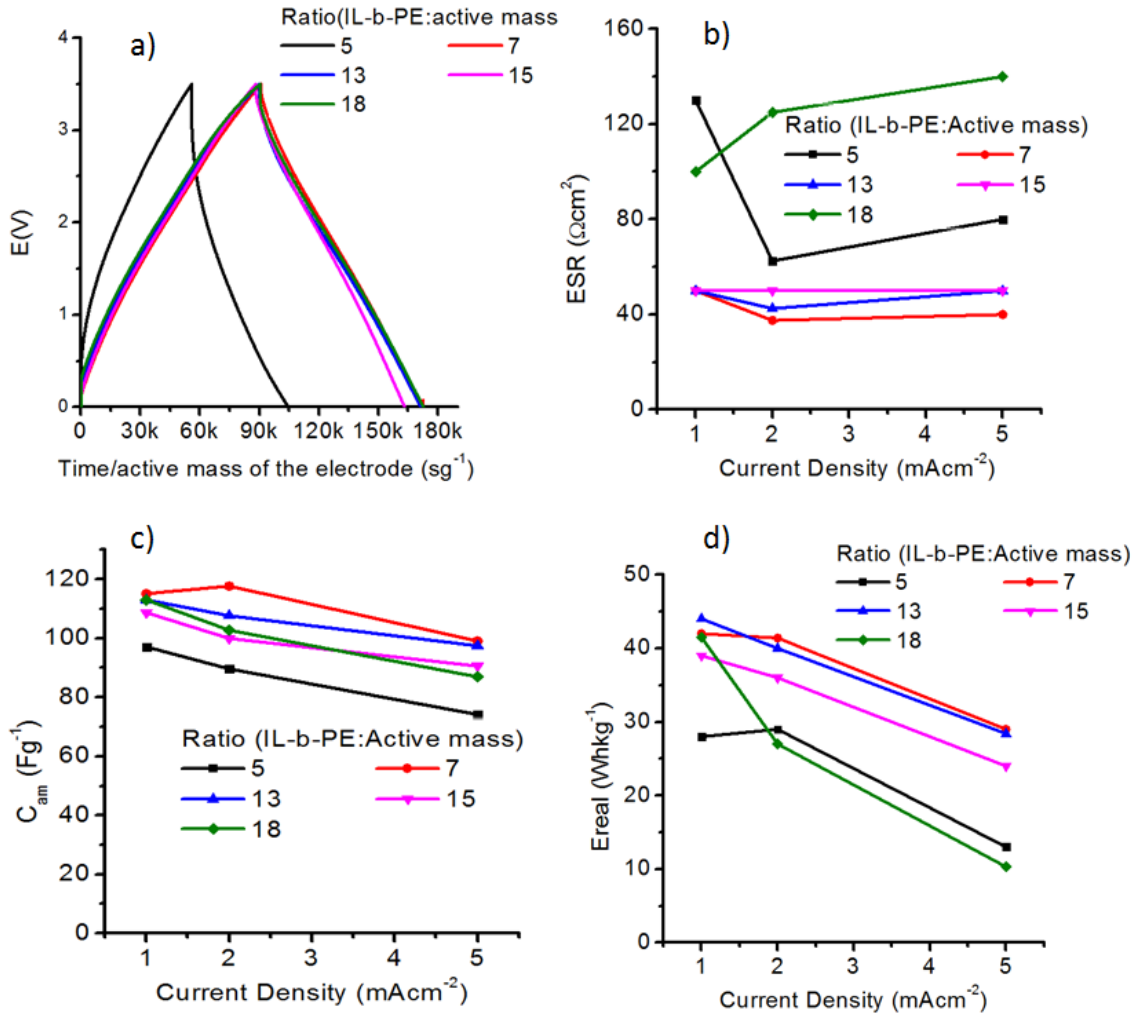

Figure 4.13. Electrochemical characterization of all-solid state supercapacitors with different impregnation ratios at 60 ºC a) representative of charge-discharge (CD at 1 $mAcm^{-2}$ b) ESR c) specific capacitance (C_{am}) and d) real energy (E_{real}) at different current densities.

ESR values calculated from charge-discharge curves of all-solid state SCs at different current densities are shown in Figure 4.13b. The results are in good agreement with impedance spectroscopy shown in Figure 4.12, indicating that the resistance of full solid state SCs assembled with IL-b-PE electrolyte decreased with increasing temperature. In general, the decrease in ESR values is due to the higher temperature which provokes faster ion transportation in the porous carbon electrode during charge-discharge. An example, ESR of SC7 decreased about ~67 % at 1 $mAcm^{-2}$ when temperature was increased from RT to 60 ºC. The trend of increasing ESR for different SCs at 60 ºC is as follows: SC7 < SC13 < SC15 < SC5 < SC18. The high values of ESR for SC5 and SC18 can be attributed to lack of sufficient IL-b-PE in the case of SC5, and to the very thick IL-b-PE layer between carbon electrodes in the case of SC18. In both

cases, it results in the lower capacitive performance of these two SCs demonstrating the importance of optimizing the thickness of polymer electrolyte film before assembling all-solid state supercapacitors. Figure 4.13c represents the specific capacitance of different SCs at different current densities at 60 °C. It is observed that C_{am} increases with temperature especially at higher current densities, showing that the ion mobility of IL-b-PE is improved during fast charge-discharge at high temperature. The maximum C_{am} of SC7 at 60 °C is increased by 5 % (115 Fg^{-1}) from the C_{am} at 1 $mAcm^{-2}$ at RT. Figure 4.13d illustrates the E_{real} calculated from charge-discharge voltage profiles at different current densities for all solid-state SCs. The general trend for E_{real} is shown as follow: SC7 ≥ SC13 > SC15 > SC5 >SC18.

In order to clearly analyze the effect of temperature, the electrochemical performance of the best performing SC7 (ratio 7) at RT and 60 °C is explained in the next paragraphs. Figure 4.14 shows the Nyquist plot of SC7 at RT and 60 °C showing that the values of ESR decreased from 95 to 43 Ωcm^2 when the temperature was increased up to 60 °C. This can be explained by the increasing IL-b-PE of ionic conductivity that changed from $5*10^{-4}$ Scm^{-1} at RT to 3 $mScm^{-1}$ at 60 °C.

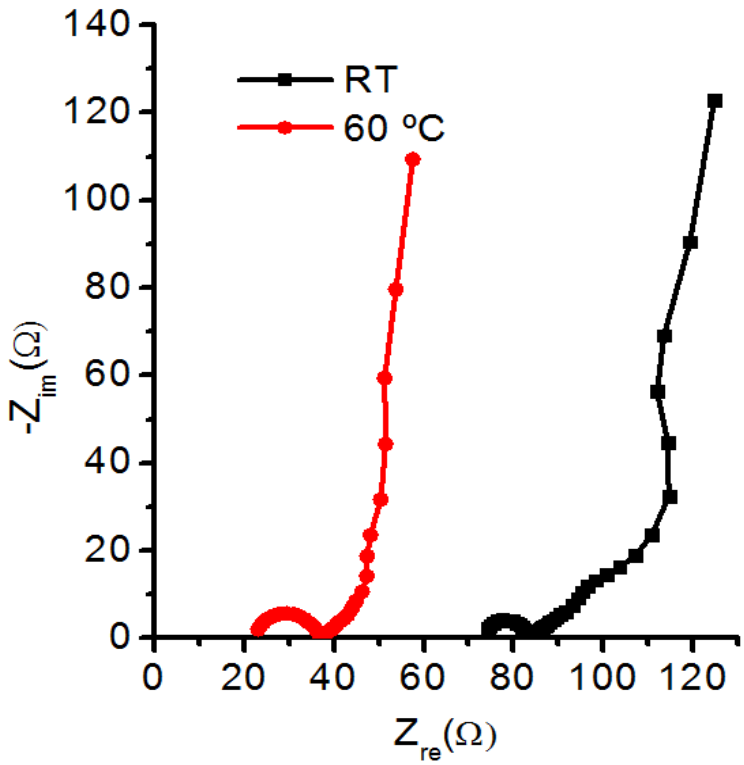

Figure 4.14. Comparison of Nyquist plots for all solid-state supercapacitors having 7 impregnation ratio (SC7) at RT and 60 °C.

Figure 4.15 shows the charge-discharge profiles and electrochemical parameters (ESR, C_{am}, and E_{real}) of SC7 at RT and 60 °C. The charge-discharge profiles in Figure

4.15a provide evidence for improved electrochemical performance at 60 °C while maintaining good reversibility (μ >95 %). The charge discharge profile in Figure 4.15a shows that the ohmic drop of SC7 drops from 0.3 V to 0.1 V at 60 °C. This is directly reflected in the ESR values that decreased from around 120 Ωcm² to about 40 Ωcm² at 2 mAcm⁻² (see Figure 4.15b) being in good agreement with impedance characterization.

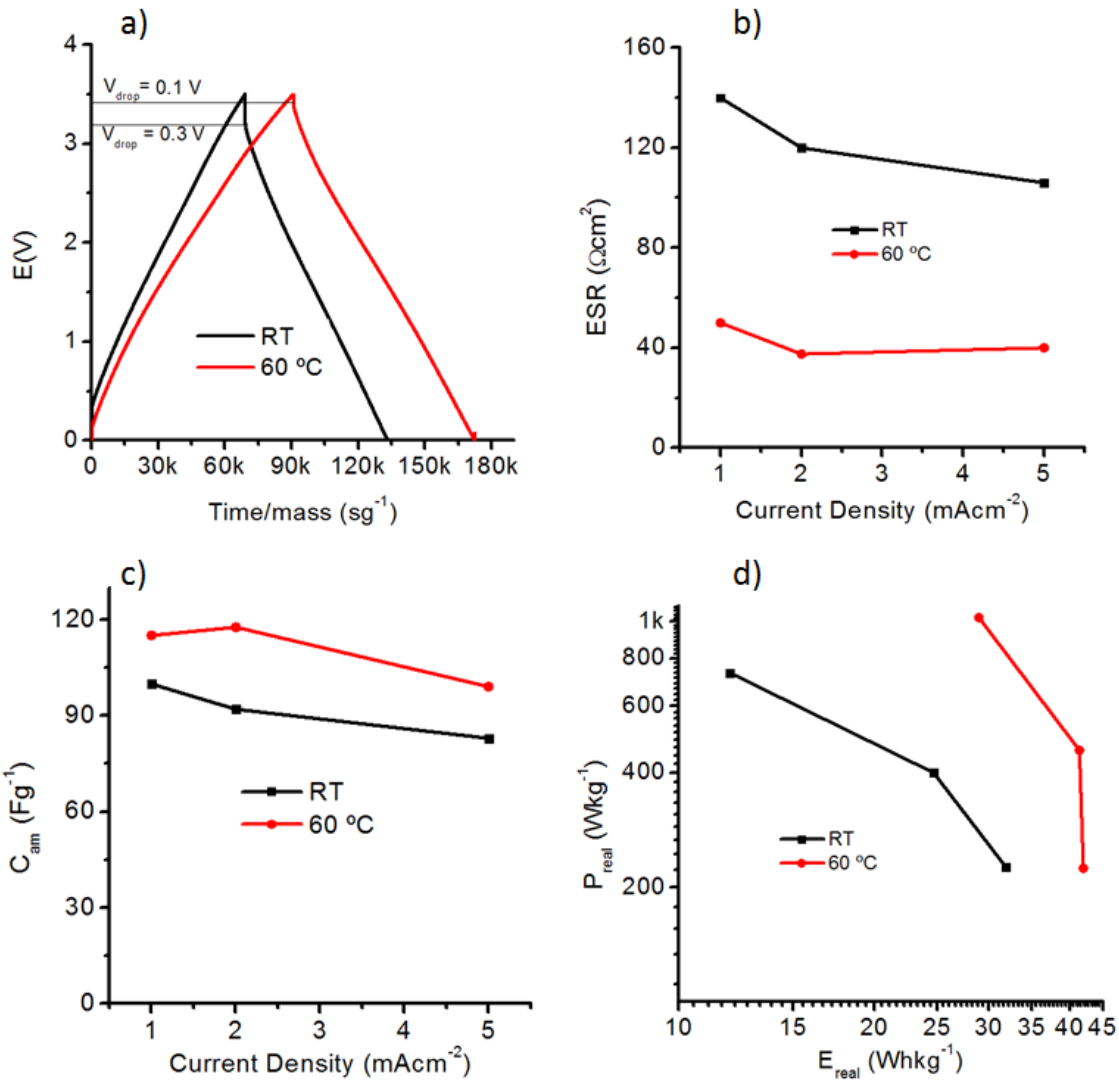

Figure 4.15. Electrochemical characterization for SC7 at RT and 60 °C, a) Charge-discharge profiles at 1 mAcm⁻² b) ESR, c) Cam d) E_{real} at different current densities

Figure 4.15c shows that specific capacitance (C_{am}) slightly increases with temperature from 100 Fg⁻¹ to 115 Fg⁻¹ at 1 mAcm². The beneficial effect of temperature is markedly observed in terms of real energy as well as power densities. Figure 4.13d shows the Ragone plot indicating that the E_{real} was increased from 32 to 42 Whkg⁻¹ at 60 °C at low current densities. The beneficial effect of temperature is even more significant at higher current densities with an E_{real} and P_{real} values as high as 30 Whkg⁻¹

and 1000 Wkg^{-1} at 5 $mAcm^{2}$. This means that the ion mobility of IL-b-PE during fast charge-discharge is significantly improved with temperature.

It is important to mention here that values of Ereal of all-solid state SCs based on IL-b-PE are better than those of solid state SCs based on conventional polymer electrolytes reported in literature. For instance, the best performing solid state SCs based on PAN/[BMIM][TFSI] electrolyte and graphene electrodes stored the maximum energy density about 30.5 $Whkg^{-1}$ [6]. Similarly, A. Lewandowski *et.al.* reported that SCs based on PAN/EMImTf/TSM and activated carbon electrodes stored 10.5 $Whkg^{-1}$ [22]. From this work, for the first time the energy density (E_{real}) of SC7 is as high as 32 $Whkg^{-1}$ and 42 $Whkg^{-1}$ at RT and 60 °C, respectively. This good performance of supercapacitors is achieved by designing polymer electrolytes with proper composition and physico-chemical properties and optimizing the thin film of polymer electrolyte on the surface of carbon electrodes. The impregnation of carbon electrodes with IL-b-PE is more appealing than the typical procedure where a free standing membrane is sandwiched between two electrodes. The reason is that during impregnation, the effective surface area of carbon electrodes will be increased compared to the membrane where the effective surface area of the interface between electrolyte and electrode is limited only to the projected surface area. By doing so, solid supercapacitors were charging at high voltage from 0 to 3.5V and stored energy density as high as 42 $Whkg^{-1}$.

4.4. Conclusion

Herein, for the first time, the electrochemical performance of all-solid state SCs based on pyrrolidinium ionic liquid based polymer electrolyte (IL-b-PE) and activated carbon electrodes was investigated at RT and at 60 °C. Pyrrolidinium IL-b-PE was composed of a binary blend of a polymeric ionic liquid and their corresponding ionic liquid both having an electrochemically stable pyrrolidinium cation and TFSI anion. It was demonstrated that all-solid state supercapacitors using this innovative IL-b-PE might be charged and discharged at operating voltages as high as in the case of pure ionic liquids (up to 3.5 V) keeping coulombic efficiencies higher than 95 %.

Moreover, the effect of different ratio of IL-b-PE to active mass of electrodes on the performance of SC was investigated by electrochemical impedance spectroscopy and charge-discharge techniques. The following trend was found; SC7 > SC13 > SC15 > SC5 > SC18 showing that the very high and the very low impregnation ratios exhibited the higher ESR and the lower C_{am} and E_{real} values. The lower ratios led to imperfect impregnation and non-homogeneous electrodes that could not be properly assembled in a SCs device. As the result, electrochemical performance of all-solid state SCs decrease at very high (>13) and very low (≤5) impregnation ratios both at RT and 60

°C. This is due to the higher thickness of IL-b-PE layer between electrodes for the higher impregnation ratios (SC13, SC15 and SC18), and results in increasing ESR and poor performance of SCs. Similarly, the lack of IL-b-PE in the pores of electrode for the lower impregnation ratio (SC5) is also resulted in less performing devices. The best performing SC was obtained at 7 ratio of IL-b-PE to active material both at RT and at 60 °C. In this optimum impregnation ratio, the maximum C_{am} and E_{real} are 105 Fg^{-1} and 32 $Whkg^{-1}$, respectively, which corresponds to lowest ESR (140 Ωcm^2) during charge-discharge at 1 $mAcm^{-2}$. When the temperature is increased to 60 °C, the maximum C_{am} and E_{real} increased by 5 % (115 Fg^{-1}) and 32 % (42 $Whkg^{-1}$), respectively, which corresponds to the lowest ESR of 50 Ωcm^2 at 1 $mAcm^{-2}$.

Lastly, it is worth noting that the electrochemical performance of all-solid state SCs based on this innovative IL-b-PE is very close to the performance of SCs using pure IL electrolytes. Moreover, C_{am} and especially E_{real} values are better than those of most of the solid state supercapacitors reported in literature. This could be explained by the conscientious selection of both the polymer matrix and the ionic liquid. Namely, the commonly used imidazolium IL was substituted by pyrrolidinium IL that possess a higher electrochemical stability window. Furthermore, the polymer matrix was chosen such that it was compatible with the ionic liquid.

In conclusion, for the future perspective, it is very important to optimize the ratio between active mass of electrode and electrolyte that are used for constructing Solid SCs. More importantly, increasing the contact area between electrode and electrolyte in all-solid state SCs is mandatory for higher energy and capacitance storage. For this reason, impregnation of electrodes with electrolyte is a good way to have a good electrode-electrolyte interface in all solid state SCs. Since both energy density and power density are dependent on the electrolyte and active material of electrode, optimization of both can help to scale up and design the device to get the best performance and pave the way for compact and flexible energy storage devices.

4.5. References

[1] J. Tao, N. Liu, W. Ma, L. Ding, L. Li, J. Su, Y. Gao, Sci. Rep. 3 (2013) 2286.

[2] Y. Matsuda, K. Inoue, H. Takeuchi, Y. Okuhama, Solid State Ionics 115 (1998) 103.

[3] R. Taniki, K. Matsumoto, T. Nohira, R. Hagiwara, J. Power Sources 245 (2014) 758.

[4] P. Simon, A. Burke, Electrochem. Soc. Interface 17 (2008) 38.

[5] S. Vaquero, R. Díaz, A. Anderson, J. Palma, R. Marcilla, M. Anderson, R.

Marcilla, J. Electrochem. Soc. 160 (2013) A2064.

[6] P. Tamilarasan, S. Ramaprabhu, Energy 51 (2013) 374.

[7] C. Meng, C. Liu, L. Chen, C. Hu, S. Fan, Nano Lett. 10 (2010) 4025.

[8] G.P. Pandey, a. C. Rastogi, C.R. Westgate, J. Power Sources 245 (2014) 857.

[9] N.A. Choudhury, P.W.C. Northrop, A.C. Crothers, S. Jain, V.R. Subramanian, J. Appl. Electrochem. 42 (2012) 935.

[10] P. Staiti, F. Lufrano, Electrochim. Acta 55 (2010) 7436.

[11] N.. . Choudhury, S. Sampath, A.K. Shukla, Energy Environ. Sci. 2 (2009) 55.

[12] C.K. Subramaniam, C.S. Ramya, K. Ramya, J. Appl. Electrochem. 41 (2011) 197.

[13] A. Lewandowski, A. Swiderska, Solid State Ionics 161 (2003) 243.

[14] A. Lewandowski, A. Swiderska, Pol. J. Chem. 78 (2004) 1371.

[15] G.P. Pandey, S.A. Hashmi, Y. Kumar, Energy & Fuels 24 (2010) 6644.

[16] G.P. Pandey, Y. Kumar, S. a. Hashmi, Solid State Ionics 190 (2011) 93.

[17] G.P. Pandey, Y. Kumar, S.A. Hashmi, Indian J. Chem. Sect. a-Inorganic Bio-Inorganic Phys. Theor. Anal. Chem. 49 (2010) 743.

[18] S. Ketabi, X. Liu, Z. Le, K. Lian, ECS Trans. 50 (2013) 411.

[19] A. Lewandowski, A. Swiderska, Appl. Phys. a-Materials Sci. Process. 82 (2006) 579.

[20] G. Pandey, Y. Kumar, S. Hashmi, Indian J. Chem. ... 49 (2010) 743.

[21] W. Lu, K. Henry, C. Turchi, J. Pellegrino, J. Electrochem. Soc. 155 (2008) A361.

[22] A. Lewandowski, A. Świderska, Appl. Phys. A 82 (2005) 579.

[23] M. Yamagata, K. Soeda, S. Ikebe, S. Yamazaki, M. Ishikawa, Electrochim. Acta 100 (2013) 275.

[24] M. Yamagata, K. Soeda, S. Yamazaki, M. Ishikawa, Electrochem. Solid-State Lett. 14 (2011) A165.

[25] M. Yamagata, M., Soeda, K., Ikebe, S., Yamazaki, S., & Ishikawa, ECS Trans. 41 (2012) 23.

[26] D. Mecerreyes, Prog. Polym. Sci. 36 (2011) 1629.

[27] M. Li, L. Yang, S. Fang, S. Dong, S. Hirano, K. Tachibana, J. Power Sources 196 (2011) 8662.

[28] G.B. Appetecchi, G.-T. Kim, M. Montanino, M. Carewska, R. Marcilla, D.

Mecerreyes, I. De Meatza, J. Power Sources 195 (2010) 3668.

[29] M. Hamedi, L. Herlogsson, X. Crispin, R. Morcilla, M. Berggren, O. Ingan??s, Adv. Mater. 21 (2009) 573.

[30] R. Marcilla, F. Alcaide, H. Sardon, J.A. Pomposo, C. Pozo-Gonzalo, D. Mecerreyes, Electrochem. Commun. 8 (2006) 482.

[31] Z. Wojnarowska, J. Knapik, A. Ortiz, I. Ortiz, M. Paluch, ACS Macromol. 47 (2014) 4056.

[32] E. Azaceta, R. Marcilla, A. Sanchez-Diaz, E. Palomares, D. Mecerreyes, Electrochim. Acta 56 (2010) 42.

[33] G.B. Appetecchi, M. Montanino, M. Carewska, M. Moreno, F. Alessandrini, S. Passerini, Electrochim. Acta 56 (2011) 1300.

[34] A.-L. Pont, R. Marcilla, I. De Meatza, H. Grande, D. Mecerreyes, J. Power Sources 188 (2009) 558.

CHAPTER V: PERFORMANCE OF SOLID STATE SUPERCAPACITORS BASED ON POLYMER ELECTROLYTES CONTAINING DIFFERENT IONIC LIQUIDS[5]

[5] Most of the results included in this chapter are published as "G.A. Tiruye, D. Muñoz-Torrero, J. Palma, M. Anderson, R. Marcilla: Performance of Solid State Supercapacitors Based on Polymer Electrolytes Containing Different Ionic Liquids. J. Power Sources xxx 2016, DOI: 10.1016/j.jpowsour.2016.03.044". Availabel online 17 March 2016.

CHAPTER V: PERFORMANCE OF SOLID STATE SUPERCAPACITORS BASED ON POLYMER ELECTROLYTES CONTAINING DIFFERENT IONIC LIQUIDS

5.1. Introduction

As mentioned in the previous chapters, the development of iongels, which contain electrochemical stable and non-volatile ionic liquids in the polymer matrix, have attracted ever-increasing interest due to the unique characteristics of ILs. Several polymer matrices, including conventional PTFE [1], PVdF/-HFP [2–5], PEO [6], PAN, PMA [7] and polysaccharides [8,9] have been investigated in combination with ionic liquids to develop solid supercapacitors. Indeed, iongels present several advantages such as high thermal and electrochemical stability, high ionic conductivity, non-volatile and non-flammable components and appropriate mechanical properties that make them suitable for wide range of applications. Although ionic conductivity of those iongels (in the range of 10^{-4}-10^{-2} Scm^{-1} at 25 ^{o}C) is generally lower than for hydrogels, they present some advantages such as higher electrochemical and thermal stability that make them promising candidates for high voltage electrochemical devices [10].

Polymeric ionic liquids (PILs) that combine the chemistry of ILs with the macromolecular architecture of polymers, provide the opportunity to create a new platform for the design of ionic liquid-based polymer electrolytes (IL-b-PE) with significantly improved properties [11]. In Chapter IV, the use of a polymer electrolyte composed of Poly(diallyldimethylammonium) bis(trifluoromethanesulfonyl)imide (PILTFSI) blended with 1-butyl-1-methylpyrrolidinium bis(trifluoromethanesulfonyl)imide ($PYR_{14}TFSI$) in solid state SCs is discussed in detail. Since both PIL and IL have the same anion (TFSI) and similar cation (pyrrolidinium) they present good compatibility, self-standing membrane even at high IL contents (up to 60 % wt.), wide electrochemical stability window, and high ionic conductivity. It was demonstrated that these solid state SCs could withstand high voltages of 3.5 V resulting in real energy and real power densities as high as 32 $Whkg^{-1}$ and 800 Wkg^{-1} respectively as discussed in Chapter IV.

In this Chapter the work is extend from Chapter IV to prepare different IL-b-PE and investigate the effect of the composition on the physicochemical properties of the polymer electrolytes. We present the synthesis of four different IL-b-PE having the

same polymer matrix but different ILs and we analyze how the different properties of the ILs are translated to the polymer electrolytes and to the final performance of assembled solid state SCs.

5.2. Experimental Methods

5.2.1. Materials

Lithium bis(trifluoromethanesulfonyl)imide (LiTFSI, ≥ 99 %), 1-butyl-1-methylpyrrolidinium dicyanamide, ($PYR_{14}DCA$, > 99.5 %), 1-butyl-1-methylpyrrolidinium bis(fluorosulfonyl)imide, ($PYR_{14}FSI$, > 99.5 %), 1-butyl-1-methylpyrrolidinium bis(trifluoromethanesulfonyl)imide, ($PYR_{14}TFSI$, ≥ 99.5 %) and 1-(2-hydroxy ethyl)-3-methylimidazolium bis(trifluoromethylsulfonyl)imide (HEMimTFSI, ≥ 99.5 %) were purchased from Solvionic and stored inside the glove box. Poly(diallyldimethylammonium)chloride solution (pDADMAC) (average Mw 400,000 to 500,000, 20 wt. % in H_2O) was obtained from Aldrich. Acetone (purity ≥ 99 %) was used for the preparation of the electrolyte solution. NMP (N- methyl-2-pyrrolidone, analytical grade), polyvinylidenefluoride (PVDF, solution in water), carbon black (Alfa Aesar GmbH & Co KG, Germany) and activated carbon (Picactif BP 10, PICA) were used to prepare the carbon electrodes.

5.2.2. Preparation of Ionic Liquid based Polymer Electrolytes (IL-b-PE)

As mentioned in the previous chapter (Chapter IV), the PIL, poly(diallyldimethylammonium) bis(trifluoromethanesulfonyl)imide (PILTFSI) was prepared by a simple ion exchange reaction from the commercially available poly(diallyldimethylammonium)chloride (pDADMAC) and Lithium bis(trifluoromethanesulfonyl)imide (LiTFSI) [12]. IL-b-PE solutions were prepared by dissolving 1.4 g of PILTFSI in 4 ml of acetone and adding the desired amount of ionic liquid; 2.1 g of $PYR_{14}TFSI$, $PYR_{14}FSI$, HEMimTFSI and 0.6 g of $PYR_{14}DCA$. Self-standing membranes were prepared by doctor blade technique using solvent casting method and dried at 100 ^{o}C under vacuum overnight. The resulting polymer electrolytes were named IL-b-PE1, IL-b-PE2, IL-b-PE3 and IL-b-PE4, respectively. Scheme 5.1 also shows that IL-b-PE1, IL-b-PE2 and IL-b-PE3 membranes were colourless, transparent and flexible whereas IL-b-PE4 membrane was whitish and fragile.

5.2.3. Preparation of Carbon Electrodes and Assembling of Solid State Supercapacitors

The method to prepare PICA carbon electrodes and the electrolyte impregnation process are explained in detail in Chapter IV. The composition of carbon electrodes was 80 % of PICA activated carbon as active material (Picactif BP 10, S_{BET}~2000 m^2 g^{-1}), 10 % of carbon black as conductivity enhancer, and 10 % of PVDF as polymeric binder. The electrode ink was prepared by mixing the three components in NMP using a ball-mill grinder. Doctor blade technique was used to spread the electrode ink onto aluminum current collector (25 µm thickness and 99% purity). After drying at 80 °C overnight, the carbon electrodes were cut into circular coin-shaped with 12 mm in diameter (geometrical area of 1.13 cm^2). The average thickness of carbon electrodes was about 100 -160 µm corresponding to an average mass loading about 2-4 mgcm-2.

In order to get optimum carbon-electrolyte interface, instead of sandwiching a membrane between two carbon electrodes, each electrode was impregnated with electrolyte solution before assembling SCs. Impregnation of carbon electrodes was performed by adding a diluted acetone IL-b-PE solution into porous carbon electrodes using a micropipette. According to the results discussed in chapter IV, the average ratio of IL-b-PE to total mass of active material in impregnated electrodes was fixed to 7 to ensure a complete electrolyte penetration into the carbon pores and the creation of a homogeneous external polymer electrolyte film of about 95-115 µm. Symmetric SCs were assembled by facing two impregnated electrodes in a two electrode Swagelok® cell.

5.2.4. Physicochemical Characterization of IL-b-PE

Fourier transform infrared spectroscopy (FTIR) was performed using a Thermo scientific instrument (Thermo NICO- LET 6700) operating in a diffuse reflectance mode (DRIFT). Thermogravimetric analysis (TGA) were performed by a DSC-TGA equipment (T.A. Instrument, model SDT Q600) from 30 °C to 650 °C (heating rate 5 °C min^{-1}) under air flow rate of 100 $mlmin^{-1}$. Both the ionic conductivity (σ) and the electrochemical stability window (ESW) were performed by sandwiching a coin-like shape polymer electrolyte membrane (0.785 cm^2 area and 40-90 µm thickness) between two stainless steel pistons in a Swagelok® cell. Ionic conductivities from -30 °C to 120 °C were obtained by Electrochemical Impedance Spectroscopy (EIS) in a multichannel Biologic VMP3 (frequency range = 1 MHz to 10 mHz, bias voltage= 0 V and amplitude=10 mV). The measurement was taken after heating the membrane for 1 hour at each temperature. Then, σ was calculated using the following equation: σ (Scm^{-1}) = t/RA, where *t* is the thickness of membrane (cm), *A* is the projected area of the

membrane (cm^2) and R is the resistance of the membrane obtained from Nyquist plot. Likewise, the electrochemical stability window (ESW) of IL-b-PE was investigated by applying linear sweep voltammetry (LSV) at 10 mVs^{-1} by sandwiching an IL-b-PE membrane in a two-electrode Swagelok cell. Similarly, the ESW of pure ionic liquids was determined by placing cellulose paper immersed with pure IL and applying a linear sweep voltammetry at a scan rate of 10 mVs^{-1}. The voltage stability limit was assigned to the voltage at which a drastic increase of current density beyond $0.15 \cdot 10^{-4}$ $A \cdot cm^{-2}$ occurs due to electrolyte decomposition.

5.2.5. Electrochemical Characterization of Solid State Supercapacitors

Electrochemical behavior of solid state SCs was characterized by Impedance Spectroscopy followed by galvanostatic charge-discharge (CD) using a multichannel Bio-Logic VMP3. Impedance spectroscopy experiments were performed over a frequency range from 200 kHz to 10 mHz using a bias voltage of 0 V and amplitude of 10 mV. CD experiments were conducted at different current densities: 5, 2 and 1 $mAcm^{-2}$ from 0 to 2.5 V for all SCs. Only SCs containing IL-b-PE1 and IL-b-PE2 were charged-discharged from 0 to 3.5 V. The common electrochemical parameters such as specific capacitance (C_{am}), equivalent series resistance (ESR), real specific power (P_{real}) and real specific energy (E_{real}) were calculated from CD experiments using *eqn.2.2 to eqn.2.6*.

5.3. Results and Discussion

5.3.1. Preparation and Physicochemical Properties of IL-b-PE

Polymer electrolyte membranes were prepared by doctor-blade technique using acetone solutions of PILTFSI and the corresponding ionic liquid: $PYR_{14}TFSI$ (IL-b-PE1), $PYR_{14}FSI$ (IL-b-PE2), HEMimTFSI (IL-b-PE3) and $PYR_{14}DCA$ (IL-b-PE4). The IL:PILTFSI mass ratio was 60:40 for IL-b-PE1, IL-b-PE2 and IL-b-PE3 whereas it was only 30:70 for IL-b-PE4.

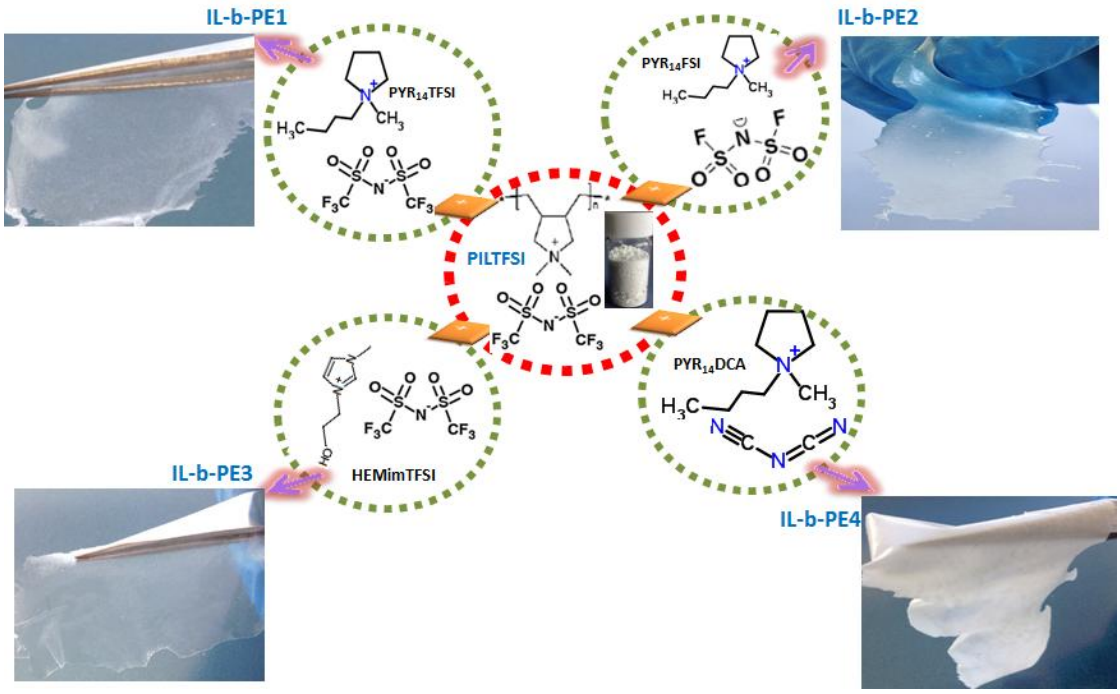

Scheme 5.1. Chemical structure of PILTFSI and different ILs ($PYR_{14}TFSI$, $PYR_{14}FSI$, $PYR_{14}DCA$ and HEMimTFSI) and the respective photo for each membrane. The mass ratio of ILs to PILTFSI for IL-b-PE1, IL-b-PE2 and IL-b-PE3 is 60:40 whereas for IL-b-PE4 is 30:70.

During blending of components in acetone, IL-b-PE1, IL-b-PE2, and IL-b-PE3 containing 60 % of IL, form transparent and homogenous solution which resulted in colourless, transparent, and free standing membranes as shown in Scheme 5.1. However, in the case of IL-b-PE4 due to the incompatibility of hydrophobic PILTFSI with hydrophilic $PYR_{14}DCA$, acetone solution of both compounds become cloudy and heterogeneous if the amount of $PYR_{14}DCA$ exceeds 30 % making impossible to prepare free standing solid membranes at high $PYR_{14}DCA$ content. Photograph in Scheme 1 shows that although the formation of free standing membrane is possible at 30:70 ratio, the turbid and pale white colour of the membrane clearly indicates less compatibility of the PILTFSI with $PYR_{14}DCA$. The brittle and fragile nature of IL-b-PE4 membrane might be attributed to the rigid nature of the dicyanide counter-anion when compared with the conformational structural flexibility of fluorinated TFSI and FSI anions [13]. This behavior confirms that, although the polymer matrix (PILTFSI) remains the same in all IL-b-PE, the membrane forming ability strongly depends on the chemical nature of the IL.

Chemical composition of polymer electrolytes is confirmed by FTIR and shown in Figure 5.1. All IL-b-PE membranes show four strong peaks at 1050, 1140, 1180 and 1350 cm^{-1} attributed to the TFSI anion from the polymer matrix. In the case of IL-b-

PE1 and IL-b-PE3 those peaks also correspond to the TFSI anion associated to the IL ($PYR_{14}TFSI$ and HEMimTFSI, respectively) [12].

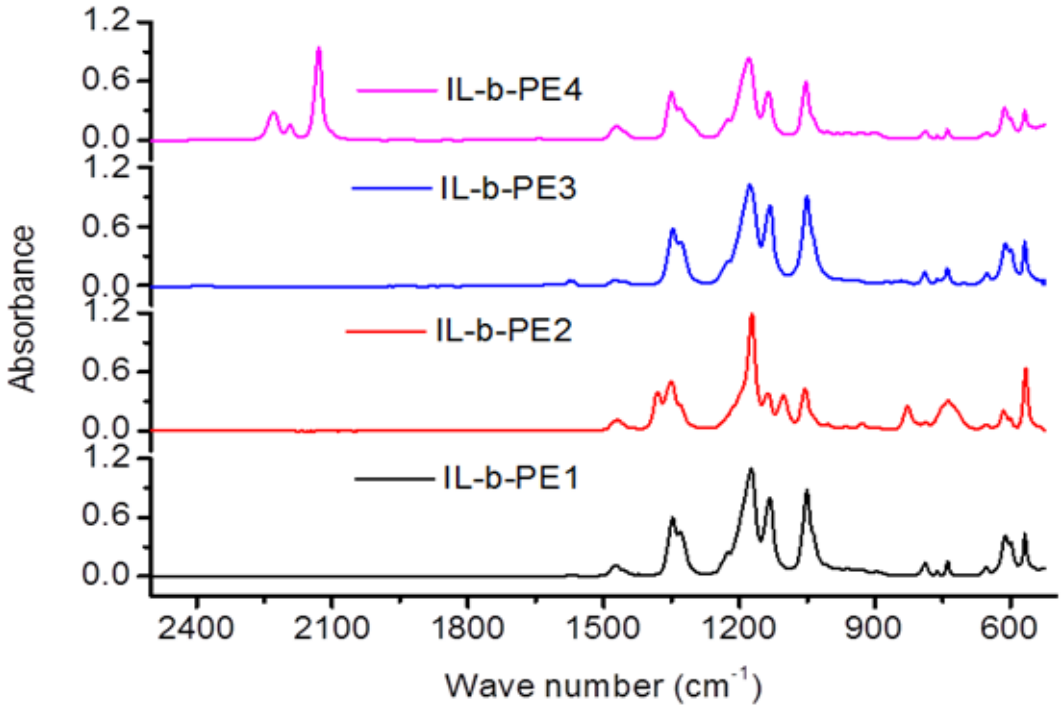

Figure 5.1. FTIR spectra of different polymer electrolytes: IL-b-PE1 (PILTFSI_$PYR_{14}TFSI$), IL-b-PE2 (PILTFSI_$PYR_{14}FSI$), IL-b-PE3 (PILTFSI_HEMimTFSI), and IL-b-PE4 (PILTFSI_$PYR_{14}DCA$).

New peaks corresponding to FSI and DCA anions from the ILs are observed in IL-b-PE2 and IL-b-PE4, respectively. For instance, peaks at around 830, 1100, 1175, 1214, 1360 and 1377 cm^{-1} corresponding to FSI anion [14] appear in FTIR of IL-b-PE2 although, in some cases, those peaks are not clearly visible since they overlapped with TFSI peaks. In the case of IL-b-PE4 three new peaks are also appeared at 2129, 2190 and 2227, cm^{-1} attributed to DCA anion [15]. No clear differences were observed between FTIR of IL-b-PE1 and IL-b-PE3 that only differ in the cation of the IL. In fact, only an additional small peak at 1570 cm^{-1} appeared in IL-b-PE3 attributed to C=C stretching in the ring of imidazolium cation. It is wort mentioning that FTIR spectra of polymer electrolytes are in good agreement with the FTIR spectra of pure $PYR_{14}TFSI$, $PYR_{14}FSI$, HEMimTFSI and $PYR_{14}DCA$ shown in Figure 5.2.

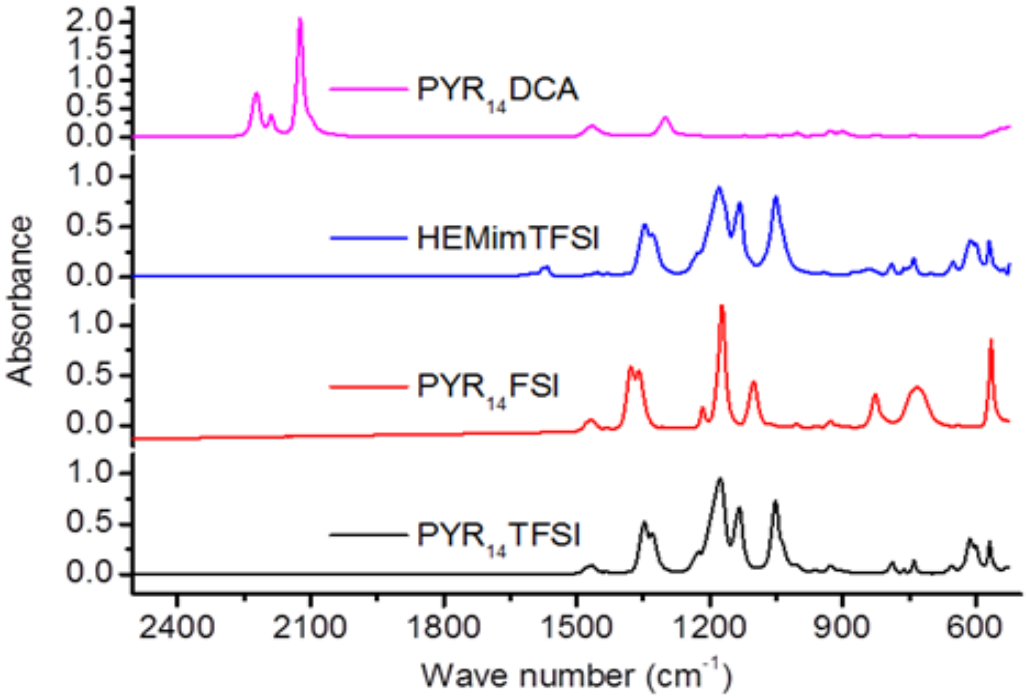

Figure 5.2. Spectra of pure ILs ($PYR_{14}TFSI$, $PYR_{14}FSI$, HEMimTFSI and $PYR_{14}DCA$)

Thermal stability of pure polymer matrix (PILTFSI) and IL-b-PE were investigated by TGA and shown in Figure 5.3. Due to the high thermal stability of TFSI anion, no significant weight loss is observed for PILTFSI up to 350-400 ºC demonstrating the high thermal stability of this polymer. Moreover, mixing PILTFSI with ILs containing the same TFSI anion results in membranes (IL-b-PE1 and IL-b-PE3) with slightly improved thermal stability independently from the type of cation in the IL. On the contrary, IL-b-PE2 and IL-b-PE4, containing $PYR_{14}FSI$ and $PYR_{14}DCA$, respectively present much lower thermal stability than pure PILTFSI due to the presence of FSI and DCA that are much less stable anions. In fact, thermal decomposition profiles of IL-b-PE2 and IL-b-PE4 show two steps; a first strong weight loss at 300 ºC attributed to the FSI and DCA anions of the ILs and a second weight loss at 350-400 ºC attributed to the TFSI anion of the polymer matrix. The different weight loss percentage observed in the first degradation step is in good agreement with the different mass percentage of IL into the polymer matrix; 60 % of $PYR_{14}FSI$ in IL-b-PE2 and 30 % of $PYR_{14}DCA$ in IL-b-PE4.

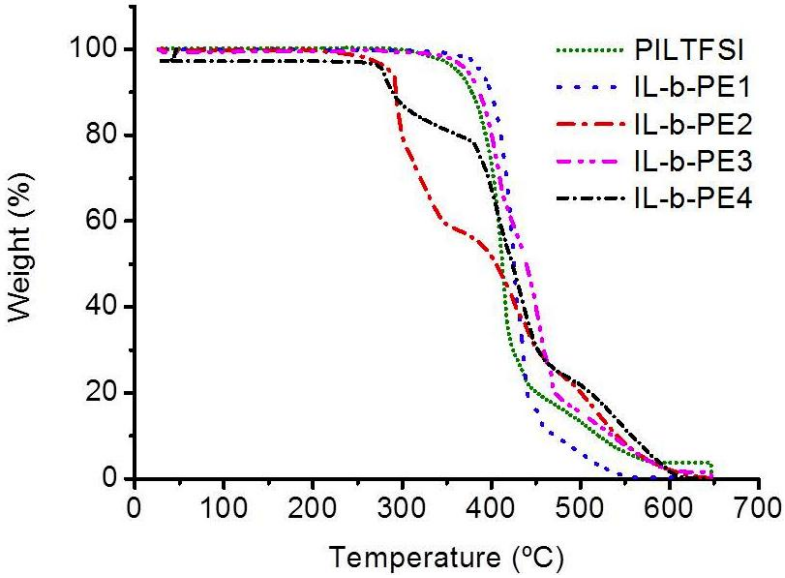

Figure 5.3. TGA of different IL-b-PE (IL-b-PE1, IL-b-PE2, Il-b-PE3, and IL-b-PE4) and the PILTFSI with heating rate at 5 °C min^{-1} under air

TGA profiles of pure ILs are shown in Figure 5.4 confirming the high thermal stability of $PYR_{14}TFSI$ and HEMimTFSI (about 400 °C) whereas $PYR_{14}FSI$ and $PYR_{14}DCA$ profiles exhibited a strong weight loss close to 250 °C.

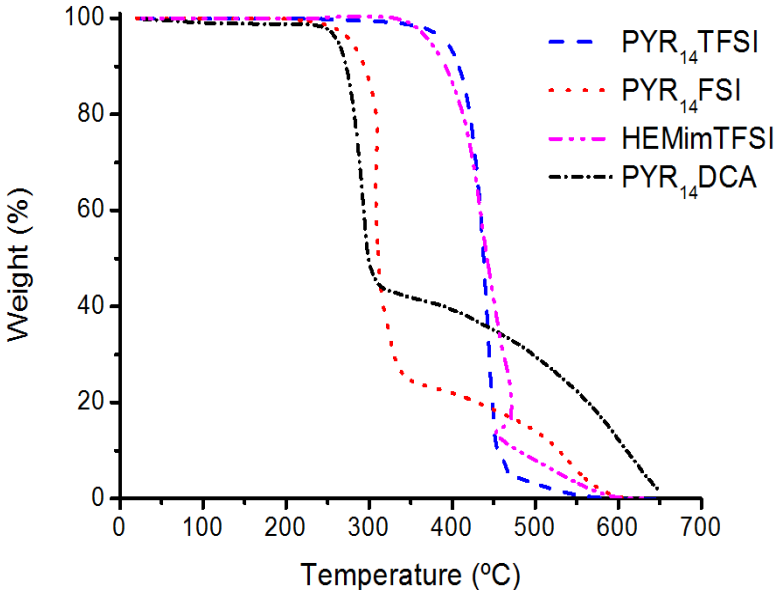

Figure 5.4. TGA curves for different pure ILs ($PYR_{14}TFSI$, $PYR_{14}FSI$, HEMimTFSI and $PYR_{14}DCA$) with heating rate at 5 °C min^{-1} under air

In summary, the results showed that thermal stability of different IL-b-PE strongly depend on the nature of the ionic liquid present in the membrane. Moreover, similarly to pure ILs, the type of anion in the IL has a more significant effect on the behavior of IL-b-PE than the type of cation. The thermal degradation on-set of pure ILs and their respective IL-b-PE is summarized in Table 5.1.

Table 5.1. Onset decomposition temperature (T_d), ionic conductivity (σ), electrochemical stability window (ESW) for pure ILs and corresponding IL-b-PE. Ionic radius for cation (r^+) and anion (r^-).

IL/IL-b-PE	T_d (°C)*	σ (mScm^{-1}) At 25 °C	ESW* (V)	r^- (nm)	r^+ (nm)
$PYR_{14}TFSI$	380	1.8 [16]	3.4	0.80 [17]	1.1 [18]
$PYR_{14}FSI$	255	4.1 [16]	3.4	0.30 [19,20]	1.1[18]
HEMimTFSI	360	2.8 [21]	2.6	0.80 [17]	0.76 [17]
$PYR_{14}DCA$	250	10 [22]	2.4	0.24 [19,23]	1.1 [18]
IL-b-PE1	380	0.41 *	3.7	0.80	1.1
IL-b-PE2	275	2.1 *	3.5	0.80 & 0.30	1.1
IL-b-PE3	365	0.86 *	2.9	0.80	1.1 & 0.76
IL-b-PE4	277	2.09 *	2.8	0.80 & 0.24	1.1

*Experimental values obtained from this research

Figure 5.5 shows ionic conductivities (σ) of different IL-b-PE membranes determined by impedance spectroscopy in a wide range of temperatures (from -30 °C to 120 °C).

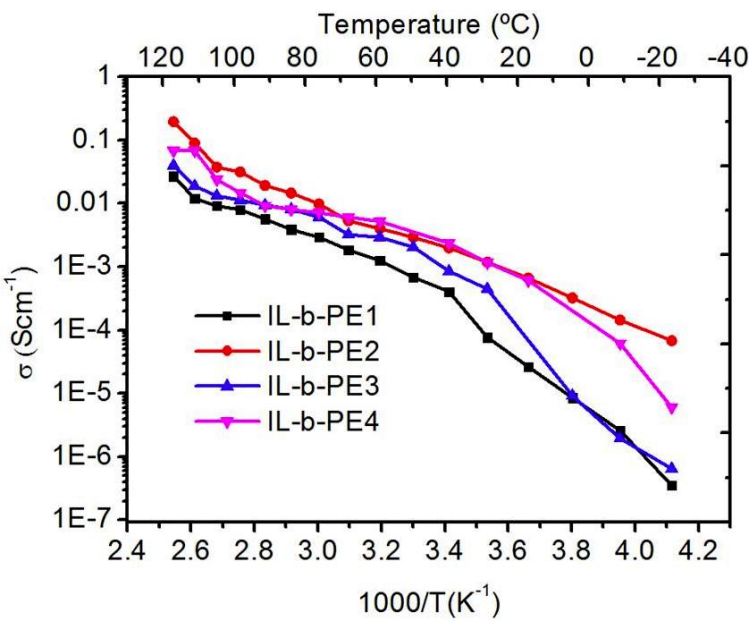

Figure 5.5. Arrhenius plots of ionic conductivity (σ) for different free standing IL-b-PE membranes (IL-b-PE1, IL-b-PE2, IL-b-PE3, and IL-b-PE4) at different temperatures from -30 to 120 °C.

It was confirmed that the temperature dependence of ionic conductivity follows the Vogel-Tamman-Fulcher (VTF) equation which has been effectively used to describe

various dynamical processes in amorphous polymeric systems [24]. The ionic conductivity varies about six orders of magnitude depending on the temperature and distinct nature of IL embedded in the polymer matrix. The trend of conductivities for different IL-b-PE membranes at 25 ºC is: IL-b-PE2 > IL-b-PE4 > IL-b-PE3 > IL-b-PE1 as shown in Figure 5.5. Although a similar trend is observed in all temperature ranges, differences in conductivity among membranes are smaller at higher temperatures than at lower temperatures.

In general, IL-b-PE1 and IL-b-PE3 containing the bigger TFSI anion in the membrane showed the lower ionic conductivities compared with IL-b-PE2 and IL-b-PE4 which consists of smaller FSI and DCA anions, respectively (Figure 5.5.). It is worth mentioning that ionic conductivity of different membranes roughly shows the same trend as the pure ionic liquids (Table 5.1) confirming that the ion transport properties of ILs are translated into the IL-b-PE. Ion transport behavior of IL-b-PE4 is particularly interesting since it shows one of the highest ionic conductivity despite having an ionic liquid content of only 30 % in comparison with the 60 % of IL-b-PE1, IL-b-PE2 and IL-b-PE3. This could be attributed to the much higher ionic conductivity of pure $PYR_{14}DCA$ in comparison to $PYR_{14}TFSI$, $PYR_{14}FSI$ and HEMimTFSI, as shown in Table 5.1.

Apart from ionic conductivity, the electrochemical stability window (ESW) is another important property of electrolytes since it determines the "safe" maximum operating voltage of a certain electrochemical device. ESW of polymer electrolytes were investigated by applying linear sweep voltammetry (LSV) in a two-electrode Swagelok cell and analyzing the drastic current increase beyond a certain polarization voltage. The voltage stability limit was assigned to the voltage at which a drastic increase of current density beyond $0.15*10^{-4}$ Acm^{-2} occurs. This voltage points out the initial decomposition of the electrolyte and consequently the ESW extent. Figure 5.6 depict the LSV of different IL-b-PE membranes at 25 ºC and the obtained values of ESW are included in Table 5.1. The following trend is observed: IL-b-PE1 ≥ IL-b-PE2 > IL-b-PE3 ≥ IL-b-PE4 indicating that when assembled in a supercapacitor, IL-b-PE1 and IL-b-PE2 can withstand voltages close to 3.5 V without significant degradation while IL-b-PE3 and IL-b-PE4 will suffer degradation at lower voltages limiting the operating voltage of supercapacitors to less than 3 V. This variation of ESW for each IL-b-PE is due to the different electrochemical stability of ionic liquids incorporated in the membrane.

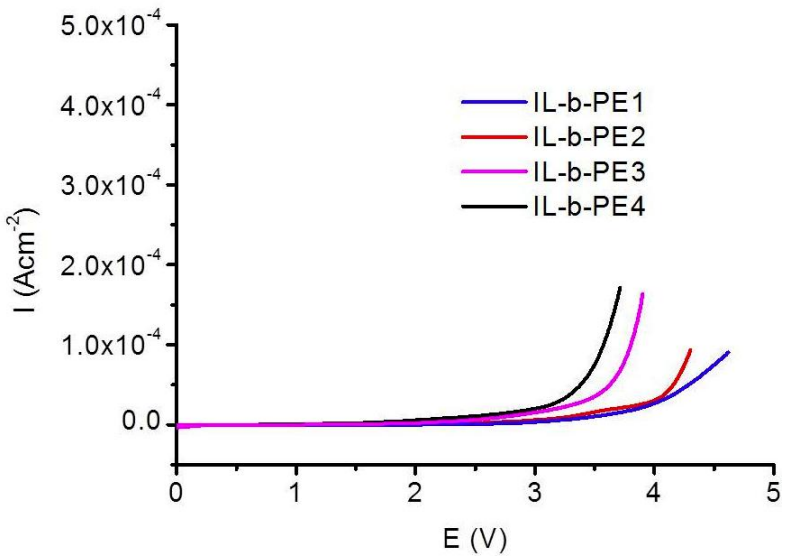

Figure 5.6. LSV for different IL-b-PE membranes determined at 25 ºC and 10 mVs^{-1}.

In fact, similar experiments were performed by placing a cellulose separator embedded with pure IL in a two electrode cell and results are shown in Figure 5.7. As previously observed in literature, pure $PYR_{14}DCA$ and HEMimTFSI containing DCA anion or imidazolium-based cation showed less electrochemical stability than $PYR_{14}TFSI$ and $PYR_{14}FSI$ with more stable cation and anions [22,25,26]. It is noteworthy that IL-b-PE are slightly more electrochemically stable than pure ionic liquids probably due to the high electrochemical stability window of the PILTFSI polymer matrix [12].

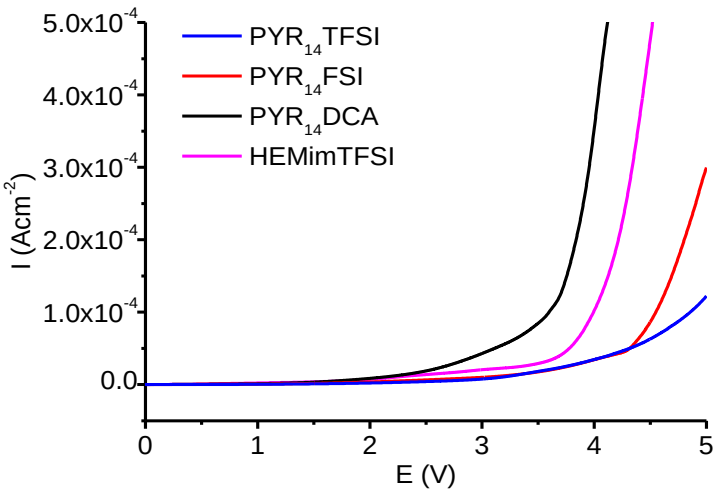

Figure 5.7. LSV for different pure ionic liquids determined at 25 ºC and 10 mV.

5.3.2. Electrochemical Performance of Solid State Supercapacitors Assembled with IL-b-PE

Solid supercapacitors (SCs) were assembled by facing two carbon electrodes previously impregnated with IL-b-PE without placing additional separator. As explained before IL-b-PE1, IL-b-PE2 and IL-b-PE3 contained 60 % of IL w/w while IL-b-PE4 only contained 30 % of $PYR_{14}DCA$. Solid state SCs were fully characterized by Electrochemical Impedance Spectroscopy (EIS) and galvanostatic charge-discharge (CD).

5.3.2.1. Electrochemical Impedance Spectroscopy (EIS)

Figure 5.8 shows the Nyquist plot for solid state SCs where the capacitive behavior of the device is revealed by the vertical line parallel to imaginary axis at low frequencies. Equivalent series resistance (ESR) can be estimated by extrapolation of the vertical line of the Nyquist plot to the x-axis and comprises bulk electrolyte resistance, electrodes intrinsic resistance, resistance associated to the current collector/electrode interface and resistance at the electrolyte/electrode interface.

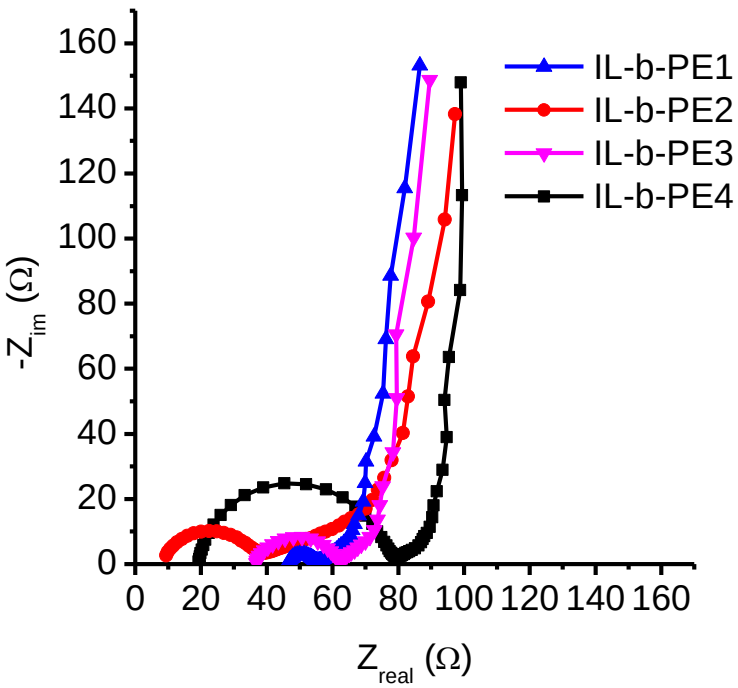

Figure 5.8. EIS Nyquist plot for different solid state SCs with different IL-b-PE at 25 ºC

Bulk resistance of the electrolyte, which is indirectly related to the ionic conductivity (σ) of membranes, can be extracted from the first intersection on x-axis at higher frequencies [27,28]. Main differences in Figure 5.8 appear within the high

frequency region denoting differences both in the electrolyte bulk resistance (first intersection on x-axis) and also in the ESR values (second intersection on x-axis of semi-circle). The general trend of bulk electrolyte resistance is: IL-b-PE2 (10 Ω) < IL-b-PE4 (20 Ω) < IL-b-PE3 (38 Ω) < IL-b-PE1 (48 Ω) being in very good agreement with the measured ionic conductivities of membranes shown in Figure 5.5. However, the trend is different for the values of ESR: IL-b-PE2 (40 Ω) < IL-b-PE3 (60 Ω) ≤ IL-b-PE1 (61 Ω) < IL-b-PE4 (80 Ω), ascribing the interfacial resistances among solid state SCs assembled with different IL-b-PE. The Nyquist plot of SC containing IL-b-PE4 is particularly interesting since it shows the highest value of ESR (the biggest semi-circle at high frequencies) despite the fact that IL-b-PE4 presents one of the highest values of ionic conductivities (Figure 5.5). The big semicircle reflects some transport limitation within the electrode/electrolyte interface probably due to the lack of homogeneity of IL-b-PE4 membrane that can resulted from a partial phase separation of PILTFSI and $PYR_{14}DCA$ mixture.

5.3.2.2. Galvanostatic Charge-Discharge (CD)

The electrochemical performance of the four solid state supercapacitors was investigated by galvanostatic charge-discharge experiments (CD) from 0 V to 2.5 V at current densities ranging from 1 to 5 $mAcm^{-2}$. The values of E_{real}, P_{real}, C_{am}, and ESR for solid state SCs were obtained according to the equations *eqn. 2.2-2.6*, in chapter two as explained above. CD profiles at intermediate current density of 2 $mAcm^{-2}$ are shown in Figure 5.9a. All of them exhibit a triangular linear profile, typical of electric-double layer capacitors. The slopes of the discharge curves which are inversely proportional to the capacitances are similar in all cases. However, CD profiles show very different ohmic drops (proportional to ESR) and consequently different values of integrated areas under each curve (proportional to E_{real}). In particular, supercapacitor assembled with IL-b-PE4 has the highest ohmic drop (ΔV), close to 0.7 V, while IL-b-PE1, IL-b-PE2 and IL-b-PE3 present ohmic drop values of about 0.3-0.4 V. Figure 5.9b depicts that the ESR values follow the trend: IL-b-PE2 < IL-b-PE3 < IL-b-PE1 <<< IL-b-PE4, in good agreement with the EIS results. Again, SCs assembled with IL-b-PE4 showed much higher ESR probably due to the poor compatibility between PILTFSI and $PYR_{14}DCA$ that impedes the homogeneous filling of the carbon pores with polymer electrolyte and can result in micro-phase separation. Figure 5.9c shows the specific capacitance values (C_{am}) that range from 80 to 130 Fg^{-1} depending on the type of polymer electrolyte and discharge current densities. In all cases, the C_{am} decreases with increasing current density being an indication of the higher ion diffusion resistance at the higher charge-discharge rates. The C_{am} follows the trend: IL-b-PE3 > IL-b-PE2 >

IL-b-PE1 > IL-b-PE4 with SC based on IL-b-PE3 exhibiting the highest value of C_{am} of about 130 Fg^{-1} while SCs with IL-b-PE4 presented the lowest C_{am} around 97 Fg^{-1} both at 1 $mAcm^{-2}$. Figure 5.9d shows the specific energy values (E_{real}) of different solid state SCs. Similarly to capacitance behaviour, decreasing of E_{real} was observed at higher charge-discharge currents. Values of E_{real} also follow the same trend as C_{am}: IL-b-PE3 > IL-b-PE2 > IL-b-PE1 > IL-b-PE4. The highest value of 22 $Whkg^{-1}$ was reached by solid state SCs assembled with IL-b-PE3 at 1 $mAcm^{-2}$. Again, the poor electrochemical performance of SC assembled with IL-b-PE4 is explained by the unsatisfactory compatibility between polymer matrix and ionic liquid within the membrane.

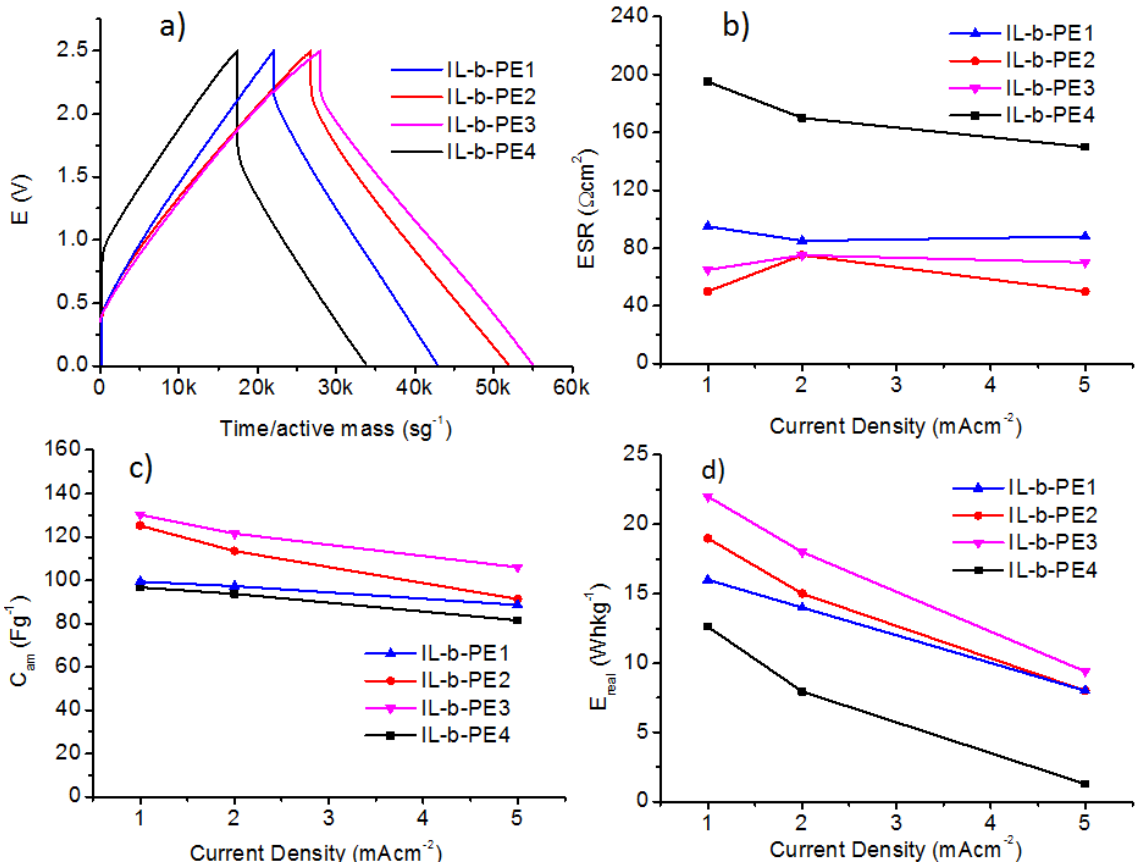

Figure 5.9.CD characterization of solid state supercapacitors assembled with different IL-b-PE a) Charge-discharge profiles from 0 V to 2.5 V at 2 $mAcm^{-2}$ b) equivalent series resistance (ESR) c) specific capacitance (C_{am}) and d) specific real energy (E_{real}) obtained from CD profiles at different current densities.

Figure 5.9 demonstrates that electrochemical performance of solid SCs based on IL-b-PE1, has been overtaken by blending the polymer matrix with ILs such as $PYR_{14}FSI$ and HEMimTFSI that are also compatible with the polymer matrix and have higher ionic conductivities than $PYR_{14}TFSI$. Although this is true when SC is charged from 0 to 2.5 V, only SCs with IL-b-PE1 and IL-b-PE2 could be charge-discharged reversibly (coulombic efficiency > 95 %) when voltage increased up to 3.5 V. The

narrower electrochemical stability windows of IL-b-PE3 and IL-b-PE4 (see Figure 5.6) explain the electrolyte degradation of those SCs operating at 3.5 V thus limiting their operation voltage to lower voltages.

Figure 5.10a represents CD profiles of SCs assembled with IL-b-PE1 and IL-b-PE2 charged from 0 to 3.5 V at 2 mAcm^{-2}. They display the typical triangular and linear response confirming the electric double layer behavior and discarding any pseudo-capacitance or redox reaction from electrode or electrolyte. ESR values for both SCs are shown in Figure 5.10b.

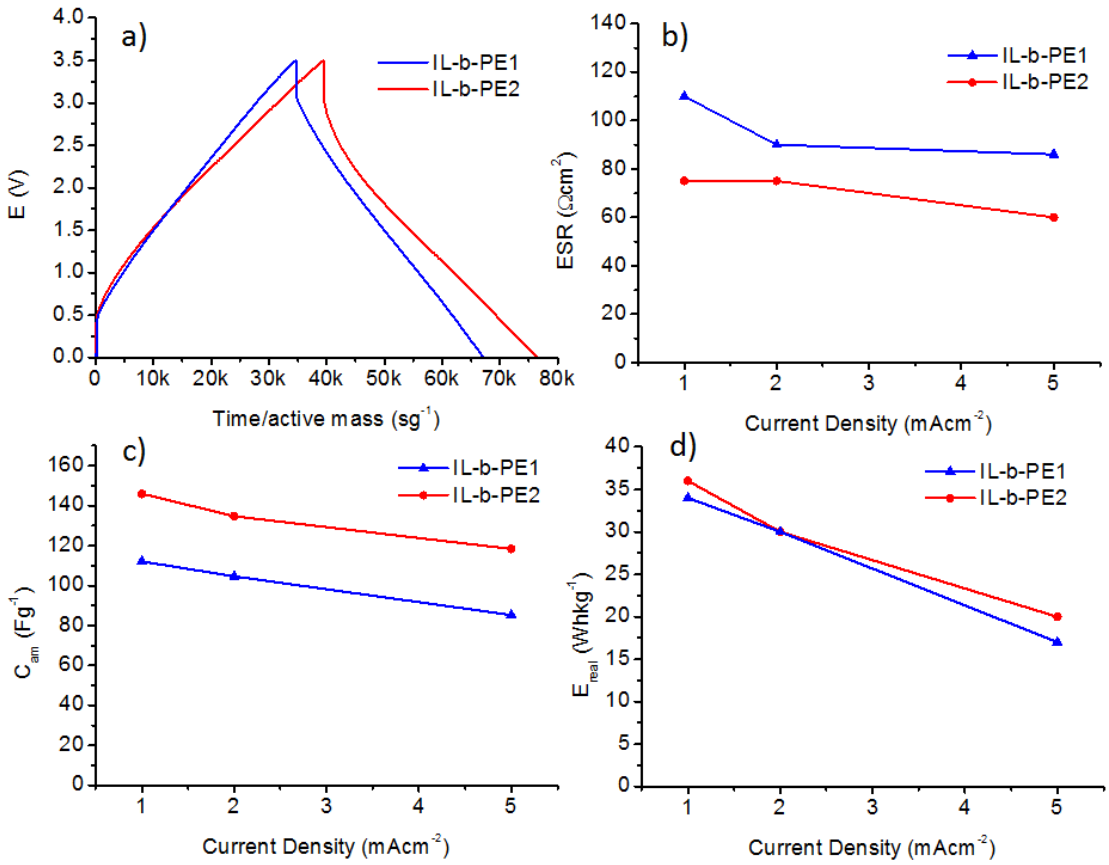

Figure 5.10. CD characterization of solid state supercapacitors impregnated with different IL-b-PE a) Charge-discharge profiles from 0 V to 3.5 V at 2 mAcm-2 b) equivalent series resistance (ESR) c) Specific capacitance (Cam) and d) specific real energy (E_{real}) obtained from CD profiles at different current densities.

It was observed that SC with IL-b-PE2 presents lower ESR values than SC with IL-b-PE1 which is in a good agreement with EIS analysis and it is probably due to the higher ionic conductivity of $PYR_{14}FSI$ in comparison with $PYR_{14}TFSI$ within the polymer electrolyte. This again confirms that the different nature of anions presents in the polymer matrix significantly influences the performance of solid state SCs. Figure 5.10c depicts that specific capacitance of SCs (C_{am}) increased by about 15-20 % with respect to those obtained when SCs were charged up to 2.5 V. Specifically, SCs

assembled with IL-b-PE1 shows C_{am} ranging from 90 to 110 Fg^{-1} whereas the IL-b-PE2 shows even highest values of C_{am} from 125 to 150 Fg^{-1} at the same discharge conditions. As expected, Figure 5.10d shows that specific energy (E_{real}) of both SCs increased significantly with operating voltage showing slightly higher values for SC containing IL-b-PE2. Solid state SCs assembled with IL-b-PE2 stored the maximum E_{real} about 36 $Whkg^{-1}$ at 1 $mAcm^{-2}$, increasing by 90 % from the E_{real} obtained at 2.5 V with the same current density (Figure 5.9d). It is worth mentioning that these capacitance and energy values are due to the very high specific surface area of PICA carbon (S_{BET} ~ 2000 m^2g^{-1}) and are also related to those obtained for similar SCs assembled with the same PICA activated carbon, but using pure $PYR_{14}TFSI$ and $PYR_{14}FSI$ as liquid electrolytes (see Chapter III). It seems that the presence of smaller FSI anion (0.30 nm) within IL-b-PE2 (in comparison with bigger TFSI anion (0.80 nm) in IL-b-PE1) facilitates ion diffusion and increases the charge carrier and the charge sites, consequently contributing to the higher capacitance. This indicates that development of solid state polymer electrolyte by embedding different ion sizes in the polymer matrix can be an advantage to increase the charge carrier, in turn, enhances the values of energy and capacitance of solid state SCs.

Figure 5.11 represents the Ragone plot, which depicts the real energy and real power density relationships for different solid state SCs assembled with IL-b-PE1, IL-b-PE2, IL-b-PE3, and IL-b-PE4. Ragone plot clearly evidences the different performance of solid SCs when charged at 2.5 V attributed to the different properties of the ionic liquids within the polymer matrix. It is also clearly indicated that the real energy (E_{real}) and real power (P_{real}) increase significantly with increasing operating voltage in IL-b-PE1 and IL-b-PE2. The diagonal dot lines in the Ragone plot depict constant discharge rates and indicate the relative time to get the charge in or out of solid state SCs. Upon discharging from 2.5 V to 0 V at 5 $mAcm^{-2}$, the discharge time was about 0.6 min corresponding to a fast power delivery of about 800-900 Wkg^{-1} for SCs assembled with IL-b-PE1, IL-b-PE2 and IL-b-PE3. Likewise, when the charging voltage was increased up to 3.5 V at 5 $mAcm^{-2}$, the discharge time increase from 0.6 to about 1 min while energy density almost double (from about 10 $Whkg^{-1}$ to 20 $Whkg^{-1}$ respectively) resulting in an effective increase of real power (P_{real}) about 30 % (from 800-900 Wkg^{-1} to 1100-1200 Wkg^{-1}). As shown in Figure 5.9d and Figure 5.10d, decreasing current densities to 1 $mAcm^{-2}$ leads to a significant increase of energy density (about 35 $Whkg^{-1}$ at operating voltage of 3.5V) approaching to the level of pseudocapacitors or even lead-acid batteries. In those experimental conditions discharging time increases considerably up to 4-8 min (depending on the maximum operating voltage). Although the higher resistance of polymer electrolytes results in solid SCs with longer discharge

times than conventional liquid electrolytes, this discharge time is still much faster than in the case of batteries and are within the time range considered for supercapacitor going from seconds to few minutes [17].

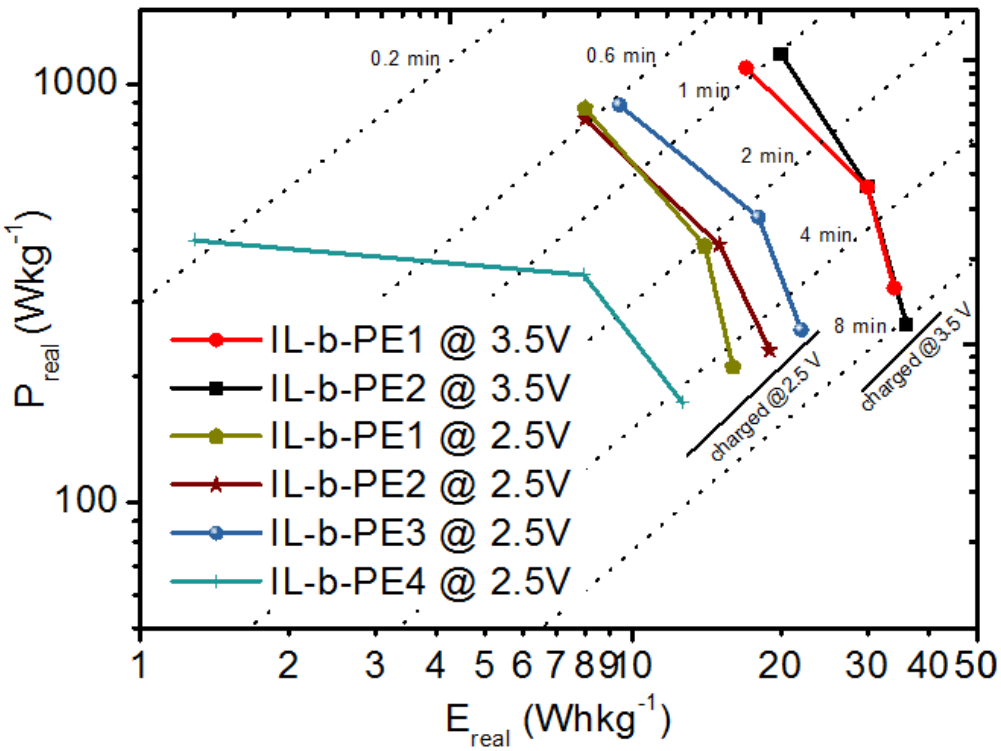

Figure 5.11. Ragone plot different supercapacitor derived from Fig. 6 (charged at 2.5 V) & Fig.7 (charged at 3.5 V), Charge-discharge current density: 1-5 $mAcm^{-2}$.

Moreover, Table 5.2 compares the best performing solid state supercapacitors in this work with other examples reported in literature. It can be seen that supercapacitors assembled with IL-b-PE1 and IL-b-PE2 present the best electrochemical performance in terms of energy and capacitance. Despite having moderate ionic conductivity, solid state SCs containing IL-b-PE1 and IL-b-PE2 exhibit slightly higher power density than other solid SCs in literature. This is due to the high stability window of these polymer electrolytes that allow the SC to operate at voltage as high as 3.5 V.

Table 5.2. Comparison of performance of IL-b-PE2 with different polymer electrolytes from literature

Active Material[a]	Gel Polymer Electrolytes	σ (mSc m^{-1})	C_{am} (Fg^{-1})	E_{real} (Whk g^{-1})	V (V)	P_{real}[c] (kWk g^{-1})	ref.
Graphene	SPEEK+H_2SO_4	-	120	4.2[b]	1	0.5	[20]
AC	Nafion+H_2SO_4	60	130	4.5[b]	1		[18]
Graphene	PVdF-HFP/BMIM BF_4	-	76	7.4	1.5	-	[24]
RGO / f-RGO	Nafion+H_2SO_4	-	118	-	1	-	[17]
AC	PVDF-HFP/EMimTFSI	1.5	-	15	3	0.15	[23]
AC	PTFE/EMimTFSI	1.1	-	17	3	0.15	[23]
AC	PVDF-HFP/EMimTFSI+LiTFSI	4.5	108	15	2	0.21	[28]
AC fiber cloth	Chitosan/EMimBF_4	16	120	27[b]	2.5	0.16	[25]
AC fiber cloth	Alginate/EMimBF_4	14	134	30	2.5	0.18	[29]
AC	PILTFSI/PYR_{14}TFSI (IL-b-PE1)	0.5	110	35	3.5	0.25	This work
AC	PILTFSI/PYR_{14}FSI (IL-b-PE2)	2.1	150	36	3.5	0.23	This work

[a]AC (Activated carbon), RGO (reduced graphene oxide), f-RGO (functionalised reduced graphene oxide), [b]Estimated according to $E=0.5CV^2$, [c]Estimated according to $P_{real} = E/t$, at the lowest value of discharge current.

5.4. Conclusion

The development of new solid state electrolytes creates opportunities for new types of energy storage devices including solid batteries and supercapacitors. Iongels or ionic liquid based polymer electrolytes (IL-b-PE), containing IL within the polymer matrix, are a promising type of polymer electrolytes with improved ionic conductivity and electrochemical stability. In this work, different IL-b-PE were synthesized by blending a polymeric ionic liquid (PILTFSI) with different ILs. It was observed that membrane

formation and their physicochemical properties such as ionic conductivity, thermal and electrochemical stability were strongly affected by the chemical nature of ILs embedded in the polymer matrix, which consequently influences the performance of solid state SCs. For instance, polymer electrolytes containing IL with small size anions such as FSI (IL-b-PE2) and DCA (IL-b-PE4) presented higher ionic conductivities than IL-b-PE1 and IL-b-PE3 containing ILs bearing a bigger size anion (TFSI). However, thermally stable TFSI anion lead to polymer electrolytes (IL-b-PE1 and IL-b-PE3) stable up to 400 ^{o}C, outperforming the thermal behavior of membranes with ILs containing FSI (IL-b-PE2) and DCA (IL-b-PE4).

Electrochemical performance of solid state SCs was found to be dependent on the chemical composition of the polymer electrolytes. When SCs were charge/discharged at moderate voltage of 2.5 V, IL-b-PE4 with high ionic conductivity exhibited the worse performance, possibly due to the low compatibility between polymer matix (PILTFSI) and $PYR_{14}DCA$ that resulted in inhomogeneous membrane with microphase separation. The behavior of solid state SCs based on IL-b-PE2 and IL-b-PE3 was better than for SCs with IL-b-PE1, possibly due to their higher ionic conductivities. Besides ionic conductivity, electrochemical stability window of polymer electrolytes, which finally determine the maximum operating voltage of SCs, was also strongly affected by the ESW of the pure ILs. Indeed, ESW of polymer electrolytes was found to follow the same trend as in pure ILs and only IL-b-PE1 and IL-b-PE2 containing both electrochemically stable cation (pyrrolidinium) and anions (TFSI and FSI) were able to withstand a charging voltage up to 3.5 V. Therefore, only SCs with IL-b-PE1 and IL-b-PE2 were tested at 3.5 V. At those conditions, the performance of SC based on IL-b-PE2, with high ionic conductivity and appropriate electrochemical stability, was slightly better than SC based on IL-b-PE1 reaching record values of C_{am}, E_{real} and P_{real} of about 150 Fg^{-1}, 36 $Whkg^{-1}$ and 1170 Wkg^{-1}, respectively. To summarize, a conscious selection of stable polymer matrixes such as PILTFSI and compatible, high ionic conductive and electrochemical stable ILs can greatly contribute to the progress of fundamental research on the development of solid polymer electrolytes, in turn, it will pave the way for development of solid, lightweight, and flexible energy storage devices.

5.5. References

[1] W. Lu, K. Henry, C. Turchi, J. Pellegrino, J. Electrochem. Soc. 155 (2008) A361.

[2] G.P. Pandey, A.C. Rastogi, MRS Proc. 1440 (2012) 12.

[3] M. Yamagata, K. Soeda, S. Ikebe, S. Yamazaki, M. Ishikawa, Electrochim. Acta 100 (2013) 275.

[4] A. Lewandowski, A. Świderska, Appl. Phys. A 82 (2005) 579.

[5] G.P. Pandey, S.A. Hashmi, Electrochim. Acta 105 (2013) 333.

[6] Y. Matsuda, J. Electrochem. Soc. 140 (1993) L109.

[7] A.A. Łatoszyńska, G.Z. Żukowska, I.A. Rutkowska, P.-L. Taberna, P. Simon, P.J. Kulesza, W. Wieczorek, J. Power Sources 274 (2015) 1147.

[8] Y. Kumar, G.P. Pandey, S.A. Hashmi, J. Phys. Chem. C 116 (2012) 26118.

[9] M. Yamagata, K. Soeda, S. Yamazaki, M. Ishikawa, Electrochem. Solid-State Lett. 14 (2011) 165.

[10] A.S. Shaplov, R. Marcilla, D. Mecerreyes, Electrochim. Acta 175 (2015) 18.

[11] D. Mecerreyes, Prog. Polym. Sci. 36 (2011) 1629.

[12] A.-L. Pont, R. Marcilla, I. De Meatza, H. Grande, D. Mecerreyes, J. Power Sources 188 (2009) 558.

[13] L.C. Tomé, M. Isik, C.S.R. Freire, D. Mecerreyes, I.M. Marrucho, J. Memb. Sci. 483 (2015) 155.

[14] L.J. Hardwick, J.A. Saint, I.T. Lucas, M.M. Doeff, R. Kostecki, J. Electrochem. Soc. 156 (2009) A120.

[15] B. Jürgens, H.A. Höppe, W. Schnick, Solid State Sci. 4 (2002) 821.

[16] P. Johansson, L.E. Fast, A. Matic, G.B. Appetecchi, S. Passerini, J. Power Sources 195 (2010) 2074.

[17] P. Simon, Y. Gogotsi, Nat. Mater. 7 (2008) 845.

[18] A. Balducci, R. Dugas, P.L. Taberna, P. Simon, D. Plée, M. Mastragostino, S. Passerini, J. Power Sources 165 (2007) 922.

[19] S. Seki, T. Kobayashi, Y. Kobayashi, K. Takei, H. Miyashiro, K. Hayamizu, S. Tsuzuki, T. Mitsugi, Y. Umebayashi, J. Mol. Liq. 152 (2010) 9.

[20] H.-B. Han, S.-S. Zhou, D.-J. Zhang, S.-W. Feng, L.-F. Li, K. Liu, W.-F. Feng, J. Nie, H. Li, X.-J. Huang, J. Power Sources 196 (2011) 3623.

[21] S.H. Yeon, K.S. Kim, S. Choi, H. Lee, H.S. Kim, H. Kim, Electrochim. Acta 50 (2005) 5399.

[22] C. Wolff, S. Jeong, E. Paillard, A. Balducci, S. Passerini, J. Power Sources 293 (2015) 65.

[23] P. Li, D.R. Paul, T.-S. Chung, Green Chem. 14 (2012) 1052.

[24] S. Seki, M.A.B.H. Susan, T. Kaneko, H. Tokuda, A. Noda, M. Watanabe, J. Phys.

Chem. B 109 (2005) 3886.

[25] G.B. Appetecchi, M. Montanino, D. Zane, M. Carewska, F. Alessandrini, S. Passerini, Electrochim. Acta 54 (2009) 1325.

[26] S.P. Ong, O. Andreussi, Y. Wu, N. Marzari, G. Ceder, Chem. Mater. 23 (2011) 2979.

[27] Q.A. Huang, R. Hui, B. Wang, J. Zhang, Electrochim. Acta 52 (2007) 8144.

[28] T. Kim, H. Lee, M. Stoller, D. Dreyer, ACS Nano 5 (2011) 336.

CHAPTER VI: CONCLUSION AND FUTURE PERSPECTIVE

CHAPTER VI: CONCLUSION AND FUTURE PERSPECTIVE

6.1. Conclusion

This PhD Thesis addresses the ever increasing demand for novel electrode materials and innovative polymer electrolytes for high performance supercapacitors. The main conclusions of this PhD Thesis are presented in two sections based on the research findings discussed in each chapter in more detail. The following two main conclusions are about novel nanocomposite carbon based materials and innovative ionic liquid based polymer electrolytes for the development of high performance supercapacitors. Specifically, the Thesis results reveal that:

i) The capacitive performance of nitrogen doped carbon (N-dC) and composites of vanadium nitride nanoparticles (VN@N-dC) as electrode for supercapacitors is influenced by the combined synergetic effects of physico-chemical properties of the electrode active materials and the intrinsic properties of electrolytes.

A facile one-step "salt templating method" was used for the synthesis of highly porous nitrogen doped carbons and composites with Vanadium nitride nanoparticles with tunable surface area, pore size, pore volume and nanoparticle size by using simple salts as porogens. It was realized that the morphology properties of as-synthesized carbon materials (N-dC and composites of VN@N-dC) are strongly influenced by the combine effect of molar concentration ratios of the respective precursors and the amount and nature of salt used as porogens during thermal treatment. Specifically, the results reveal that:

- Generally, the specific surface area of N-dC was decreased by 10-40 % from that of the non-doped carbon due to the collapse of carbon walls and blocking primary pores by the doped nitrogen functionalities in the carbon matrix. Using small mass ratio of $NaCl/ZnCl_2$ salt (1:1) promotes the formation of highly microporosity with specific surface area (S_{BET}) *ca.* 1197 m^2g^{-1} during heat-treatment of a mixture of urea and tannic acid (TA) (9:1, urea:TA), while increasing the salt ratios (1:3, 1:5 and 1:7) enhances additional mesopores with S_{BET} up to 1353 m^2g^{-1}. Changing the salt for $LiCl/ZnCl_2$ further increases the S_{BET}, recording up to 1409 m^2g^{-1} whereas using $KCl/ZnCl_2$ eutectic salt results in N-dC with lower values of S_{BET} (~1251 m^2g^{-1}) and does not significantly improve the morphology or textural properties compared with other carbons.

- The nitrogen content incorporated within N-dC was proportionally increased from 0.72 % up to 8.8 % with increasing urea content in the precursor blend from 0:1 to 17:1 (urea:TA), respectively. However, the electrical conductivity of N-dC was not directly proportional to the nitrogen content but to the type of nitrogen functionalities incorporated in the carbon matrix. In fact, the highest conductivity of 76 Scm^{-1} (almost 8 times higher than conductivity of non-doped carbon) was achieved with 9:1 ratio of urea to TA (GT_9_NaZ carbon) since this N-dC with 9:1 ratio exhibited the highest content of structural nitrogen groups, responsible for increasing conductivity.
- VN@N-dC properties can be also conveniently controlled by the variation of the salt type and composition of the precursor mixtures. For instance, increasing concentration of cesium acetate as porogen creates bigger vanadium nitrate (VN) nanoparticles with increasing specific surface areas (S_{BET}) up to 2400 m^2g^{-1} through a simple heat-treatment of mixtures consisting of a vanadium precursor ($VOCl_3$) and ionic liquid (Emim-dca) which was served as carbon/nitrogen precursors. It was also observed that the size of VN nanoparticles is smaller when Zinc acetate or mixtures of Zinc acetate and cesium acetate are used as porogens. Moreoever, textural properties can be tuned by using different vanadium precursor since NH_4VO_3 promotes mesopososity whereas $VOCl_3$ promotes micropososity.
- Finally, electrochemical characterization of as-synthesized materials in both aqueous electrolyte and ionic liquids demonstrated that the physico-chemical properties of N-dC and VN@N-dC have a significant influence on the electrochemical properties of these materials. Moreover, the electrochemical performance of N-dC and VN@N-dC was also highly influenced by the different intrinsic properties of the electrolytes used during measurement. In general, about double values of specific capacitance (C_{am}) were obtaining for N-dC in 1 M H_2SO_4 in comparison with $PYR_{14}FSI$ electrolyte probably due to the difference in effective surface area that can be accessed by ions of the respective electrolyte (*i.e.,* $S_{eff>0.53\ nm}$=949 m^2g^{-1} and $S_{eff>1.1\ nm}$=517 m^2g^{-1} for H_2SO_4 and $PYR_{14}FSI$, electrolytes respectively). The highest C_{am} was obtained for the carbon synthesized with mixtures of 9:1 ratio of urea to TA and 1:3 ratios of recursors (urea+TA) to NaCl/$ZnCl_2$ (GT_9_NaZ carbon) (295 Fg^{-1} in 1 M H_2SO_4 and 110 Fg^{-1} in $PYR_{14}FSI$ electrolyte). This carbon (GT_9_NaZ) exhibited an optimal combination of textural properties, nitrogen content, and high electrical conductivity. Due to the wide electrochemical stability window (ESW) of ionic liquids, supercapacitors using $PYR_{14}FSI$ electrolyte were charged up to 3.5 V,

resulting in devices with higher energy density than those with aqueous electrolytes that were charged only to 1 V.

- VN@N-dC composites were characterized in two ionic liquids having the same cation and different anion; $PYR_{14}TFSI$ and $PYR_{14}FSI$. Capacitive performance of VN@N-dC materials in $PYR_{14}FSI$ were slightly better than $PYR_{14}TFSI$ probably due to the smaller size of FSI anion and its higher ionic conductivity of $PYR_{14}FSI$ electrolyte. The highest specific capacitance (C_{am}) and energy density (E_{real}) was exhibited by the VN@N-dC composites synthesized with highe content of CsAc and $VOCl_3$ vanadium precursor (VN@N-dc-1000-CsAc-$VOCl_3$), reaching about 125 Fg^{-1} and 37 $Whkg^{-1}$, respectively. The VN nano particle shows significant improvement of C_{am} and E_{real} by 13-15 % from that of the best performing N-dC (GT_9_NaZ) in the same electrolyte ($PYR_{14}FSI$). In conclusion, those results indicate that optimizing parameters (precursor's composition, salt type and composition) will lead to the best synergetic properties of the composite material as electrode for high performance supercapacitors.

ii) For the first time, all-solid state supercapacitors (SCs) based on innovative ionic liquid based polymer electrolyte (IL-b-PE) was developed. Those solid state supercapacitors might be charged at an operating voltage as high as 3.5 V due to the high electrochemical stability of developed polymer electrolytes (IL-b-PE). Both the high operating voltage and the high capacitance values resulted in solid state supercapacitors with excellent energy densities.

After synthesizing innovative carbon based nanocomposite materials as electrode for supercapacitors, another objective of the PhD Thesis is to synthesize novel polymer electrolytes and develop high performance all-solid state supercapacitors without additional separator. Initially, an ionic liquid based polymer electrolyte (IL-b-PE) was developed by combining a polymeric ionic liquid (PIL), poly(diallyldimethylammonium) bis(trifluoromethanesulfonyl)imide (pDADMATFSI) and a ionic liquid ($PYR_{14}TFSI$). After optimizing the impregnation of electrodes and the ratio of polymer electrolyte to active material other polymer electrolytes were developed by mixing the same PILTFSI with four different ionic liquids. Specific conclusions are briefly explained as follow:

- It was realized that impregnation of carbon electrodes with IL-b-PE enhances the capacitive performance of solid state supercapacitors compared with those assembled by sandwiching the IL-b-PE membrane between two carbon electrodes. In the latter case, the IL-b-PE membrane cannot fill into the small

pores of carbon electrodes and, consequently the formation of the double layer is limited to the geometrical area of electrodes.

- The optimum ratio of IL-b-PE to active material of electrode was 7. Below this ratio the impregnation process was not homogeneous and above 7 ratio, the resistance of solid SCs increases due to the increasing thickness of polymer IL-b-PE thin layer between the two carbon electrodes.
- Physicochemical properties such as ionic conductivity, thermal and electrochemical stability of polymer electrolytes were strongly affected by the chemical nature of ILs embedded in the polymer matrix, which consequently influences the capacitive performance of all-solid state SCs. For instance, IL-b-PE having IL with TFSI anion (0.8 nm diameter) leads to polymer electrolytes (IL-b-PE1 and IL-b-PE3) stable up to 400 ^{o}C, with acceptable range of ionic conductivities at 25 ^{o}C (0.41 $mScm^{-1}$ and 0.86 $mScm^{-1}$, respectively). Moreover, ionic conductivity of IL-b-PE was further increased up to 2.1 $mScm^{-1}$ by embedding ILs containing relatively smaller size of anions such as such as FSI (0.3 nm) in IL-b-PE2 (2.1 $mScm^{-1}$) and DCA (0.24 nm) in IL-b-PE4 (2.09 $mScm^{-1}$). In addition ESW was found to be wider (up to 3.5 V) for IL-b-PE containing ILs with pyrrolidinium cation and TFSI as well as FSI anions compared to IL-b-PE containing imidazolium cation and DCA anion.
- Electrochemical performance of solid state supercapacitors was found to be dependent on the chemical composition of the IL-b-PE. When supercapacitors were charged/discharged at moderate voltage of 2.5 V, the behavior of solid state supercapacitors based on IL-b-PE2 (with $PYR_{14}FSI$) and IL-b-PE3 (with HEMimTFSI) was better than for SCs with IL-b-PE1 (with $PYR_{14}TFSI$), possibly due to their higher ionic conductivities. However, only supercapacitors assembled with IL-b-PE1 and IL-b-PE2 were able to withstand operating voltages as high as 3.5 V. At this voltage, the performance of supercapacitors based on IL-b-PE2, with high conductivity and appropriate electrochemical stability, was slightly better than supercapacitors based on IL-b-PE1, reaching record values of C_{am}, E_{real} of about 150 Fg^{-1}, 36 $Whkg^{-1}$, respectively. These results confirm that the performance all solid state supercapacitors is determined by the combined effect of IL embedded in the polymer matrix, and the impregnation ratios of IL-b-PE to mass of active material of electrodes.
- The performance of all solid state supercapacitors based on IL-b-PE from this PhD Thesis is better than other solid supercapacitors based on conventional polymer electrolytes reported in literature. This result is achieved by conscious selection of stable polymer matrixes such as PILTFSI and compatible ILs as well

as integrating and optimizing IL-b-PE with carbon electrodes. In conclusion, by combining different designing parameters of supercapacitors, optimizing electrode materials, and polymer electrolytes, all solid-state supercapacitors will turn over a new leaf and its flexible applications and availability in the market niche will be increased in the near future.

6.2. Conclusiones

Esta tesis doctoral aborda el reto que supone la creciente demanda de nuevos materiales para electrodos y electrolitos poliméricos innovadores para su aplicación en supercondensadores de altas prestaciones. Las principales conclusiones de esta tesis se presentan en dos secciones basadas en los resultados obtenidos y discutidos en detalle en cada capítulo. Las dos conclusiones principales siguientes hacen referencia a los innovadores nanocomposites de materiales carbonosos y al nuevo electrolito basado en líquido iónico polimérico para el desarrollo de supercondensadores de altas prestaciones. Específicamente, los resultados de la tesis revelan que:

i) El comportamiento capacitivo del carbón dopado con nitrógeno (N-dC) y los composites de nanopartículas de nitruro de vanadio (VN@N-dC) como electrodos para supercondensadores está marcado por la combinación de los efectos sinérgicos de las propiedades físico-químicas de los materiales activos del electrodo y las propiedades intrínsecas de los electrolitos.

El método elegido para la síntesis de los carbones dopados con nitrógeno de alta porosidad y los composites con nanopartículas de nitruro de vanadio es sencillo y consta de una sola etapa. Dicho método se denomina “salt templating” y permite el ajuste del área superficial, el tamaño de poro, volumen de poro y el tamaño de nanopartícula utilizando sales como agentes porógenos. Se observa que las propiedades morfológicas de los materiales carbonosos (N-dC) y de los composites (VN@N-dC) así sintetizados están fuertemente influenciados por la concentración molar de los respectivos precursores y la cantidad y naturaleza de la sal utilizada como porógeno durante el tratamiento térmico. Específicamente los resultados revelan que:

- Generalmente, el área específica superficial de N-dC disminuye entre un 10-40% respecto de la obtenida con el carbón no dopado, debido al colapso de las paredes del carbón y al bloqueo de poros primarios por el dopaje con nitrógeno en la matriz del carbón. El uso de un ratio másico de sal $NaCl/ZnCl_2$ pequeño (1:1) favorece la formación de alta microporosidad,

con un área específica superficial (S_{BET}) de 1197 m^2g^{-1} durante el tratamiento térmico de la mezcla de urea y ácido tánico (TA) (9:1, urea:TA), mientras que incrementando el ratio de sal (1:3, 1:5 y 1:7) se genera mesoporosidad adicional con un S_{BET} hasta 1353 m^2g^{-1}. Cambiando la sal por $LiCl/ZnCl_2$ se consigue un aumento de S_{BET} llegando hasta 1409 m^2g^{-1}, mientras que con el uso de la sal eutéctica $KCl/ZnCl_2$ se obtienen menores valores de S_{BET} (~1251 m^2g^{-1}), lo que no supone una mejora significativa de la morfología o las propiedades texturales comparado con otros carbones.

- El contenido de nitrógeno incorporado en N-dC se incrementó proporcionalmente desde 0.72% hasta 8.8% con el aumento en el contenido de urea en la mezcla de precursor de 0:1 hasta 17:1 (urea:TA), respectivamente. Sin embargo, la conductividad eléctrica de N-dC no aumentó de manera directamente proporcional con el contenido de nitrógeno, pero sí con los grupos funcionales de nitrógeno incorporados en la matriz carbonosa. De hecho, la mayor conductividad, 76 Scm^{-1} (casi 8 veces mayor que la conductividad del carbón no dopado) se obtuvo con un ratio 9:1 de urea a TA (GT_9_NaZ carbón), debido a que este N-dC presenta la mayor cantidad de grupos nitrogenados estructurales, responsables del aumento de la conductividad.
- Las propiedades de los composites VN@N-dC pueden ser controladas mediante la variación del tipo de sales y su composición en la mezcla inicial con el líquido iónico (Emim-dca) que hace la función de precursor de carbón y de nitrógeno. Por ejemplo, el aumento de la concentración de CsAc en una mezcla con precursor de vanadio ($VOCl_3$) y líquido iónico (Emim-dca) da lugar a composites con nanopartículas de nitruro de vanadio (VN) más grandes y a un incremento en el área superficial específica (S_{BET}) alcanzando valores de 2400 m^2g^{-1}. También se observa que el tamaño de las nanopartículas de VN es menor cuando se usa como porógeno acetato de zinc (ZnAc) o mezclas de acetato de zinc y acetato de cesio. Además, las propiedades texturales pueden controlarse mediante el uso de diferentes precursores de vanadio ya que se observó que el NH_4VO_3 favorece la mesoporosidad mientras que el $VOCl_3$ favorece la microporosidad en los materiales compuestos.
- Finalmente, la caracterización electroquímica de estos materiales en electrolitos acuosos y en líquidos iónicos, demostró que las propiedades físico-químicas de N-dC y VN@N-dC tienen una influencia significativa en sus propiedades electroquímicas. Además, el comportamiento

electroquímico de N-dC y VN@N-dC está también fuertemente influenciado por las diferentes propiedades intrínsecas de los electrolitos utilizados. En general, se obtienen valores de capacitancia específica (C_{am}) del doble para N-dC en 1 M H_2SO_4 en comparación con el electrolito $PYR_{14}FSI$, probablemente debido a la diferencia en el área efectiva a la que tienen acceso los iones de cada electrolito (*i.e.,* $S_{eff>0.53\ nm}$=949 m^2g^{-1} y $S_{eff>1.1\ nm}$=517 m^2g^{-1} para H_2SO_4 y $PYR_{14}FSI$, respectivamente). La C_{am} más alta se obtuvo para el carbón sintetizado con mezclas de ratio 9:1 de urea a TA y ratio 1:3 de precursor (urea+TA) para $NaCl/ZnCl_2$ (GT_9_NaZ carbón) (295 Fg^{-1} en 1 M H_2SO_4 y 110 Fg^{-1} en electrolito $PYR_{14}FSI$). Este carbón (GT_9_NaZ) presenta una combinación óptima de propiedades texturales, contenido en nitrógeno y alta conductividad eléctrica. Debido a la ancha ventana de estabilidad electroquímica (ESW) de los líquidos iónicos, los supercondensadores con $PYR_{14}FSI$ como electrolito pudieron ser cargados hasta 3.5V, obteniendo dispositivos con mayor densidad de energía que aquellos con electrolitos acuosos que se cargaron hasta sólo 1 V.

- Los composites de VN@N-dC fueron caracterizados en dos líquidos iónicos con el mismo catión y diferente anión; $PYR_{14}TFSI$ y $PYR_{14}FSI$. El comportamiento capacitivo en $PYR_{14}FSI$ fue ligeramente mejor que en $PYR_{14}TFSI$, probablemente debido al menor tamaño del anión FSI y la mayor conductividad iónica del $PYR_{14}FSI$. Los valores más altos de capacitancia específica y densidad de energía fueron obtenidos para el composite VN@N-dc-1000-CsAc-$VOCl_3$, sintetizado con el mayor contenido de CsAc y utilizando $VOCl_3$ como precursor de vanadio. Estos parámetros alcanzaron valores de 125 Fg^{-1} y 37 $Whkg^{-1}$, respectivamente. Los composites de VN@N-dC mostraron una mejora significativa en C_{am} y E_{real} del 13-15 % respecto del mejor resultado de N-dC (GT_9_NaZ) en el mismo electrolito ($PYR_{14}FSI$). En conclusión, estos resultados indicaron que la optimización de parámetros (composición del precursor, tipo y composición de sal) conduce a las mejores propiedades sinérgicas de los materiales compuestos para electrodos de supercondensadores de altas prestaciones.

ii) Por primera vez han sido desarrollados SCs en estado sólido con electrolitos poliméricos basados en nuevos líquidos iónicos (IL-b-PE). Estos supercondesadores en estado sólido pueden ser cargados a potenciales de operación tan altos como 3.5 V, debidos a la alta estabilidad electroquímica de los electrolitos poliméricos desarrollados. El alto voltaje de operación y

los altos valores de capacitancia dieron lugar a SCs sólidos con excelentes densidades de energía.

Después de la síntesis de materiales carbonosos innovadores como electrodos para SCs, otro objetivo de la tesis es la síntesis de nuevos electrolitos poliméricos y el desarrollo de SCs sólidos de altas prestaciones. Inicialmente, se sintetizó un electrolito polimérico (IL-b-PE) mediante la combinación de un líquido iónico polimérico (PIL), poly(diallyldimethylammonium) bis(trifluoromethanesulfonyl)imide (pDADMATFSI) y un líquido iónico de similar naturaleza ($PYR_{14}TFSI$). Tras la optimización del proceso de impregnación de los electrodos y la determinación del ratio óptimo de electrolito polimérico/material activo, se desarrollaron electrolitos poliméricos diferentes mediante la mezcla del mismo PILTFSI con cuatro líquidos iónicos diferentes. Las conclusiones específicas son resumidas a continuación:

- La impregnación de los electrodos de carbón con IL-b-PE mejora el comportamiento capacitivo de los supercondensadores en estado sólido en comparación con aquellos en los cuales el montaje se realiza poniendo una membrana de IL-b-PE entre dos electrodos de carbón. En este último caso, la membrana de IL-b-PE no puede llegar a los pequeños poros de los electrodos de carbón y por consiguiente la formación de la doble capa está limitada al área geométrica de los electrodos.
- El ratio óptimo de IL-b-PE y material activo de electrodo es 7. Por debajo de este ratio el proceso de impregnación no es homogéneo y por encima del mismo, la resistencia de los supercondensadores sólidos se incrementa debido al aumento del espesor de la fina capa de polímero IL-b-PE entre los dos electrodos de carbón.
- Las propiedades fisicoquímicas como conductividad iónica y estabilidad térmica y electroquímica de los electrolitos poliméricos se ve fuertemente afectada por la naturaleza química de los ILs embebidos en la matriz polimérica, como consecuencia, el comportamiento capacitivo de los SCs en estado sólido también está afectado. Por ejemplo, el IL-b-PE que tiene un IL con anión TFSI (0.8 nm de diámetro) conduce a electrolitos poliméricos (IL-b-PE1 y IL-b-PE3) estables hasta 400ºC, con un rango de conductividad iónica aceptable a 25ºC (0.41 $mScm^{-1}$ y 0.86 $mScm^{-1}$, respectivamente). Además, la conductividad iónica de IL-b-PE aumenta hasta 2.1 $mScm^{-1}$ cuando se utilizan ILs que contienen aniones relativamente pequeños como FSI (0.3 nm) en IL-b-PE2 (2.1 $mScm^{-1}$) y DCA (0.24 nm) en IL-b-PE4 (2.09

mScm^{-1}). Además, la ESW es más ancha (hasta 3.5 V) en electrolitos poliméricos que contienen ILs con catión pirrolidinio y TFSI y FSI como aniones en comparación con aquellos con ILs con catión imidazolio o anión DCA.

- El comportamiento electroquímico de los SCs sólidos depende de la composición química del electrolito polimérico (IL-b-PE). Cuando los SCs se cargan/descargan a voltajes moderados de 2.5 V, el SCs con IL-b-PE2 ($PYR_{14}FSI$) y IL-b-PE3 (HEMimTFSI) presentaron mejor comportamiento que aquellos SCs con IL-b-PE1 ($PYR_{14}TFSI$), posiblemente debido a que su conductividad iónica es más alta. Sin embargo, sólo los SCs ensamblados con IL-b-PE1 y IL-b-PE2 fueron capaces de aguantar voltajes de operación tan altos como 3.5 V. A este voltaje, el comportamiento de los SCs con IL-b-PE2, que presenta alta conductividad y apropiada estabilidad electroquímica, fue ligeramente mejor que los supercondensadores basados en IL-b-PE1, alcanzando valores récord de C_{am} y E_{real} de 150 Fg^{-1} y 36 Whkg^{-1}, respectivamente. Estos resultados confirman que el comportamiento de los SCs sólidos está determinado por el efecto combinado del tipo de IL embebido en la matriz polimérica, y el ratio de impregnación electrolito polímero/material activo de los electrodos.
- El comportamiento de los SCs sólidos desarrollados en esta tesis es mejor que SCs basados en electrolitos poliméricos convencionales descritos en la literatura. Estos resultados se alcanzaron mediante una meticulosa selección de matrices poliméricas estables como PILTFSI y ILs compatibles, así como la integración y optimización de IL-b-PE con los electrodos de carbón. En conclusión, mediante la combinación de los diferentes parámetros de diseño de los supercondensadores, la optimización de los materiales de electrodo y de los electrolitos poliméricos, los SCs en estado sólido se convertirán en una nueva generación de dispositivos para aplicaciones flexibles y su disponibilidad en el mercado aumentará en un futuro próximo.

6.3. Future Perspectives

In spite of considerable achievements during this thesis, yet some challenges remained to increase specific capacitance, and real specific energy density of supercapacitors without deteriorates its power density and safety. A number of directions can be identified that require further improvements in the future:

i) *Innovative Nanocomposite Materials:* Combining/doping different materials to design innovative nanocomposite is a vital approach for *further* development of high capacitive performance of supercapacitors in the future. Nanocomposite materials can have a synergistic effect through enhancing specific surface area, inducing porosity, facilitating electron and ion conduction, improving cycling stability, increasing wettability of electrode, providing short/diffusion path lengths for ions and electrons leading faster kinetics, creating more efficient interfaces between electrolytes and electrodes, increasing active sites, resulting fast charge-discharge and providing extra pseudocapacitance even at high current densities. As a result, the obtained nanocomposite materials can overcome the shortcoming of the individual substances and incorporate the advantages of all constituents of the nanocomposite materials.

ii) *Optimizing Textural Properties of Electrode Materials:* According to some studies, matching the pore size of electrode materials with the ion size of electrolyte would improve the overall performance of supercapacitors. However, some discrepancies and different theories have been reported in literature to explain the relationship between pore size of electrode materials and size of ions and electrochemical properties of materials. To address this issue, more fundamental experiments are still required to fully understand the relationship.

iii) *Designing Innovative Ionic Liquid based Polymer Electrolytes with High Ionic Conductivity:* There are still opportunities to develop IL-b-PE with better ionic conductivity and ESW by designing and playing with the chemical structure of polymer and monomers or embedding different types of pure IL electrolytes into the polymer matrix.

iv) *Developing New Generation of Flexible Solid-State Supercapacitors:* This might be achieved by combining the nanocomposites electrode materials that contain active sites and innovative new polymer electrolytes that would able to undergo redox reactions and interact with the active sites of electrode materials, thereby exhibiting pseudocapacitance contributions. For this purpose, the innovative polymer electrolyte should contain different functional groups in the polymer matrix, bearing multifunctional groups. This might be achieved by the utilization of macromolecule engineering and/or copolymer engineering methods for the development of innovative polymer structures as graft-copolymers block copolymers (di- or tri-block copolymers), or random block copolymers, e.t.c...

LIST OF PUBLICATIONS AND PRESENTATIONS

LIST OF PUBLICATIONS AND PRESENTATIONS

Peer-Reviewed Publications

Published

2016 **G. A. Tiruye,** D.M. Torrero, J. Palma, M. Anderson, R. Marcilla, 2016: "Performance of All-Solid State Supercapacitors based on Polymer Electrolytes Containing Different Ionic Liquids", Journal of Power Resources, DIO. 10.1016/j.jpowsour.2016.03.044 (in Press), Available online 17 March 2016.

2015 **G. A. Tiruye,** D.M. Torrero, J. Palma, M. Anderson, R. Marcilla, **2015**: "All-Solid State Supercapacitors Operating at 3.5 V by Using Ionic Liquid based Polymer Electrolytes". Journal of Power Sources, 2015, 279, 472-480.

2015 **G. A. Tiruye,** D.M. Torrero, J. Palma, M. Anderson, R. Marcilla, **2015**: "Desarrollo de Supercondensadores Sólidos mediante el uso de Electrolitos Poliméricos basados en Líquidos Iónicos". REVISTA DE PLÁSTICOS MODERNOS, 2015,109, 702.

2014 N. Fechler, **G. A. Tiruye**, R. Marcilla, M. Antonietti, **2014**: "Vanadium Nitride@N-doped Carbon Nanocomposites: Tuning of Pore Structure and Particle Size through Salt Templeting and Its Influence on Supercapacitance on IL Media". RSC Advances, 2014, 4, 51, 26981.

Book chapter

2015 **G. A. Tiruye,** R. Marcilla, 2015. "Ionic Liquids and Polymers in Energy": D. Mecerreyes .ed. Applications of Ionic Liquids in Polymer Science and Technology, pp. 199-229, Springer-Verlag Berlin Heidelberg, **DOI**:10.1007/978-3-662-44903-5_8, **ISBN**:978-3-662-44903-

Work in progress

2016 **G. A. Tiruye,** D.M. Torrero, T. Berthold, M. Antonietti, N. Fechler, R. Marcilla, 2016: "Enhanced Electrochemical Performance of Porous Nitrogen-Doped Carbon in Ionic Liquuid based Supercapacitor"(*to be submitted*)

Oral Presentations in Conferences and Meetings

Peer-Reviewed Oral Presentation in conferences

2015 **G. A. Tiruye,** D.M. Torrero, J. Palma, M. Anderson, R. Marcilla, 2015: "All-Solid State Supercapacitors based on Poly (Ionic Liquids) Matrix Embedded with Different Ionic Liquids", ISEECap2015, Montpellier, France, 8-12 June 2015

2014 **G. A. Tiruye,** D.M. Torrero, J. Palma, M. Anderson, R. Marcilla, 2014: "All-Solid State Supercapacitors Based on the Binary Mixtures of Ionic Liquids and Polymeric Ionic Liquids", 65th annual meeting of International Society of Electrochemistry, Lausanne, Switzerland, 31 August -5 September 2014

Oral Presentations in Workshops and Meetings

2015 **G. A. Tiruye,** D.M. Torrero, J. Palma, M. Anderson, R. Marcilla, 2015: "Performance of All-Solid State Supercapacitors based on Polymer Electrolytes Containing Different Ionic Liquids". 4th Annual Young Researchers Workshop, IMDEA Energy Institute Madrid, Spain, 11 December 2015

2015 **G. A. Tiruye**, "N-doped Carbon for All-Solid State Supercapacitors: To Empower the Future", Max Planck Institute of Colloid and Interface class trip 2015, Feriendorf an der Ostee, Wholenberg, Germany, 04-06 May, 2015

2015 **G. A. Tiruye,** R. Marcilla, 2015: "All solid State Supercapacitors based Ionic Liquid Based Polymer Electrolytes with Mixed Counter

Anions". RENAISSANCE Project meeting in Liege, Belgium, 5-6 February, 2015

2014 **G. A. Tiruye,** R. Marcilla, 2014: "All solid State Supercapacitors Based on Ionic Liquid Based Polymer Electrolytes and Carbon Electrodes", 3rd Annual Young Researchers Workshop, IMDEA Energy Institute, Madrid, Spain, 12 December 2014

2014 **G. A. Tiruye,** R. Marcilla, 2014: "All-Solid State Supercapacitors based on Solid Electrolytes", Summer school on "Polymer for Sustainable World" San-Sebastian, Spain, 24-27 June, 2014

2014 **G. A. Tiruye,** R. Marcilla, 2014: "Application of Innovative Polyelectrolytes and Graphitic Materials in Supercapacitors", RENAISSANCE ITN Project Mid-Term Meeting at P&G Brussels, Belgium, 13-14 March 2014

2013 **G. A. Tiruye**, N. Fechler, M. Antonietti, R. Marcilla 2013: "The electrochemical performance of supercapacitors based on N-doped carbon electrodes and ionic liquids as electrolytes", Renaissance. ITN Meeting, IMDEA Energy Institute, Madrid, Spain. 13-14 October 2013

2013 **G. A. Tiruye,** R. Marcilla, 2013: "Application of Innovative Polyelectrolytes and Graphitic Materials in Supercapacitors", RENAISSANCE ITN Project Ecole Nationale Supérieure de Chimie, Biologie et Physique (ENSCBP), Bordeaux, France, 30-30 May, 2013

Poster Presentation

2015 **G. A. Tiruye,** D.M. Torrero, J. Palma, M. Anderson, R. Marcilla, 2015: "Distinct Performance of Ionic Liquid based Polymer Electrolytes based on Incorporated Ionic Liquids", 4th Young researchers Seminar IMDEA Energy Institute, 11th December 2015

2015 D. M. Torrero, **G. A. Tiruye**, T. Berthold, M. Antonietti, N. Fechler, R. Marcilla, 2015: "Performance of Nitrogen doped Carbons as Electrode in Ionic Liquid Based Supercapacitors", 4th

Young researchers Seminar IMDEA Energy Institute, 11th December 2015

2014 **G. A. Tiruye,** J. Palma, M. Anderson, R. Marcilla, 2014: "All-Solid State SCs based on IL based Polymer Electrolytes and Activated Carbon Electrodes", 3th Young researchers Workshop, IMDEA Energy Institute, 12th December 2014

2014 **G. A. Tiruye**, N. Fechler, M. Antonietti, R. Marcilla, 2014: "The Performance of Vanadium Nitride@ N-doped Carbon as Electrode Materials for Supercapacitors with Ionic Liquid Electrolytes". Power the Future 2014, Vitoria, Spain, 1-4 April, 2014

2013 **G. A. Tiruye,** J. Palma, M. Anderson, R. Marcilla, 2013, "Application of Ionic Liquids in Supercapacitors", Summer School on Ionic Liquids, O Grove, Spain 9-12 June, 2013

"Logic will get you from A to Z, Imagionation will get you everywhere"

Albert Einstein